

University of Trento
University IUAV of Venezia

Yufan Huang

SEISMIC BEHAVIOR OF CONCRETE FILLED STEEL TUBULAR BUILT-UP COLUMNS

Advisor:

Prof. Enzo Siviero
Università IUAV di Venezia, Venice, Italy

Co-Advisors:

Prof. Bruno Briseghella, Prof. Baochun Chen
Fuzhou University, Fuzhou, China
Prof. Tobia Zordan
Tongji University, Shanghai, China

2015

UNIVERSITY OF TRENTO

Engineering of Civil and Mechanical Structural Systems

Final Examination 22 / April / 2015

Board of Examiners

Prof. Jiří Máca	(Czech Technical University in Prague)
Prof. Maria Rosaria Pecce	(Università degli Studi del Sannio)
Prof. Daniele Zonta	(Università degli Studi di Trento)
Dott. Paolo Clemente	(UTPRA - Unità Tecnica Caratterizzazione, Prevenzione e Risanamento Ambientale ENEA CRE Casaccia)
Dott. Loris Vincenzi	(Università di Modena e Reggio Emilia)

SUMMARY

With the advantages of CFST built-up columns, including the higher confinement in the concrete, delay of the steel local buckling, higher compressive and flexural strength, earthquake and fire resistance, rapid construction, savings in the construction costs, etc. CFST built-up columns are increasingly adopted in structural members with larger load eccentricity ratio and slenderness ratio, such as stadium, industrial buildings, bridge pier and pillar, and electrical transmission tower. However, the research is mainly focused on static performance, seldom research has been reported on the dynamic behavior of CFST built-up columns.

The present research investigates the seismic behavior of CFST built-up columns. A detailed literature survey on the CFST built-up structures, including mechanical characteristics, applications, ductility in seismic design, previous experimental researches, and finite element formulation, is firstly illustrated. Six specimens with different grades of concrete and brace arrangements are designed and tested subjected to cyclic loading. The hysteretic behavior, such as failure mode, deformed shape, displacement ductility, rigidity and strength degradation, and energy dissipation capacity of test specimens are discussed. The corresponding validated finite element model (FEM) simulations are developed for parametric analysis, to discuss the hysteretic behavior, affected by axial load ratio, chord spacing, brace spacing, diameter to thickness ratio, and steel yield strength. Results indicate that the hysteretic characteristics of specimens are saturated and exhibited good ductility. The concrete strength and steel yield strength played a slight effect to the displacement ductility factor. While the ductility will be significantly affected by axial load ratio and geometrical types. Based on extended parametric analysis and regression analysis, a simplified method, consisted by equivalent slenderness ratio, axial load ratio and steel yield strength, is proposed to calculate the displacement ductility factor of CFST battened columns and laced columns, respectively. The accuracy is validated with test results. After that, to investigate the seismic performance of built-up columns used in practice, an innovative lightweight bridge with CFST composite truss girder and CFST lattice pier is studied as case study. For the purpose, FEM simulation and shaking table test are carried out. The FEM results agree with experimental data. In addition, the plastic hinges were predicted under transverse and longitudinal excitation respectively, revealed that CFST built-up columns has a favorable seismic performance.

SOMMARIO

Le colonne tralicciate realizzate con tubi riempiti in calcestruzzo stanno diventando sempre piu' diffuse per le loro caratteristiche di leggerezza, facilita' di costruzione ed economicita', unite ad una buona resistenza a compressione, flessione, instabilita', il benefico effetto di confinamento del calcestruzzo, il buon comportamento sismico e al fuoco. In particolare sono utilizzate per elementi snelli compressi e soggetti a carico fortemente eccentrico in strutture quali stadi, edifici industriali, pile da ponte e torri per l'elettricit 

In questa ricerca si indaga il comportamento sismico di colonne tralicciate realizzate con tubi iniettati in calcestruzzo (CFST). Nei primi capitoli si illustra, sulla base di una dettagliata ricerca bibliografica, il loro comportamento meccanico, e in particolare quello sismico, la loro simulazione con modelli EF e le applicazioni piu' significative.

Successivamente si riportano la progettazione e i risultati di una campagna di prove sperimentali cicliche su pile in CFST aventi differenti geometrie e classi di cls realizzata presso il laboratorio di Strutture del College of Civil Engineering della Fuzhou University (Fuzhou, China). I risultati ottenuti in termini di comportamento isteretico, modalita' di rottura, duttilita', degrado di rigidezza ed energia dissipata sono discussi nel dettaglio.

In seguito, un modello EF precedentemente implementato e tarato in base ai risultati delle prove sperimentali viene utilizzato per un'analisi parametrica al fine di indagare la risposta strutturale in funzione della geometria dei controventi, spessori e diametri dei tubi, caratteristiche dei materiali.

I risultati hanno confermato il buon comportamento sismico della tipologia di colonne analizzate, evidenziando la sensibilita' nella risposta alla variazione della geometria adottata e all'eccentricita' del carico.

In base all'estesa analisi parametrica eseguita viene successivamente proposta una formulazione semplificata per determinare la duttilita' in spostamento di colonne CFST tralicciate con controventi diagonali o orizzontali.

Infine si considera come caso studio un ponte recentemente realizzato in Cina con pile tralicciate in CFST alte attorno ai 100 m con soli controventi orizzontali.

Il comportameto sismico di tale ponte viene analizzato sia teoricamente con diversi modelli EF a scala diversa che sperimentalmente con un'ampia campagna su tavole vibranti realizzata su un provino in scala 1:8 rappresentativo di 2 campate (tre pile) eseguita anche questa presso la Fuzhou University.

I risultati ottenuti hanno confermato il buon comportamento sismico di tale tipologia strutturale e la correttezza delle ipotesi fatte nella fase di modellazione strutturale.

DEDICATION

*To my parents
and
my wife*

ACKNOWLEDGEMENTS

I would like to express my sincere gratitude to my advisor Prof. Enzo Siviero and Prof. Baochun Chen for the opportunity of my Ph.D. study. Valuable learning opportunities inspires my enthusiasm on scholar. Their knowledge and expertise also have been a precious reference during these three years.

I would like to express my special appreciation and thanks to Prof. Bruno Briseghella and Prof. Tobia Zordan for their great kindest helps and advices on my studies. They have supported me throughout my thesis with their patience and knowledge, also create harmonious atmosphere and comfortable writing environment in Bolina Srl. during these three years.

Thanks go to Prof. Qingxiong Wu in Fuzhou University, who gives me some advices to my studies. Thanks to Structural Laboratory of Fuzhou University provides me with the help in specimen test, and master students from SIBERC Center, such as Changsheng Liu, Yinhua Lv, and Huixiong Cai, who have participated with me during research and their invaluable contribution to my data collection.

I want to thank the University of Trento for offering me the Ph.D. fellowship to commence this thesis.

I have also enjoyed a lot of support and sheared countless happiness in last three years. Thanks to all my dear friends I have meet in Italy.

Lastly, I want to give special thanks to my wife, my parents and my parents-in-law, who give me selfless love and strong support to my studies.

CONTENTS

SUMMARY	I
SOMMARIO	III
DEDICATION	V
ACKNOWLEDGEMENTS.....	VII
CONTENTS.....	IX
LIST OF FIGURES	XII
LIST OF TABLES.....	XVII
CHAPTER 1	1
1. INTRODUCTON	1
1.1. The Concept of Concrete Filled Steel Tubular Built-up Columns.....	1
1.2. The Advantages and Disadvantages of CFST Built-up Columns.....	3
1.2.1 <i>Advantages</i>	3
1.2.2 <i>Disadvantages</i>	5
1.3. Critical Issues	6
1.4. The Objectives and Methodologies.....	8
1.5. Structure of the Thesis	9
CHAPTER 2	11
2. STATE-OF-ART	11
2.1. Application of CFST Truss Structure	11
2.1.1 <i>Buildings</i>	11
2.1.2 <i>Bridges</i>	13
2.1.3 <i>Electrical transmission tower</i>	18
2.2. Ductility in Seismic Design	19
2.2.1 <i>Bridge pier failure in earthquakes</i>	19
2.2.2 <i>Ductility definition</i>	21
2.2.3 <i>Approaches in various codes</i>	22
2.3. Previous Experimental Research Studies.....	26
2.3.1 <i>Static Performance</i>	27
2.3.2 <i>Dynamic Performance</i>	30
2.4. Finite Element Formulation.....	39

2.4.1 Fiber beam-column element.....	41
2.4.2 Truss finite element model.....	44
2.4.3 Finite element implementation.....	47
2.4.4 Material Constitutive	49
CHAPTER 3	61
3. HYSTERETIC TESTING OF CFST BUILT-UP COLUMNS	61
3.1. Introduction.....	61
3.2. Specimen Design and Fabrication.....	61
3.3. Material Properties.....	66
3.4. Test Setup and Procedure	67
3.5. Experimental Results and Discussions	69
3.5.1 Failure Modes and Deformed Shapes.....	69
3.5.2 Load Displacement Hysteretic Curves.....	72
3.5.3 Displacement Ductility.....	74
3.5.4 Rigidity and Strength Degradation.....	77
3.5.5 Energy Dissipation Capacity	79
CHAPTER 4	81
4. NUMERICAL ANALYSIS OF HYSTERETIC BEHAVIOR.....	81
4.1. Introduction.....	81
4.2. Proposed Finite Element Model.....	81
4.3. Finite Element Model Verification	84
4.3.1 Comparison with Test Results.....	84
4.3.2 Comparison with Previous Experimental Study	89
4.4. Parametric Analysis	96
4.4.1 Axial Load Ratio.....	97
4.4.2 Chord Spacing.....	99
4.4.3 Brace Spacing	102
4.4.4 Diameter to Thickness Ratio	104
4.4.5 Steel Yield Strength	108
4.4.6 Comparison of strength and ductility with different parameters	111
4.5. Proposed Method to Calculate Displacement Ductility Factor	112
4.5.1 Equivalent Slenderness Ratio	112
4.5.2 Regression Analysis	118
4.5.3 Error Estimation for Proposed Formula	122
CHAPTER 5	127
5. SEISMIC PERFORMANCE OF A CFST TRUSS BRIDGE	127

5.1. Case Study-Ganhaizi Bridge	127
5.2. Finite Element Model	134
5.2.1 Modelling of structure.....	134
5.2.2 Materials.....	136
5.3. Modal Analysis.....	136
5.4. Response Spectrum Analysis.....	139
5.4.1 Design conditions.....	139
5.4.2 Internal forces analysis	143
5.4.3 Displacement analysis	154
CHAPTER 6	159
6. SHAKING TABLE TEST.....	159
6.1. Introduction.....	159
6.2. Specimen Design.....	160
6.2.1 Similitude criteria theory.....	160
6.2.2 Test device	161
6.2.3 Design parameters control	163
6.2.4 Specimen manufacture	166
6.3. Test Instruments and Setup	168
6.4. Test Program	175
6.5. Dynamic Characteristics Analysis.....	175
6.6. Earthquake Response Analysis.....	178
6.6.1 Under Transverse Excitations	178
6.6.2 Under Longitudinal Excitations	181
6.6.3 Under Bi-directional Excitations.....	183
6.7. Finite Element Model Analysis.....	185
6.7.1 Finite element model.....	185
6.7.2 Validation of FEM.....	187
6.7.3 Predicted behavior of plastic zone.....	189
6.7.4 Influence of ground motions	192
CONCLUSIONS	197
BIBLIOGRAPHY	203
APPENDIX	215

LIST OF FIGURES

Fig. 1 Cross-section form: a) Two chords; b) Three chords; c) Four chords	2
Fig. 2 Types of CFST built-up columns: a) Parallel-shape; b) V-shape; c) M-shape; d) N-shape.....	2
Fig. 3 Axial compressive behavior of CFST stub column (Han et al., 2014).....	3
Fig. 4 Tianjin International Convention & Exhibition Center, China, completed in 2003	12
Fig. 5 Hengyang Heavy Machinery, China, completed in 2009	12
Fig. 6 Canton Tower, China, completed in 2010	13
Fig. 7 Cross-sectional types of CFST arch rib (Chen & Wang, 2009)	14
Fig. 8 Cross sections of arch rib (Chen & Wang, 2009).....	14
Fig. 9 Relationship between cross sections and spans (Chen & Wang, 2009).....	14
Fig. 10 Longest CFST arch bridges.....	16
Fig. 11 CFST built-up columns used for pillar (Mengdonghe River Bridge, Hunan, China, under construction)	17
Fig. 12 CFST built-up columns used for continuous beam bridge (Ganhaizi Bridge, Sichuan, China, completed in 2012)	18
Fig. 13 Zhoushan electricity pylon, China	19
Fig. 14 Confinement failure on the top of pier, Mission Gothic Overpass Bridge, Northridge Earthquake, USA, 1994	20
Fig. 15 Flexural failure of the whole bridge, Hanshin Expressway, Kobe Earthquake, Japan, 1995.....	20
Fig. 16 Shear failure of the tie beam and flexural failure at the base of column, Baihua Bridge, Wenchuan Earthquake, China, 2008	21
Fig. 17 Test photos: a) Buckling near end of the specimen; b) typical failure of the whole column (Ou et al., 2011).....	28
Fig. 18 Cross-section of tested battened specimens (Han et al., 2012)	29
Fig. 19 Failure modes of tested battened specimens (Han et al., 2012)	29
Fig. 20 Failure modes of tested laced specimens (Han et al., 2012)	30
Fig. 21 Behaviors of tubular members under monotonic axial loading (Kawano & Matsui, 1988).....	31
Fig. 22 Horizontal load-deformation relationships of different types of frame model (Kawano & Matsui, 1988).....	32
Fig. 23 Stability condition I: a) Column curves for CFTs and vacant tubes; b) M-N strength interaction (Kawano & Sakino, 2000b)	33

Fig. 24 Stability condition II: a) Column curve for pre-stretched CFT; b) L_{kr2} -D strength interaction (Kawano & Matsui, 2000b).....	35
Fig. 25 CFT truss specimen subjected to cyclically repeated horizontal loads (Kawano & Matsui, 2003).....	35
Fig. 26 The non-dimensional energy dissipation prior to the fracture w (Kawano & Matsui, 2003).....	36
Fig. 27 Global deformation and failure at the bottom of specimens (Luo, 2013)	38
Fig. 28 Comparison of force-displacement curves (Luo, 2013).....	38
Fig. 29 Schneider's FEM (Schneider, 1998)	40
Fig. 30 Hu's FEM: a) circular section; b) square section; c) square section stiffened with steel reinforcing ties forming an octagonal shape (Hu et al., 2003)	40
Fig. 31 Fiber beam-column model (Taucer et al., 1991).....	41
Fig. 32 Modelling for circular hollow sectional trusses.....	45
Fig. 33 Modelling for Vierendeel truss	46
Fig. 34 Design moment resistance of welded joints between circular hollow sections (Wardenier et al., 2010)	46
Fig. 35 Component classes in OpenSees.....	48
Fig. 36 Idealized diagram of a circular CSFT section (Denavit and Hajjar, 2010)....	52
Fig. 37 Confined concrete constitutive model proposed by Susantha et al. (Susantha et al., 2001).....	55
Fig. 38 Confined concrete constitutive model proposed by Liang and Fragomeni (Liang and Fragomeni, 2009)	57
Fig. 39 Cyclic response of uniaxial stress-strain models in OpenSees (Perea, 2010)	58
Fig. 40 Cyclic response of steel stress-strain models in OpenSees.....	59
Fig. 41 Benchmark specimen (Unit: mm).....	65
Fig. 42 Specimens with different brace arrangements (Unit: mm)	66
Fig. 43 Test setup	68
Fig. 44 Displacement loading histories	68
Fig. 45 Failure modes of CFST battened columns	70
Fig. 46 Failure modes of CFST laced columns	72
Fig. 47 Horizontal loading P versus displacement Δ hysteretic curves for all specimens	73
Fig. 48 P - Δ envelope curves	74
Fig. 49 Global P - Δ skeleton curve	75
Fig. 50 P - Δ cycles.....	75
Fig. 51 Definition of structural ductility	76
Fig. 52 Definition of rigidity coefficient K_j	78
Fig. 53 K_j - Δ/Δ_y relationship.....	78

Fig. 54 $\lambda_j\text{-}\Delta/\Delta_y$ relationship	79
Fig. 55 Cumulative energy dissipation capacities of specimens	80
Fig. 56 Finite element model in OpenSees	82
Fig. 57 Fiber section and aggregator in OpenSees.....	83
Fig. 58 Comparison of P- Δ hysteretic curves.....	86
Fig. 59 Comparison of P- Δ envelope curves.....	87
Fig. 60 Comparison of cumulative energy absorption capacities.....	88
Fig. 61 Test specimen.....	90
Fig. 62 Test device.....	91
Fig. 63 Horizontal force-displacement curves under monotonic loading	92
Fig. 64 Out-of-plane local buckling in the test (Kawano et al., 1996)	92
Fig. 65 Horizontal force-displacement curves under cyclic loading.....	93
Fig. 66 Photo of specimen SCC1 (Luo, 2013).....	94
Fig. 67 Comparison of force-displacement curves	95
Fig. 68 Parameters abbreviation	96
Fig. 69 Comparison of P- Δ hysteretic curves.....	98
Fig. 70 Comparison of P- Δ envelope curves.....	98
Fig. 71 Comparison of cumulative energy.....	99
Fig. 72 Comparison of P- Δ hysteretic curves.....	100
Fig. 73 Comparison of P- Δ envelope curves.....	101
Fig. 74 Comparison of cumulative energy.....	101
Fig. 75 Comparison of P- Δ hysteretic curves.....	102
Fig. 76 Comparison of P- Δ envelope curves.....	103
Fig. 77 Comparison of cumulative energy.....	103
Fig. 78 Comparison of P- Δ hysteretic curves.....	106
Fig. 79 Comparison of P- Δ envelope curves.....	106
Fig. 80 Comparison of cumulative energy.....	107
Fig. 81 Comparison of P- Δ hysteretic curves.....	109
Fig. 82 Comparison of P- Δ envelope curves.....	110
Fig. 83 Comparison of cumulative energy.....	110
Fig. 84 Comparison of strength and ductility with different parameters.....	112
Fig. 85 Comparison of strength and ductility with different parameters.....	112
Fig. 86 Shear deformations of battened built-up members.....	114
Fig. 87 Shear deformations of laced built-up members	116
Fig. 88 Relationship between equivalent slenderness ratio and ductility.....	118
Fig. 89 Surface fitting of ductility based on steel yield strength.....	120
Fig. 90 Surface fitting of ductility based on axial load ratio and equivalent slenderness ratio	121

Fig. 91 Surface fitting of ductility based on axial load ratio and equivalent slenderness ratio.....	122
Fig. 92 The relationship between actual data and best-fit values by residuals schematic	123
Fig. 93 Panorama of Ganhaizi Bridge.....	127
Fig. 94 Evaluation layout of Ganhaizi Bridge (Unit: cm)	128
Fig. 95 CFST trusses girder (Unit: mm)	129
Fig. 96 CFST lattice columns (Unit: mm)	130
Fig. 97 CFST composite columns (Unit: mm)	130
Fig. 98 Connection types.....	131
Fig. 99 Rubber bearing with high damping.....	131
Fig. 100 Phases on Ganhaizi Bridge during construction	133
Fig. 101 FEM of Ganhaizi Bridge.....	134
Fig. 102 FEM details	135
Fig. 103 Horizontal design acceleration response spectrum	140
Fig. 104 Chinese Seismic Ground Motion Parameter Zonation Map	141
Fig. 105 Horizontal design acceleration response spectrum	142
Fig. 106 Horizontal seismic input direction.....	143
Fig. 107 Defined points at the edge of steel tubes and concrete	144
Fig. 108 Maximum stress distribution at the edge of steel tubular sections under parallel seismic input direction.....	146
Fig. 109 Maximum stress distribution at the edge of concrete sections under parallel seismic input direction.....	148
Fig. 110 Maximum stress distribution at the edge of steel tubular sections under perpendicular seismic input direction.....	152
Fig. 111 Maximum stress distribution at the edge of concrete sections under perpendicular seismic input direction.....	154
Fig. 112 Maximum displacement distribution under parallel seismic input direction	156
Fig. 113 Maximum displacement distribution under perpendicular seismic input direction.....	157
Fig. 114 Panorama of the three bi-axial shaking table array system.....	161
Fig. 115 Schematic drawings of the system on top view	162
Fig. 116 Schematic drawings of the table on bottom view	162
Fig. 117 Elevation layout of the specimen (unit: cm)	164
Fig. 118 The drawing of girder (unit: cm)	165
Fig. 119 Elevation layout of pier (unit: cm).....	165
Fig. 120 Reinforcement of the RC webs (unit: cm).....	166
Fig. 121 Specimen manufacture.....	167

Fig. 122 Details of instruments.....	170
Fig. 123 View of instrument arrangement details	171
Fig. 124 Relationship between I and t	173
Fig. 125 Artificial seismic excitation for prototype.....	174
Fig. 126 Artificial seismic excitation for specimen	174
Fig. 127 Normalized response spectrum	174
Fig. 128 Power spectral analysis.....	176
Fig. 129 Calculation method of damping ratio (Kikunaga and Arakawa, 2012)	177
Fig. 130 Time histories of displacement under transverse excitation.....	179
Fig. 131 Maximum transverse displacement under transverse excitation.....	179
Fig. 132 Maximum transverse acceleration under transverse excitation.....	180
Fig. 133 Time histories of displacement under Longitudinal excitation	181
Fig. 134 Maximum longitudinal displacement under longitudinal excitation	182
Fig. 135 Maximum longitudinal acceleration under longitudinal excitation	183
Fig. 136 Vertical strain comparison	184
Fig. 137 Displacement comparison	185
Fig. 138 FEM details	187
Fig. 139 Comparison of displacement time histories.....	188
Fig. 140 Comparison of vertical strain envelope	189
Fig. 141 Strain envelopes at the extreme edge of steel tubes	190
Fig. 142 Displacement envelopes of CFST column	190
Fig. 143 Time histories of CFST columns.....	192
Fig. 144 Time histories of natural records.....	193
Fig. 145 Spectral characteristics	194
Fig. 146 Acceleration envelope of pier.....	194
Fig. 147 Displacement envelope of pier.....	195
Fig. 148 Time histories at the top of column	196
Fig. 149 Normalized strain envelope at the extreme edge of steel tube.....	196

LIST OF TABLES

Table 1 Longest arch bridge spans in the world (Wikipedia, 2014).....	16
Table 2 Ductility types (Ferrario, 2004).....	22
Table 3 Types of connections.....	45
Table 4 Design parameters of lattice piers in Ganhaizi Bridge	62
Table 5 Design parameters of composite piers in Ganhaizi Bridge.....	63
Table 6 Data of six specimens	66
Table 7 Material properties.....	67
Table 8 Displacement ductility coefficient	77
Table 9 Steel mechanical properties adopted in Steel02 model	85
Table 10 Steel mechanical properties adopted in Concrete02 model	85
Table 11 Displacement ductility coefficient	88
Table 12 Test parameters	90
Table 13 Specimen scantling	91
Table 14 Steel sectional properties.....	91
Table 15 Steel mechanical properties.....	91
Table 16 Specimen scantling	94
Table 17 Material mechanical properties	94
Table 18 Comparison of ductility coefficient under different axial load ratios	99
Table 19 Comparison of ductility coefficient under different chord spacing.....	101
Table 20 Comparison of ductility coefficient under different brace spacing.....	104
Table 21 Comparison of ductility coefficient under different diameter to thickness ratio	107
Table 22 Comparison of ductility coefficient under different steel yield strength ..	111
Table 23 Summary of equivalent slenderness ratio and corresponding displacement ductility ratio.....	118
Table 24 Summary of R^2 and adjusted R^2	124
Table 25 Comparisons of displacement ductility factor between test results and proposed method.....	125
Table 26 Main features of the piers	132
Table 27 Stiffness values of the bearing	135
Table 28 Concrete mechanical properties	136
Table 29 Steel mechanical properties.....	136
Table 30 Modal shapes and frequencies	138
Table 31 Modal comparison between load test and FEM.....	139
Table 32 Seismic importance factor C_i of various types of bridges.....	140

Table 33 Site coefficient C_s	141
Table 34 Design acceleration adjustment corresponding to characteristic period on the response spectrum.....	141
Table 35 The peak acceleration of horizontal design ground motion.....	142
Table 36 Maximum displacement at the top of pier under parallel seismic input direction.....	155
Table 37 Maximum displacement at the top of pier under perpendicular seismic input direction	156
Table 38 Summary of scale factors for earthquake response of structures.....	161
Table 39 Summary of equipment specification	163
Table 40 Similitude relation of quantities	172
Table 41 Material properties.....	172
Table 42 Parameters with different durable time.....	174
Table 43 Test procedure	175
Table 44 Fundamental frequency comparison between prototype and specimen	177
Table 45 Modal shape comparison between prototype and specimen.....	178
Table 46 Maximum strain under transverse excitation	181
Table 47 Maximum strain in longitudinal excitation	183
Table 48 Maximum strain comparison under different excitations	184
Table 49 Maximum displacement comparison under different excitations	184
Table 50 Fundamental frequency comparison between specimen and no mass FEM	187
Table 51 Fundamental frequency comparison between prototype and full mass FEM.....	188

1. INTRODUCTION

1.1. The Concept of Concrete Filled Steel Tubular Built-up Columns

The generalized built-up columns are a kind of compression member consisting of several identical longitudinal elements slightly separated and connected to each other at only a few places along their length (Sahoo & Rai, 2007). According to the mode of connection of the web members to the chords, it can be divided into two types of built-up columns, referred as CFST battened columns and CFST laced columns, respectively. The first type involves battens with fixed ends to the chords and functioning as a rectangular panel. The second type contains diagonals (and possibly struts) designed with pinned ends. Any hot rolled section can be used for the chords and the web members of built-up columns. However, channels or I-sections are most commonly used as chords. Their combination with angles presents a convenient technical solution for built-up columns with laces or battens. Flat bars are also used in built-up column as battens (European Committee for Standardization, 2006).

These members are frequently used as light compression members, such as struts in truss moment frames and as columns in lightweight steel structures, the most widely used is in industrial buildings. Built-up columns provide relatively light structures with a large inertia. Indeed, the position of the chords, far from the centroid of the built-up section, is very beneficial in producing a great inertia. These members are generally intended for tall structures for which the horizontal displacements are limited to low values (e.g. columns supporting crane girders).

On the other hand, it is well known that concrete filled steel tubular (CFST) members, also termed as CFT in some literatures, have an excellent performance in compression with high strength and ductility. Therefore, it can be combined with traditional built-up columns, which concrete filled steel tube columns are used for chords, and hollow steel tubes as web members connected with chords, namely as CFST laced columns. Due to the confinement of the concrete is much more likely in circular sections because the steel may develop an effective hoop tension, whereas the flat sides of a rectangular tube are not effective in resisting perpendicular pressure (Furlong R. W., 1967), circular hollow section (CHS) are more adopted in

practice, both in chord and lacing. It can also be classified as truss configurations, where concrete filled in the chords as compressive columns.

The common chord component includes two chords, three chords and four chords, and Fig. 1 shows the cross-section form. From the mode of connection of the web members to the chords, there are mainly four types of CFST built-up column, here referred as parallel-shape (CFST battened columns), V-shape, M-shape and N-shape (CFST laced columns), seen in Fig. 2. In truss configurations, there are namely as Vierendeel truss (parallel-shape), Warren truss (V-shape) and Pratt truss (N-shape), respectively (Wardenier et al., 2010). X-shape is another connection type usually adopted in built-up column. However, it is not convenient for tubular structure in practice, thus not mentioned in this thesis.

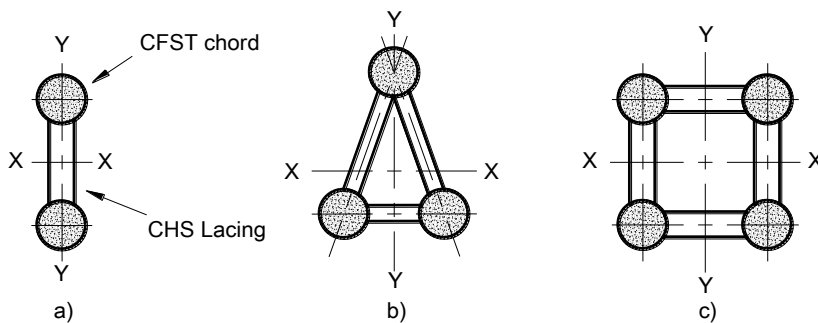


Fig. 1 Cross-section form: a) Two chords; b) Three chords; c) Four chords

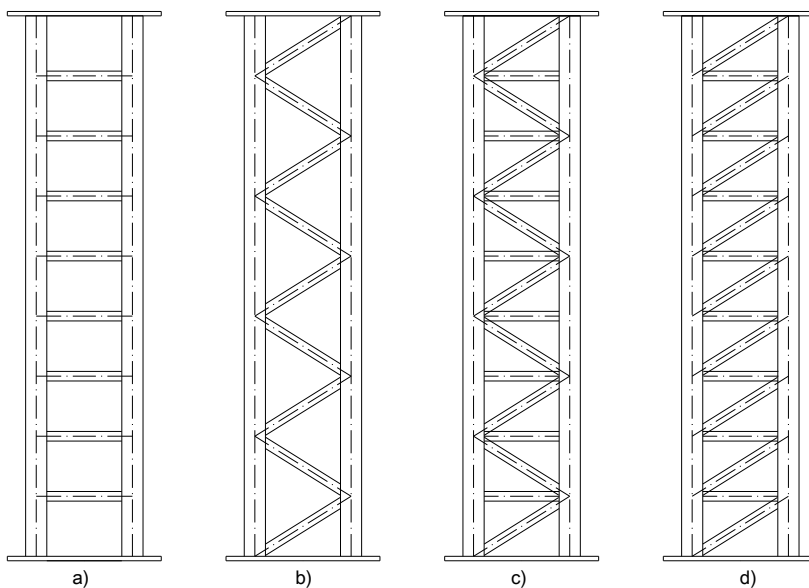


Fig. 2 Types of CFST built-up columns: a) Parallel-shape; b) V-shape; c) M-shape; d) N-shape

As the increasing construction activities of large-span spatial structures and long-span bridge structures, such as roof structures, sports stadiums and arch bridges, not only for economy reasons but also for aesthetic appeals are considered (Han et al., 2012). Compared with single CFST column, CFST built-up columns can be more widely used in large structures.

1.2. The Advantages and Disadvantages of CFST Built-up Columns

Compared with ordinary steel or reinforced concrete (RC) columns, there are several distinct advantages and disadvantages related to CFST built-up columns in both terms of structural performance and construction sequence, summarized as follows.

1.2.1 Advantages

Higher confinement in the concrete

The steel column section can add confinement to the concrete core, which causes an increment both in strength and ductility for the concrete. Circular CFST cross-sections provide a higher confinement than rectangular CFST, due to the shape of circular section provides the higher hoop stresses. This confinement is also influenced by the diameter-to-thickness ratio (D/t) of the tubes. In Fig. 3, it clearly shows that the ultimate strength for a concrete-filled steel tube is even larger than the summation of the strength of the steel tube and the RC column, which is described as “1(steel tube) + 1(concrete core) greater than 2 (simple summation of the two materials)” (Han et al., 2014).

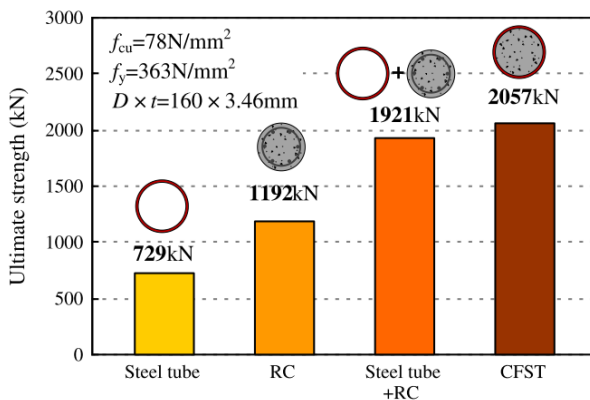


Fig. 3 Axial compressive behavior of CFST stub column (Han et al., 2014)

Delay of the steel local buckling

Local buckling of the chord, especially around the joint, can be prevented or delayed due to the support from the core concrete to the steel tube and thus can increase the strength and the ductility of the structures (Xu et al., 2014). Even if the concrete cracks, the delay of local buckling in CFST sections will still occur since the concrete expands and bears against the steel tube, maintaining the concrete-steel contact. Due to the concrete core forces all local buckling modes outward, thinner steel sections may be used that still ensure the yield strength will be reached in the tube before buckling occurs.

Higher compressive and flexural strength

The concrete filling gives a higher load compressive capacity without increasing the outer dimensions. With concrete CFST built-up columns is very beneficial in producing a great moment inertia through the position of the chords being far from the centroid of the column. When the spacing is larger in the pier, the lacing connections can even use truss hollow sections.

Earthquake and Fire Resistance

CFST columns have become the preferred form for many seismic-resistant structures. Subjected to severe earthquakes, concrete encasement cracks resulting in reduction of stiffness but the steel core provides shear capacity and ductile resistance to subsequent cycles of overload (Shanmugam & Lakshmi, 2001). In contrast to reinforced concrete columns with transverse reinforcement, the steel tube also prevents spalling of the concrete and minimizes congestion of reinforcement in the connection region, particularly for seismic design. Therefore, CFST columns have been used for earthquake-resistant structures. Compared to hollow steel tube structure, the fire resistance can be considerably increased by concrete filling. The concrete can work as a fireproofing to the steel section.

Rapid construction

The tedious process of framework preparation and steel fixing in the RC construction is absent in CFST structures since the steel tube acts as the framework, which decreases workload (Abed et al., 2013). In moderate- to high-rise construction, CFST column can ascend more quickly than a comparable reinforced concrete structure since the steelwork can precede the concrete by several stories (Webb, 1993). The hollow steel tubes are also conveniently hoisted and stitched. Once the concrete has hardened and the composite action has been developed,

the system can achieve its final strength and stiffness, to support the designated gravity and lateral loads.

Savings in the construction costs

Due to the fast erection and an optimal design, the constructions costs may be reduced. Because of its higher strength, a composite column is lighter than a typical RC column with a similar strength, which reduces the loads on and cost of the foundation, and the cost and amount of reinforcement bars. The steel section can word as formwork and is stiffened by the concrete in CFST columns, is much lighter than a conventional steel column, which also reduces substantially the steel costs.

1.2.2 Disadvantages

Limited Applications

From the many structure has been built, it can be seen that the use of CFST are trusses also limited to columns, piers, arch ribs, etc. Currently, very few precedents of CFST trusses using in beams. Because beams are generally made of rectangular shape, while rectangular CFST has a more complex mechanical performance, tedious requirements and poor economic returns.

Complex load transferring mechanism

For transport or erection it may be that bolted joints are preferred or required, whereas for space structures prefabricated connectors are generally used. However, the simplest solution is to profile the ends of the members which have to be connected to the through member (chord) and weld the members directly to each other. Nowadays, end profiling does not give any problem and the end profiling can be combined with the required bevelling for the welds. Although the directly welded joint is the simplest and cleanest solution, the load transfer is rather complex due to the non-linear stiffness distribution along the perimeter of the connected braces. The design rules have been based on simplified analytical models in combination with experimental evidence, resulting in semi-empirical design formula (Wardenier et al., 2010).

Significant second-order effects

Collapse prevention is a fundamental objective of earthquake resisting design. Collapse may occur if an individual story displaces sufficiently so that the second-order effects (termed $P-\Delta$ or $P-\delta$ effects) fully offset the first-order story shear resistance and instability occurs. It is one of the major concerns in seismic design to

avoid excessive $P-\Delta$ effects (Gupta & Krawinkler, 2000). Similarly, CFST built-up columns can be used in high-rise structure, while slender columns with small diameter of the tubes will inevitable increase the $P-\Delta$ effects.

Construction technology

The butt welding of steel tubes is a key point in the manufacture process. It requires keeping straight of the post-weld steel tubes, which need to take appropriate measures during welding. Taking into account the effects of welding deformation and welding sequence. Before butt welding, the pipe with small diameter should be used for spot positioning to the one with large diameter. For the pipe with larger diameter, should be welded to another with additional reinforcement for temporary associated fixation. For lacing columns assembling, accurate dimensions and angles are strictly required.

Adjustable diameter tube are adopted in the high-rise structures, therefore it is another difficulty for adjustable tube butt. The complex joints will appear in the position of adjustable connections, which will undoubtedly affect the progress of construction.

Pouring concrete into hollow tubes is an invisible process, it is not visually to inspect the quality of in-filled concrete. If dense parts are detected, it needs to drill and grout the pipe, then re-weld and cement the holes.

In terms of pouring concrete, if using pumping method, not only a complete set of pumps and conveying equipment, but also the particle size of coarse aggregate, cement ratio and slump, are stringent requirements. If using high dropping method, the mixture proportion design of concrete is also strict. The experiment for determine the water-cement ratio must be done before casting.

Therefore, there must be more strict construction technology, organization and management than ordinary construction of reinforced concrete structures.

1.3. Critical Issues

As the above stated, CFST built-up columns have an excellent performance in compression with high strength and good ductility. At present, a large number of studies have been conducted on CFST column (Gourley B.C. et al., 2008), steel tubular trusses (Rahami H. et al., 2008; Jin M. et al., 2011) and built-up columns

(Gjelsvik A., 1990). However, the behavior of CFST built-up columns has seldom been reported, especially in seismic behavior, such as the structural failure mode, stiffness degradation, and hysteretic behavior have not been wildly studied.

Current code provisions, such as AISC (American Institute of Steel Construction, 2010), AASHTO (American Association of State Highway and Transportation Officials, 2012), Eurocode (European Committee for Standardization, 2004a; 2004b; 2005a; 2005b), CIDECT (Kurobane et al., 2004), etc., have filled many gaps in the design of composite elements, such as steel-concrete composite columns resist horizontal earthquake loads by moment resisting frames or by braced frames. Those frames are called dual structures in Eurocode 8 (European Committee for Standardization, 2004b). In these structures the dissipative zones are mainly located in plastic hinges near the beam-column connections and energy is dissipated by means of cyclic bending. Braced frames resist horizontal loads by axial forces in the bracings. In these frames the dissipative zones are mainly located in tension and/or compression bracings (Kurobane et al., 2004). In seismic design, Eurocode 8 (European Committee for Standardization, 2004b) recommends the values of the behavior factor q depending on the type of structures. However, there still lack clearly definition on the CFST built-up columns with different types of lacing.

Accurate nonlinear static and dynamic computational formulations are required for developing response factors. The models should directly simulate all predominate inelastic effects from the onset of yielding through strength and stiffness degradation causing collapse, while being sufficiently robust to track inelastic force redistribution without convergence problems up to the point of collapse (Federal Emergency Management Agency, 2009). Such a model would also aid in investigations of CFST built-up columns and establishing guidelines using in seismic analysis and design. To these ends, an advanced finite element formulation need to be developed.

At the present time is still difficult to predict the structural response of CFST built-up columns based on a typical frame analysis. Fiber Analysis or Finite Element Model (FEM) Analysis can be used to get a better response prediction, but not very common yet.

1.4. The Objectives and Methodologies

In order to investigate the seismic behavior of CFST built-up columns, the primary objectives and methodologies of this research are:

1. Survey on the applications in worldwide, especially the current development of CFST built-up columns and CFST trusses;
2. Conduct the literature review on CFST built-up columns, to find the suitable methods in the design, and then propose and verify finite element models for CFST built-up columns that could simulate the hysteretic behavior, $P-\Delta$ effect, non-linearity in materials, and so on.
3. To obtain the experimental response of CFST built-up columns under quasi-static test, and investigate the response characteristics. From this, hysteretic performance, such as failure mode, deformed shapes, load displacement hysteretic curves, displacement ductility, rigidity and strength degradation, and energy dissipation capacity, are discussed.
4. Improve the analytical prediction through evaluation and calibration of both material constitutive models and element models. Compared with test results and previous experimental studies.
5. Perform parametric study on CFST built-up columns based on FEM analysis, to further understand the performance of CFST built-up column and find the key components of the structures will affect the seismic response.
6. Based on regression analysis, aim to identify the corresponding displacement ductility factor for CFST built-up columns. Proposed formula to calculate displacement ductility factor of CFST built-up columns.
7. Verify and investigate the seismic performance of Ganhaizi Bridge, which is an innovative lightweight bridge, consisted with CFST composite truss girder and lattice pier. Take it as case study, FEM analysis and shaking table test are developed.

1.5. Structure of the Thesis

Besides this chapter, in the main body of the thesis, it consists of 6 chapters, from Ch.2 to Ch.6 that introduced as following:

Chapter 2, it states the current applications of CFST built-up columns in practice. Previous experimental and analytical research studies and their main contributions are summarized and commented upon.

Chapter 3, it describes the hysteretic testing of CFST built-up columns in detail, a description of the specimens, the instrumentation plan, the test settings, the experimental response and test results are documented in this chapter.

Chapter 4, it presents a finite element analysis of CFST built-up columns. The FE model validity is validated firstly, then a parametric analysis is developed for each type of columns. Based on parametric analysis and regression analysis, proposed a method to calculate the displacement ductility factor of CFST build-up columns.

Chapter 5, it presents a case study on performance of an existing innovative lightweight bridge with CFST composite truss girder and lattice pier-Ganhaizi Bridge. Based on FEM analysis, the dynamic characteristics and seismic response is investigated.

Chapter 6, taken Ganhaizi Bridge as prototype, a multi-shaking table test on a 1:8 scale specimen with two spans and three lattice high piers was designed and performed. Adopted design seismic wave of prototype, dynamic characteristics, seismic performance and failure characteristics were analyzed. Besides experiment, FEM was developed and validated through compare with test results. Based on computational analyses, plastic behavior of this structure was studied.

Finally, the conclusions drawn from the research and recommendations for future investigation will be presented.

2. STATE-OF-ART

A comprehensive literature survey helps not only to deepen the basic knowledge on the studied subject but also to emphasize advantages and disadvantages of previous experiences, so to give researchers space for further improvements. To provide a unitary framework, a detailed literature survey about the topic of CFST built-up column is presented.

First of all, application of CFST truss structures are investigated. Then, the past efforts to the experimental research studies of CFST built-up columns are reviewed. After that, the modelling methods of CFST built-up columns are summarized.

2.1. Application of CFST Truss Structure

Due to the advantages and the cost of using CFST columns in construction makes it more attractive than other alternatives (Abed et al., 2013). Concrete filled steel tube columns are increasingly used in bridges and larger-span buildings, which are presents as follows, respectively.

2.1.1 Buildings

The applications of structural truss hollow sections nearly cover all fields. Sometimes hollow sections are used because of the beauty of their shape, to express a lightness or in other cases their geometrical properties determine their use. It can be used in the roof of airport, railway station and stadium. The concrete-filled steel tube used in buildings can avoid having a very large size column. CFST built-up columns can be achieved larger flexural rigidity with a smaller diameter columns. The column mainly subjected to the axial loads, hence the larger compressive strength characteristics of CFST column can be exerted, so CFST built-up columns are widely used in structural members with larger load eccentricity ratio and slenderness ratio, such as stadium (Fig. 4) and industrial buildings (Fig. 5).

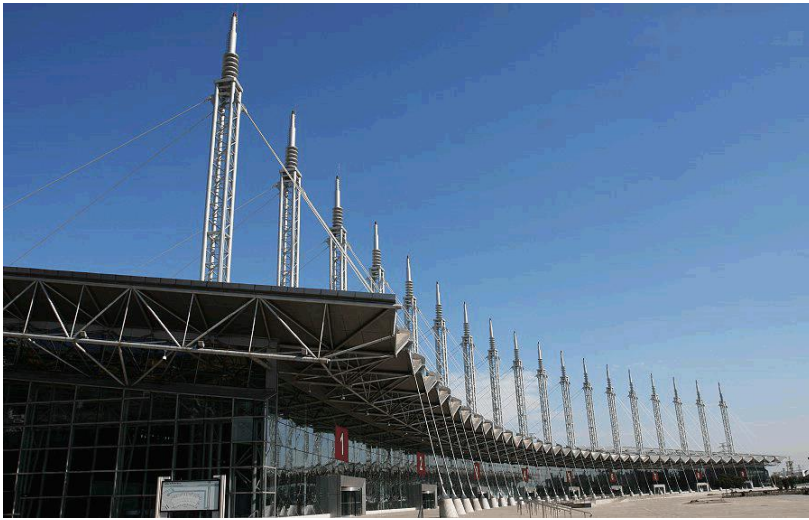


Fig. 4 Tianjin International Convention & Exhibition Center, China, completed in 2003



Fig. 5 Hengyang Heavy Machinery, China, completed in 2009

Fig. 6 shows the Canton Tower in Guangzhou, China. The structure consists of a space lattice composite frame and a RC core. The height of the main body is 454 meters, and the pinnacle height is 600 meters. A total of 24 inclined concrete filled steel circular tubular members are utilized, with a maximum tube diameter of 2000 mm and a maximum wall thickness of 50 mm (Han et. al, 2014).



Fig. 6 Canton Tower, China, completed in 2010

2.1.2 Bridges

The top 20 of longest arch bridge spans in the world are summarized in Table 1 (Wikipedia, 2014). Truss typology is adopted for nearly all the arch ribs of steel and CFST bridges. Usually in design of arch ribs, equivalent beam-column methods are used to estimate the ultimate bearing capacity of CFST truss arches. In other words, the arch is fitted to the equivalent length column for calculating the ultimate bearing capacity (Wei et al., 2009). Therefore, the truss arch rib can be classified as one type of CFST built-up columns. Compared with developed countries, such as USA and Japan, where steel arch bridges are more towards chosen, developing country such as China, generally incline to CFST arch bridge, which is more economical. Since the first CFST arch bridge is used in 1990, it is now the common method to build arch bridges throughout China, especially when the bridge needs to cross a deep gorge or ravine.

Based on the different cross sections of arch ribs, there are singular tube arches, dumbbell type arches, and multi-tube type arches also called truss type, shown in Fig.7 (Chen & Wang, 2009).

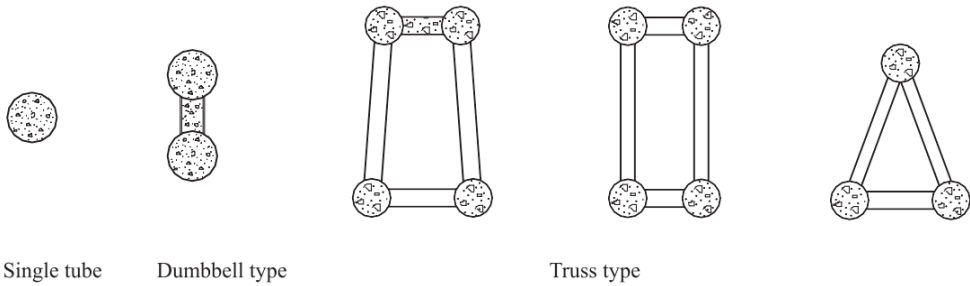


Fig. 7 Cross-sectional types of CFST arch rib (Chen & Wang, 2009)

Chen and Wang (Chen & Wang, 2009) investigate 119 CFST arch bridges in China, found that truss cross section represents 55% and dumbbell cross section 35%, the remaining 10% is for single-tube and others see Fig. 8. The relationship between the shapes of cross sections and spans is shown in Fig. 9. It indicates that truss section is adopted most widely and is suitable for long span bridges. In bridges with dumbbell sections, the longest span is only 160 m. The top 5 longest CFST arch bridge are shown in Fig. 10, all the cross-sections are truss type.

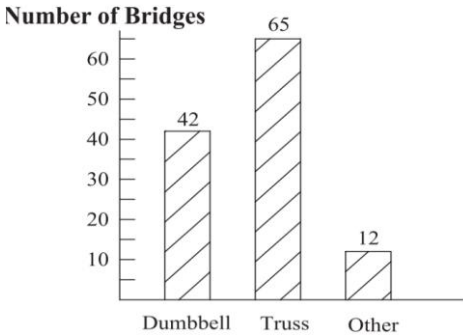


Fig. 8 Cross sections of arch rib (Chen & Wang, 2009)

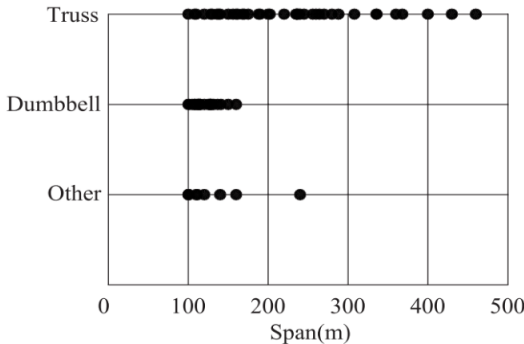


Fig. 9 Relationship between cross sections and spans (Chen & Wang, 2009)

Rank	Name	Span (m)	Material	Year opened	Location	Country
1	Chaotianmen Bridge	552	Steel	2009	Chongqing	China
2	Lupu Bridge	550	Steel	2003	Shanghai	China
3	Bosideng Bridge	530	CFST	2012	Hejiang County Sichuan	China
4	New River Gorge Bridge	518	Steel	1977	Fayetteville West Virginia	USA
5	Bayonne Bridge	510	Steel	1931	Kill Van Kull New Jersey	USA
6	Sydney Harbour Bridge	503	Steel	1932	Sydney	Australia
7	Wushan Bridge	460	CFST	2005	Wushan Chongqing	China
8	Minzhou Bridge	450	Steel	2011	Ningbo Zhejiang	China
9	Zhijinghe River Bridge	430	CFST	2009	Dazhipingzhen Hubei	China
10	Xinguang Bridge	428	Steel	2008	Guangzhou Guangdong	China
11	Wanxian Bridge	420	Concrete	1997	Wanzhou District Chongqing	China
12	Caiyuanba Bridge	420	Steel	2007	Chongqing	China
13	Liancheng Bridge	400	CFST	2008	Xiangtan Hunan	China
14	Daninghe Bridge	400	Steel	2010	Wushan Chongqing	China
15	Krk Bridge	390	Concrete	1980	Krk	Croatia
16	Fremont Bridge	382	Steel	1973	Portland Oregon	USA
17	Hiroshima Airport Bridge	380	Steel	2010	Hiroshima	Japan

18	Maocaojie Bridge	368	CFST	2006	Yiyang Hunan	China
19	Old Port Mann Bridge	366	Steel	1964	Surrey British Columbia	Canada
20	Zhaohua Jialing River Bridge	364	Concrete	2012	Guangyuan Sichuan	China

*Table 1
Longest arch bridge spans in the world (Wikipedia, 2014)*



a) Bosideng Bridge, Sichuan, China



b) Wushan Bridge, Chongqing, China



c) Zhijinghe River Bridge, Hubei, China



d) Liancheng Bridge, Hunan, China



e) Maocaojie Bridge, Hunan, China

Fig. 10 Longest CFST arch bridges

During recent constructional activities in China, CFST built-up columns also be applied for the pillar of deck arch bridge-Mengdonghe River Bridge (Fig. 11), which will reduce the self-weight of spandrel structure, and decrease the arch rib deformation. To some extent, the structural rigidity and the stress distribution of the whole bridge will be improved, which will advance the competitive for lager span CFST arch bridges.



Fig. 11 CFST built-up columns used for pillar (Mengdonghe River Bridge, Hunan, China, completed in 2013)

Meanwhile, CFST built-up column also adopted in piers the beam bridges-Ganhaizi Bridge, located in Sichuan Province, China (Fig. 12). It is connected with CFST composite truss girders. The significant advantage of this type is that, the tedious process of framework preparation and steel fixing in the RC construction are absent. Moreover, with the favourable ductility of CFST materials and lightweight truss structure, the earthquake resistant properties of high pier bridge is expected to promote. This type of bridge is a new exploration in the bridge selection when used in the high mountains and deep valleys area, especially in seismic zones. It will be introduced as a case study in details in later chapters.



Fig. 12 CFST built-up columns used for continuous beam bridge (Ganhaizi Bridge, Sichuan, China, completed in 2012)

2.1.3 Electrical transmission tower

In many countries, electrical transmission towers are made of angle sections with simple bolted connections. Nowadays, architectural appearance becomes more important and due to the environmental restrictions, the protection and maintenance is more expensive. These factors stimulate designs made of hollow sections (Wardenier et al., 2010). Fig. 13 shows a long-span transmission tower built in Zhoushan, China, in 2009. It is the largest electricity pylons in the world with a height of 370 meters. This tower is a tubular lattice one with four concrete-filled steel tubular columns. The diameter of the CFST column is 2000 mm, and the concrete is filled up to 210 meters height (Han et al., 2014).



Fig. 13 Zhoushan electricity pylon, China

2.2. Ductility in Seismic Design

2.2.1 Bridge pier failure in earthquakes

In this research, we mainly focus on the CFST built-up columns as for one new type of bridge pier. Therefore, the concept of ductility is also aimed to bridge engineering. Before 1970s, the bridge design is based on the strength theory. However, during some serious earthquakes in last three decades, such as Northridge (USA, 1994), Kobe (Japan, 1995) and Wenchuan (China, 2008), some bridge failures and collapses due to lack of good ductility, which has made engineers recognized that it is important to take into account the plastic design in the bridge design practice. Regarding the seismic design, the interest is focused on how to dissipate the input seismic energy better. The basic problem in this approach is reflected to the concept of ductility, which considered as the capacity of the structure subjected to serious plastic deformations but without losing its strength.

Different with building construction, where the design concept of strong-column and weak-beam will make building work as a whole structure under earthquakes, even if some weakness failures will not cause building collapse, for bridge engineering, the

pier plays the most important role during the earthquake, which nearly controls the seismic performance of the whole structure. Pier failure always leads to bridge collapse, especially for the traditional reinforcement concrete (RC) piers, where reinforcing steel bar and stirrup exhibit the ductility performance. Under serious seismic actions, confinement failure, flexural failure and shear failure, etc., usually happen in the weak section without fine reinforcement ratio, see Fig. 14 to Fig. 16. Hence, the pier design with good ductility is a key issue for the bridge seismic activity.

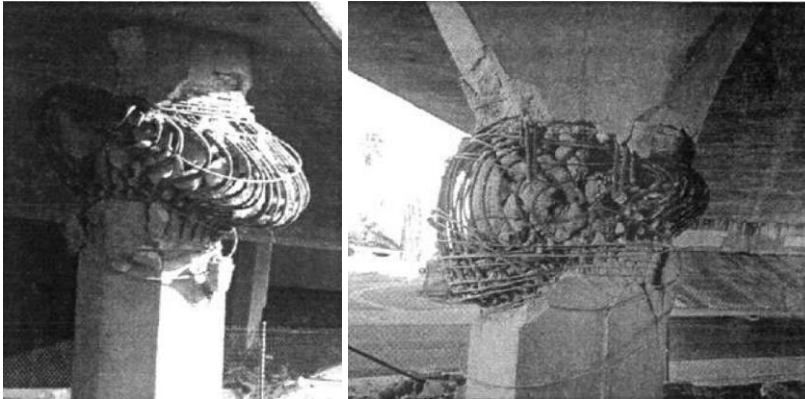


Fig. 14 Confinement failure on the top of pier, Mission Gothic Overpass Bridge, Northridge Earthquake, USA, 1994



Fig. 15 Flexural failure of the whole bridge, Hanshin Expressway, Kobe Earthquake, Japan, 1995



Fig. 16 Shear failure of the tie beam and flexural failure at the base of column, Baihua Bridge, Wenchuan Earthquake, China, 2008

2.2.2 Ductility definition

Before the 1960s the ductility notion was used only for characterizing the material behaviour, after Baker's studies in plastic design and Housner's research works in earthquake problems (1997), this concept was extended to the structural level and associated with the notions of strength and stiffness of the whole structure. In practice of structural plastic design, the concept of ductility defines the ability of a structure to undergo deformations after its initial yield without any significant reduction in ultimate strength. The structural ductility permits to predict the structural ultimate capacity, which is the most important criterion for designing structures subjected to conventional load modes. Meanwhile, the structural ductility evaluates the structural seismic performance and indicates the energy dissipation capacity of one structure. The concept of ductility gives the possibility to reduce seismic design forces and allows the production of some controlled damage in the structure, also in case of strong earthquakes. The following ductility types are widely used in literature (Ferrario, 2004).

- a) Material ductility, or axial ductility, which characterizes the material plastic deformations;
- b) Cross-sectional ductility, or curvature ductility, which refers to the plastic deformations of cross-section, taking the interaction between the parts composing the cross-section into account;
- c) Member ductility, or rotation ductility, when the properties of member are considered;
- d) Structural ductility, or displacement ductility, which considers the global behavior of the whole structure.

Ductility types	Schematic diagram	Definition
Material ductility (Axial)		$\mu_{\epsilon} = \frac{\epsilon_u}{\epsilon_y}$
Cross-section ductility (Curvature)		$\mu_{\chi} = \frac{\chi_u}{\chi_y}$
Member ductility (Rotation)		$\mu_{\theta} = \frac{\theta_u}{\theta_y}$
Structure ductility (Displacement)		$\mu_{\delta} = \frac{\delta_u}{\delta_y}$

Table 2
Ductility types (Ferrario, 2004)

2.2.3 Approaches in various codes

Currently, in seismic design practice, majority of countries have adopted the elastic response spectra theory, calculate the elastic seismic internal forces, then multiply one termed reduction coefficient, to get the design seismic internal forces.

Eurocode

The behaviour factor q is defined in Eurocode 8 (European Committee for Standardization, 2005b), globally for the entire structure and reflects its ductility

capacity, i.e. The capability of the ductile members exhibits with acceptable damage but without failure, and keep seismic actions in the post-elastic range. Among that, value of q factor is associate with structural fundamental period T

$$\begin{cases} q = \mu_d, & \text{if } T \geq T_0 \\ q = 1 + (\mu_d - 1) \frac{T}{T_0}, & \text{if } T < T_0 \end{cases} \quad (1)$$

Where $T_0 = 1.25T_c$, T_c is the corner period of the elastic response spectra, μ_d is the displacement ductility factor.

AASHTO code

Similar with Eurocode, AASHTO (American Association of State Highway and Transportation Officials, 2012) specifies that seismic design force effects for substructures and the connections between parts of structures, shall be determined by dividing the force effects resulting from elastic analysis by the appropriate response modification factor, R . If an inelastic time history method of analysis is used, the response modification factor, R , shall be taken as 1.0 for all substructure and connections.

Moreover, bridges subject to earthquake ground motion may be susceptible to instability due to $P-\Delta$ effects. Inadequate strength can result in ratcheting of structural displacements to larger and larger values causing excessive ductility demand on plastic hinges in the columns, large residual deformations, and possibly collapse. AASHTO also makes specification for the limitation of $P-\Delta$ effects. The maximum value for Δ is intended to limit the displacements such that $P-\Delta$ effects will not significantly affect the response of the bridge during an earthquake.

The displacement of any column or pier in the longitudinal or transverse direction shall satisfy

$$\Delta P_u < 0.25\phi M_n \quad (2)$$

In which, P_u is axial load on column or pier; ϕ is flexural resistance factor for column; M_n is nominal flexural strength of column or pier calculated at the axial load on the column or pier; Δ is displacement of the point of contra-flexure in the column or pier relative to the point of fixity for the foundation, $\Delta = R_d\Delta_e$; Δ_e is

displacement calculated from elastic seismic analysis; R_d is factor for calculation of seismic displacements due to inelastic action, expressed as follows,

$$\begin{cases} R_d = \left(1 - \frac{1}{R}\right) \frac{1.25T_s}{T} + \frac{1}{R}, & \text{if } T < 1.25T_s \\ R_d = 1, & \text{if } T \geq 1.25T_s \end{cases} \quad (3)$$

Where T is period of fundamental mode of vibration; T_s is corner period specified in elastic response spectrum; R is response modification factor.

Caltrans code

A ductile member is defined (Caltrans, 2013) as any member that is intentionally designed to deform inelastically for several cycles without significant degradation of strength or stiffness under the demands generated by the Design Seismic Hazards. For ordinary standard bridges, the global displacement demand estimate Δ_D , can be determined by linear elastic analysis utilizing effective section properties. Displacement ductility demand is a measure of the imposed post-elastic deformation on a member. Displacement ductility is mathematically defined by the ratio of estimated global frame displacement demand Δ_D and the yield displacement of the subsystem from its initial position to the formation of plastic hinge $\Delta_{y(i)}$, see in Eq. (4)

$$\mu_D = \Delta_D / \Delta_{y(i)} \quad (4)$$

The target displacement ductility demand is different depended on the types of column and boundary conditions with the foundation, ranges from 1 to 5. Also, the local displacement capacity of a member based on its rotation capacity is defined, which in turn is based on its curvature capacity. The curvature capacity shall be determined by $M-\phi$ analysis. The structural system's displacement capacity, Δ_c is the reliable lateral capacity of the bridge or subsystem as it approaches its Collapse Limit State. Ductile members must meet both the local displacement capacity requirements and the global displacement criteria.

Japanese code

Because of the unsatisfactory performance of highway bridges in the 1995 Kobe earthquake, the Japanese Design Specifications of Highway Bridges was revised in 2002 (Japan Road Association, 2002). The ductility check of reinforced concrete piers which was included in the 1990 Design Specifications was upgraded to the

ductility design method which applies to every structural components in which seismic effect is predominant. In ordinary bridges, a bridge is designed assuming a principal plastic hinge at bottom of pier so that the following requirement is satisfied.

$$P_a \geq S_{es} W / g \quad (5)$$

In which P_a is lateral capacity of a pier, S_{es} is equivalent response acceleration and W is tributary weight. Assuming the equal energy principle $S_{es} = S_s / \sqrt{2\mu_a - 1}$, in which μ_a is allowable displacement ductility factor of the pier and S_s is elastic response acceleration for the equivalent static analysis. Since the maximum μ_a for a single reinforced concrete piers is 8, the response modification factor $R = \sqrt{2\mu_a - 1}$ is smaller than 3.8 (Kawashima, 2000).

New Zealand Code

The newest NZ Bridge manual (NZ Transport Agency, 2014) updates and refines the structural ductility factor μ using in calculating earthquake design actions, appropriate to the limit state being considered. For a structure represented as a single-degree-of-freedom oscillator, the minimum horizontal seismic base shear force v for the direction being considered, shall be calculated as

$$V = C_d(T_1)W_t \quad (6)$$

Where $C_d(T_1)$ is horizontal design action coefficient, W_t is total dead weight plus superimposed dead weight (force units) assumed to participate in seismic movements in the direction being considered.

The horizontal design action coefficient $C_d(T_1)$ shall be

$$C_d(T_1) = \frac{C(T_1)S_p}{\kappa_\mu} \quad (7)$$

Where $C(T_1)$ is the ordinate of the elastic site hazard spectrum for the fundamental translational period of vibration; S_p is structural performance factor, κ_μ is the modification factor for ductility, defined as following which depend on the soil classes condition,

For soil classes A, B, C and D as defined by the manual,

$$\begin{cases} \kappa_{\mu} = \mu, & \text{for } T_1 \geq 0.7s \\ \kappa_{\mu} = \frac{(\mu - 1)T_1}{0.7} + 1, & \text{for } T_1 < 0.7s \end{cases} \quad (8)$$

For soil classes E as defined by the manual,

$$\begin{cases} \kappa_{\mu} = \mu, & \text{for } T_1 \geq 1.0s \text{ or } \mu < 1.5 \\ \kappa_{\mu} = (\mu - 1.5)T_1 + 1.5, & \text{for } T_1 < 1.0s \text{ and } \mu \geq 1.5 \end{cases} \quad (9)$$

Where μ is displacement ductility factor for structures of limited capacity or demand, determined from actual structural characteristics.

Compared with various codes, it is found that for bridge seismic design, one of key issue is determined the displacement ductility factor of bridge pier. In spite of there is definite regulation for the RC pier, however, still vacant area for CFST built-up columns.

2.3. Previous Experimental Research Studies

The first study of steel-concrete composite members began as early as 1908 at Columbia University (Viest et al. 1996). The combined material strength was not appreciated in the early days and the design concept considered two individual materials by either conservatively neglecting the contribution from one or another or by adding them separately.

Connections in composite structural system differ from conventional connections in steel system due to different force transfer mechanism and constructability. Extensive experimental and analytical studies have been conducted to understand the behaviour of the composite columns mainly from the 1960s (Shanmugam & Lakshmi, 2001). There are many types have been proposed and tested in many countries, mostly in the China, Japan and USA. From these investigations, different design codes have been formulated to reflect the design philosophies and practices in the respective countries, such as Australia, China, Japan, USA and European countries (Tao et al., 2008).

Gourley and Hajjar (Gourley & Hajjar, 1993) made the first version of a synopsis for CFST beam-columns subjected to monotonic and cyclic loads. The database

had been updated and refined with more data in later versions in 1995, 2001 and 2008 (Gourley et al., 2008), respectively. In the newest version in 2008, Gourley et al. (Gourley et al., 2008) provided a summary of a significant amount of research that has been conducted worldwide on the behavior of concrete filled steel tubes in the past five decades. The behavior and experimental work of concrete filled steel tube members, connections, and frames that were reported in detail in the literature. The mechanical properties of CFST, including axially loaded, pure bending, combined axial load and bending, shear, torsion and connection, were well investigated.

In 2006, Goode also published online a database for CFST columns and beam columns, which was updated in 2007 (Goode, 2007). The latest ASCCS Database of Concrete Filled Steel Tube Column Tests summarized the tests on 1819 CFST columns and compared the test results with Eurocode 4 (European Committee for Standardization, 2004a). This database had been used by Goode and Lam (Goode & Lam, 2008) for the evaluation of the strength predicted by the Eurocode 4; the comparison between the experimental strength and the EC4 prediction in this study had shown good predictions in general for CFST. Graphs of Test strength versus EC4 strength and of the ratio Test/EC4 against concrete strength (for short columns) or slenderness (for long columns) are included for each series. A Table summarizing the results for all series of tests is given in the Summary of Database, giving data collected to December 2008.

As mentioned above, extensive studies regarding the performance of concrete-filled steel tubes have been carried out over the last several decades. Only the relative CFST trusses research are highlighted in the follows.

2.3.1 Static Performance

Ou et al. (Ou et al., 2011) presented an experimental and analytical investigation of concrete-filled steel tubular (CFST) laced columns (Fig. 17). The specimens consisted of four concrete-filled steel tubes that are laced together. A total of 27 experimental tests were conducted to quantify the column failure mechanism at ultimate loads. The experiments were designed to obtain the load-deflection curves. Experimental results indicated that the compression force in the longitudinal members dominated the failure mechanism in the CFST columns. In-plane bending occurred when member segments reached the compression failure load. The forces in the lacing members (diagonal and horizontal bracing) were found to be small and remained in the elastic range through failure. The experimental study was used to

validate an analytical parametric study. The analytical study showed that the eccentricity and slenderness ratios have a large influence on the capacity of CFST laced columns. The load capacity decreased gradually with an increase in the slenderness ratio and eccentricity. It was found that the global strength reduction factor could be expressed as a product of the eccentricity reduction factor and the stability factor. Additionally, finite-element analyses of CFST columns based on four in situ structures were performed to determine the ultimate load-carrying capacity and were subsequently compared to several building codes. On the basis of the analytical results, a new methodology for calculating the ultimate load-carrying capacity was proposed. This proposed methodology was compared with five different building codes to quantify the increased accuracy.

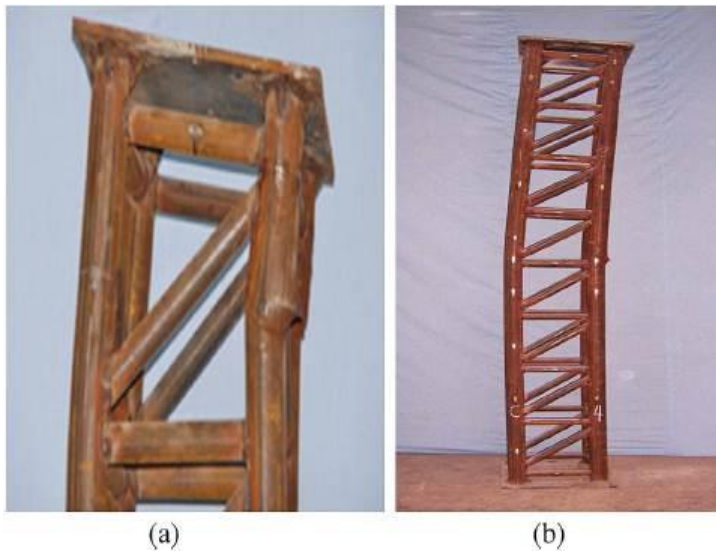


Fig. 17 Test photos: a) Buckling near end of the specimen; b) typical failure of the whole column (Ou et al., 2011)

Han et al. (Han et al., 2012) conducted the research of axial compressive capacity on curved concrete-filled steel tubular (CCFST) latticed members (Fig.18-20). A total of 20 specimens, including 18 CCFST built-up members and 2 curved hollow tubular built-up columns, were tested to investigate the influence of variations in the tube shape (circular and square), initial curvature ratio (β_r , from 0 to 7.4%), nominal slenderness ratio (λ_n , from 9.9 to 18.9), section pattern (two main components, three main components and four main components), as well as brace pattern (battened and laced) on the performance of such composite built-up members. The experimental results showed that the load bearing capacity, the initial stiffness and the ductility of curved latticed members are significantly increased when chord tubes are filled with concrete. The axial compressive strength N_{ue} of the hollow tube

specimen is only 30.9%-38.9% of those of the corresponding concrete-filled specimen. The load-bearing capacity of the laced built-up members increased by about 45.2%-68.2% compared with that of the corresponding battened members. The deformation ability of built-up members with circular components was generally superior to that of specimens with square components. The experimental results also demonstrated that the ultimate strength and stiffness of the curved concrete latticed specimen decreases with the increase of the initial curvature β_r and the nominal slenderness ratio λ_n . The influence of β_r on curved build-up specimens was quite similar to that of load eccentricity on single members. Finally, a simplified model was derived in this paper to predict the load carrying capacity of curved built-up members. The capacities predicted by the simplified method was in good agreement with the experimental results.

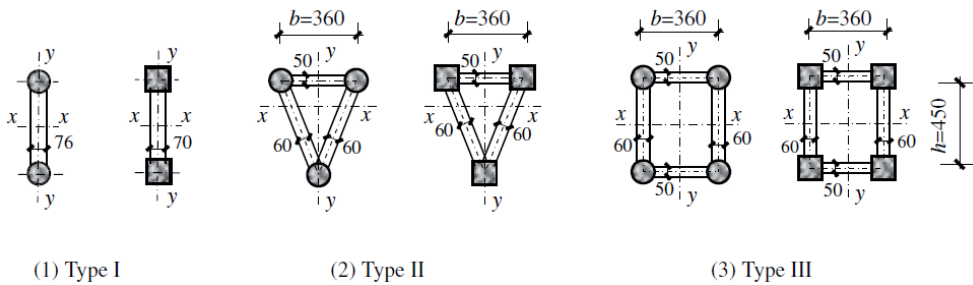


Fig. 18 Cross-section of tested battened specimens (Han et al., 2012)



Fig. 19 Failure modes of tested battened specimens (Han et al., 2012)

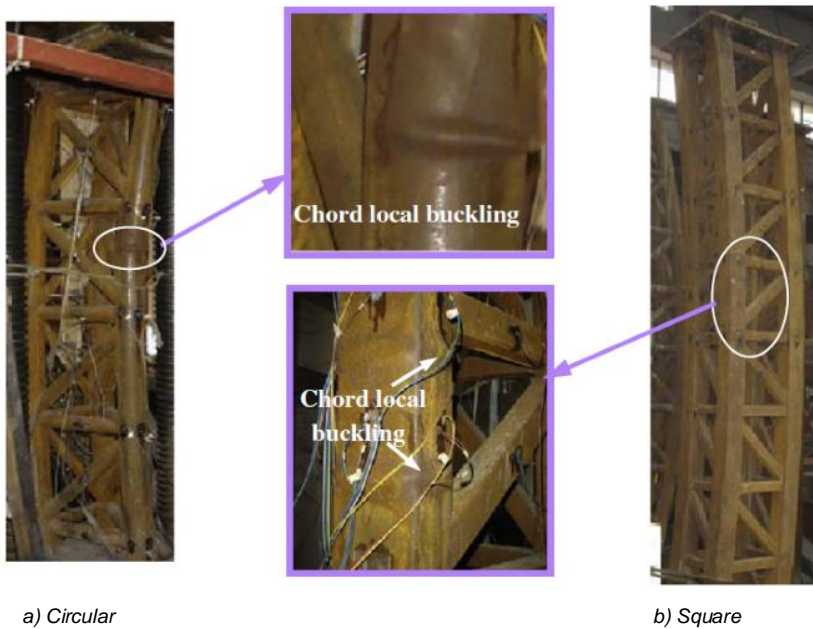


Fig. 20 Failure modes of tested laced specimens (Han et al., 2012)

2.3.2 Dynamic Performance

For seismic design, stiffness degradation and strength deterioration are two very significant indicators for comparative performance studies.

Liu and Goel (Liu & Goel, 1988) compared hollow and concrete-filled rectangular tube braces. Nine full-scale specimens made from A500 Grade B cold-formed steel tubes were tested under quasi-static cyclic loading. The main parameters of the study were: 1) presence of concrete; 2) strength of concrete; 3) effective slenderness ratio; and 4) width-thickness ratio. The test results showed that the presence of concrete could increase the number of cycles to failure, and dissipated more energy than the hollow counterpart under the same loading history, except in tube specimens with rather small width thickness ratios. In tension, only the steel effectively resisted the axial force. In compression, concrete could change the local buckling mode, reduce its severity, and delay the occurrence of cracking under cyclic loading. For rectangular bracing members under cyclic loading, the member was perturbed at incipient buckling, causing the compression flange to buckle locally in an outward direction. Then followed by an inward pinching of the webs, which formed longitudinal cracks at the corners that propagate along the member

until failure occurs. After many cycles of loading, the concrete at the hinge point crushed, which delayed the failure.

Matsui and Kawano (Matsui & Kawano, 1988) reported that stable behavior of the trusses could be ensured if the buckling strength was greater than the yield strength. Consequently, the column slenderness ratio should be limited to increase the CFT buckling capacity. When selecting the limiting value of the column slenderness ratio, both the strain-hardening and Bauschinger effect should be taken into account because strain-hardening increases the strength of the steel, while the Bauschinger effect tends to lead to a lower buckling strength. These effects both reduce the limiting column slenderness ratio.

Kawano and Matsui (Kawano & Matsui, 1988) investigated the behavior of circular hollow steel tubes (HTs) and concrete filled steel tubes (CFTs) under repeated axial loading. Fig. 21(a) shows load-deformation relationships of concrete filled and hollow tubular members subjected to compressive load, and Fig. 21(b) shows the relationships subjected to tensile load.

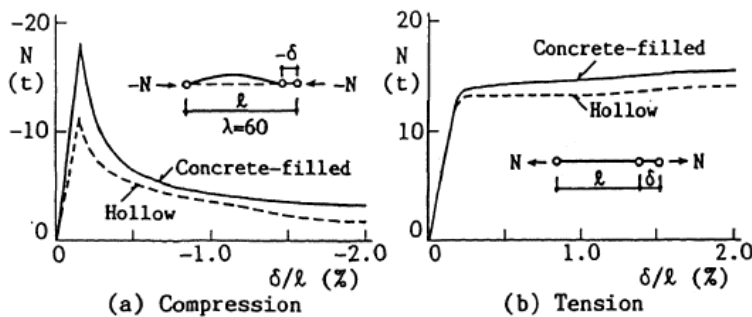


Fig. 21 Behaviors of tubular members under monotonic axial loading (Kawano & Matsui, 1988)

In addition, the response of the frames having tubular bracing members was examined analytically, see Fig. 22. The specimens were simply supported at the ends. Two loading schemes were selected. The first one, the axial load was applied with repeated large amplitude axial deformation and a repeated axial load. The second one was with gradually increasing amplitude. It was found that the failure mostly occurred when the second loading scheme was applied. The in-filled concrete delayed local buckling and provides high deformation capacity. The failure of the CFT members took place with local buckling at various locations along the length and then tension cracking at the top of one of these local buckling bulbs. The dissipated energy up to breaking failure of concrete-filled tubular specimens were

considerably larger than the corresponding hollow ones under repeated axial loading. The energy of concrete-filled tubular specimen which slenderness ratio of steel tube was 60 had 3.2 times as the energy of the hollow one.

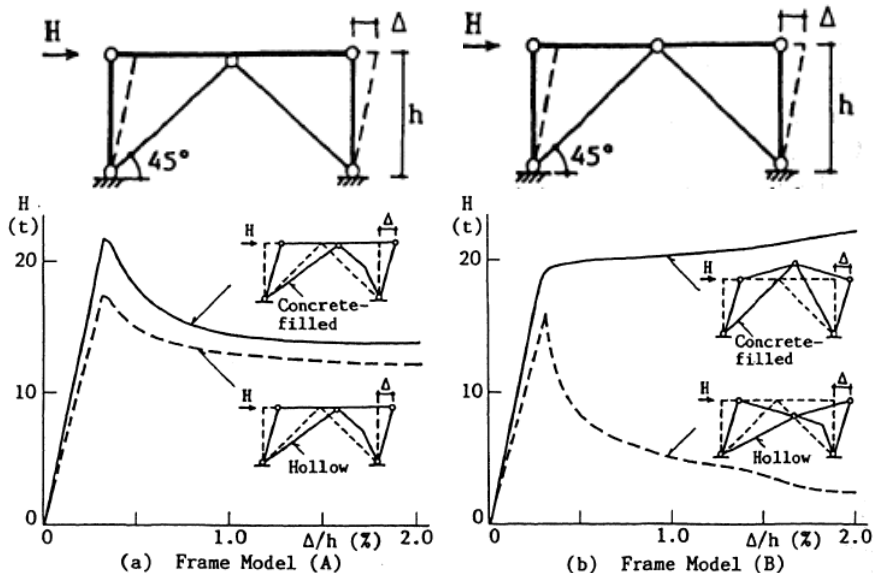


Fig. 22 Horizontal load-deformation relationships of different types of frame model (Kawano & Matsui, 1988)

After the test, the behavior K-braced portal frames made up of tubular braces was investigated theoretically. Two types of frames were analysed, respectively. The first type had a beam hinged at the middle where the braces were connected. For this type of frames, the both of frames had almost same behavior and the horizontal strengths deteriorated due to buckling of the bracings. However, the CFT braces improved the behavior under repeated horizontal loading. For the second type of frames, the beam was hinged at mid-length. In this case, CFT braces achieved a more stable behavior compared to hollow tube braces and no deterioration in strength was obtained.

Kawano and Sakino (Kawano & Sakino, 2000a) made the comparative study with a previous test on small-scale specimens revealed that the scale effect on the fracture might be negligible for CFT with ordinary sizes and, therefore, a formula to predict fracture, which had been derived from small-scale specimens, could be used on large specimens cyclic local buckling and fracture of concrete filled tubular members.

Kawano and Matsui (Kawano & Matsui, 2000b) presented a prediction method for the deformation capacity of the truss is proposed both for monotonic loading and cyclically repeated loading. The latter is determined based on the energy dissipation capacity of CFT chords. The predicted deformation capacity of CFT trusses showed a good agreement with test results, and the capacity is comparable to that of full web steel members. The deformation capacity of this sort of CFT truss is dominated by the capacity of the CFT chords. A CFT truss is a tubular truss composed of parallel chord members made of concrete-filled circular tubes. The web members are not necessarily CFTs but steel tubes or shapes, and they are designed to not yield before the chord members. There are two stability conditions necessary to prevent chord members from buckling. One of the conditions is for tension chord yielding prior to compression chord buckling, and the other is for preserving the CFT compression strength even under repeated loading.

The condition for a CFT truss subjected to the axial load N as well as bending moment M is shown in the M - N strength interaction diagram in Fig. 23.

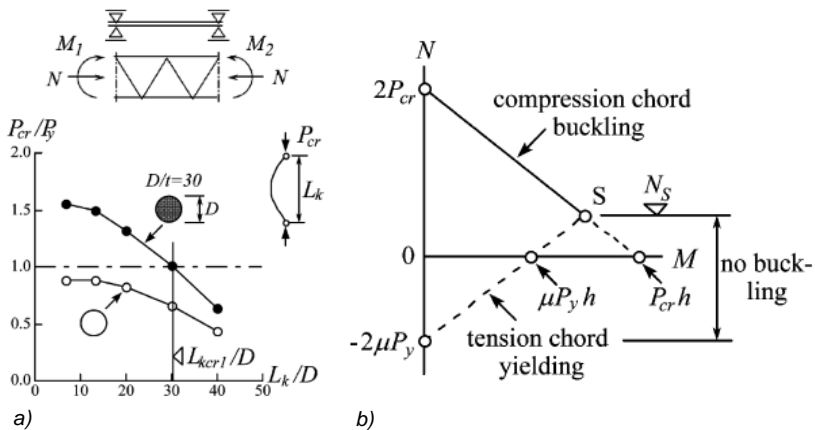


Fig. 23 Stability condition I: a) Column curves for CFTs and vacant tubes; b) M - N strength interaction (Kawano & Sakino, 2000b)

The diagram consists of two lines, one of which is derived from the compression chord buckling (solid line), the other of which from the tension chord yielding (broken line), where P_{cr} and P_y are the buckling strength and the tensile yield strength of the chord, h is the centre distance between the two chords, and μ is a safety factor. In order to take the account of unexpected chord buckling due to strain hardening or scattering of member strengths, the P_{cr} should be compared with the magnified tensile yield strength μP_y . When the axial load N of the truss is

less than the axial force at the intersection of the two lines N_s , the chord never buckles. This condition is expressed as:

$$N < N_s \quad (10)$$

Where N and N_s are defined as positive in compression. The condition expressed by Eq. (10) is referred to as stability condition I.

Concrete in a tube will not contribute to any compressive resistance once the tube has experienced plastic stretching and the concrete has open cracks. Given this consideration, the behaviour of a CFT member under this condition might be similar to that of a vacant tubular member. Fig. 24(a) shows the $P_{cr}-L_k$ relation of a CFT member that has undergone a pre-stretched plastic strain E_{pr} of 2%. The column curve consists of two portions divided by a critical effective length L_{kcr2} . In the range of $L_k > L_{kcr2}$, the buckling strength is that of a vacant tubular member. In the range of $L_k < L_{kcr2}$, a CFT member maintains the original buckling strength, which is nearly equal to the compressive strength of a cross section. The L_{kcr2} varies depending on the dimensions and material properties of the tube and concrete. From the finite element analysis, L_{kcr2} was estimated as shown in Fig. 24(b). The method of analysis is using a beam-column element that is composed of stress fibers to express the material nonlinearity of concrete and steel. The element coordinate system moves, so that geometric nonlinearity may be ensured over a large deformation range. The CFT chords will not lose their original compressive strength if they satisfy the condition

$$L_{kv} < L_{kcr2} \quad (11)$$

Where L_{kv} is the effective length of a CFT chord in which the concrete contains open cracks. The L_{kv} may be equal to $0.5l$, where l denotes the length between the neighboring truss nodes, or the yielded region of a chord. The condition expressed by Eq. (11) is referred to as the stability condition II. Simply put, when the D/t ratio of a tube is not less than 30 and the ε_{pr} is not larger than 3%, the L_{kcr2} may be thought to be $3D$ or more.

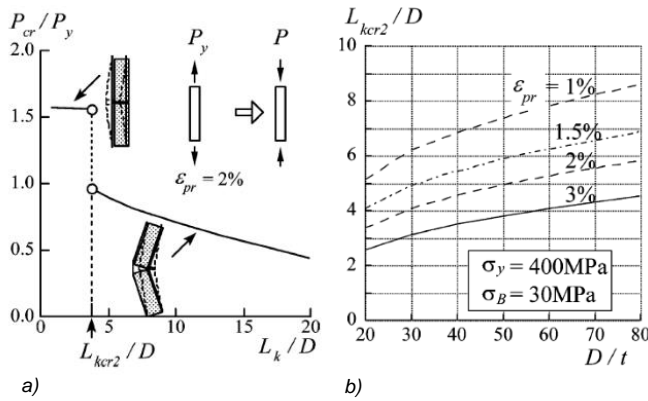


Fig. 24 Stability condition II: a) Column curve for pre-stretched CFT; b) L_{kcr2} - D strength interaction (Kawano & Matsui, 2000b)

The CFT truss specimen shown in Fig. 25 is subjected to cyclically repeated horizontal loads H , and is braced in the out-of-plane direction at the top and mid-height, as well as at the fixed base. Both of the stability conditions I and II are satisfied for both chords. In the cyclic responses of the truss specimen, no strength reduction was found at the hysteresis reverse points, meaning that no flexural buckling occurred in either of the chords. Slip phenomena in the hysteresis curves of latter cycles were caused by the cyclic local buckling of a CFT chord member. At the reverse point, the cracks in the concrete closed and the compression strength of the member recovered.

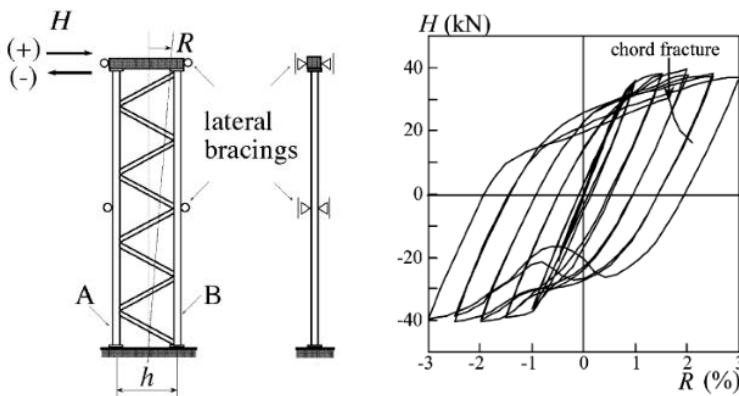


Fig. 25 CFT truss specimen subjected to cyclically repeated horizontal loads (Kawano & Matsui, 2003)

Fig. 26 presents the cyclic axial behavior of a CFT specimen (Kawano & Matsui, 2003). The D/t of the tubes is approximately 30, and the L_k/D is 5. The energy dissipation was terminated by fracture after cyclic local buckling. Based on

experimental and theoretical investigation, the non-dimensional energy dissipation prior to the fracture w is derived for various D/t ratios and various effective lengths.

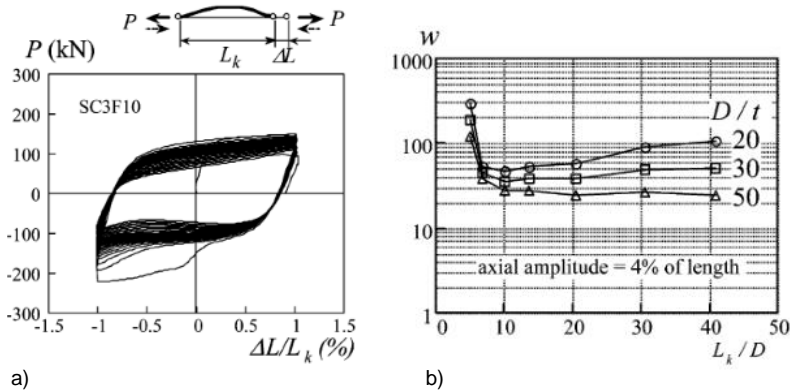


Fig. 26 The non-dimensional energy dissipation prior to the fracture w (Kawano & Matsui, 2003)

The axial deformation amplitude in the figure is 4% of the length of a member, which for practical purposes may be thought of as the upper limit. Therefore, the w indicated in the figure may be the lowest practical evaluation. The w is defined as

$$w < \frac{U}{P_y \epsilon_y} \quad (12)$$

Where U is the energy dissipation capacity of a CFT member until fracture, l is the yielded length, and ϵ_y is the elastic strain at the yield stress of the tubes. As indicated in the figure, the w for each D/t ratio decreases and reaches a low and constant level as the L_k/D increases. In contrast, a very stocky member (having an L_k/D of 5.0 or less) has a large capacity of w . The lower boundary of w for a very stocky member allowing for a safe-side margin may be approximately listed as follows,

$$\begin{aligned} w &= 150 \text{ for } D/t = 20 \\ w &= 100 \text{ for } D/t = 30 \\ w &= 50 \text{ for } D/t = 50 \end{aligned} \quad (13)$$

The energy dissipation of a CFT truss that simultaneously satisfies stability conditions I and II in both chords is dominated by a fracture after cyclic local buckling in either of the two chords. The w denotes the ultimate capacity of the

accumulated plastic deformation ratio η of a CFT chord until fracture, where η is the ratio of the accumulated plastic axial deformation in relation to the elastic elongation at the tensile yield load. Therefore, the safety of the CFT truss can be ensured by monitoring the η of CFT chords in comparison with w .

Based on the theory as mentioned above, Kawano and Sakino (Kawano & Sakino, 2003) proposed a new earthquake-resistant system of multi-storey frames using CFT trusses, and investigated this system using both static and dynamic response analyses. Result showed that the structural damage, which is evaluated by the accumulated plastic deformation ratio, is observed in the beam ends, column bases, and CFT chords at the bottom or lower stories. The beam-end damage distributes almost uniformly in the vertical direction in either frame. The CFT chords may survive safely, so that the maximum extent of damage to the CFT chords is sufficiently smaller than the capacity. Therefore, it was determined that a multi-storey frame using CFT trusses has excellent seismic resistance, and the system may be practical.

Luo (Luo, 2013) carried out low-cycle loading experiment of six CFST laced columns, which took three parameters (including axial load ratio, slenderness ratio and the decorated tube size) into account (Fig. 27). Test results indicated that the stiffness and ultimate load carrying capability of the CFST laced columns reduces with the increase of slenderness ratio. Improving the axial load ratio properly improves the bearing capacity but descends the ductility of members.

In addition, the 3D solid finite element model were developed based on the test results by ABAQUS software. A total of 67 FEMs were analyzed and consider the influence of axial load ratio, concrete strength, strength of brace steel tube, lace bar size and the strength of lace bar steel. Results indicated that the reasonable value of axial ratio is within 0.2 to 0.6, and the suitable nominal slenderness ratio is less than 10. Then slenderness ratio can be reduced by increasing the distance of brace when the column height is limited. However, the FEM results seems not fit well with the test result, due to the quality of in-filled concrete which causes obvious pinch effect in force-displacement curves and the idealized constitutive model in the FEM which leads to saturated force-displacement curves, as illustrated in Fig. 28.

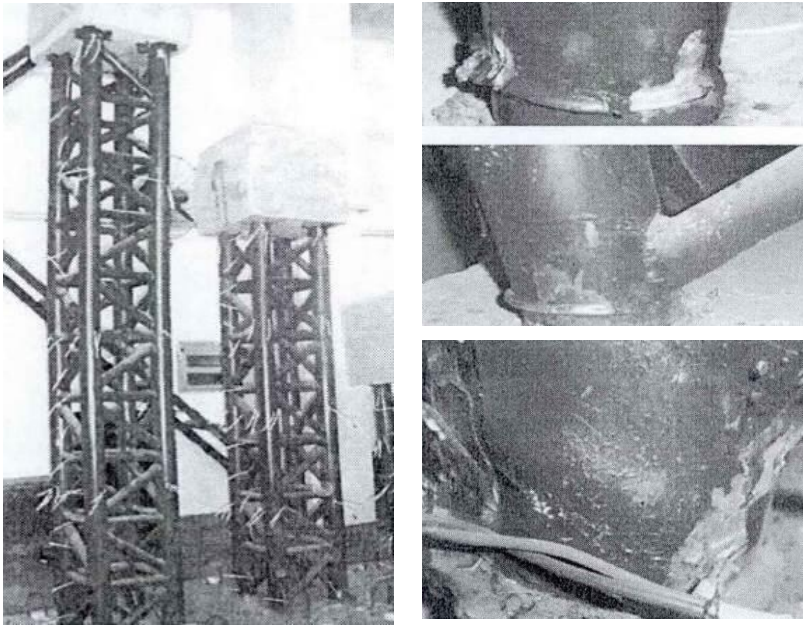
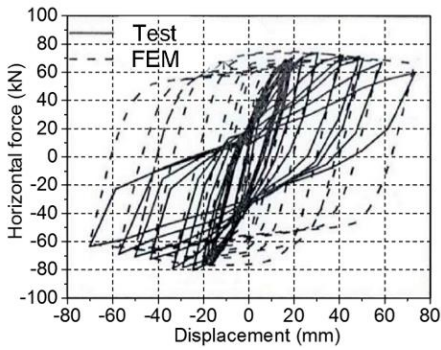
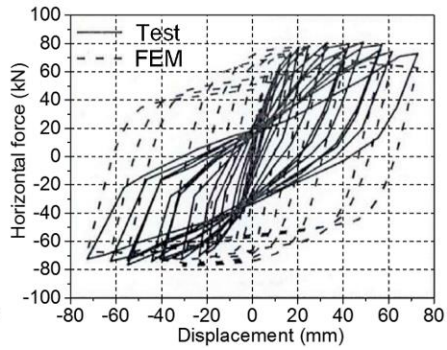


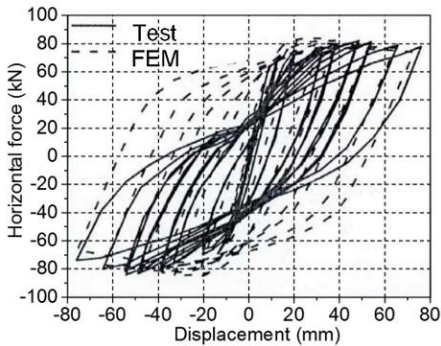
Fig. 27 Global deformation and failure at the bottom of specimens (Luo, 2013)



a) Specimen SCC1



b) Specimen SCC4



c) Specimen SCC6

Fig. 28 Comparison of force-displacement curves (Luo, 2013)

2.4. Finite Element Formulation

For finite element model simulation, the accurate nonlinear static and dynamic computational formulations are required for developing rational system response factors. The models should directly simulate all predominate inelastic effects from the onset of yielding through strength and stiffness degradation causing collapse, while being sufficiently robust to track inelastic force redistribution without convergence problems up to the point of collapse (Federal Emergency Management Agency, 2009). Finite element (FE) technique is becoming more and more popular in modelling CFST columns thanks to the existence of many commercially available software, such as ABAQUS and ANSYS. Three-dimensional solid model analysis allows the direct modelling of the composite action between the steel and concrete components with different factors. Local and global imperfections, residual stresses and boundary conditions can be precisely considered. The prediction accuracy of a FE model, however, is greatly affected by the input parameters, especially by the selection of a suitable concrete constitutive model (Tao et al., 2013).

Three-dimensional solid model analysis allows for detailed simulation of CFST members. In this type of analysis, the concrete core is commonly modeled with solid elements, while the steel tube is modeled with shell elements. The interface between the two materials are assembled together by some connector or interface elements to simulate the interaction between the steel and concrete components. Three-dimensional continuum analysis allows for detailed simulation of CFST members, many researchers adopted solid model for simulating the static performance of CFST columns. For example, Schneider (Schneider, 1998) presented an experimental and analytical study on the behavior of short, concrete-filled steel tube columns concentrically loaded in compression to failure. 20-node brick element and 8-node shell element are adopted for simulating concrete and steel tube, respectively (Fig. 29). Hu et al. (Hu et al., 2003) performed numerical simulations of CFST columns with different cross-sectional shapes subjected to axial compressive loads (Fig. 30).

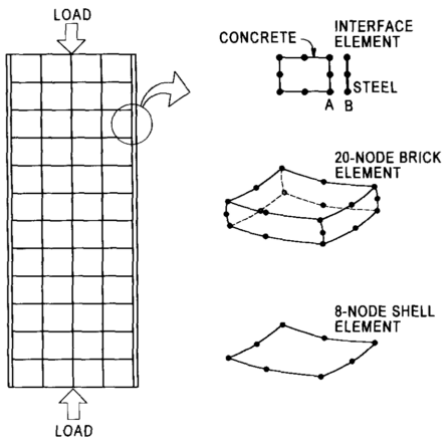


Fig. 29 Schneider's FEM (Schneider, 1998)

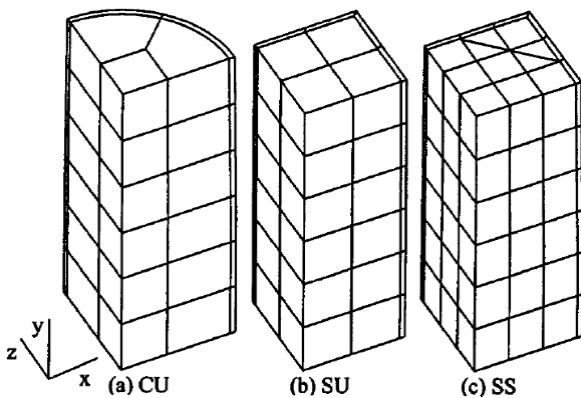


Fig. 30 Hu's FEM: a) circular section; b) square section; c) square section stiffened with steel reinforcing ties forming an octagonal shape (Hu et al., 2003)

Typically, in the solid finite element model, all types of nonlinearity (i.e. local, global, geometrical and material nonlinearities) can be explicitly incorporated in the formulation, whereas in frame elements some of the nonlinearities such as local buckling of steel tube can be just implicitly and, in an approximate sense, taken into account. However, the most disadvantages of using solid finite element model are that, they are quite complicated and computationally intensive because of a very refined discretization of the structures with large numbers of degrees of freedom. It is also difficult to properly model the interaction between steel and concrete components. In addition, the computational expense prevents three-dimensional solid model from being a viable option for analysis of composite structure, especially in dynamic analysis. Therefore, discrete frame models, based on fiber beam-column element model, are more adopted for predicting the global response of CFST structure with reasonable accuracy and high efficiency.

2.4.1 Fiber beam-column element

Fiber beam-column model is a different type of beam modeling technique. Originally developed by Mahin and Bertero (Mahin & Bertero, 1975), the fiber beam-column element is a two-node, two-dimensional element with multiple-fiber control sections. The fiber model discretizes a beam section such that the beam is idealized as a series of uniaxial elements that run parallel to the longitudinal axis of the beam as shown in Fig. 31. Each one of uniaxial members is referred to as a fiber and is given an appropriate cross-sectional area and material constitutive. It is based on the assumption that plane sections remain plane and normal to the longitudinal axis during the deformation history, which leads to a simple geometric relation between section curvature and axial strain, and fiber strains. The nonlinear characteristics of the element derives entirely from the material nonlinearity fiber stress-strain relationship. Based on the strain, the stress and modulus of each fiber are computed and aggregated to obtain the sectional response. The fiber approach is appealing because of the ability to account either explicitly or implicitly for all the salient features of CCFT members (e.g., concrete cracking, confinement, local buckling, etc.) through relatively simple uniaxial stress-strain models. The state determination is based on an iterative solution that strictly satisfies element equilibrium and compatibility as it converges to the nonlinear section force-deformation relation with the specified tolerance.

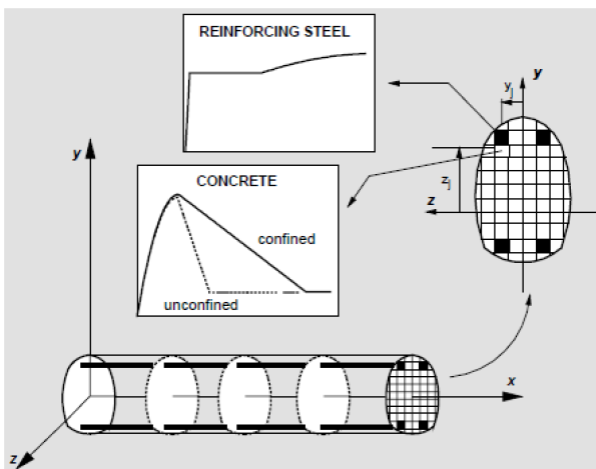


Fig. 31 Fiber beam-column model (Taucer et al., 1991)

According to the nonlinearity type, a classification distinguishes concentrated and distributed plasticity formulations model. For the former, the material nonlinearity

only at hinges, usually adopting zero length, at the element ends while assuming the element remains elastic in between the hinges (Hajjar & Gourley, 1997; El-Tawil & Deierlein, 2001; Inai et al., 2004). For the latter, the material nonlinearity throughout the element, monitoring inelasticity at specific integration points along the length of the element (Hajjar et al., 1998; Aval et al., 2002; Varma et al., 2002; Tort & Hajjar, 2007). Compared with concentrated plasticity model, the distributed plasticity model has more accurate and more computationally expensive, since inelasticity is traced at multiple points along the length of the element rather than just the element ends. While in several cases (e.g., double curvature of a beam-column) material nonlinearity is mostly limited to the element ends, the distributed plasticity approach is appealing because of its accuracy and generality. Both the concentrated and distributed plasticity approaches, initiation and evolution of cross-sectional behaviors needs to be established.

According to the variables which are taken as the primary unknowns, a classification distinguishes displacement-based element, force-based element and mixed elements. The former is termed stiffness-based, elements regard nodal displacements as the primary unknowns (Hajjar & Gourley 1997; Aval et al. 2002; Alemdar & White 2005). Then element deformations are computed using interpolation functions. Element equilibrium is satisfied only in a variational sense, i.e., element internal forces computed from the assumed displacement field do not strictly satisfy equilibrium. This type of formulation is considered easy to implement and to extend to geometric nonlinear behavior. The latter is termed flexibility-based, elements regard element forces as the primary unknowns (De Souza 2000; El-Tawil & Deierlein 2001; Alemdar & White 2005). Stress resultants along the length of the element are computed using interpolation functions. Element equilibrium is strictly satisfied, however, the compatibility of deformations within the element is satisfied only in a variational sense. Compared with displacement-based elements, force-based elements are often more computationally expensive and have more elaborate state determination procedures. Mixed elements regarding both element forces and nodal displacements as primary unknowns, allowing interpolation functions for both element deformations and stress resultants along the length of the element (Nukala & White 2004; Alemdar & White 2005; Tort & Hajjar 2007). Despite the complexity of the state determination procedure, which is typically greater than for displacement- or force-based elements, the mixed method provides a favorable balance of accurate assessment of nonlinear curvatures along the length of the element and capability to include geometric nonlinearity directly.

The accuracy of the element response and the entire structure are affected by the mesh selection, which is the number of sections in the discretization and the number of fibers in one cross-section. It is believed that a large number of fibers certainly gives better results, but computational cost increases at the same time.

Based on the concept mentioned above, fiber beam-column elements can reduce the three-dimensional behavior to one-dimension, utilizing a kinematic assumption (e.g., initially plane sections remain plane) to describe the deformations of any point within the member by the deformations of cross sections along the length of the member. The finite element model would also establish guidelines for the computation of equivalent composite column rigidity to be used in seismic analysis and design of composite columns. Three-dimensional fiber beam-column element formulation has been developed for investigation of CFST structures and validation is provided versus experiments from the literature for a range of single CFST column and CFST beam-column frames.

Liang and Fragomeni (Liang & Fragomeni, 2009; Liang & Fragomeni, 2010) used nonlinear analysis methods for circular CFST columns relies on the use of accurate models for confined concrete. A generic fiber element model that incorporated the proposed constitutive models of confined concrete was created for simulating the nonlinear inelastic behavior of circular CFST short columns under axial loading and eccentric loading, respectively. The generic fiber element model was verified by comparisons of computational results with existing experimental data. The theoretical model and formulas developed were shown to be effective simulation and design tools for the nonlinear inelastic behavior of circular CFST beam-columns under axial loading and eccentric loading, respectively.

Chung (Chung, 2010) provided an efficient method to predict the pre- and post-peak hysteretic behavior of concrete-filled circular steel tube columns under the combination of constant axial load and cyclic lateral load. A simplified nonlinear fiber element method is used to investigate uni-axial stress and strain relationship of materials in terms of the composite action between the steel tube and the concrete.

Valipour and Foster (Valipour & Foster, 2010) presented a flexibility-based element for the nonlinear analysis of CFST beam-columns. The element stiffness is derived based on the exact force interpolation functions while the section stiffness is determined by employing modified fiber element approach.

For the analytical models of CFST columns under cyclic loading, Hajjar and Tort (Hajjar & Tort, 2010), Denavit and Hajjar (Denavit & Hajjar, 2012) conducted numerical studies on rectangular and circular CFST structures, respectively, where the three-dimensional fiber-based beam finite-element models were developed. The results showed that this mixed finite element formulation could predict both detailed local response and overall structural response, and could be utilized in the analysis of a complete structural system.

2.4.2 Truss finite element model

In the truss model analysis, the effects of the behaviour of the joints on the distribution of internal forces and moments within a structure, and on the overall deformations of the structure, should generally be taken into account, but where these effects are sufficiently small they may be neglected.

In the past, most designers have designed beam-to-column connections either as pinned or as rigid. However, in reality, the actual stiffness of a connection will nearly always be somewhere between these two extremes, i.e. the connection will behave in a semi-rigid manner. Also the capacity of an unstiffened connection might be less than that of the connected beam, in which case it is termed partial strength (Kurobane Y, 2004).

According to Eurocode 3 (European Committee for Standardization, 2006), for an elastic global analysis, the connections are classified according to their stiffness, for a rigid plastic analysis the connections are classified according to their strength and for an elastic-plastic analysis the connections are classified according to both stiffness and strength, see Table 3.

According to CIDECT1 (Wardenie et al., 2008), a rigid joint frame analysis is not recommended for most planar, triangulated, single-chord, directly welded trusses, as it generally tends to exaggerate brace member moments, and the axial force distribution will still be similar to that for a pin-jointed analysis. Hence, the circular hollow sectional trusses is usually performed by assuming that all members are pin connected. For the pinned joint analysis, the modal eccentricities beyond the center lines produce primary bending moments, which should be taken into account by treating it as a beam-column. In this case, the truss can be modelled by considering a continuous chord with brace members pin connected to it at distances of $+e$ or $-e$ from it (e being the distance from the chord centerline to the intersection of the

brace member centerlines). The links to the pins are treated as being extremely stiff as indicated in Fig. 32. This model can automatically generate a sensible distribution of bending moments.

Method of global analysis	Type of connections		
	Elastic	Nominally pinned	Rigid
Rigid-Plastic	Nominally pinned	Full-strength	Partial-strength
Elastic-Plastic	Nominally pinned	Rigid and full-strength	Semi-rigid and partial-strength Semi-rigid and full-strength Rigid and full-strength
Type of joint model	Simple	Continuous	Semi-continuous

Table 3
Types of connections

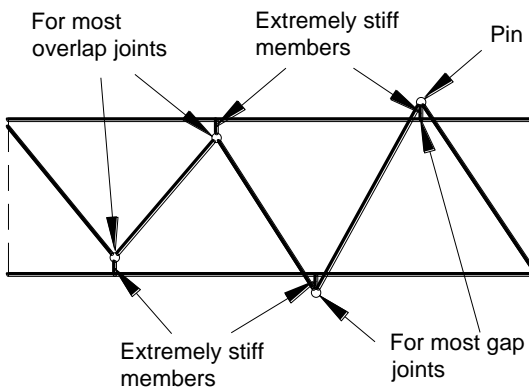


Fig. 32 Modelling for circular hollow sectional trusses

For Vierendeel trusses with top and bottom chords having the same bending stiffness, initially a simplified design calculation can be used, if there conditions are meet: 1) the loads act at the joints; 2) the joint are rigid; 3) the longitudinal displacements on the chords can be disregarded. Then the modelling for Vierendeel truss can be as shown in Fig. 33.

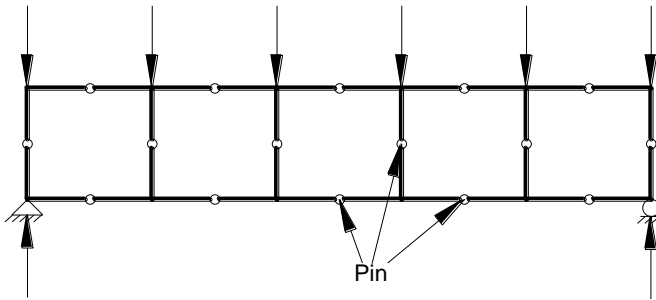


Fig. 33 Modelling for Vierendeel truss

The strength of moment connections between circular hollow sectional beams and columns is based on the chord plastification and the chord punching shear criterion. However, only few researches on connections between circular hollow sections with the through member (chord or column) filled with concrete has been carried out. Makino et al. (Makino et al., 2001) report the results of an investigation on axially loaded X- and K-joints. These investigations showed that the connection strength for tension can be based on the chord punching shear criterion. For compression loading no joint failure was recorded. It seems to be acceptable to design moment connections of circular hollow sections on the basis of the punching shear criterion given in Fig. 34 and Eq. (14) (Wardenier et al., 2010).

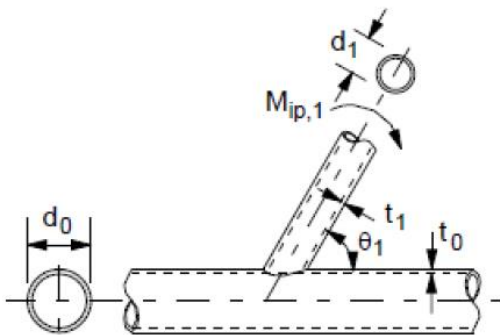


Fig. 34 Design moment resistance of welded joints between circular hollow sections (Wardenier et al., 2010)

For chord plastification

$$M_{ip,1,Rd} = 4.3 \frac{f_{y0} t_0^2 d_1}{\sin \theta_1} \beta \gamma^{0.5} Q_f \quad (14)$$

For chord punching shear ($d_1 \leq d_0 - 2t_0$)

$$M_{ip,1,Rd} = 0.58 f_{y0} t_0 d_1^2 \frac{1 + 3 \sin \theta_1}{4 \sin^2 \theta_1} \quad (15)$$

In which, d_0 is the outside diameter of chord; t_0 is the thickness of chord; d_1 is the outside diameter of brace; t_1 the thickness of brace; θ_1 is the angle between chord and brace; γ is half diameter or half width-to-thickness ratio of the chord: $\gamma = d_0/2t_0$; f_{y0} is yield strength of steel tube; β is diameter or width ratio between braces and chord, and Q_r can be expressed as Eq. (16),

$$Q_r = (1 - |n|)^{C_1} \quad (16)$$

Where

$$n = \frac{N_{0,Ed}}{N_{pl,0,Rd}} + \frac{M_{0,Ed}}{M_{pl,0,Rd}} \quad (17)$$

$$C_1 = 0.45 - 0.25\beta, \text{ for chord compression stress } (n < 0) \quad (18)$$

$$C_1 = 0.20, \text{ for chord tension stress } (n \geq 0) \quad (19)$$

In which, $N_{0,Ed}$ and $M_{0,Ed}$ are the design axial load and bending moment of a chord, respectively; $N_{pl,0,Rd}$ and $M_{pl,0,Rd}$ are the design axial yield capacity and design value of the plastic moment capacity of a chord, respectively.

It is expected that this is conservative due to the stiffness of the concrete, the moment resistance arm is longer than in the case of an unfilled chord or column.

2.4.3 Finite element implementation

The finite element implementation can be conducted by the open-source FE framework of OpenSees (The Open System for Earthquake Engineering Simulation) (OpenSees, 2013). The main component classes in OpenSees is shown in Fig. 35, composed of four parts: *ModelBuilder*-constructs the objects in the model and adds them to the domain; *Domain*-holds the state of the model at time t_i and (t_i+dt) & is responsible for storing the objects created by the *ModelBuilder* object and for

providing the *Analysis* and *Recorder* objects access to these objects; *Analysis*-move the model from state at time t_i to state at time and (t_i+dt) ; *Recorder*-monitors user-defined parameters in the model during the analysis.

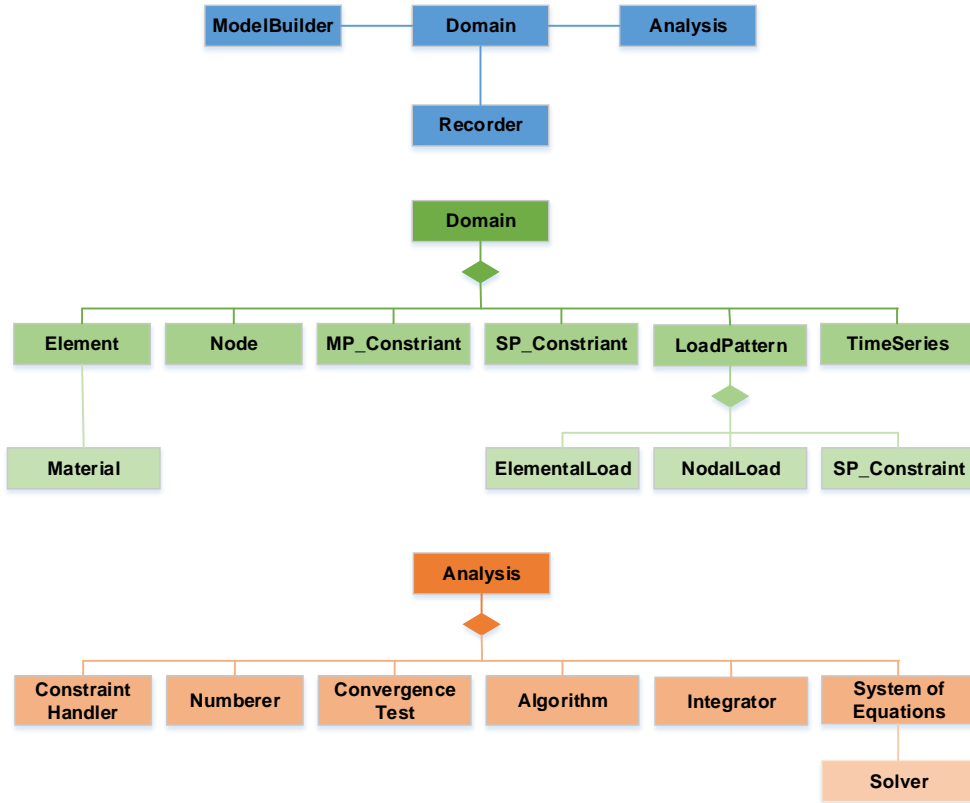


Fig. 35 Component classes in OpenSees

In the *ModelBuilder* section, *Geometric Transformation* needs to be pointed out, which is defined to provide multiple definitions of the force, deformation, and stiffness transformations necessary between the global and local coordinate systems (Scott et al. 2008). Including three subclasses, *Linear Transformation*, *P-Delta Transformation* and *Corotational Transformation*, contain implementations of specific transformation procedures with various kinematic and equilibrium assumptions. *Linear Transformation*, used to construct a linear coordinate transformation object, which performs a linear geometric transformation of beam stiffness and resisting force from the basic system to the global-coordinate system. *P-Delta Transformation*, used to construct the P-Delta Coordinate Transformation object, which performs a linear geometric transformation of beam stiffness and resisting force from the basic system to the global coordinate system, considering second-order P-Delta effects. *Corotational Transformation*, used to construct the

Corotational Coordinate Transformation object. Corotational transformation can be used in large displacement-small strain problems (Mazzoni et al, 2006). For the analyses presented in this work, the *Linear Transformation* is used for the braces, and *P-Delta Transformation* was used for chords.

So far, OpenSees framework provides a number of elements, ranging from truss element, elastic beam-column element, nonlinear beam-column elements and zero-length elements, to brick and quadrilateral elements for continuum analysis. Beam elements include: two- and three-dimensional elastic elements, concentrated plasticity elements, displacement-based distributed plasticity elements, and force-based distributed plasticity elements (Mazzoni et al, 2006).

Regards the materials, a wide variety of uniaxial materials used in fiber sections to define sectional response also already exist. Materials include: elastic, elastically perfectly plastic, hardening, and several models specifically for concrete and steel, among others. A kinematic assumption (e.g., initially plane sections remain plane) is adopted to determine the longitudinal strain at the centroid of each fiber. Based on this strain, the stress and modulus of each fiber are computed and aggregated to obtain the sectional response. Through relatively simple uniaxial stress-strain models, the fiber approach in OpenSees implements the ability to account (either explicitly or implicitly) for all the salient features of composite members, such as concrete cracking, confinement, the ductility, hysteretic behavior, etc., which is appealing for seismic analysis. The typical material constitutive will be presented in next section.

2.4.4 Material Constitutive

The CFST built-up columns usually work subjected to constant compression force, in this case, the steel tube and filled concrete will expand laterally due to the Poisson's effect. Since the Poisson's ratio of steel tube ($\nu_s=0.3$) is larger than corresponding value in the concrete ($\nu_c=0.2$), the steel tube expands at a greater rate in the early stage. The interaction between the steel and concrete will occurs when the concrete start developing micro-cracks under increasing external force. It grows a confinement pressure on the concrete and a hoop stress in the steel tube. If flexural buckling, steel local buckling, or any other loading tend to reduce the composite action on the member, the interaction between steel and concrete will disappear. This steel-concrete interaction is difficult to simulate and track under complex loading protocols, such as cyclic loading.

In order to simulate the overall response and predict the response of CFST build-up columns, the accuracy materials constitutive both in steel and concrete are strongly depended. The available material constitutive models are initially developed for reinforced concrete only and structural steel only without the steel-concrete composite interaction. The Analyses, used a fiber discretization to define section behaviour, are relied on uniaxial material models that govern the behaviour of the subdivisions of the cross sections. Hence, for uniaxial constitutive models of CFST materials, the multi-dimensional nature of the composite interaction need to be taken into account.

There are many options to account for the material properties of CFST members. Most of these were originally developed for reinforced concrete members or steel-only members, but have been adapted to CFST composite members. The main differences in all these models are the assumptions in the parameters that influence the stress-strain envelope, and mainly on the hysteretic rules and the strength-stiffness degradation on the cyclic non-linear response.

In this section, the presented constitutive models for CFST members are only focus on circular CFST section, where circular section are investigated in this work.

a) Concrete Stress-Strain Relationship

Numerous relations have been proposed to estimate the increasing strength due to the confinement acting. Some constitutive model formulation for reinforce concrete model has been reported, such as Rechart et al. (Rechart et al., 1929), Kent and Park (Kent & Park, 1971), Popovics (Popovics 1973), Mander et al. (Mander et al., 1988), Chang and Mander (Chang & Mander, 1994), etc. Cyclic characteristics of these formulations are modelled by introducing internal variables and incorporating them with the constitutive relations.

The expression for monotonic stress-strain curve in compression is defined using normalized values of strain, stress and tangent modulus, presented in Eq. (20)

$$\left\{ \begin{array}{l} x = \frac{\varepsilon_c}{\varepsilon_{cc}'} \\ y = \frac{f_c}{f_{cc}'} \\ n = \frac{E_c \varepsilon_{cc}'}{f_{cc}'} \end{array} \right. \quad (20)$$

In which, x is normalized strain, y is normalized stress, n is normalized modulus, and E_c is initial modulus of elasticity.

Popovics's equation (Popovics, 1973) defined the stress-strain relation equation, depending the parameters: the initial slope-initial modulus of elasticity (E_c) and peak coordinate-strain at the peak point (ε_{cc}' , f_{cc}'), which are modified by Mander et al. (Mander et al., 1988), see Eq. (21)

$$\left\{ \begin{array}{l} y = \frac{rx}{r-1+x^r} \\ r = \frac{n}{n-1} \end{array} \right. \quad (21)$$

The most common for CFST are developed from those proposed by Rechart et al. (Rechart et al., 1929), shown in Eq. (22) and Eq. (23), respectively.

$$f_{cc}' = f_c' + 4.1f_l \quad (22)$$

$$\varepsilon_{cc}' = \varepsilon_c' [1 + 5(f_{cc}' / f_c' - 1)] \quad (23)$$

In which, f_{cc}' is the peak compressive strength of the concrete core; f_c' is the peak compressive strength of unconfined concrete, ε_{cc}' is the corresponding strain at the peak compressive strength of the concrete core, and ε_c' is the corresponding strain at the peak compressive strength of unconfined concrete.

Then the Eq. (21) is developed by Tsai (Tsai, 1988), which add the r factor to control the post-weak behaviour, presented in Eq. (24). For the case of $r=n/(n-1)$, Eq. (24) is simplified to Eq. (21).

$$\left\{ \begin{array}{l} y = \frac{nx}{D(x)} \\ D(x) = \begin{cases} 1 + (n - \frac{r}{r-1})x + \frac{x^r}{r-1} & \text{for } r \neq 1 \\ 1 + (n-1+\ln x)x & \text{for } r = 1 \end{cases} \end{array} \right. \quad (24)$$

To derive a relation between the hoop stress in the steel tube and the confining pressure in the concrete core, a typical to utilize the idealized stress distribution shown in the free body diagram in Fig. 36 (Denavit and Hajjar, 2010).

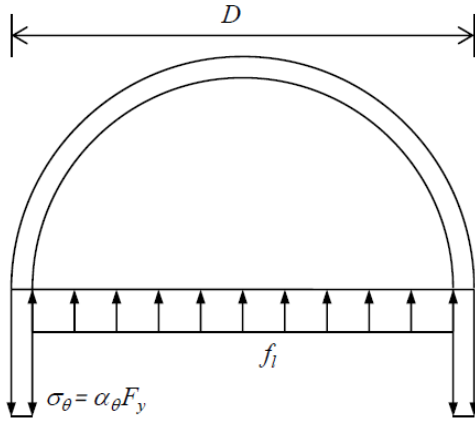


Fig. 36 Idealized diagram of a circular CSFT section (Denavit and Hajjar, 2010)

In the figure, f_i is the confining pressure in the concrete core, which is a key component of many existing concrete constitutive relationships and is often assumed to be constant throughout the section (Susantha et al., 2001). D is the outside diameter of the steel tube, t is the thickness of the steel tube, and $\alpha_\theta F_y$ is the hoop stress in the steel tube expressed as the product of the ratio of hoop stress to steel yield stress and steel yield stress. The relation formula can be expressed as follows,

$$\sum F = 2t\alpha_\theta F_y - (D - 2t)f_i = 0 \quad (25)$$

$$f_i = \alpha_\theta F_y \frac{2}{D/t - 2} \quad (26)$$

The classic Von Mises yield criterion is employed. Assuming a biaxial state of stress exist in the steel tubes, the yield criteria is written as in Eq. (27),

$$\alpha_{\theta}^2 - \alpha_{\theta}\alpha_z + \alpha_z^2 = 1 \quad (27)$$

In which, α_{θ} is the ratio of hoop stress to steel yield stress and α_z is the ratio of axial stress to steel yield stress.

Therefore, for a given hoop stress ratio, yield occurs at different axial stress ratios in the positive and negative direction, which can be computed as Eq. (28) and Eq. (29), respectively.

$$\alpha_{z,positive} = 0.5(\alpha_{\theta} + \sqrt{4 - 3\alpha_{\theta}^2}) \quad (28)$$

$$\alpha_{z,negative} = 0.5(\alpha_{\theta} - \sqrt{4 - 3\alpha_{\theta}^2}) \quad (29)$$

Susantha et al. (Susantha et al., 2001) carried out the test subjected to tri-axial compressive stresses caused by axial load plus lateral pressure due to the confinement action in circular, box and octagonal shaped concrete-filled steel tubes. Available empirical formulas are adopted to determine the lateral pressure exerted on concrete in circular concrete-filled steel columns. The formula is also based on Popovics's equation, while some key points is determined by his method.

$$E_c = 3320\sqrt{f'_c} + 6900(Mpa) \quad (30)$$

$$\epsilon'_c = \begin{cases} 0.002 & \text{for } \leq 82(Mpa) \\ 0.002 + \frac{f'_c - 28}{54000} & \text{for } 28 \leq f'_c \leq 82(Mpa) \\ 0.003 & \text{for } \geq 82(Mpa) \end{cases} \quad (31)$$

$$f'_{cc} = 0.85f'_c + 4.0f_l \quad (32)$$

In which, f_l is the lateral confining pressure on the concrete core. Confining pressure models have been proposed by Tang et al. (Tang et al., 1996) that account for the effects of material properties and the column geometry.

$$\alpha_{\theta} = v_e - v_s \quad (33)$$

Where, ν_e and ν_s are the Poisson's ratios of a steel tube with and without filled-in concrete, respectively. ν_s is taken as 0.5 at the maximum strength point, and ν_e is defined by Tang et al. (Tang et al., 1996),

$$\nu_e = 0.2312 + 0.3582\nu'_e - 0.1524\left(\frac{f'_c}{F_y}\right) + 4.843\nu'_e\left(\frac{f'_c}{F_y}\right) - 9.169\left(\frac{f'_c}{F_y}\right)^2 \quad (34)$$

In which, ν'_e is defined by as follows,

$$\nu'_e = 0.881 \times 10^{-6} \left(\frac{D}{t}\right)^3 - 2.58 \times 10^{-4} \left(\frac{D}{t}\right)^2 + 1.953 \times 10^{-2} \left(\frac{D}{t}\right) + 0.4011 \quad (35)$$

The post-peak region of the compressive stress-strain curve for the confined concrete is expressed by Susantha et al. (Susantha et al., 2001).

$$f = \begin{cases} f'_{cc} - Z(\varepsilon - \varepsilon'_{cc}) & \text{for } \varepsilon'_{cc} \leq \varepsilon \leq \varepsilon_{cu} \\ f'_{cc} - Z(\varepsilon_{cu} - \varepsilon'_{cc}) & \text{for } \varepsilon > \varepsilon_{cu} \end{cases} \quad (36)$$

For circular CFST section, slope Z and ultimate strain ε_{cu} are determined based on Susantha et al. (Susantha et al., 2001) as

$$Z = \begin{cases} 0 & \text{for } R_t \left(\frac{f_c}{F_y}\right) \leq 0.006 \\ 1.0 \times 10^5 R_t \frac{f_c}{F_y} - 600 & \text{for } R_t \left(\frac{f_c}{F_y}\right) > 0.006 \text{ and } F_y \leq 283 \text{ Mpa} \\ \left(\frac{F_y}{283}\right)^{13.4} [1.0 \times 10^5 R_t \frac{f_c}{F_y} - 600] & \text{for } R_t \left(\frac{f_c}{F_y}\right) > 0.006 \text{ and } 283 \leq F_y \leq 336 \text{ Mpa} \\ 1.0 \times 10^6 R_t \frac{f_c}{F_y} - 600 & \text{for } R_t \left(\frac{f_c}{F_y}\right) > 0.006 \text{ and } F_y > 336 \text{ Mpa} \end{cases} \quad (37)$$

$$\varepsilon_{cu} = 0.025 \text{ for circular steel tubes} \quad (38)$$

In which, R_t is the radius-to-thickness ratio parameter defined by

$$R_t = \sqrt{3(1-\nu^2)} \frac{F_y}{E_s} \frac{D}{2t} \quad (39)$$

In which ν and E_s are the Poisson's ratio and Young's modulus of the steel tube. The maximum value of R_t is 0.125. The selection criteria are based on the relationship proposed by Usami and Ge (Usami & Ge, 1998) for local buckling strength of plates in CFST columns as follows

$$\frac{F_b}{F_y} = 0.8 + \frac{0.25}{R_t} \leq 1.0 \quad (40)$$

In which, F_b is local buckling strength of CFST columns.

In summary, the proposed stress–strain relationship consists of a non-linear ascending branch up to the peak (i.e., part OA), a linear descending branch beyond the peak (i.e., part AB) and constant residual strength after strain ϵ_{cu} (i.e., part BC) as illustrated in Fig. 37. The key points of A and B are important during the analysis.

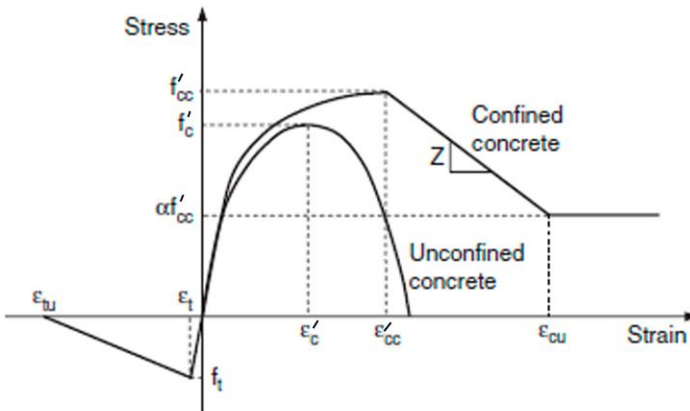


Fig. 37 Confined concrete constitutive model proposed by Susantha et al. (Susantha et al., 2001)

Liang and Fragomeni (Liang & Fragomeni, 2009) indicates that Susantha model generally overestimates the lateral confining pressures for high strength concrete. An accurate confining pressure model was finally proposed by Liang and Fragomeni (Liang & Fragomeni, 2009), which developed from Susantha model and can be used for both normal and high strength concrete, and the changing formulas are highlighted in the following, the remaining are same as previous.

$$f'_{cc} = \gamma_c f'_c + k_1 f_t \quad (41)$$

Where, k_1 is taken as 4.1, γ_c is the strength reduction factor, consider the column section size effect, expressed by

$$\gamma_c = 1.85D_c^{-0.135} \quad (0.85 \leq \gamma_c \leq 1.0) \quad (42)$$

In which, D_c is the diameter of the concrete core.

$$\varepsilon'_{cc} = \varepsilon'_c \left(1 + k_2 \frac{f_l}{\gamma_c f'_c} \right) \quad (43)$$

In which, k_2 are taken as 20.5.

$$\varepsilon'_c = \begin{cases} 0.002 & \text{for } \leq 82(\text{Mpa}) \\ 0.002 + \frac{\gamma_c f'_c - 28}{54000} & \text{for } 28 \leq f'_c \leq 82(\text{Mpa}) \\ 0.003 & \text{for } \geq 82(\text{Mpa}) \end{cases} \quad (44)$$

Based on the research of Hu et al. (Hu et al., 2005), f_l is defined by eq. (45)

$$f_l = \begin{cases} 0.7(v_e - v_s) \frac{2t}{D-2t} F_y & \text{for } \frac{D}{t} \leq 47 \\ (0.006241 - 0.0000357 \frac{D}{t}) F_y & \text{for } 47 \leq \frac{D}{t} \leq 150 \end{cases} \quad (45)$$

Similarly, Liang and Fragomeni (Liang & Fragomeni, 2009) defined the parts AB and BC of the stress-strain curve developed from Susantha model, which the key values can be expressed by Eq. (46) and shown in Fig. 38.

$$\sigma_c = \begin{cases} \beta_c f'_{cc} + \left(\frac{\varepsilon_{cu} - \varepsilon_c}{\varepsilon_{cu} - \varepsilon'_{cc}} \right) (f'_{cc} - \beta_c f'_{cc}) & \text{for } \varepsilon'_{cc} < \varepsilon_c \leq \varepsilon_{cu} \\ \beta_c f'_{cc} & \text{for } \varepsilon_c > \varepsilon_{cu} \end{cases} \quad (46)$$

Where ε_{cu} is taken as 0.02, based on the experimental results, β_c is a factor, reflects the confinement effect provided by the steel tube on the post-peak strength and ductility of confined concrete, which is given by Hu et al. (Hu et al., 2005) as

$$\beta_c = \begin{cases} 1.0 & \text{for } \frac{D}{t} \leq 40 \\ 0.0000339\left(\frac{D}{t}\right)^2 - 0.010085\left(\frac{D}{t}\right) + 1.3491 & \text{for } 40 < \frac{D}{t} \leq 150 \end{cases} \quad (47)$$

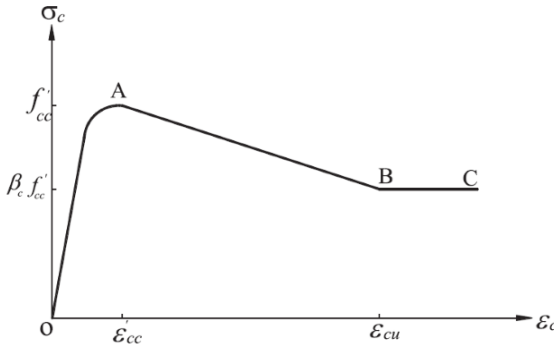


Fig. 38 Confined concrete constitutive model proposed by Liang and Fragomeni (Liang and Fragomeni, 2009)

Usually, the uniaxial constitutive relationships of tensile response of the concrete for CFST materials are neglected in analysis, such as Elremaily and Azizinamini (Elremaily & Azizinamini, 2001), Sakino et al. (Sakino et al., 2004), and Hatzigeorgiou (Hatzigeorgiou, 2008). However, modeling the tensile response of concrete has been shown to improve the accuracy of nonlinear finite element models for composite members (Hajjar and Gourley 1997). In this work, the shape of the stress-strain response of concrete in tension is similar to that of concrete in compression, which is also recommended by Chang and Mander (Chang & Mander, 1994). The equation (Eq. 20 and Eq. 21 as mentioned above), with normalized variables defined with respect to tensile values for the peak stress, f'_t , the strain at peak stress, ϵ'_t , and the post-peak factor, r_p , are defined as follows, seen in Fig.37.

$$f'_t = 0.5\sqrt{f'_c} \text{ (Mpa)} \quad (48)$$

$$\epsilon'_t = 1.23 \frac{f'_t}{E_c} \quad (49)$$

$$r_p = 4 \quad (50)$$

Once the key points are defined by the previous equations in monotonic stress-strain relationship, *concrete02 model* in OpenSees, is adopted under the cyclic

loading. It is applicable to predict the response of the concrete components in CFST members, and with better convergence of the solution than other model as author's experience. Taken into account that the envelope curves for the case of load reversals and also transitions between transition curves for the case of partial load reversals, the model is presented in Fig. 39.

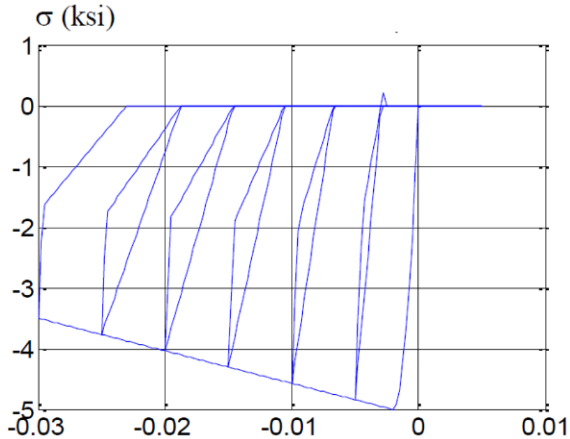


Fig. 39 Cyclic response of uniaxial stress-strain models in OpenSees (Perea, 2010)

b) Steel Stress-Strain Relationship

In this work, the steel tubes are simulated using the well-known nonlinear hysteretic model proposed by Menegotto and Pinto (Menegotto & Pinto, 1973), as modified by Filippou et al. (Filippou et al., 1983), to include isotropic strain-hardening effects. This model can be implemented by the *Steel02 model (Giuffre-Menegotto-Pinto model)* available in OpenSees material library, which can consider smooth elastic-to-plastic transition, elastic unloading, isotropic and kinematic hardening, and Bauschinger effects. The curved transition are present in Fig. 40. Among that, E_0 is the elastic asymptote slope, E_1 is the yield asymptote slope, b is the strain-hardening ratio between E_0 and E_1 , R is the factor which affects the curvature of the transition curve between the two asymptotes and represents the Bauschinger effects.

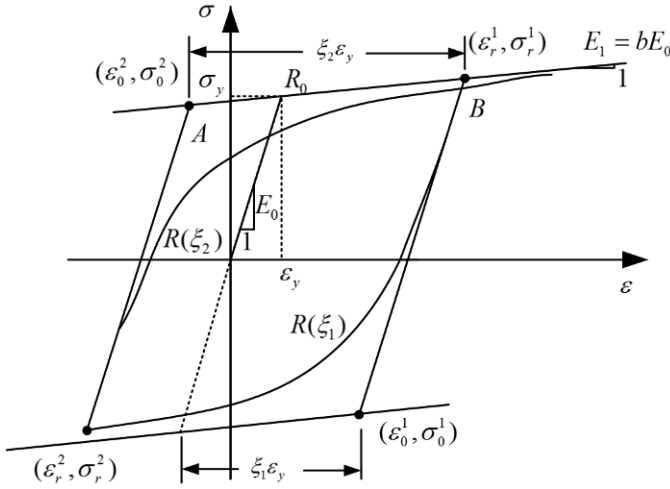


Fig. 40 Cyclic response of steel stress-strain models in OpenSees

The uniaxial hysteretic stress-strain relation of Menegotto and Pinto model (Menegotto & Pinto, 1973) are defined as follows.

$$\sigma^* = b\varepsilon^* + \frac{(1-b)\varepsilon^*}{(1+\varepsilon^{*R})^{1/R}} \quad (51)$$

Eq. (51) defines the curved transition from E_0 to E_t , in which,

$$\varepsilon^* = \frac{\varepsilon - \varepsilon_r}{\varepsilon_0 - \varepsilon_r} \quad (52)$$

$$\sigma^* = \frac{\sigma - \sigma_r}{\sigma_0 - \sigma_r} \quad (53)$$

Where, σ_r and ε_r are the stress and strain at the point of strain reversal, σ_0 and ε_0 are the stress and strain at the point of intersection of the two asymptotes. The strain and stress pairs $(\varepsilon_r, \sigma_r)$ and $(\varepsilon_0, \sigma_0)$ are updated after each strain reversal.

Then, the tangent modulus E_t of the stress-strain relation can be expressed by Eq. (54)

$$E_t = \frac{d\sigma}{d\varepsilon} = \left(\frac{\sigma_0 - \sigma_r}{\varepsilon_0 - \varepsilon_r} \right) \frac{d\sigma^*}{d\varepsilon^*} \quad (54)$$

Where,

$$\frac{d\sigma^*}{d\varepsilon^*} = b + \left[\frac{1-b}{(1+\varepsilon^{*R})^{1/R}} \right] \left[1 - \frac{\varepsilon^{*R}}{1+\varepsilon^{*R}} \right] \quad (55)$$

The curvature factor R is dependent on the absolute strain between the current asymptote intersection point and the previous maximum or minimum strain reversal point. It is also defined by Menegotto and Pinto (Menegotto & Pinto, 1973),

$$R = R_0 - \frac{a_1 \xi}{a_2 + \xi} \quad (56)$$

In which, R_0 is the initial parameter under monotonic or cyclic loading, a_1 and a_2 are experimentally parameters which can reflect the degradation of the curvature within subsequent cycles. ξ is the absolute strain difference between the current asymptote intersection point and the previous maximum or minimum strain reversal point, defined by Eq. (57).

$$\xi = \left| \frac{(\varepsilon_m - \varepsilon_0)}{\varepsilon_y} \right| \quad (57)$$

In which, ξ_m is the maximum or minimum strain value at the point of strain reversal, ξ_0 is the strain at the current intersection point of the two asymptotes, ξ_y is the strain at monotonic yield point. Therefore, ξ is updated depending the strain reversal.

3. HYSTERETIC TESTING OF CFST BUILT-UP COLUMNS

3.1. Introduction

In contrast to the extensive hysteretic experimental research on the seismic behavior of CFST single columns, little effort has been devoted to study the hysteretic behavior of CFST built-up columns. Toward this aim, a group of six specimens were designed for hysteretic test by the author, which based on the prototype of Ganhaizi Bridge. The experimental activity was conducted on August 2014, depending on the Multi-structural Testing System (MTS hydraulic servo loading system) in Fuzhou University, China. In this chapter, the author presents the specimen design, manufacture, testing procedure and results discussion. Under quasi-static loading, the hysteretic characteristics of CFST built-up columns, such as failure modes, deformed shapes, load displacement hysteretic curves, displacement ductility, rigidity and strength degradation, and energy dissipation capacity are analyzed.

3.2. Specimen Design and Fabrication

Generally, the relationships between specimen and prototype can be derived through Buckingham's Pi Theorem (Harris & Sabnis, 1999). Then, specimen test data obtained could be linked with the prototype. Hence, the specimen geometry, material properties, initial conditions, boundary conditions and load cases need to be determined firstly.

Based on the case of Ganhaizi Bridge, (introduced in Ch.5 in details) and the test condition in laboratory of Fuzhou University, the scale ratio was 1:8 for the cyclic test. In order to exclude the slope effect along the height of prototype, the specimen was designed erective. The material of specimen can be chosen the same as the prototype. For the column in prototype, the initial conditions was under the dead load transferred from the girder. Regards the boundary conditions, each column was fixed at the bottom and rigid connected with girder. Therefore, the specimen was fixed at the bottom. At the top, subjected to low cyclic loading in horizontal

direction with constant loading in vertical direction. The design parameters of all the lattice and composite piers of Ganhaizi Bridge are summarized in Table 4 and Table 5. Among that, the axial load ratio n is defined as Eq. (58).

$$n = N / N_0 \tag{58}$$

Where N is the dead load on the top of pier; N_0 is the nominal bearing capacity which is determined by the four CFST columns, by Eq. (59).

$$N_0 = 4(f_y A_s + f_{ck} A_c) \tag{59}$$

Where f_y and f_{ck} are the yield strength of steel and the prism compressive strength of concrete, respectively. A_s and A_c represent the steel area and concrete area of the cross section, respectively.

No.	Pier height h (m)	Spacing at the bottom B (m)	Spacing at the top b (m)	$(B+b)/2$ (m)	Scale width (mm)	Axial load ratio n
2	24.284	2.111	1.14	1.625	203	0.15
3	32.227	2.429	1.14	1.784	223	0.15
4	40.207	2.748	1.14	1.944	243	0.15
5	49.542	3.122	1.14	2.131	266	0.15
6	49.695	3.128	1.14	2.134	267	0.15
7	40.067	2.743	1.14	1.942	243	0.15
8	26.642	2.206	1.14	1.673	209	0.15
9	24.153	2.106	1.14	1.623	203	0.15
14	34.295	2.512	1.14	1.826	228	0.14
15	60.058	3.918	1.516	2.717	340	0.17
26	67.29	4.212	1.52	2.866	358	0.17
27	54.771	3.331	1.14	2.236	280	0.14
28	42.825	2.853	1.14	1.997	250	0.15
29	32.567	2.443	1.14	1.792	224	0.16
30	26.701	2.208	1.14	1.674	209	0.12

Table 4
Design parameters of lattice piers in Ganhaizi Bridge

No.	Pier height h (m)	Spacing at the top of RC web B (m)	Spacing at the top b (m)	(B+b)/2 (m)	Scale width (mm)	Height-width ratio $2(h-30)/(B+b)$	Axial load ratio n
16	95.8	5.247	1.607	3.427	428	19	0.17
17	104.897	5.247	1.607	3.427	428	22	0.17
18	105.451	5.247	1.607	3.427	428	22	0.17
19	103.961	5.247	1.607	3.427	428	22	0.17
20	107.249	5.248	1.608	3.428	429	23	0.17
21	107.036	5.247	1.607	3.427	428	22	0.17
22	105.324	5.247	1.607	3.427	428	22	0.17
23	102.111	5.247	1.607	3.427	428	21	0.17
24	96.998	5.247	1.607	3.427	428	20	0.17
25	95.086	5.248	1.608	3.428	429	19	0.17

Table 5

Design parameters of composite piers in Ganhaizi Bridge

From Table 4 and Table 5, it is found that the 1:8 scale width ranges from 203mm to 429mm, and the axial load ratio ranges from 0.12 to 0.17. Considering the lower pier will prior to failure than the higher pier, hence, the length and width of specimen should be shorten. Owing to the test condition of MTS system (500kN actuator, range ± 250 mm), the height of specimen should also guarantee the ultimate displacement can be reached within maximum displacement range. Moreover, the circular hollow steel lacing can be welded easily during fabrication. Finally, the benchmark specimen was determined with the height 2500mm, centerline spacing between the two chords was 500mm. According to the 1:8 scale ratio, CFST chords with Q345 steel tube, diameter 110mm, thickness 2mm, in-filled with C50 grade concrete; brace with steel tube with diameter 50mm, thickness 2mm, spacing between lacings were 250mm. Moreover, one of the most important parameters considered in the practical design and ductility evaluation of circular steel bridge piers were the radius-thickness ratio parameter R_t , which are expressed as Eq. (39) in Ch.2.4.1. Due to the seismic design specification (Japan Road Association, 2002), it is specified that thickness of circular columns should be designed such that $R_t \leq 0.08$ to prevent a decrease in strength and ductility due to local buckling. Therefore, from Eq. (39), the R_t becomes 0.076, meet the requirement.

For the configuration of specimen, at the bottom, CFST chords were not directly welded with steel plates, while instead of concrete tie-down footing, to prevent local buckling under horizontal cyclic loading. The tie-down footing was made of concrete

block, $\phi 12$ rebar embed in it and set through gusset plate welded with the chords. Four additional holes through hollow pipes were reserved at the block, to ensure specimen and ground are connected by bolt connection provided by laboratory. On the top, CFST chords were also inserted into concrete block, and connected with the actuator through bolts, to make sure the horizontal loading apply uniformly on the specimen and prevent any premature failure during loading procedure. Meanwhile, constant vertical axial force were applied on the top of concrete block through 1000kN hydraulic jacks, to simulate the dead load with axial load ration $n=0.15$. When subjected to cyclic loading along in-plane direction (longitudinal), in order to ensure out of plane direction (transverse) was stronger member inertia axis, the center spacing between chords in transverse was 700mm, larger than that in longitudinal direction. Geometric details of the benchmark specimen is shown in Fig. 41.

In addition to compare with benchmark specimen, by the influence of the concrete grade and different brace arrangement were investigated. Another five specimens were also designed and fabricated for the test, including 2 specimens with different concrete grade (C40 and C60), and 3 specimens with different brace arrangements (V shape, M shape and N shape). Fig. 42 shows the 3 specimens with different brace arrangements, where only varies in longitudinal view, the rest are the same configuration with the benchmark specimen. Data of six specimens are summarized in Table 6.

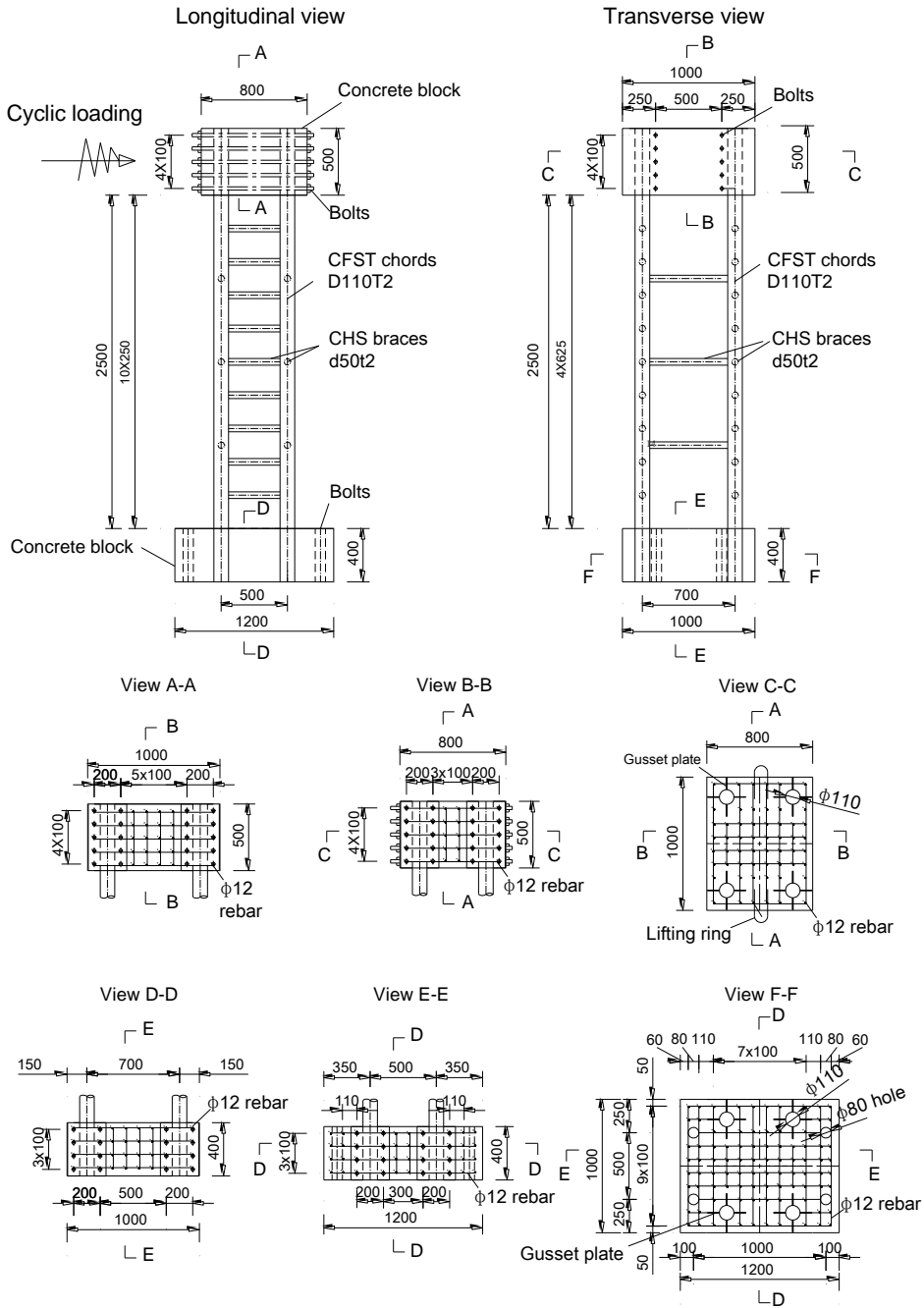
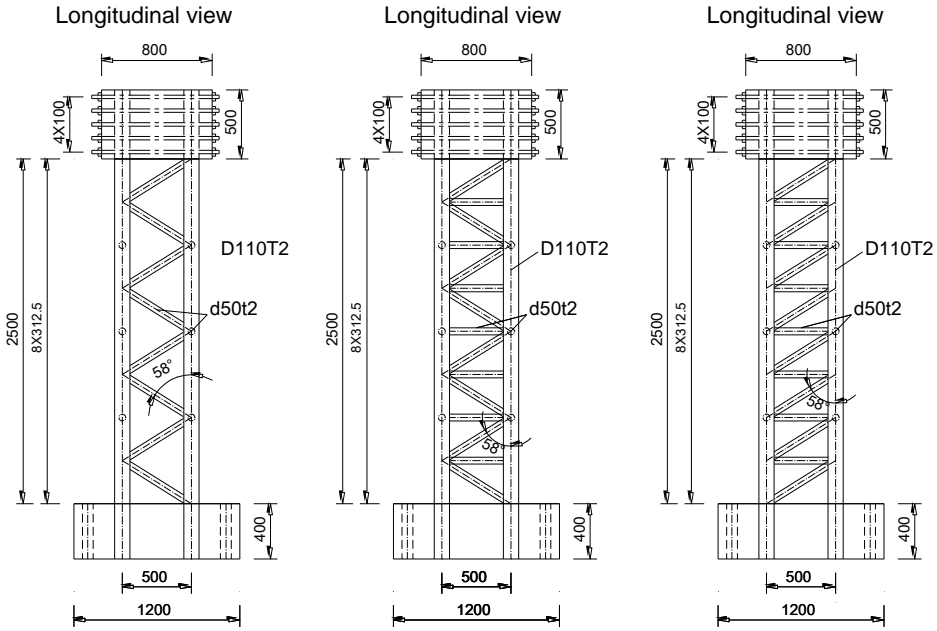


Fig. 41 Benchmark specimen (Unit: mm)

SEISMIC BEHAVIOR OF CONCRETE FILLED STEEL TUBULAR BUILT-UP COLUMNS



a) V shape

b) M shape

c) N shape

Fig. 42 Specimens with different brace arrangements (Unit: mm)

Specimen No.	In-filled concrete grade	Brace arrangement	Axial load ratio n
S1(Benchmark)	C50	Parallel	0.15
S2	C40	Parallel	0.15
S3	C60	Parallel	0.15
S4	C50	V shape	0.15
S5	C50	M shape	0.15
S6	C50	N shape	0.15

Table 6

Data of six specimens

3.3. Material Properties

The material properties of steel and concrete were obtained according to the requirements defined in China National Standards GB/T 50081-2002 (China National Standard, 2002) and GB/T 228.1-2010 (China National Standard, 2010a). Test coupons were fabricated with the steel material used for constructing the steel tubes and tested in tension. The yield strength f_y was determined by the 0.2% proof stress. The average yield strength f_y , ultimate strength f_u and elastic modulus E_s for steel coupons of chord and brace are summarized in Table 7, respectively.

Concrete cubes $150 \times 150 \times 150 \text{mm}^3$ made at the time of concrete casting were tested to determine the concrete properties. Average cube compressive strengths f_{cu} for Grade C40, C50 and C60 on the 28th day are also presented in Table 7, respectively. According to code for design of concrete structures GB 50010-2010 (China National Standard, 2010b) in China, the prism compressive strength f_{ck} is equal to 0.67 times the cube compressive strength f_{cu} .

Concrete	E_c (MPa)	f_{cu} (MPa)	Steel tube	E_s (MPa)	f_{sy} (MPa)	f_{su} (MPa)	Poisson's ratio ν
C40	3.25×10^4	40.3	Chord	2.36×10^5	345	420	0.28
C50	3.45×10^4	48.5	Brace	2.07×10^5	374	472	0.29
C60	3.60×10^4	57.5					

Table 7
Material properties

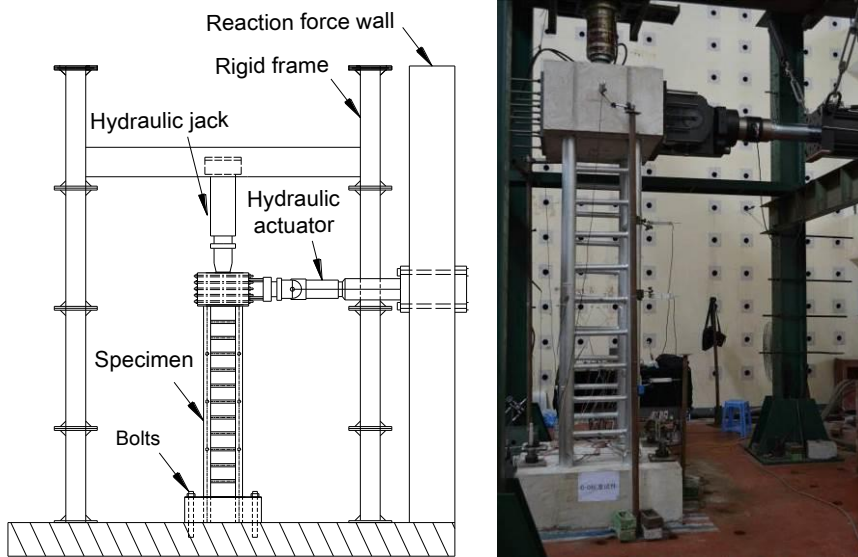
3.4. Test Setup and Procedure

The general view of test setup and panorama used in experiment are shown in Fig. 43. A constant axial load (axial load ratio $n=0.15$, $N=330\text{kN}$) was applied to the specimen through 1000kN hydraulic jack. Cyclic horizontal loading was applied to the specimen through 500kN electrohydraulic servo actuator. The constant axial load and cyclic lateral loads were recorded by corresponding load sensors. The imposed horizontal displacement was measured with both the displacement transducer of the actuator and a linear variable displacement transducer arranged at the opposite side of the horizontal loading point. Both vertical and longitudinal electrical resistance strain gauges were attached on the surface of steel tube at the chords and braces of the specimen to record the axial and longitudinal strains, respectively.

Before the test, a pre-loading procedure ($0.5N=165\text{kN}$) was performed, in order to eliminate the asymmetry of specimen, keep all parts of the structure as normal working state, meanwhile test the reliability of apparatus and instruments. Then the axial compressive load was increased gradually to the full level and maintained till the end of the test.

Currently, the quasi-static test are commonly used on dynamic experiment, which is the primary method to evaluate specimen's seismic performance. There are three

popularly methods in loading control, including displacement control, force control, and hybrid control. In this test, displacement control was chosen, displacement loading histories shown in Fig. 44. Only one cycle was imposed at each load level in elastic stage. After the estimated yield displacement $\bar{\delta}_y$, three cycles were imposed at the incremental displacement levels of $1.5\bar{\delta}_y$, $2\bar{\delta}_y$, $2.5\bar{\delta}_y$, $3\bar{\delta}_y$..., respectively. During the testing, the cyclic loading speed was controlled at a rate of 1 mm/s for the displacement control stage. The tests were performed under cyclic loading and would stop when it met one of the following two conditions: 1) it had been found that the strength of specimens decreased to smaller than 85% peak load at certain appointed displacement; 2) it had obvious failure characteristics, such as buckling at the chords footing, break at the brace.



a) General view
Fig. 43 Test setup

b) Panorama

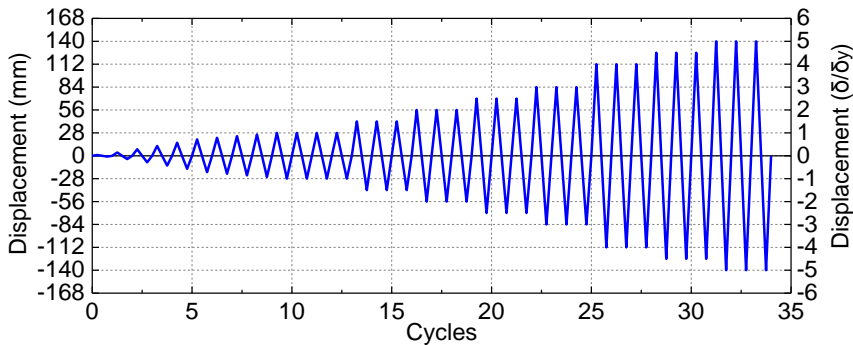
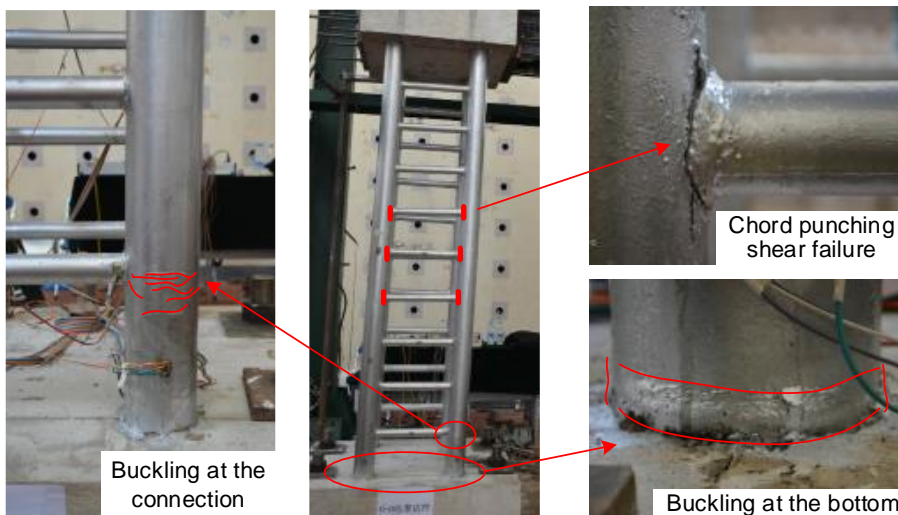


Fig. 44 Displacement loading histories

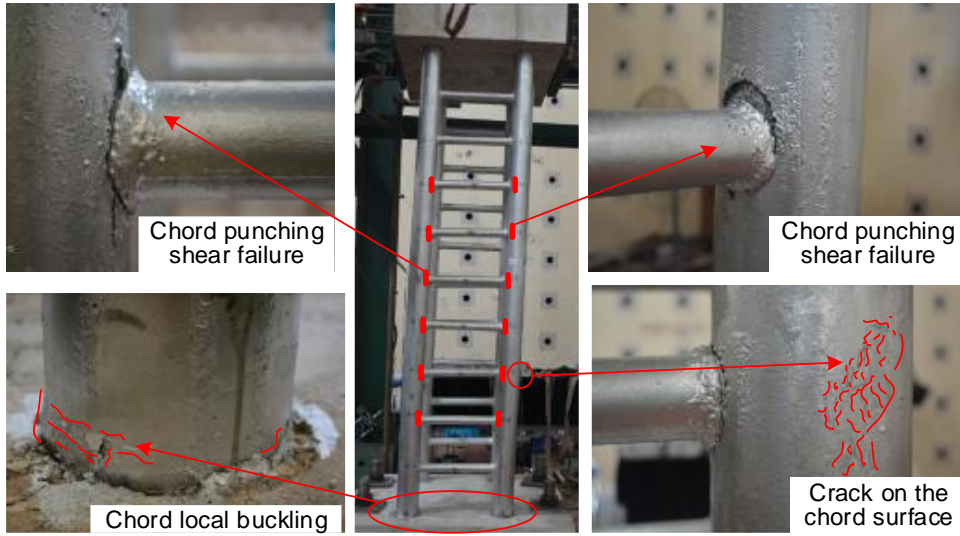
3.5. Experimental Results and Discussions

3.5.1 Failure Modes and Deformed Shapes

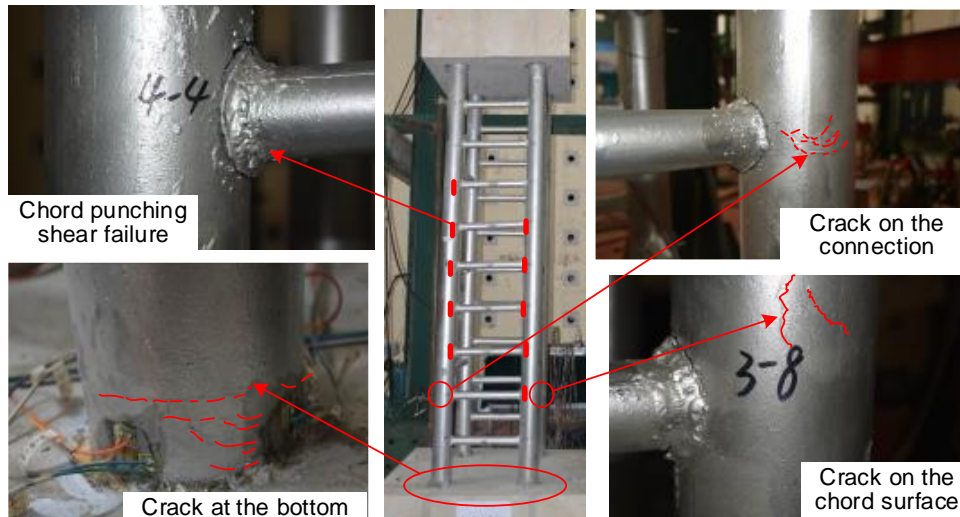
The photos of six specimens taken after the test were completed are shown in Fig. 45 and Fig. 46. As expected, all the specimens show overall lateral deformation. However, the failure modes for CFST battened columns and CFST laced columns were different. As for battened members (Fig. 45), both the chords and battens would be simultaneously subjected to bending moment and shear force. Therefore the maximum bending moment of a battened specimen was at one of the connections of chords and the batten. When the displacement on the top was approximately 2.5 times to the yield displacement, the footing of chord started to appear cracks. As the displacement increased, the cracks continuously developed and spread around the steel tubes, then buckling gradually appears on the steel tubes. As a result, the local buckling waves have spread in four chords of each specimen, and energy dissipated continuously without a serious damage at a specific point. The connections of the weakest part, would fail due to chord punching shear when the global deformation increased remarkably, and cause the strength of specimens decrease to smaller than 85% peak load at certain appointed displacement. Therefore, we can say that the failure mode of the specimen are the buckling waves concentrated at the bottom of chords resulting in elephant foot buckling mode, meanwhile, chord punching shear failure appears at the weakest part of connection, the deformed shapes are overall lateral deformation.



a) Specimen 1



b) Specimen 2

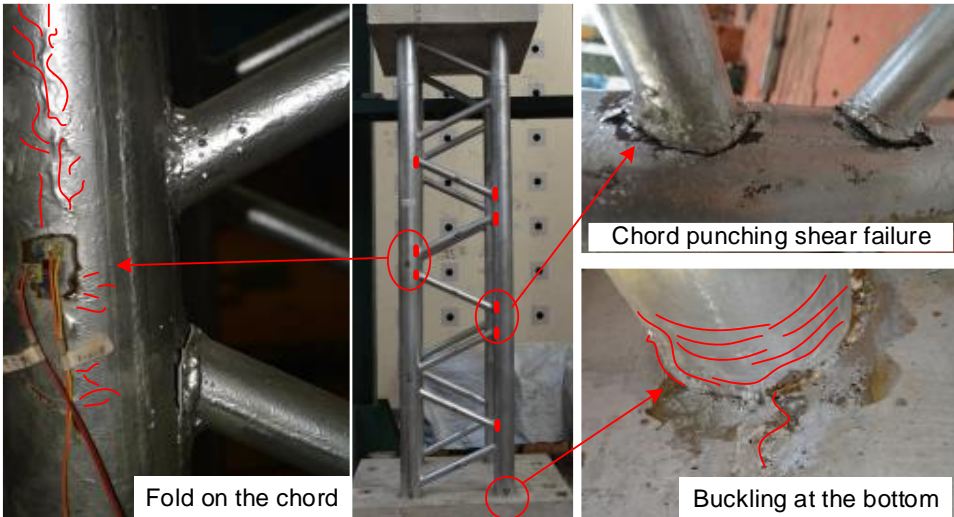


c) Specimen 3

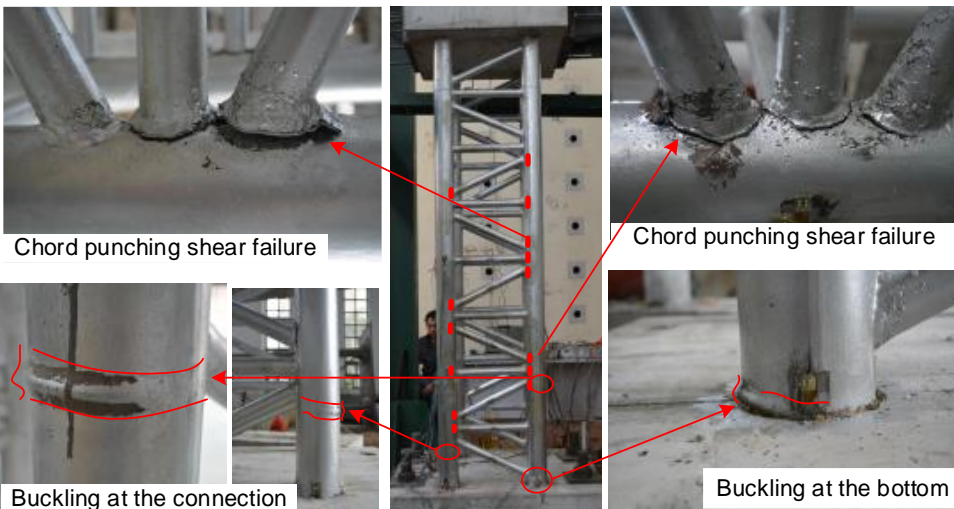
Fig. 45 Failure modes of CFST battened columns

For laced members (Fig. 46), both chords and braces were mainly subjected to axial forces. Due to the diagonal braces of the laced member restrained the relative deformations of battens and chords effectively, the ultimate horizontal force is significantly increased. However, when the weakest part at the connection between chord and brace broken, the strength of specimens quickly decreased to smaller than 85% peak load. Moreover, fold on the chord surface at the connection was obviously observed, due to the crush of the in-filled concrete under axial forces.

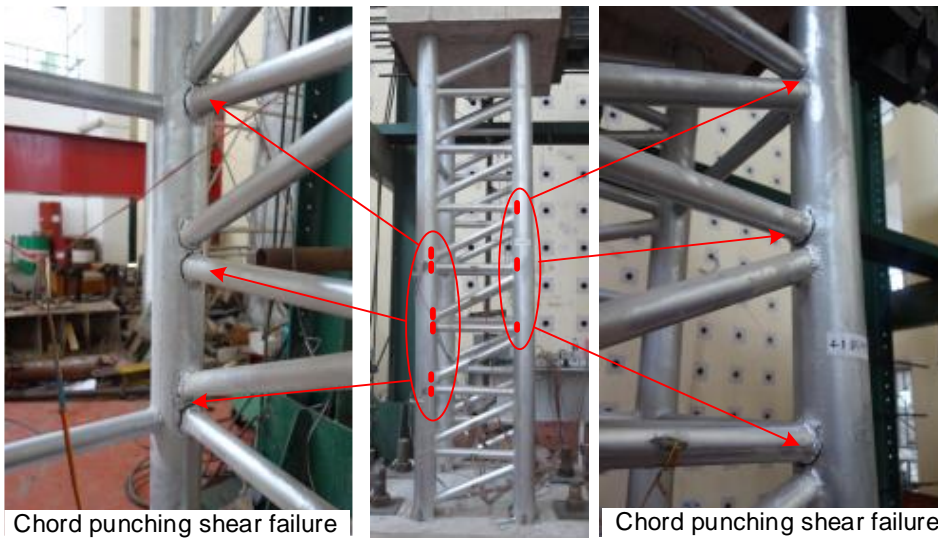
Compared with V and N shape specimen, M shape specimen exhibited more desirable mechanics properties, where buckling appeared on the bottom of chord, and connection between chord and braces, while not observed on the V and N shape specimen. It is indicated that M shape arrangement is more reasonable than V and M arrangement under cyclic loading.



a) Specimen 4



b) Specimen 5

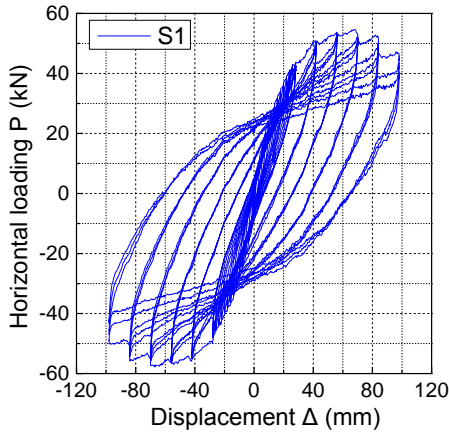


c) Specimen 6

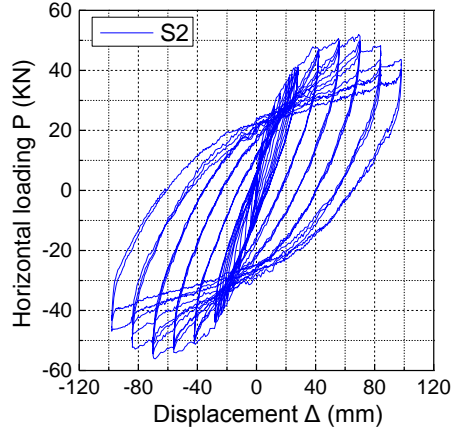
Fig. 46 Failure modes of CFST laced columns

3.5.2 Load Displacement Hysteretic Curves

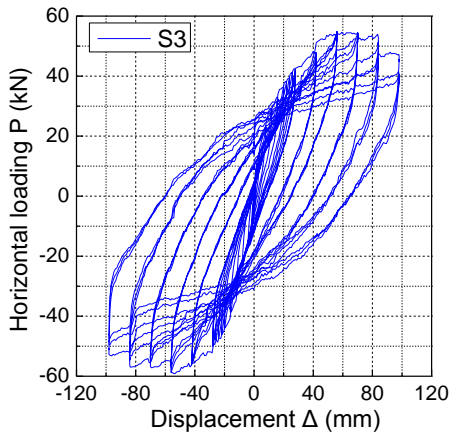
The horizontal loading P versus corresponding horizontal displacement Δ hysteretic curves for all specimens are shown in Fig. 47. It can be seen that the hysteretic curves of CFST battened columns (S1-S3) are generally saturated and show spindle-shaped, which indicates that the specimen have excellent hysteretic behavior. After the maximum strength achieved, each displacement degrades as cycling proceeds loading. It is mainly due to increased local buckling of the steel tubes, which will also cause accumulated damage to the in-filled concrete, then cause the stiffness degrades as the horizontal displacement increases. However, there is no obvious loading capacity degradation was observed during the loading process. On the contrary, different results can be observed for the CFST laced columns (S4-S6), the horizontal ultimate loads for laced columns can be significantly increased, more than two times to CFST battened column. After that, due to the punching shear failure at the connection between braces and chords, a sharp decline of P - Δ appears. For S4 and S6 specimen, the maximum horizontal displacement is approximately half of that to CFST battened columns. For S5 specimen, the hysteretic curves are also saturated.



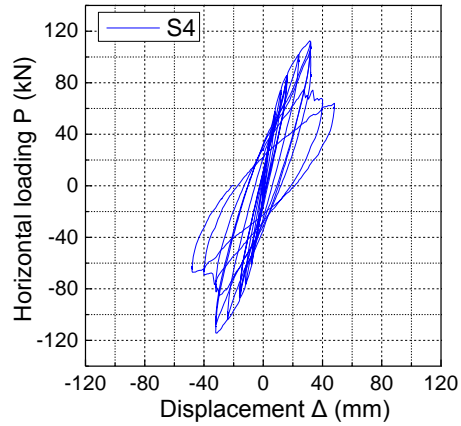
a) Specimen 1



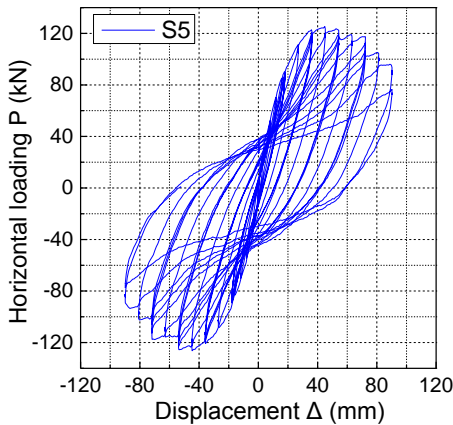
b) Specimen 2



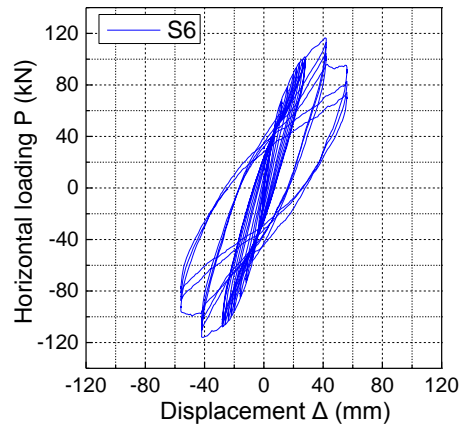
c) Specimen 3



d) Specimen 4



e) Specimen 5



f) Specimen 6

Fig. 47 Horizontal loading P versus displacement Δ hysteretic curves for all specimens

As the $P-\Delta$ hysteretic curves for specimens show the whole loading procedure in the test, but it is not clear to compare the results among different specimens. The $P-\Delta$ envelop curves are compared in Fig. 48, which connected with each peak values under each cyclic loading. It can be seen that for CFST battened columns, three curves are nearly coincidence in elastic range, when the displacement exceeds the maximum displacement, the maximum and ultimate lateral load of reduces with a decrease by the concrete strength. It is expected that as the concrete grade increase, the maximum loading and displacement will be increased, but there is no obvious different of the $P-\Delta$ envelop curves between specimens with different concrete grades, only a slight increase with the concrete grade increase. Hence, the influence of the concrete grade is less significant. For CFST laced columns, both the initial stiffness and ultimate bearing capacity are increased, meanwhile, ultimate displacement appears in advance.

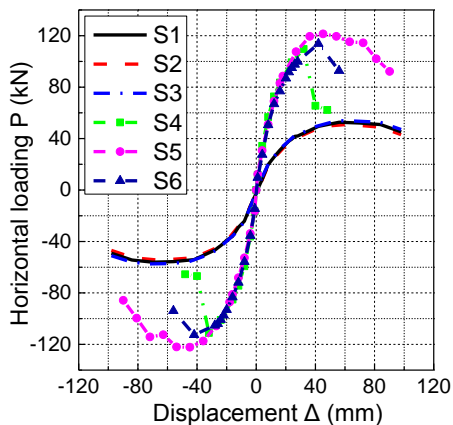


Fig. 48 $P-\Delta$ envelope curves

3.5.3 Displacement Ductility

The favorable ductility is one of the most significant characteristics of CFST built-up columns, which is beneficial to evaluate the seismic resistance capability. However, no unified formula is available to determine the ductility of CFST built-up columns. In Eurocode 8 (European Committee for Standardization, 2005c), for bridge pier, the design value of the structural ductility (available displacement ductility) is defined as the ratio of the ultimate limit state displacement d_u to the yield displacement d_y , both measured at the center of mass, see Eq. (60).

$$u_d = d_u / d_y \quad (60)$$

The yield displacement defining the elastic branch is selected so as to best approximate the design curve up to the design resisting force, see Fig. 49. The ultimate displacement d_u is defined as satisfying that the structure is capable to sustain at least 5 full cycles of deformation to the ultimate displacement, or without a drop exceeding 20% of the resisting force, see Fig. 50. However, this method is not easy to directly find the yield displacement from the test result.

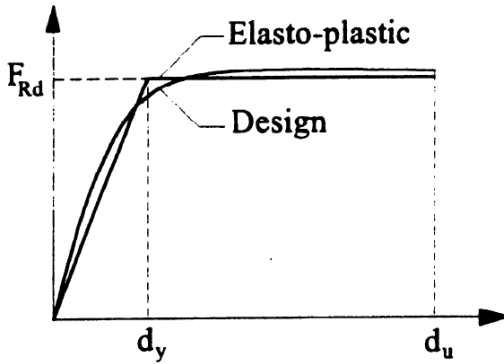


Fig. 49 Global $P-\Delta$ skeleton curve

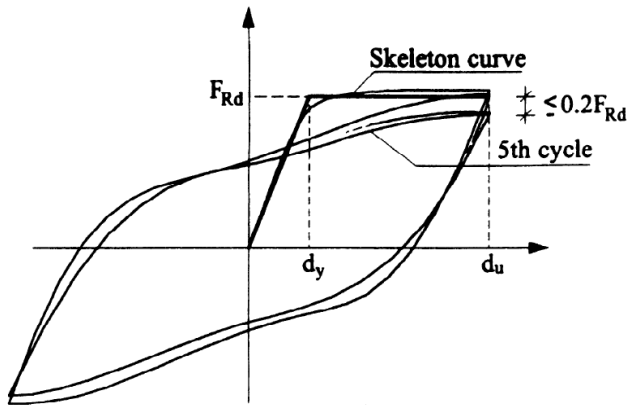


Fig. 50 $P-\Delta$ cycles

Usually, yield load and displacement are obtained by theoretically or experimentally. Susantha et al. (Susantha et al., 2008) determined by experimentally by monitoring the strain gauge reading at the extremely compressed location of steel plates at the base of the compression side. Due to the $P-\Delta$ envelope curves relatively smooth and not obvious phenomenon at the yield point, in this work, we define the yield displacement by theoretically, which is based on JGJ101-96 (China National Standard, 1997), also adopted by the cyclic loading test of CFST structural specimens from Han et al. (Han et al., 2003), Tu et al. (Tu et al., 2014) and Liao et

al. (Liao et al., 2014). Similarly with Eurocode 8, the ductility coefficient μ of the CFST columns can be defined as Eq. (61)

$$\mu = \Delta_u / \Delta_y \quad (61)$$

Where Δ_u is the lateral displacement corresponding to P_u , which is 85% of the ultimate lateral load P_{max} . Δ_y is the lateral displacement when the cross section of CFST column is in yield range, see Fig. 51. The yield displacement Δ_y can be defined as the displacement of the intersection point of two lines: the initial elastic tangent of the envelop curve and the flat tangent of the ultimate point on the envelop curve. Then the yield loading P_y is determined corresponding to Δ_y .

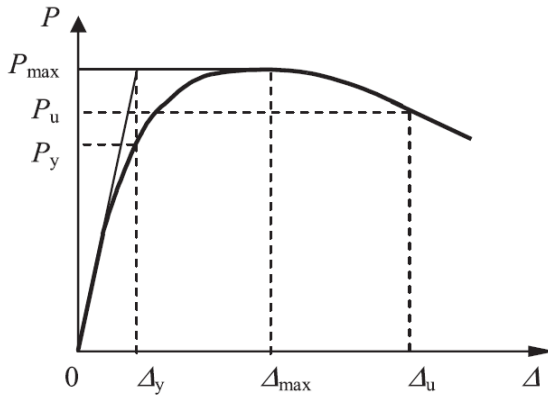


Fig. 51 Definition of structural ductility

From the $P-\Delta$ envelope curves and Eq. (61), the force and displacement of yield point, peak point, and failure point can be calculated, then the ductility coefficient μ of each specimen are obtained, summarized in Table 8. Only positive value in push direction is chosen for analysis, where the absolute value seems lower than that in negative value of pull direction, considered as relatively conservative. Usually, ability to deform up to $5\Delta_y$ without excessive load deterioration is considered as a very good earthquake resistant performance (Susantha et al., 2008). It can be seen that, four specimens (S1-S3 and S5) have a ductility of larger than 4, thus the CFST built-up columns show excellent load deformation characteristics, can satisfy the required ductile performance of seismic design in practical engineering. Moreover, as the concrete grade increase, ductility coefficient only a slight increase.

Specimen	Yield		Peak		Failure		Ductility
	P_y (kN)	Δ_y (mm)	P_{max} (kN)	Δ_{max} (mm)	P_u (kN)	Δ_u (mm)	μ
S1	36.35	20.52	52.71	56.03	44.80	98.01	4.77
S2	35.31	20.74	51.07	56.02	43.41	98.04	4.73
S3	35.68	19.65	53.98	56.03	45.88	98.01	4.99
S4	55.92	10.96	109.65	32.05	93.20	35.03	3.20
S5	92.13	19.69	121.38	45.21	103.17	80.35	4.08
S6	68.21	14.57	113.76	42.03	96.70	53.48	3.67

Table 8
Displacement ductility coefficient

3.5.4 Rigidity and Strength Degradation

The rigidity degradation of the specimens with increasing displacement was observed during the testing. The index of looped rigidity coefficient K_j is thus defined with reference to JGJ 101-96 (JGJ-96, 1997) to illustrate the degradation of the joint specimens. K_j is defined as Eq. (62)

$$K_j = \frac{\sum_{i=1}^k P_j^i}{\sum_{i=1}^k u_j^i} \quad (62)$$

In which P_j^i and u_j^i are the maximum load and corresponding displacement respectively, under the i^{th} loading cycle when the relative displacement Δ/Δ_y equals to j ; and k is the cycle time of loading, see Fig. 52. The parameter K_j is expected to demonstrate the rigidity degradation contributed by two factors, such as decreasing rigidity with the increase of displacement and rigidity degradation due to the repeating cycles under the same displacement.

Fig. 53 depicts the rigidity degradation K_j of the specimen as a function of relative displacement Δ/Δ_y . The specimens show obvious and stable rigidity degradation due to the buckling of steel tubes and crushing of in-filled concrete under cyclic loading. The K_j - Δ/Δ_y relation of the specimens with different concrete grade levels is almost identical to each other. The rigidity of laced columns is approximately three times to that of battened columns. However, rigidity degradation of laced columns (decrease 80%) are even more than that of battened columns (decrease 75%).

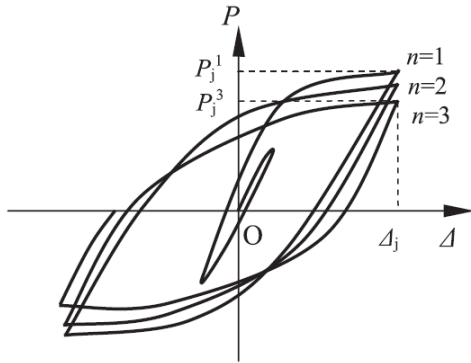
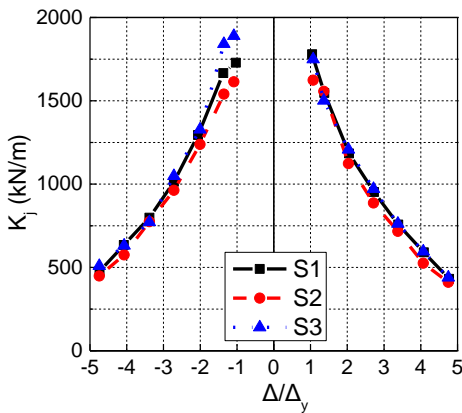
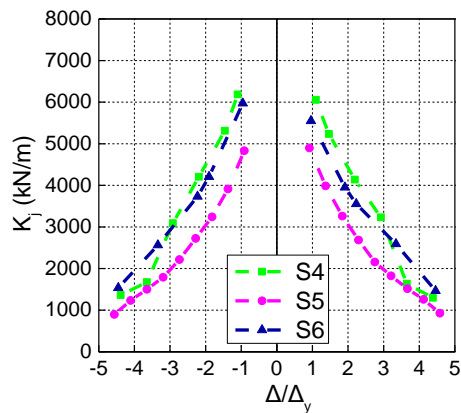


Fig. 52 Definition of rigidity coefficient K_j

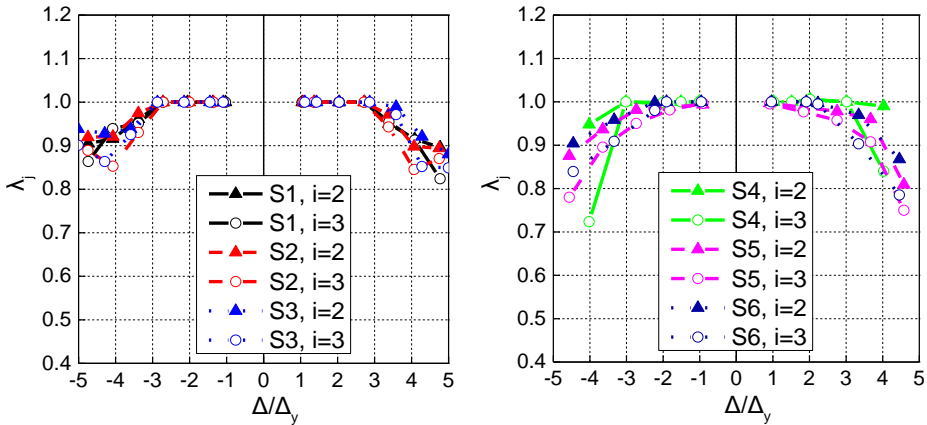


a) CFST battened columns (S1-S3)
Fig. 53 K_j - Δ/Δ_y relationship



b) CFST laced columns (S4-S6)

From the P - Δ hysteretic curves illustrated in Fig. 47, it could be seen that the strength of specimens tended to decrease as cyclic loading increase at the same displacement level Δ/Δ_y . Therefore, a coefficient λ_j , defined by dividing the ultimate load of second or third cycle with that of the first cycle at the same displacement level, can be used to evaluate the strength degradation (Han & Li, 2010). Typical λ_j - Δ/Δ_y relations are shown in Fig. 54, in which i is the number of load cycles. It is found that when Δ/Δ_y exceeds 3, which means after the ultimate strength P_{max} is reached, the strength decreases gradually, generally kept in a range from 0.85 to 0.95 for battened columns, and 0.7 to 0.9 for laced column, until the Δ/Δ_y reaches 5. At a same Δ/Δ_y level, λ_j decreases as the number of load cycles i increases, more or less 10% after each cyclic loading.



a) CFST battened columns
Fig. 54 λ_f - Δ/Δ_y relationship

b) CFST laced columns

3.5.5 Energy Dissipation Capacity

Energy dissipation capacity is also an important consideration in the seismic design. The dissipated energy in each cycle could be calculated from the loading P versus displacement Δ curve as the area bound by the hysteretic hoop of that cycle. The relations of the dissipated energy E versus the accumulative relative displacement Δ/Δ_y are illustrated in Fig. 55, where E is the total energy dissipated obtained by accumulating the energy from each cycle. It can be seen that before yield displacement Δ_y , the specimen was in elastic range, cause the E value is very small. With increasing displacement, E increases faster, indicating that the specimen has an excellent energy dissipation capacity. Among that, M shape specimen exhibits the best energy dissipation capacity to the battened columns. Due to the punch shear failure of V and N shape columns, relative poor hysteretic performance is observed, compared with battened columns.

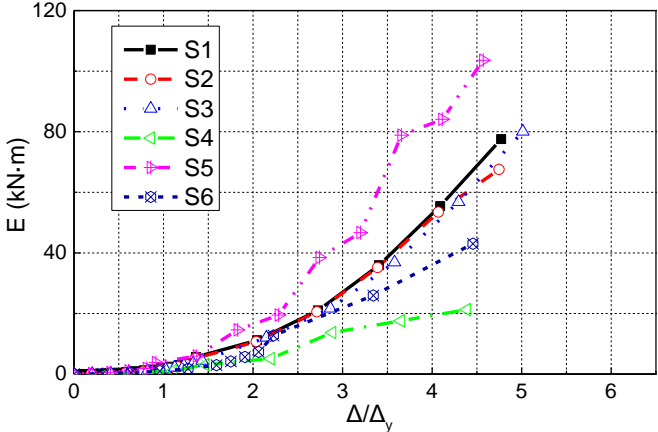


Fig. 55 Cumulative energy dissipation capacities of specimens

4. NUMERICAL ANALYSIS OF HYSTERETIC BEHAVIOR

4.1. Introduction

The possibility to develop finite element simulation and fit with experimental results is of great significance since it allows to get reference FEM, suitable for wider study of proposed technology, in substitution of experimental real scale testing, which is often limited by the experimental condition and funds.

Experimental survey over hysteretic testing of CFST built-up columns reported in Ch.3 is adopted to this purpose, since the collected data provide a comprehensive picture about specimen's response during testing. Numerical analyses are conducted using OpenSees platform (Version 2.4.4). Compared with others software, this tool offers the advantage in dynamic analysis, depending on the fiber beam-column implementation, a wide library of material constitutive, and improved solution convergence capability during iterative process within less time requirement.

In this chapter, the capability of FEM to reproduce experimental evidences is firstly evaluated, which allows for a thorough validation of implemented numerical models. Parameter analysis is developed, in order to discuss the displacement ductility and energy dissipation capacity of CFST built-up columns by the influence of axial compression ratio, chord spacing, brace spacing, diameter to thickness ratio, and steel yield strength. Based on regression analysis, the formula to calculate displacement ductility factor for CFST battened columns and laced columns are proposed.

4.2. Proposed Finite Element Model

Due to the symmetry of CFST build-up columns in transverse direction, hence two-dimensional nonlinear elements are generally used to simulate through OpenSees platform (Version 2.4.4). The *nonlinearBeamColumn* element is adopted for both chord and brace components, which is assumed *Gauss-Lobatto* integration with a copy of the same section force-deformation model at each integration point, here for

each element, set 5 integration points along axis. The *Zerolength* elements are used to simulate pin connection between chord and brace. These elements are defined by two nodes at the same location. The master node (Chord) and salver node (brace) are constraint through *EqualDOF* function. In the finite element model, bottom is directly fixed and the top is used an elastic beam element to simulate the loading side. In the analysis procedure, displacement control method are adopted to simulation both monotonic and cyclic loadings, and the nonlinear equilibrium equation is solved by the Newton-Raphson iterative method.

The constant load N is divided into two and set on the top of each chord. The horizontal load is simulated though displacement control in the OpenSees both under monotonic and cyclic loadings. Fig. 56 shows the finite element model with paralleled and V shaped braces in OpenSees, respectively.

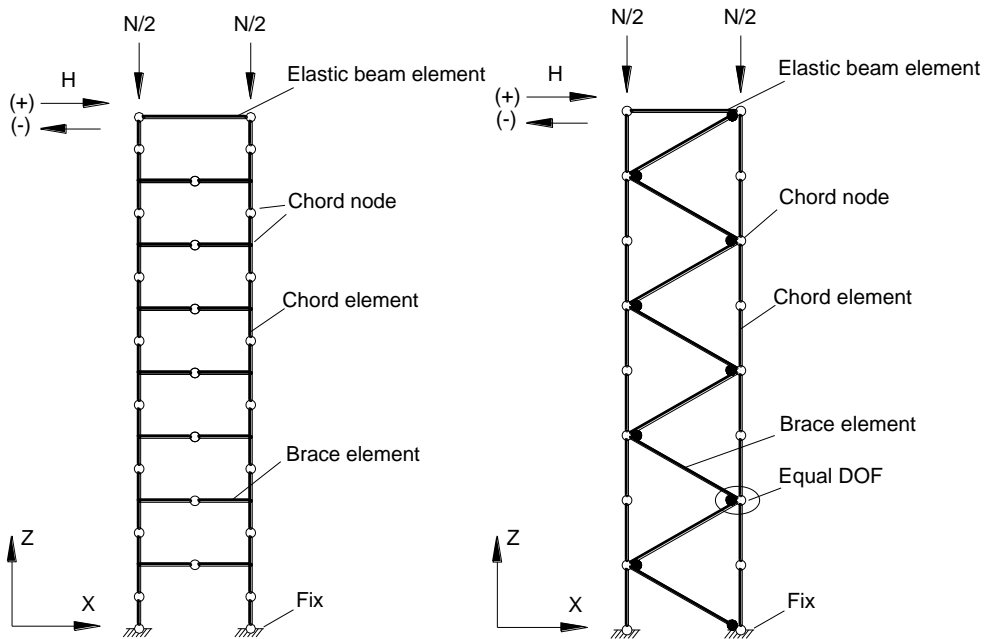


Fig. 56 Finite element model in OpenSees

The constitutive behaviour of concrete and steel are defined by the *uniaxialMaterial* objects, which can reflect material nonlinearity. The geometric parameters and defined with respect to a planar local coordinate system (y, z) are shown in Fig. 57. The interaction among axial force, shear and flexure are implemented through section aggregator function. The effects of nonlinear geometry are accounted for by using the $P-\Delta$ approximation (Filippou & Fenves, 2004).

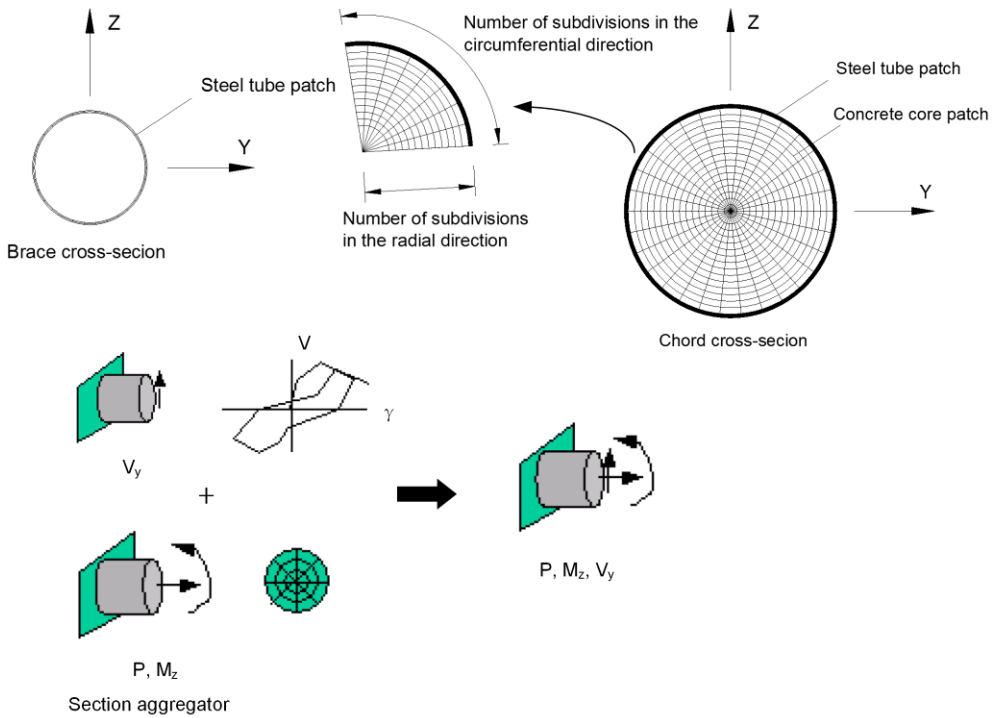


Fig. 57 Fiber section and aggregator in OpenSees

For the case of segments of the cross section that are circular in shape, the fiber discretization was defined by the number of subdivisions (fiber) in the circumferential and radial directions. The number of fibers for these directions was selected such that the size of any individual fiber did not exceed the nominal fiber size. Usually, relatively cross-section fiber discretization schemes is approximately 20 fibers can achieve accurately predict the cyclic inelastic response of structural steel and reinforced concrete members (Kostic & Filippou, 2012). In this work, the fiber discretization is 30 in the circumferential direction, both for concrete and steel. In the radial direction, 16 for concrete and 2 for steel. The resulting number of fibers do not pose any computational problems during analysis, and at less computing time than for a solid finite-based model.

It is noticed that the fiber model assumes the steel-concrete remain in contact, neither local buckling, loss of confinement, nor slip can occur in, which is neglected in the uniaxial fiber model. Moreover, the local buckling, initial overall and local geometric imperfections of the steel tube of CFST columns are also not considered. Regards section aggregator, the shear material constitutive is assumed in elastic, and the shear stiffness of CFST is calculated by Eq. (63)-(67).

$$GA = G_s A_s + G_c A_c \quad (63)$$

$$G_s = \frac{E_s}{2 \times (1 + \nu_s)} \quad (64)$$

$$A_s = \pi r t_w \quad (65)$$

$$G_c = \frac{E_c}{2 \times (1 + \nu_c)} \quad (66)$$

$$A_c = 0.45 \pi d^2 \quad (67)$$

Where, GA is the shear stiffness of CFST section, G_s is the shear modulus of steel, A_s is the shear area of steel, r is the centerline radius of steel tube, t_w is the steel thickness, G_c is the shear modulus of concrete, A_c is the shear area of concrete, d is the diameter of concrete.

4.3. Finite Element Model Verification

4.3.1 Comparison with Test Results

First of all, six FEMs are developed through proposed FEM method and compared with the test results. The geometry of FEM are dependent on Fig. 56 and Fig. 57. In FEM, two-dimensional nonlinear elements are used, hence the value of force P need to be multiplied 2, to simulate 4 chords in real case, then compare with test results together.

Regards materials properties in the FEM, *uniaxialMaterial Steel02*, uniaxial Giuffre-Menegotto-Pinto steel model with isotropic strain hardening, is adopted for steel tube; *uniaxialMaterial Concrete02*, uniaxial concrete material with tensile strength and linear tension softening, is adopted for concrete core. The key points of material are determined by the material mechanical properties in the test and as previous mentioned for CFST materials. Materials properties of FEM in OpenSees are summarized in Table 9 and Table 10.

In Table 9, F_y is yield strength, E_0 is the initial elastic tangent, adopted from steel mechanical properties test; b is ratio between post-yield tangent and initial elastic tangent, $R0$, $CR1$ and $CR2$ control the curvature of the transition from the elastic to the plastic-hardening branch, determined by the recommend values in OpenSees manual; $a1$ is isotropic hardening parameters, increase of compression yield envelope as proportion of yield strength after a plastic strain of $a2 \times (F_y/E_0)$; $a3$ is isotropic hardening parameters, increase of tension yield envelope as proportion of yield strength after a plastic strain of $a4 \times (F_y/E_0)$.

Component	Parameter setting									
	F_y (Mpa)	E_0 (Mpa)	b	$R0$	$CR1$	$CR2$	$a1$	$a2$	$a3$	$a4$
Chords	345	2.36×10^5	0.01	18	0.925	0.15	-0.1	1	-0.1	1
Braces	374	2.07×10^5	0.01	18	0.925	0.15	-0.1	1	-0.1	1

Table 9
Steel mechanical properties adopted in Steel02 model

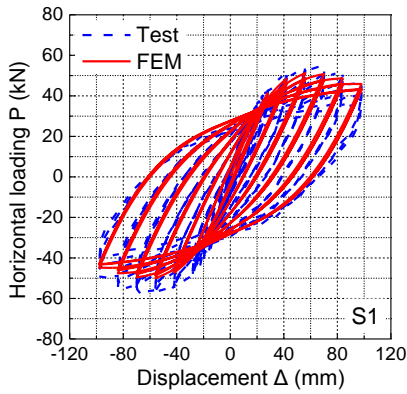
In Table 10, negative value is in compression, the values of stress and strain at the yield point and ultimate point consider the increasing strength due to the confinement acting, according to equations by Liang and Fragomeni (Liang and Fragomeni, 2009) as illustrated in Ch.2.4.

Component	Concrete Grade	Parameter setting			
		f'_{cc} (Mpa)	ϵ'_{cc}	$\beta_c f'_{cc}$	ϵ_{cu}
In-filled concrete	C40	-29.00	-0.0042	-26.01	-0.02
	C50	-33.59	-0.004	-30.13	-0.02
	C60	-38.78	-0.039	-34.78	-0.02

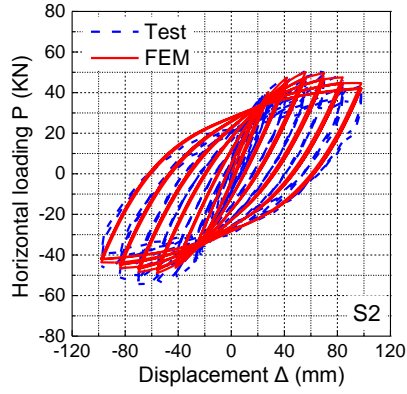
Table 10
Steel mechanical properties adopted in Concrete02 model

In the solution algorithm, 1000 time sub-steps, which will result in a displacement increment for horizontal displacement at the top of chord to be a prescribed value, are set in each displacement control step, in order to obtain better solution convergence. When checking capability of a FEM to reproduce an experimental response, the most important issue is to compare horizontal loading P versus horizontal displacement Δ hysteretic curves, which reflects the whole test procedure. Fig. 58 shows the comparison results. It can be seen that the hysteretic loops between simulation and test results are agree well, indicating that the proposed

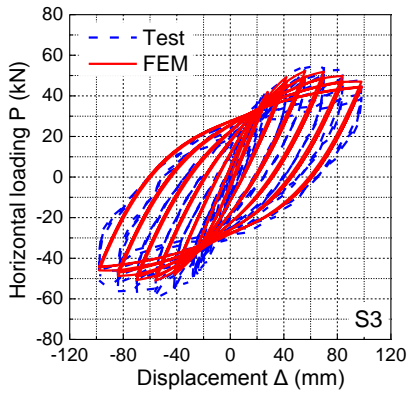
finite element model has an acceptable accuracy to predict the seismic behaviour of CFST built-up columns.



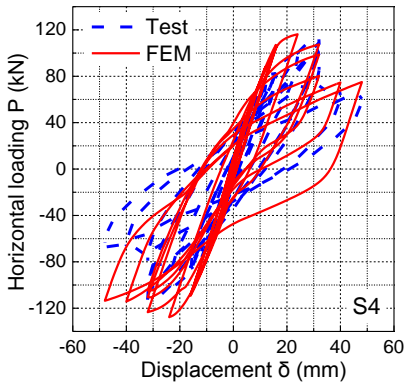
a) Specimen 1



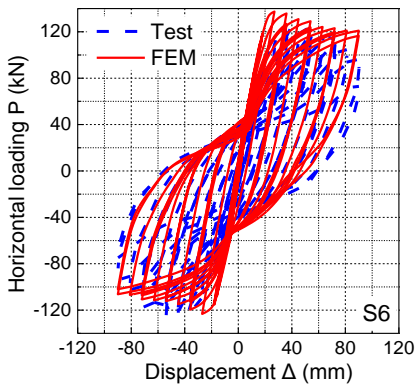
b) Specimen 2



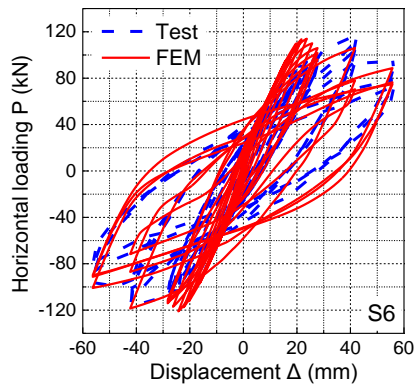
a) Specimen 3



b) Specimen 4



a) Specimen 5



b) Specimen 6

Fig. 58 Comparison of $P-\Delta$ hysteretic curves

The comparison of FEM and test envelop curves for all specimens are illustrated in Fig. 59. Due to the symmetry of specimen with parallel braces, the both the value in positive and negative should be symmetrical in theory, as illustrated in FEM results. However, the negative value of test results will be a little larger than positive side, potentially caused by the measure during test or manufacture procedures. Overall, the figures show that the results from the FE analysis almost coincided with the experimental results.

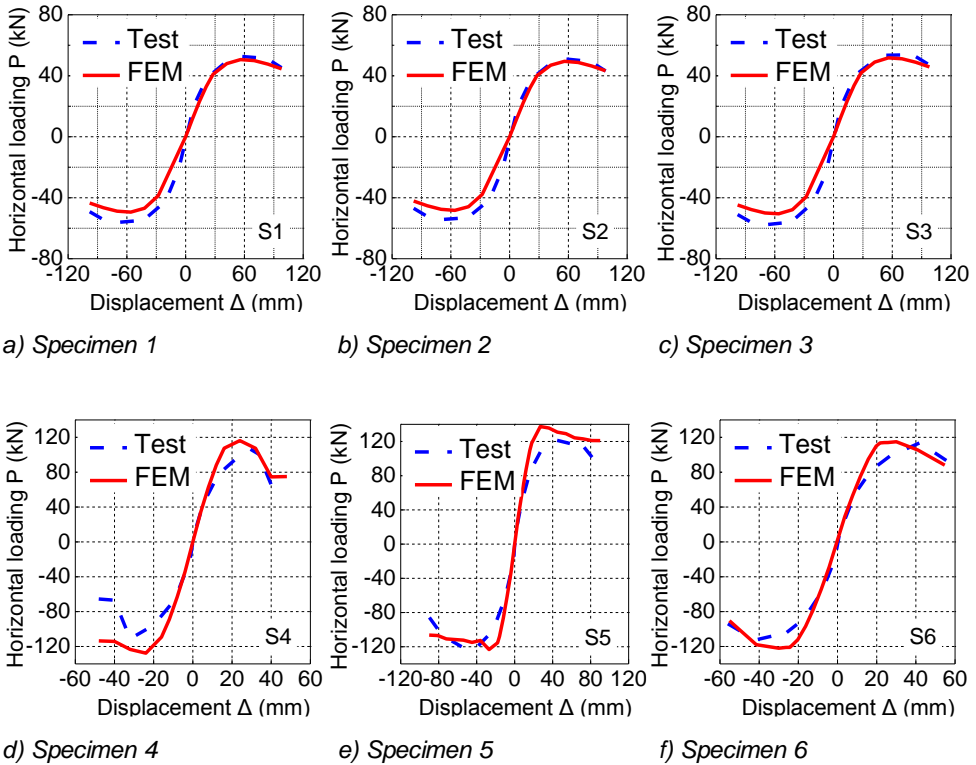


Fig. 59 Comparison of $P-\Delta$ envelope curves

To provide an objective evaluation to matching level between experimental and FEM results, the yield load, peak load and failure load are compared in Table 11, respectively. Among that, yield point in FEM are obtained through the method mentioned in Ch.3.5.3, plot the initial elastic tangent of the envelop curve and the flat tangent of the ultimate point on the envelop curve, the yield loading P_y is determined corresponding to Δ_y . It shows that the yield load in FEM will be slightly larger than test results, mean that the elastic stiffness of FEM will be lower than specimen, which reasonably occurs some error in the specimen fabrication and materials properties. For the peak load and failure load, the error are within 15%, which means satisfactory FEM results are achieved.

No.	Yield load			Peak load			Failure load		
	Test (kN)	FEM (kN)	Error (%)	Test (kN)	FEM (kN)	Error (%)	Test (kN)	FEM (kN)	Error (%)
S1	36.35	38.1	4.81	52.71	50.62	-3.97	44.8	44.52	-0.62
S2	35.31	37.89	7.31	51.07	49.46	-3.15	43.41	43.25	-0.37
S3	35.68	38.31	7.37	53.98	51.72	-4.19	45.88	47.2	2.88
S4	55.92	55.84	-0.14	109.65	116.24	6.01	93.2	98.8	6.01
S5	92.13	100.68	9.28	121.38	137.44	13.23	103.17	116.82	13.23
S6	68.21	73.75	8.12	113.76	115.03	1.12	96.7	97.78	1.12

Table 11
Displacement ductility coefficient

Moreover, the cumulative energy absorption capacities of both specimen obtained from tests and FEM analysis are presented in Fig. 60. The simulated results of energy dissipation in both specimens are slightly smaller than the corresponding results from at the beginning, after displacement exceeds 3 times to yield displacement, the energy of FEM will increase fast. At the end of failure load, the cumulative energy dissipation between FEM and test have a well agreement.

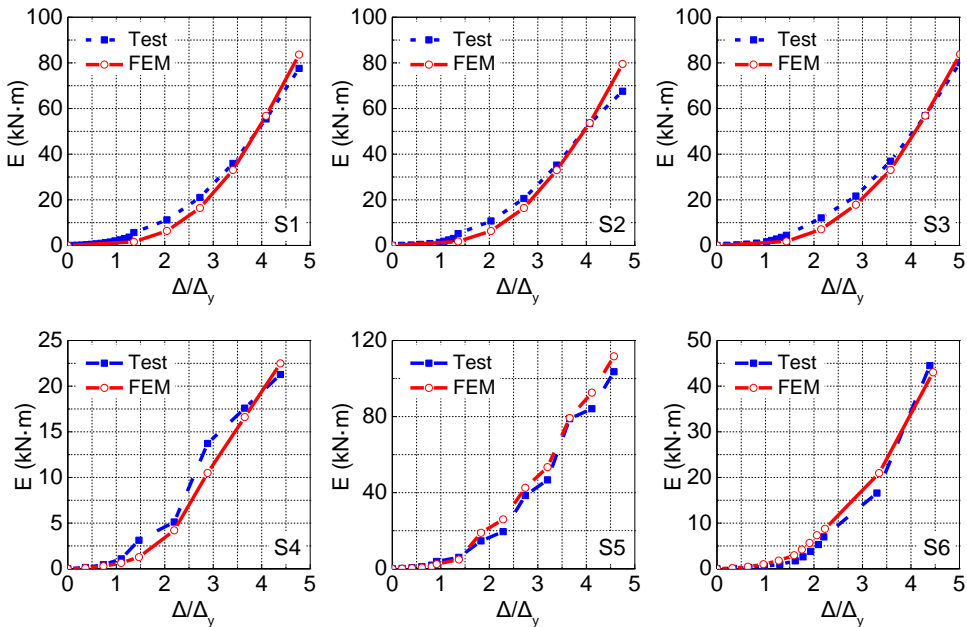


Fig. 60 Comparison of cumulative energy absorption capacities

With the aim of providing a FEM as a reference for all subsequent analysis presented in the following, the author compares the main parameters in hysteretic analysis, such as $P-\Delta$ hysteretic curves and skeleton curves, key point loading and cumulative energy absorption capacities. Overall, the FEM through OpenSees platform are shown to accurately simulate the behavior of test specimens and are thereby validated for use in further parametric studies.

4.3.2 Comparison with Previous Experimental Study

In this section, other two comparisons with previous experimental studies are carried out, for the purpose of proposed FEM method being more reliable and accurate. Until now, there are still seldom experimental studies reported on the dynamic performance of CFST built-up columns. Kawano et al. (Kawano et al., 1996) investigated the experimental study on the elasto-plastic behavior and deformability of concrete-filled tubular truss beam-columns under cyclic loading. Luo (Luo, 2013) also reported low-cycle loading experiment of six CFST laced columns as introduced in Ch.2.2.2. Here the author presents as much as possible the test data from Kawano's and Luo's test, which are essential for the FEM simulation. Then some specimens are adopted for verification, mainly compared with the force-displacement curves. The FEM method is the same as last section, not introduced repeatedly.

a) Kawano's test

Fig. 61 shows the specimen details and a total of 12 specimens are test. The angle between the chord and braces are 60° . Taken into account lateral bracing, chord type, loading method and axial compression ratio as parameters, shown in Table 12. It is point out that the compression ratio n for CFST truss is calculated by the formula Eq. (68)-(69).

$$n = N / N_u \quad (68)$$

$$N_u = 2(A_s f_y + A_c f'_c) \quad (69)$$

Where, N is the axial load applied to the test, N_u is the axial compressive capacity of the two CFST chords, A_s and A_c are the cross-sectional area of steel and concrete, respectively. f_y is the yield stress of steel, and f'_c is the compressive strength of concrete, equal to 30.4MPa.

The specimen scantling, steel sectional properties and mechanical properties are summarized in Table 13-15, respectively. Regards the concrete mechanical properties, only the compressive strength f_c was mentioned in the literature. The test device is shown in Fig. 62.

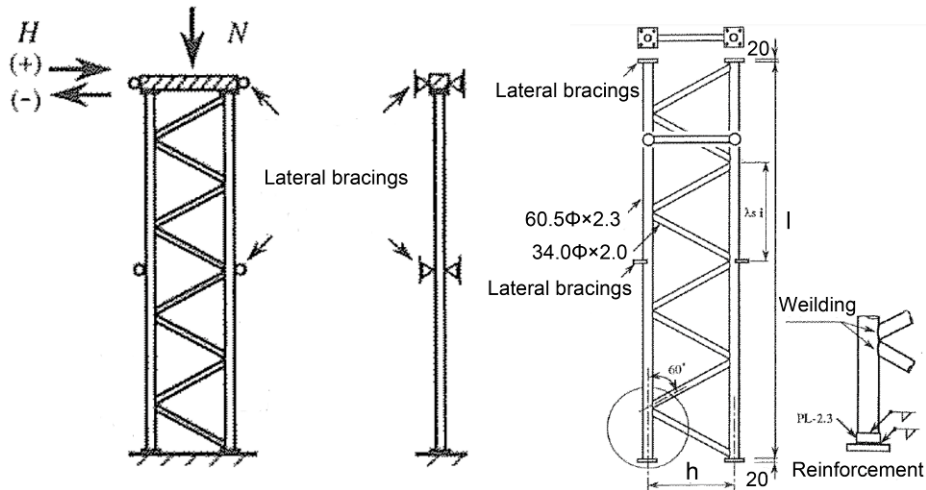


Fig. 61 Test specimen

Specimen	Chord type	Lateral bracing	Loading method	Axial compression ratio
VB1M	Vacant	Bracing	Monotonic	0.1
VB1R		No	Recycle	0.1
VN1M		Bracing	Monotonic	0.1
VN1R		No	Recycle	0.1
CB1M	CFST	Bracing	Monotonic	0.1
CB1R		No	Recycle	0.1
CN1M		Bracing	Monotonic	0.1
CN1R		No	Recycle	0.1
CB0M	CFST	Bracing	Monotonic	0.0
CB0R		No	Recycle	0.0
CB2M		Bracing	Monotonic	0.2
CB2R		No	Recycle	0.2

Table 12
Test parameters

Specimen	Chord (mm)	Bracing (mm)	Length (cm)	Chord spacing (cm)	Slenderness ratio between joints (λ_s)
Value	60.5 ϕ \times 2.3	34.0 ϕ \times 2.0	243.4	52.6	29.5

Table 13
Specimen scantling

Steel tube	D, d (cm)	T, t (cm)	A_s (cm ²)	I (cm ⁴)	i (cm)	$D/T, d/t$
60.5 ϕ \times 2.3	6.05	0.211	3.86	16.5	2.07	28.7
34.0 ϕ \times 2.0	3.39	0.208	2.08	2.65	1.13	16.3

Table 14
Steel sectional properties

Test method	Steel tube	P_y (Ton)	P_u (Ton)	f_y (t/cm ²)	f_u (t/cm ²)	E (t/cm ²)	ϵ_u (%)
Compression	60.5 ϕ \times 2.3	14.6	17.1	3.78	4.44	2197	-
	34.0 ϕ \times 2.0	8.43	9.93	3.89	4.43	2153	-
Tension	60.5 ϕ \times 2.3	15.6	18.4	4.05	4.78	2089	23

Table 15
Steel mechanical properties

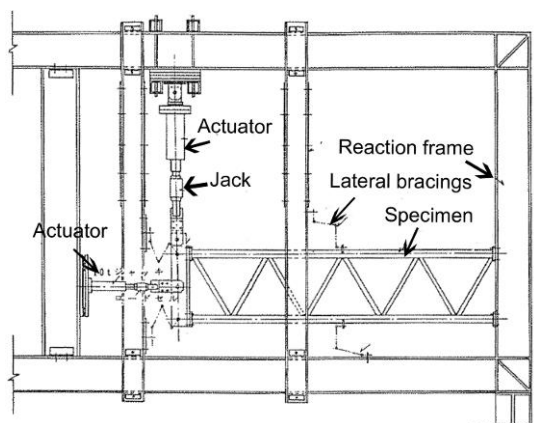
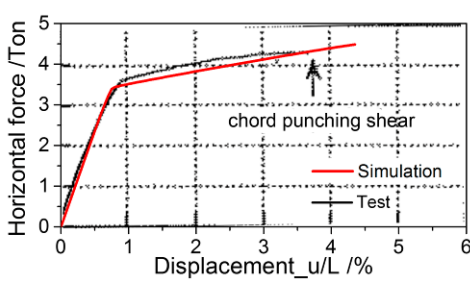


Fig. 62 Test device

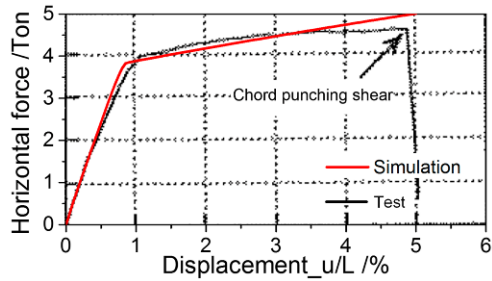
A total of 8 specimens are checked including 4 specimens in monotonic loadings and 4 specimens under cyclic loadings. The later bracing is not considered as a parameters, which is no influenced in the two-dimensional numerical simulation. For predicting the global response of CFST trusses, force and displacement relationship

on the top of specimen are compared, which is the most important factor to evaluate the elasto-plastic behaviour and deformability.

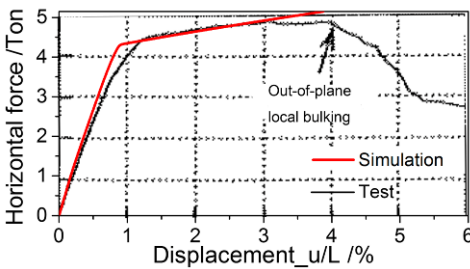
Fig. 63 shows the horizontal force-displacement curves under monotonic loading, where abscissa corresponds to the ratio of measured horizontal displacement u dividing to the height of specimen L , and vertical coordinate is the horizontal force. It can be found that the simulation results show an agreement with test result. Due to some specimens, such as CB2M and VN1M, are out-of-plane local buckling in the test procedure, see Fig. 64, which lead some inevitably deviations, however, do not reflect in two- dimensional finite element model.



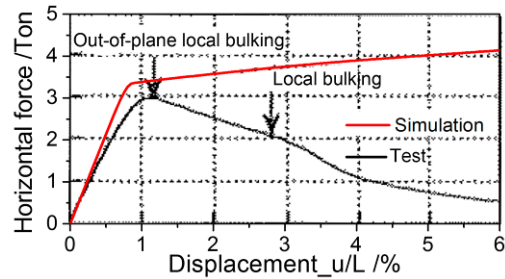
a) Specimen CB0M



b) Specimen CN1M



c) Specimen CB2M



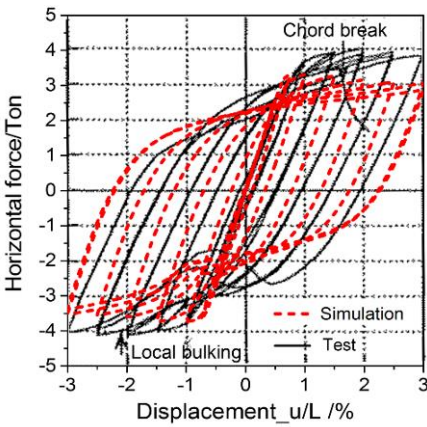
d) Specimen VN1M

Fig. 63 Horizontal force-displacement curves under monotonic loading

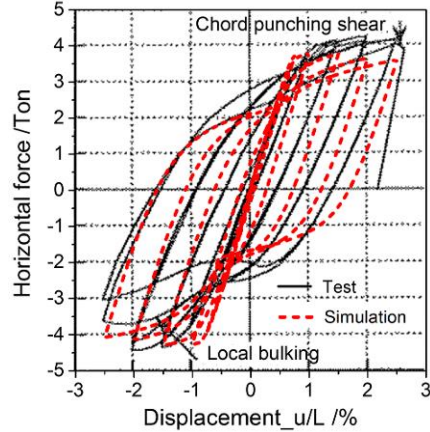


Fig. 64 Out-of-plane local buckling in the test (Kawano et al., 1996)

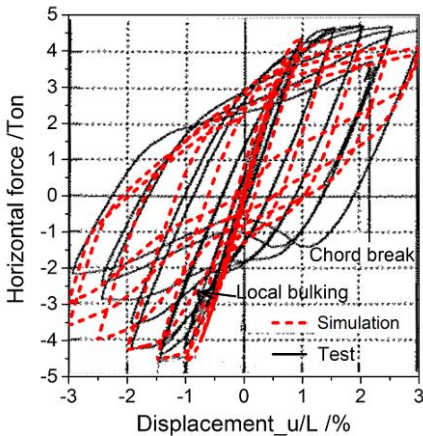
Similarly, comparison of horizontal force-displacement curves under cyclic loading are presented in Fig. 65, it can be found that the simulation results also show an agreement with test result in cyclic loadings. The hysteresis curves of hollow chord specimen (VN1R) showed a sharp negative-slope trend after reached maximum lateral load. However, for the CFST chords (CB0R, CB1R and CB2R), the rigidity of pier will be increased since the internal concrete once again participated in transmitting the lateral load applied on the top of chords.



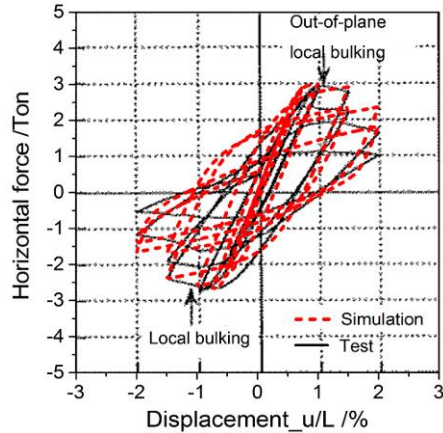
a) Specimen CB0R



b) Specimen CB1R



c) Specimen CB2R

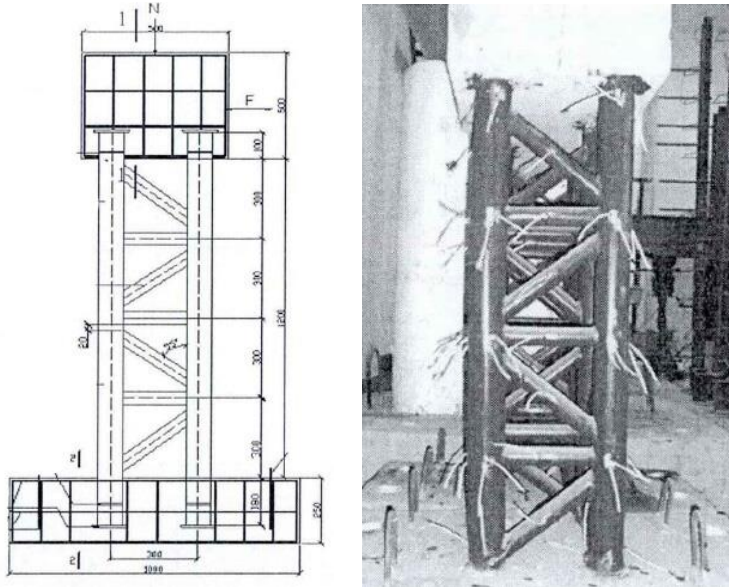


d) Specimen VN1R

Fig. 65 Horizontal force-displacement curves under cyclic loading

b) Luo's test

As introduced in Ch.2.2.2, Luo (Luo, 2013) reported low-cycle loading experiment of six CFST laced columns. Fig. 66 shows the view of specimen SSC1. Three specimens reported from Luo's test were selected for comparison. The specimen scantling and mechanical properties in the literature are summarized in Table 16-17, respectively.



a) General view

b) Panorama

Fig. 66 Photo of specimen SCC1 (Luo, 2013)

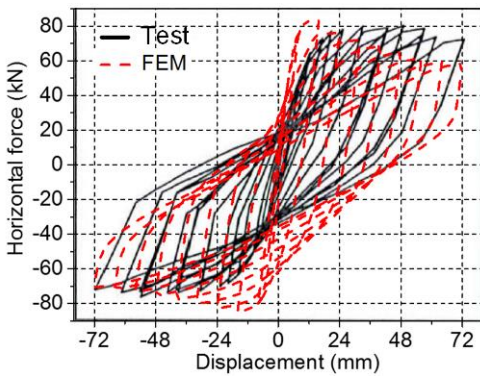
No.	Chord (mm)	Bracing (mm)	Length (mm)	Chord spacing (mm)	Axial load ratio (n)	Axial load (kN)
SCC1	86 ϕ \times 1.5	48 ϕ \times 2.5	1200	300	0.2	236.8
SCC4	86 ϕ \times 1.5	48 ϕ \times 2.5	1200	300	0.3	355.2
SCC6	86 ϕ \times 1.5	48 ϕ \times 2.5	2100	300	0.2	208.6

Table 16
Specimen scantling

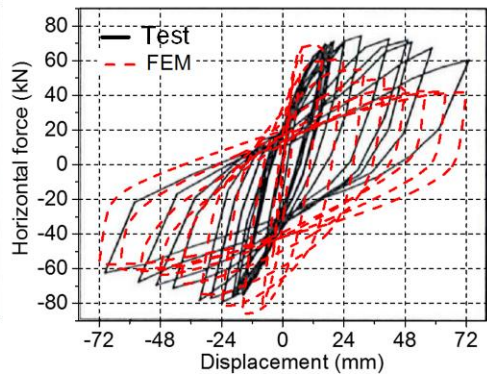
Steel tube	E_s (MPa)	f_{sy} (MPa)	f_{su} (MPa)	Concrete	E_c (MPa)	f_c (MPa)
Chord	2.06×10^5	315	390	In-filled	2.56×10^4	15.51
Brace	2.06×10^5	320	400			

Table 17
Material mechanical properties

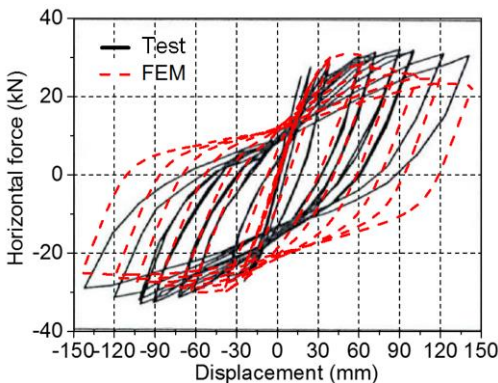
Compared with Kawano’s test with two chords specimen, four chords can prevent specimen from out of plane buckling during test. Due to the structural symmetry, two-dimensional nonlinear elements are adopted in FEM simulation, the result of force should be multiplied 2, then compared with test results together. Other calculated parameters are not repeated explanation, similar with Ch.4.2. Fig. 67 shows the comparison of force-displacement curves on the top of columns. It can be found that the simulation results also show an agreement with test result in cyclic loadings. Compared with the FEM simulation as illustrated in Fig. 28, the improvement in pinch effect simulation is obviously achieved through OpenSees platform.



a) Specimen SCC1



b) Specimen SCC4



c) Specimen SCC6

Fig. 67 Comparison of force-displacement curves

Therefore, the accuracy of numerical simulation is calibrated with previous experimental study, and the FEMs exhibit favourable accuracy and high efficiency, can be adopted in further parametric analysis.

4.4. Parametric Analysis

Large amounts of experimental and theoretical studies have been conducted on the single CFST columns subjected to cyclic loading with various sectional shapes, such as circular section (Susantha et al., 2008; Chung, 2010; Hajjar & Tort, 2010; Xiao et al., 2011), rectangular section (Ge & Usami, 1996; Han et al., 2003, Pater et al., 2014), T shaped section (Tu Y.Q. et al., 2014) and double skin section (Han et al., 2009). Among that, the hysteretic behavior of single CFST column is affected by the axial compression ratio (n), concrete compressive strength (f_{ck}) and steel yield strength (f_{sy}), slenderness ratio, diameter to thickness ratio (d/t) for circular section (depth to thickness ratio for rectangular section). For the CFST built-up column, some more parameters are expected to affect the hysteretic behavior, such as chord center spacing (w), brace center spacing (l), illustrated in Fig. 68.

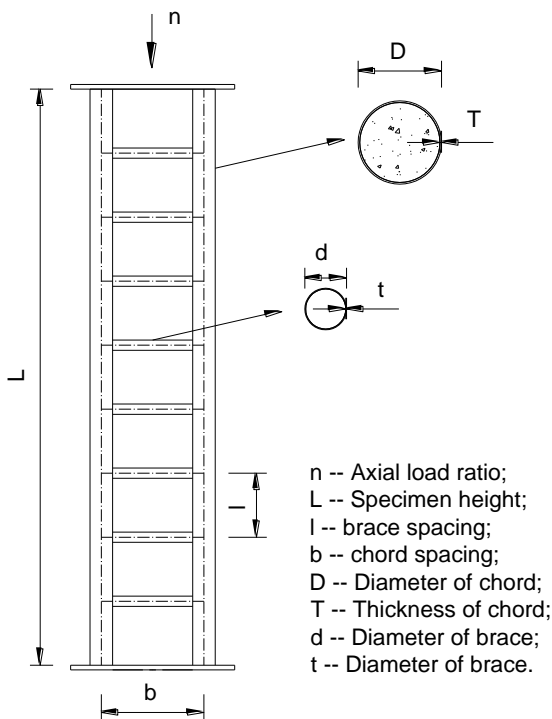


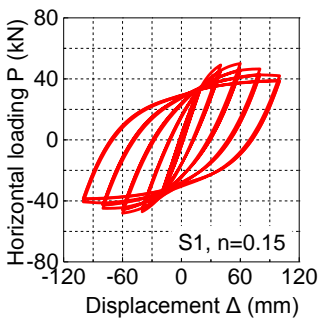
Fig. 68 Parameters abbreviation

The concrete compressive strength is not considered as a parameter, as observed in the test, which will not lead to significant influence in the hysteretic behavior of CFST built-up columns. As a result, take benchmark specimen (S1) as standard,

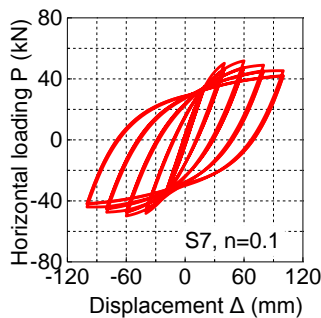
effect of six parameters are individually taken into consideration through calibrated FEM. A total of 32 FEMs (namely from S7 to S38, avoid duplication with test number) subjected to cyclic loading are analyzed parametrically. All the models are imposed to the same cyclic loading pattern, with calculated yield displacement $\delta_y=20\text{mm}$ in the hysteretic test. One cycle was adopted at each load level in elastic stage at the incremental displacement levels of $0.25\delta_y$, $0.5\delta_y$, $0.75\delta_y$, after the yield displacement δ_y , three cycles are imposed at the incremental displacement levels of $1\delta_y$, $2\delta_y$, $3\delta_y$, $4\delta_y$, $5\delta_y$. If the lateral displacement corresponding to P_u (85% of the ultimate lateral load P_{max}) has not achieved, continue increasing the loading pattern until meet the requirement.

4.4.1 Axial Load Ratio

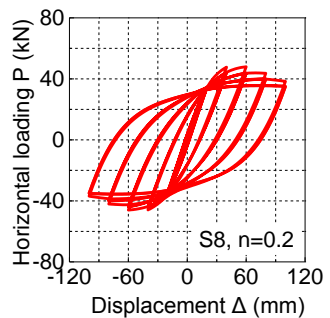
Based on the specimens of axial load ratio is 0.15, five axial load ratios ranging from 0.1 to 0.5 are chosen to investigate the effect of axial load ratio on the hysteretic behavior of CFST built-up columns. The $P-\Delta$ hysteretic curves for specimens (S1, S7-S11) are shown in Fig. 69. It can be seen that the hysteretic curves of specimen are generally saturate, when axial load ratio exceeds 0.2 and the specimen meet maximum horizontal loading, the stiffness decreases obviously. Since increasing axial load, the $P-\Delta$ effects are more severe and the in-filled concrete can more easily to achieve the maximum compressive stress and become crushed. However, the hysteretic loops is not presented the pinching effect, indicating the favorable hysteretic behavior of the structure.



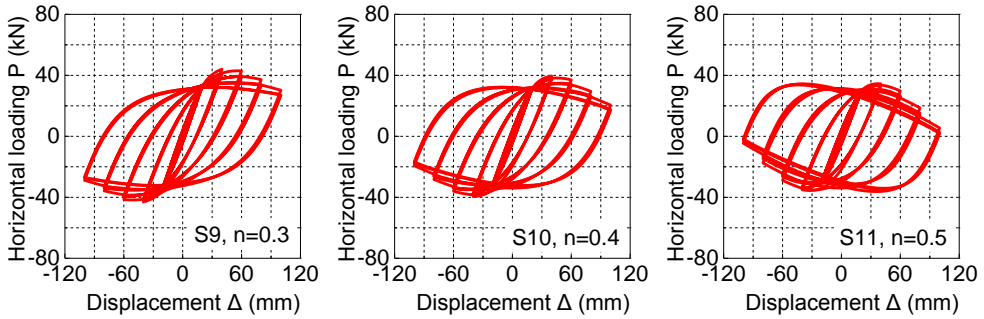
a) Specimen 1



b) Specimen 7



c) Specimen 8



d) Specimen 9

e) Specimen 10

f) Specimen 11

Fig. 69 Comparison of $P-\Delta$ hysteretic curves

Fig. 70 shows the typical computed $P-\Delta$ envelop curves under different axial load ratios. It can be found that when the axial load ratio is less than or equal to 0.2, the $P-\Delta$ envelop curves shape is nearly the same. While the curves shape decreases faster if the axial load ratio is greater than 0.3. Due to the structural characteristics have not changed, the cumulative energy dissipation under different axial load ratio are the same, as illustrated in Fig. 71. Table 18 summarizes the ductility coefficient under different axial load ratios. Compared with S1, as the load compressive ratio ranging from 0.3 to 0.5, the horizontal ultimate load decreases by 9%, 17% and 26%, also the ultimate displacement will advances to 40mm. Moreover, the ductility coefficient shows the similar variation, decreases faster by 23%, 31% 39%. Therefore, it is evident that for this type of column, superstructure loading significantly affects the column's hysteretic behavior, and axial load ratio within 0.3 is a reasonable restrictions to exhibit ductility.

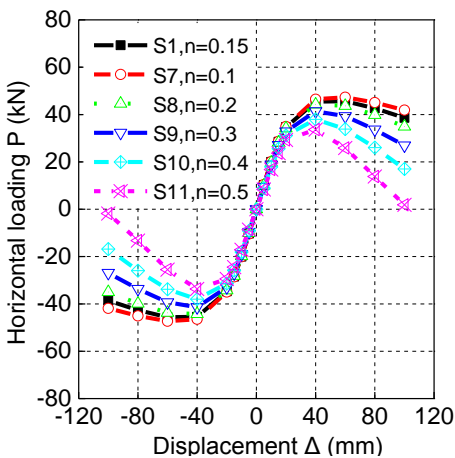


Fig. 70 Comparison of $P-\Delta$ envelope curves

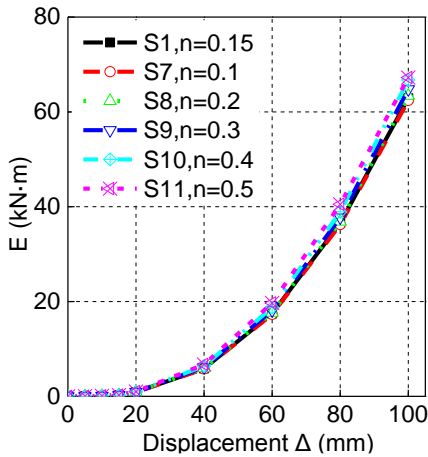


Fig. 71 Comparison of cumulative energy

Specimen	Parameter n	Yield		Peak		Failure		Ductility
		P_y (kN)	Δ_y (mm)	P_{max} (kN)	Δ_{max} (mm)	P_u (kN)	Δ_u (mm)	μ
S1	0.15	35.94	22.38	45.62	60	38.78	98.13	4.38
S7	0.1	36.63	22.76	47.3	60	40.21	100	4.39
S8	0.2	35.18	22.32	44.25	40	37.61	88.46	3.96
S9	0.3	33.62	21.86	41.37	40	35.16	74.27	3.40
S10	0.4	31.55	21.18	37.95	40	32.26	63.63	3.00
S11	0.5	29.01	19.68	33.65	40	28.6	52.96	2.69

Table 18

Comparison of ductility coefficient under different axial load ratios

4.4.2 Chord Spacing

In the prototype of Ganhaizi Bridge, the center spacing of chord in longitudinal direction ranges from 1.14m to 5.248m, and according to similitude relationship with 1:8 ratio, the width varies between 143mm to 656mm. Here we set three specimens with the chord spacing from 200mm to 700mm, at the incremental displacement of 100mm. The $P-\Delta$ hysteretic curves for specimens (S12-17) are shown in Fig. 72. It can be seen that the hysteretic curves of specimen are generally saturate, the hysteretic loops with 200mm of chord spacing ($L/w=12.5$) is obviously smaller than others. In other words, it means that when the chord spacing is smaller than the brace spacing, poor hysteretic behavior is appeared.

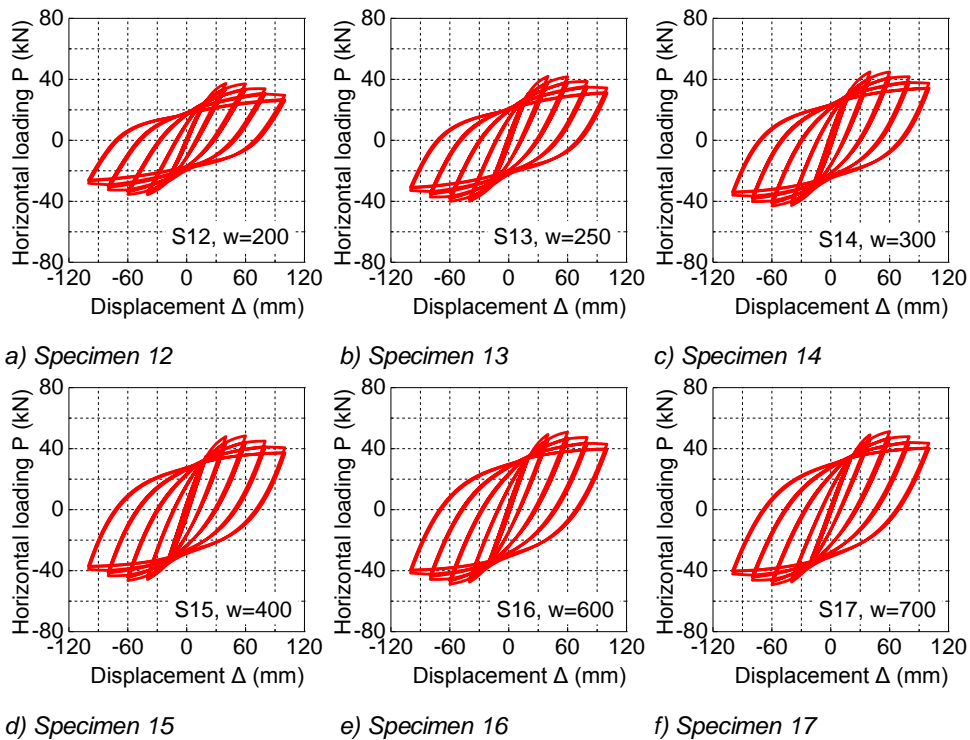


Fig. 72 Comparison of $P-\Delta$ hysteretic curves

Fig. 73 shows the $P-\Delta$ envelop curves under different chord spacing. It can be found that when the spacing exceed 300mm ($L/w > 8.33$), the curves seem the same, indicating that enlarge chord spacing only increase the strength and ductility in some extent. However, the initial stiffness and peak load with 200mm spacing are obvious smaller. Fig. 74 presents the comparison of cumulative energy. The dissipation capacity with 200mm spacing is approximate 2/3 with others. Table 19 summarizes the ductility coefficient under different chord spacing. Compared with S1, the horizontal ultimate load of S12 decreases by 25%, the ultimate displacement advances to 40mm, and the ductility coefficient decreases by 10%. S13 shows a better balance between strength and ductility, with 6% decrease in strength and 10% increase in ductility. Therefore, when the chord spacing roughly 300mm ($L/w = 8.33$), the hysteretic behavior is better than other size.

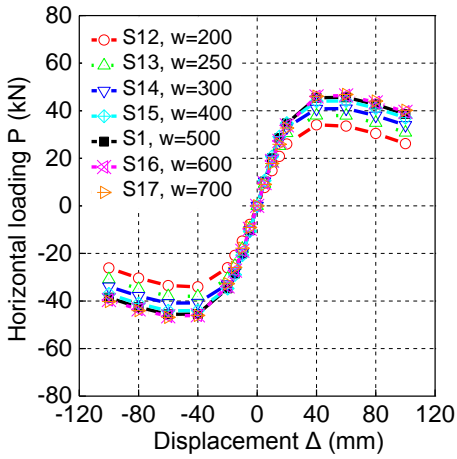


Fig. 73 Comparison of $P-\Delta$ envelope curves

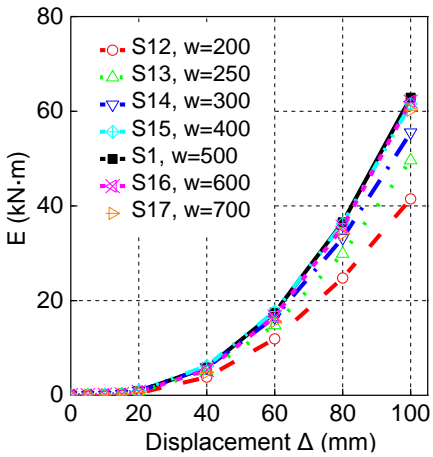


Fig. 74 Comparison of cumulative energy

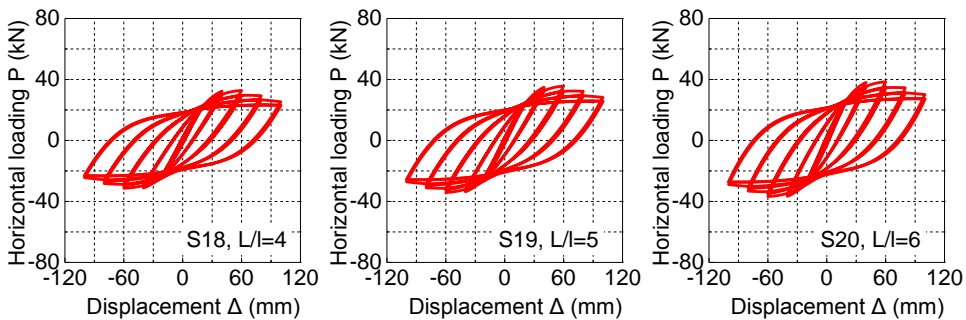
Specimen	Parameter w (mm)	Yield		Peak		Failure		Ductility μ
		P_y (kN)	Δ_y (mm)	P_{max} (kN)	Δ_{max} (mm)	P_u (kN)	Δ_u (mm)	
S12	200	26.72	22.01	34.04	40	28.93	86.84	3.95
S13	250	30.73	20.24	38.02	40	32.32	92.86	4.59
S14	300	32.95	19.89	40.91	60	34.77	95.88	4.82
S15	400	35.08	20.72	44.11	60	37.49	97.82	4.72
S1	500	35.94	22.38	45.62	60	38.78	98.13	4.38
S16	600	36.31	24.07	46.42	60	39.46	100.20	4.16
S17	700	36.59	25.81	46.84	60	39.81	101.70	3.94

Table 19

Comparison of ductility coefficient under different chord spacing

4.4.3 Brace Spacing

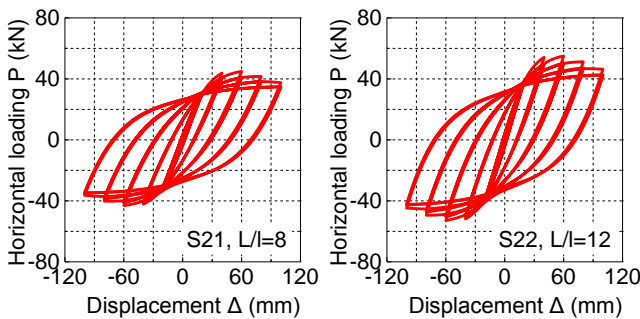
In the prototype of Ganhaizi Bridge, the brace spacing is 2m, the scale width is 250mm with 1:8 ratio, which adopted in S1. Therefore, the ratio of L/l is 10 for S1, another five FE models with L/l equal to 4 ($l=625\text{mm}$), 5 ($l=500\text{mm}$), 6 ($l=417\text{mm}$), 8 ($l=312.5\text{mm}$) and 12 ($l=208\text{mm}$) are added for comparison, respectively. The $P-\Delta$ hysteretic curves for specimens (S18-22) are shown in Fig. 75. It can be seen that the hysteretic curves are obviously better as increasing the number of braces, due to the brace can share bending moment and share forces. Thus, increasing the number of brace will promote the hysteretic behavior of CFST battened column, but from an aesthetic viewpoint, the busy braces will not be welcomed by the designer.



a) Specimen 18

b) Specimen 19

c) Specimen 20



d) Specimen 21

e) Specimen 22

Fig. 75 Comparison of $P-\Delta$ hysteretic curves

Fig. 76 shows the $P-\Delta$ envelop curves under different brace spacing. It can be found that as the number of brace increase, the initial stiffness, peak load will be gradually promoted. Fig. 77 presents the comparison of cumulative energy. The dissipation capacity also show the same phenomenon. As the number of brace

increases, the cumulative energy capacity increases approximate 11%-13% at each level of displacement. Table 20 summarizes the ductility coefficient under different brace spacing. From S15, S1 to S16, although the horizontal yield load, ultimate load and failure increases by approximate 5%, the ductility coefficient seems to be affected with the small amplitude.

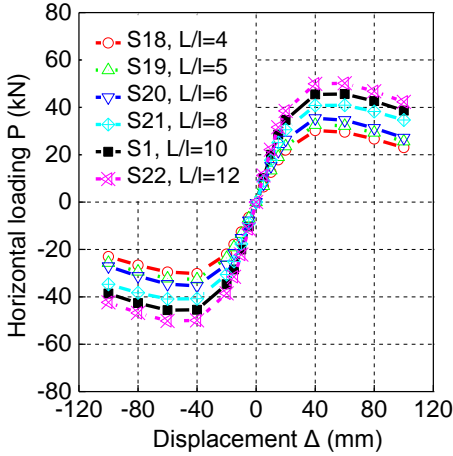


Fig. 76 Comparison of $P-\Delta$ envelope curves

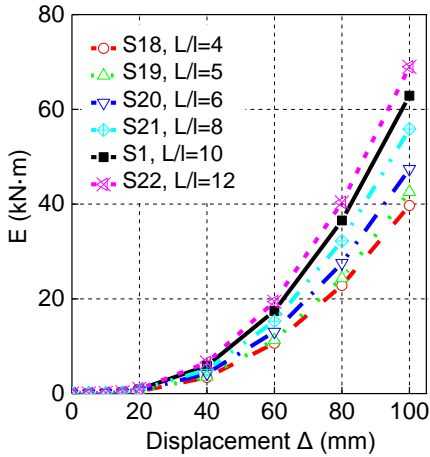


Fig. 77 Comparison of cumulative energy

Specimen	Parameter L/l	Yield		Peak		Failure		Ductility
		P_y (kN)	Δ_y (mm)	P_{max} (kN)	Δ_{max} (mm)	P_u (kN)	Δ_u (mm)	μ
S18	4	23.34	23.40	30.17	40	25.64	85.41	3.65
S19	5	25.30	23.85	32.62	40	27.73	88.91	3.73
S20	6	27.59	22.77	35.40	40	30.09	85.97	3.78

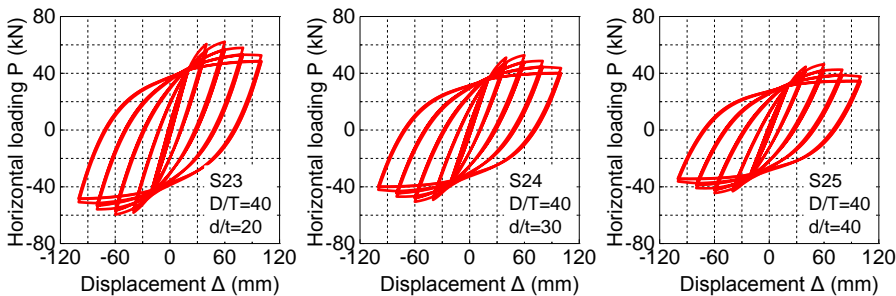
S21	8	31.86	22.59	40.9	60	34.77	99.37	4.40
S1	10	35.94	22.38	45.62	60	38.78	98.13	4.38
S22	12	39.67	22.04	50.16	60	42.67	98.44	4.47

Table 20

Comparison of ductility coefficient under different brace spacing

4.4.4 Diameter to Thickness Ratio

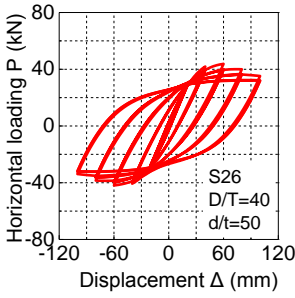
The diameter to thickness ratio in Ganhaizi Bridge is ranged from 45 to 68 for chord section D/T , and 41 for brace section d/t . Since both the diameter to thickness ratio of chord and brace will simultaneously affect the hysteretic behavior of CFST battened columns, 16 (4x4) FEMs are analyzed in this section, including $D/T=50, 60, 70, 80$ and $d/t=20, 30, 40, 50$. Number of FEMs are termed as S23-S26 for fixed $D/T=50$ and d/t ranging from 20 to 50, S27-S30 for fixed $D/T=60$ and d/t ranging from 20 to 50, S31-S34 for fixed $D/T=70$ and d/t ranging from 20 to 50, S35-S38 for fixed $D/T=80$ and d/t ranging from 20 to 50, respectively. $P-\Delta$ envelop curves of different D/T and d/t ratio is presented in Fig. 78. It can be seen that when the D/T is a fixed value, the initial flexural stiffness, ultimate horizontal load and initial stiffness decrease with an increase in the d/t value. Because thicker brace steel tubes may undergo larger bending moment and shear forces. While the initial stiffness is not affected obviously, since the chord keep the same cross-sectional area. Similarly, when the d/t is a fixed value, the ultimate horizontal load decrease with an increase in the D/T value, owing to the thicker chord steel tubes causes an increment both in strength and ductility to in-filled concrete. The results suggest that the hysteretic behavior of CFST battened column can be significantly increased by using a smaller D/T and d/t ratio for the cross section in design.



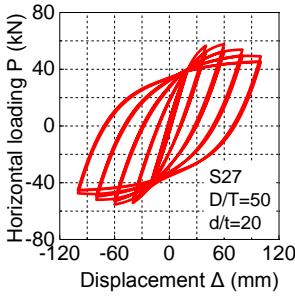
a) Specimen 23

b) Specimen 24

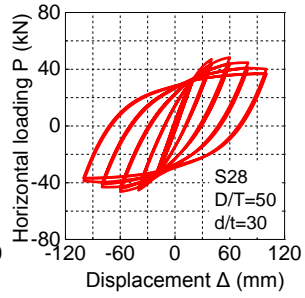
c) Specimen 25



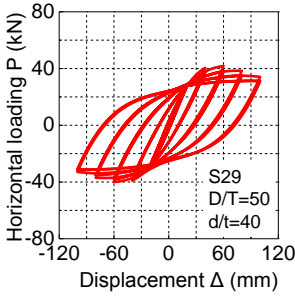
d) Specimen 26



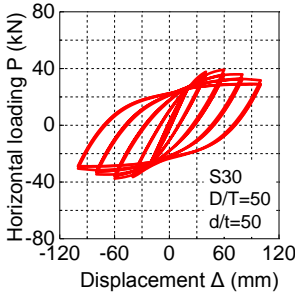
e) Specimen 27



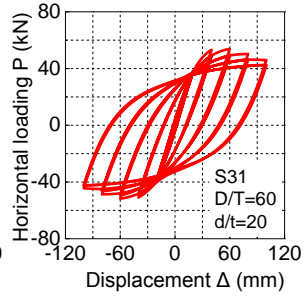
f) Specimen 28



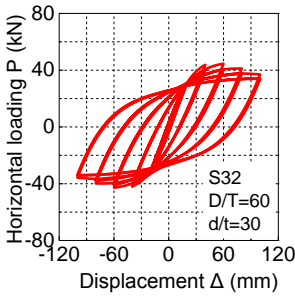
g) Specimen 29



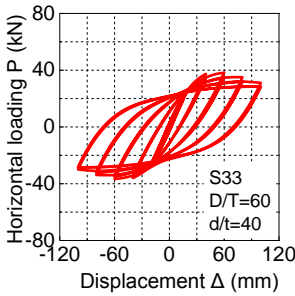
h) Specimen 30



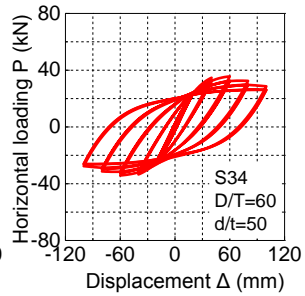
i) Specimen 31



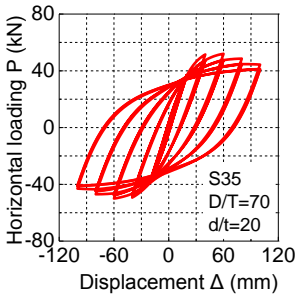
j) Specimen 32



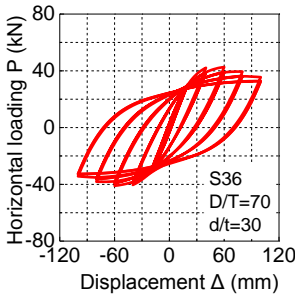
k) Specimen 33



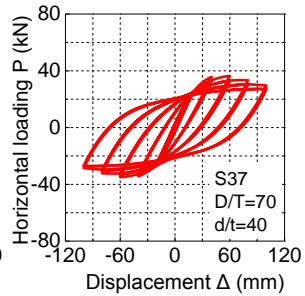
l) Specimen 34



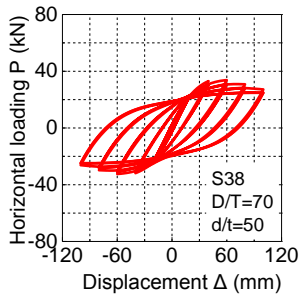
m) Specimen 35



n) Specimen 36



o) Specimen 37



p) Specimen 38

Fig. 78 Comparison of $P-\Delta$ hysteretic curves

Fig. 79 shows the $P-\Delta$ envelop curves under different D/T and d/t ratio. It can be found that as the values of D/T and d/t increase, the initial stiffness, peak load will be gradually decreased. Fig. 80 presents the comparison of cumulative energy. The dissipation capacity also show the same phenomenon. As the d/t decreases, the average cumulative energy capacity increases approximate 8.3%, 18.0%, 21.3%, respectively (from blue layer to black layer). As the D/T value decreases, the average cumulative energy capacity increases approximate 4.8%, 8.8%, 10.0%, respectively. Therefore, the thickness of brace relatively affects much more than that of chord. Table 21 summarizes the ductility coefficient under different brace spacing. As the d/t decreases, the average horizontal peak load increases 6.9%, 15.6%, 20.0%, and ductility increases by 2.8%, 5.6%, 5.6%, respectively. As the D/T decreases, the average horizontal peak load increases 4.3%, 8.2%, 9.3%, however, on the contrary, the ductility decreases by 2.2%, 2.8%, 3.8%. Therefore, properly increasing the thickness of brace steel tubes, will promote the hysteretic behavior of CFST battened columns.

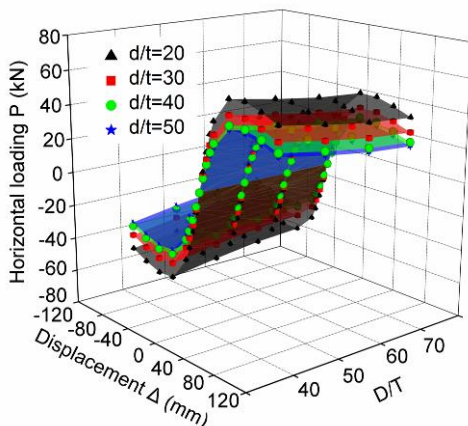


Fig. 79 Comparison of $P-\Delta$ envelope curves

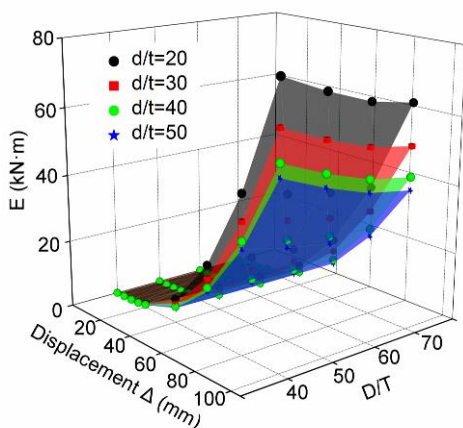


Fig. 80 Comparison of cumulative energy

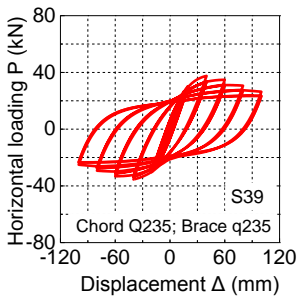
Specimen	Parameter D/T & d/t	Yield		Peak		Failure		Ductility μ
		P_y (kN)	Δ_y (mm)	P_{max} (kN)	Δ_{max} (mm)	P_u (kN)	Δ_u (mm)	
S1	55 & 25	35.94	22.38	45.62	60	38.78	98.13	4.38
S23	40 & 20	44.29	23.16	56.59	60	48.10	100.81	4.35
S24	40 & 30	37.22	23.52	47.85	60	40.67	96.35	4.10
S25	40 & 40	32.35	23.97	42.01	60	35.71	93.25	3.89
S26	40 & 50	30.33	24.37	39.58	60	33.64	92.00	3.78
S27	50 & 20	41.52	22.69	52.61	60	44.72	101.88	4.49
S28	50 & 30	34.21	22.64	43.92	60	37.33	97.00	4.28
S29	50 & 40	29.35	23.35	37.95	60	32.26	94.16	4.03
S30	50 & 50	27.34	23.63	35.53	60	30.20	92.95	3.93
S31	60 & 20	39.1	22.01	49.23	60	41.85	102.19	4.64
S32	60 & 30	31.98	22.12	40.57	60	34.48	97.13	4.39
S33	60 & 40	27.01	22.35	34.83	40	29.61	93.16	4.17
S34	60 & 50	25.07	22.63	32.45	40	27.58	91.60	4.05
S35	70 & 20	37.87	21.89	47.54	60	40.41	103.85	4.74
S36	70 & 30	30.68	21.66	38.95	40	33.11	97.15	4.49
S37	70 & 40	25.87	21.84	33.24	40	28.25	93.19	4.27
S38	70 & 50	23.85	22.06	30.85	40	26.22	91.39	4.14

Table 21

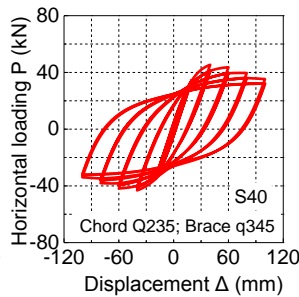
Comparison of ductility coefficient under different diameter to thickness ratio

4.4.5 Steel Yield Strength

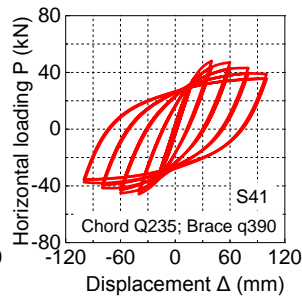
Steel tubes with different steel yield strengths, which are 235MPa, 345Mpa, 390MPa and 420MPa in the engineering practice, are analyzed by FEM. Since both the steel yield strength of chord and brace will simultaneously affect the hysteretic behavior, 16 (4x4) FEMs are analyzed, where steel yield strength of brace namely as Q and steel yield strength of brace namely as q . Number of FEMs are termed as S39-S42 for fixed $Q=235\text{MPa}$ and q ranging from 235MPa to 420MPa; S43-S45 for fixed $Q=345\text{MPa}$ and q ranging in 235MPa, 390MPa, 420MPa; S46-S49 for fixed $Q=390\text{MPa}$ and q ranging from 235MPa to 420MPa, S50-S53 for fixed $Q=420\text{MPa}$ and q ranging from 235MPa to 420MPa, respectively. Fig. 81 gives $P-\Delta$ envelop curves with different steel yield strengths. It appears that the ultimate cyclic lateral load of column is found to increase significantly with an increase in the steel yield strength. Because the moment capacity of the cantilever column is significantly increased by increasing the steel yield stress. While the steel yield strength does not have an effect on the initial flexural stiffness of the column, only increases the lateral peak load.



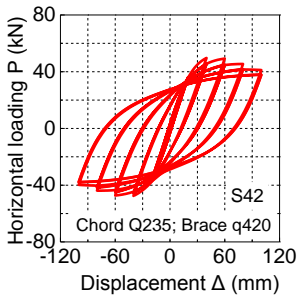
a) Specimen 39



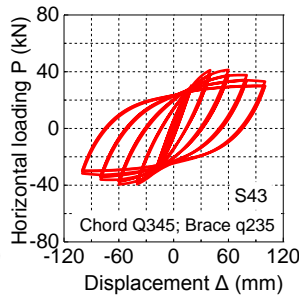
b) Specimen 40



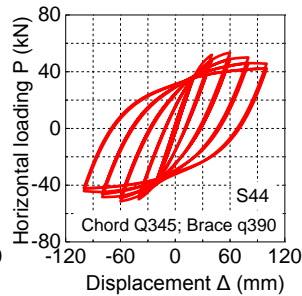
c) Specimen 41



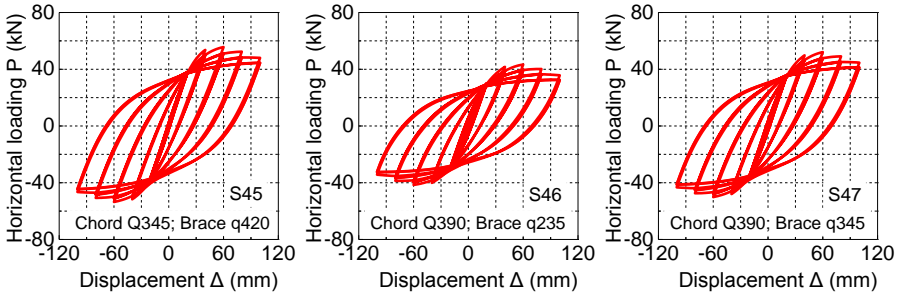
d) Specimen 42



e) Specimen 43



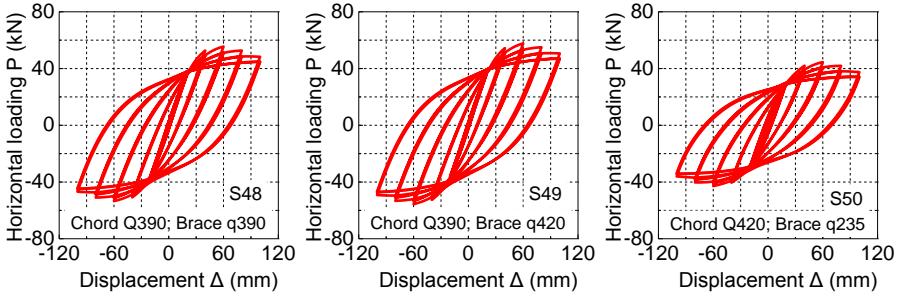
f) Specimen 44



g) Specimen 45

h) Specimen 46

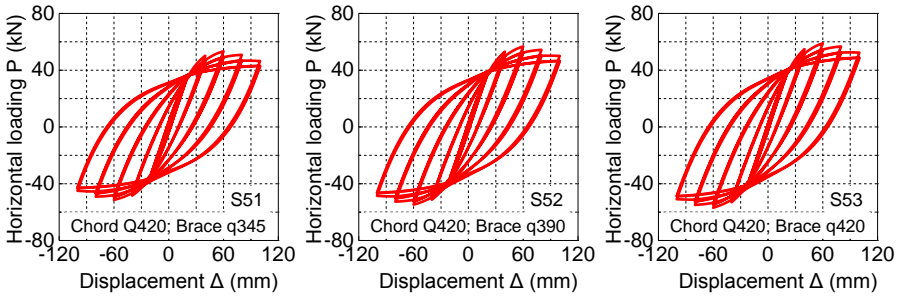
i) Specimen 47



j) Specimen 48

k) Specimen 49

l) Specimen 50



m) Specimen 51

n) Specimen 52

o) Specimen 53

Fig. 81 Comparison of $P-\Delta$ hysteretic curves

Fig. 82 shows the $P-\Delta$ envelop curves under different steel yield strength. It can be found that the steel yield strength does not have an effect on the initial flexural stiffness of the column, only increase the lateral peak load. Fig. 83 presents the comparison of cumulative energy. Compared with yield strength 235Mpa, the dissipation capacity with higher yield strength will be increased more than 24%. However, when the yield strength exceeds 345MPa, the dissipation capacity will not increase obviously. Table 22 shows the $P-\Delta$ envelop curves under different yield strengths. It can be found that as the yield strength increases from 235Mpa to 420Mpa, the peak load will be gradually promoted by 36.6%, 11.9% and 6.8%,

respectively. On the contrary, the ductility will decrease by 7.0%, 3.4% and 2.1%. Consequently, in case of the load-carrying capacity meets the requirements, increasing the yield strength of steel tubes is not an appropriate approach for the seismic performance.

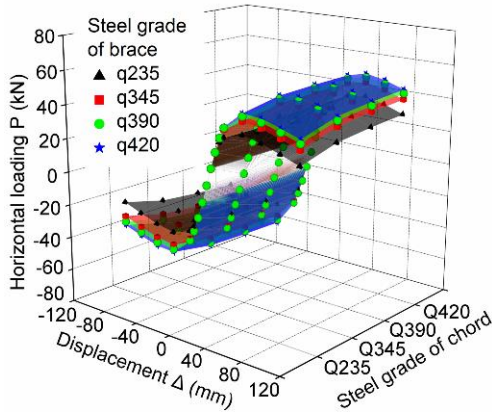


Fig. 82 Comparison of P-Δ envelope curves

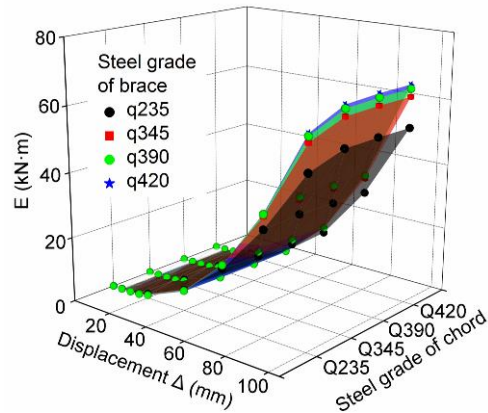


Fig. 83 Comparison of cumulative energy

Specimen	Parameter Chord & Brace f_{sy} (MPa)	Yield		Peak		Failure		Ductility μ
		P_y (kN)	Δ_y (mm)	P_{max} (kN)	Δ_{max} (mm)	P_u (kN)	Δ_u (mm)	
S39	235 & 235	27.05	15.85	33.39	40	28.38	75.15	4.74
S40	235 & 345	33.85	19.59	41.06	40	34.90	88.54	4.52
S41	235 & 390	35.77	20.85	43.84	40	37.26	91.08	4.37
S42	235 & 420	36.74	21.65	45.56	40	38.73	94.46	4.36

S43	345 & 235	28.78	18.77	37.85	40	32.17	88.87	4.73
S1	345 & 345	35.94	22.38	45.62	60	38.78	98.13	4.38
S44	345 & 390	38.23	23.87	48.88	60	41.55	102.84	4.31
S45	345 & 420	39.85	25.00	51.00	60	43.35	104.90	4.20
S46	390 & 235	29.28	19.56	39.40	60	33.49	92.35	4.72
S47	390 & 345	36.62	23.62	47.76	60	40.60	102.50	4.34
S48	390 & 390	39.23	25.27	51.03	60	43.38	106.78	4.23
S49	390 & 420	40.98	26.33	53.15	60	45.18	109.17	4.15
S50	420 & 235	29.64	20.30	40.79	60	34.67	95.88	4.72
S51	420 & 345	37.14	24.41	49.13	60	41.76	105.20	4.31
S52	420 & 390	39.82	26.06	52.39	60	44.53	109.84	4.21
S53	420 & 420	41.75	27.16	54.50	60	46.33	112.50	4.14

Table 22

Comparison of ductility coefficient under different steel yield strength

4.4.6 Comparison of strength and ductility with different parameters

Fig. 84 and Fig. 85 summarizes the displacement ductility factor and cumulative energy dissipation capacity under the effect of parameters mentioned above, respectively. It is observed that axial load ratio has greatest impact to the ductility of columns. Compared with S1, as axial load ratio exceeds from 0.3 to 0.5, the ductility factor decreases faster by 23%, 31% 39%. It is evident that for CFST battened columns, superstructure loading significantly affects the column's hysteretic behavior, and axial load ratio within 0.2 is a reasonable restrictions to exhibit ductility. Ductility is also effected by structural geometrical types, including chord spacing, brace spacing and diameter to thickness ratio. The chord spacing is roughly within 300mm-400mm ($L/b=6.25-8.33$), brace spacing is less than 312.5mm ($L/l=8$). From S23 to S38, it is seen that the diameter to thickness ratio significantly affect the ductility and energy dissipation of CFST built-up columns. Properly increasing the thickness of brace steel tubes will promote the hysteretic behavior of CFST built-up columns. Compared with the diameter to thickness ratio between chord D/T and brace d/t , the latter has more impact than the former. Steel yield strength shows relatively less impact than other parameters. However, increasing the steel yield strength of chord and brace (S39 to S53), the ductility will have a slightly decrease. Therefore, increasing the yield strength of steel tubes is not an appropriate approach for the hysteretic behavior. Overall, the ductility coefficient can approximately meet between 4 and 5 by the proper design.

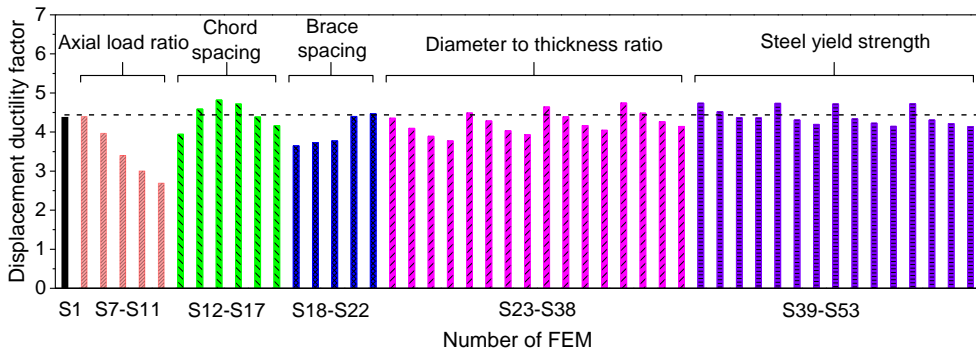


Fig. 84 Comparison of strength and ductility with different parameters

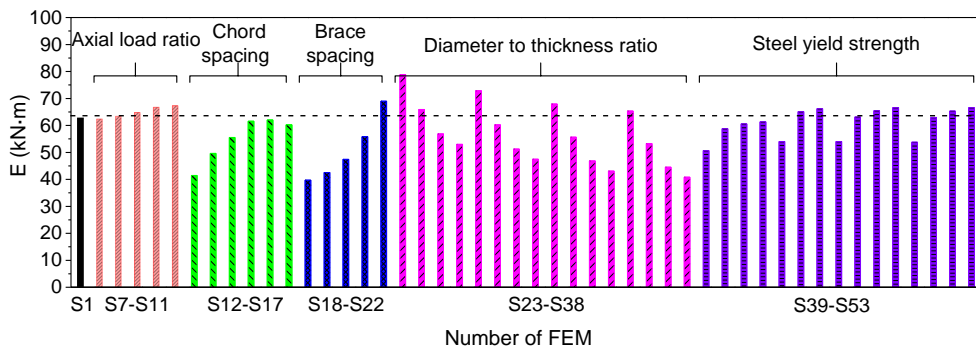


Fig. 85 Comparison of strength and ductility with different parameters

4.5. Proposed Method to Calculate Displacement Ductility Factor

Based on the parametric analysis and regression analysis, the author proposed the formula to calculate the ductility factor of CFST built-up columns in this section.

4.5.1 Equivalent Slenderness Ratio

As discussed the parameters in last section, it can be found that there are mainly three factors will influence the structural ductility, axial load ratio, structural arrangement (including chord spacing, brace spacing and diameter to thickness ratio) and steel yield strength. If the formula consists only main three arguments, it will be simple to adopt in calculating the structural ductility.

Some existing design codes, such as Eurocode 3 (European Committee for Standardization, 2006), AISC 2005 (AISC 360-10, 2010), GB 50017-2003 (China

National Standard, 2003), specify that to predict the load-bearing capacity, steel built-up columns should be designed using an equivalent slenderness ratio, which consider the influence of the shear deformation in compression. The formula usually take the chord width, brace width and diameter to thickness of both chord and brace into consideration. Herein, if we can use the concept of equivalent slenderness ratio for both battened and laced CFST columns, it will decrease the parameters and easy to fine relationship between ductility and equivalent slenderness ratio.

Until now, there is no specific definition to calculate the equivalent slenderness ratio of CFST built-up columns. Based on Timoshenko's elastic theory, Han et al. (Han et al., 2012) derived the formula to calculate slenderness ratio of CFST built-up columns with battened and laced shapes for two, three and four chords, respectively. Here, the equivalent slenderness ratio of four chords are introduced. For the axially compressive column, the critical buckling load N_{cr} can be expressed as Eq. (70)

$$N_{cr} = \frac{\pi^2 (EI)_{sc}}{L^2} \left[\frac{1}{1 + \frac{\pi^2 (EI)_{sc}}{L^2} \gamma} \right] = \frac{\pi^2 (EI)_{sc}}{(\mu L)^2} = \frac{\pi^2 (EA)_{sc}}{(\lambda_{ox})^2} = \frac{\pi^2 (EA)_{sc}}{\lambda_{ox}^2} \quad (70)$$

Where λ_{ox} is the equivalent slenderness ratio about x-axis, $\lambda_{ox} = \mu \lambda_x$, in which λ_x is the overall nominal slenderness ratio about x-axis; $\gamma = \frac{k}{GA}$ is the shear rigidity of the built-up member (unit shear angle); $(EI)_{sc}$ and $(EA)_{sc}$ are the flexural rigidity about the x-axis and the composite stiffness of the built-up member, respectively; μ is the shear influence coefficient, which can be given as Eq. (71)

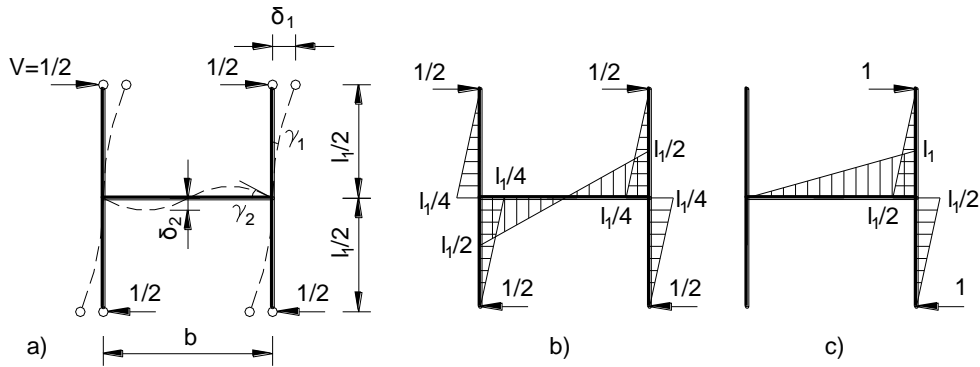
$$\mu = \sqrt{1 + \frac{\pi^2 (EI)_{sc}}{L^2} \gamma} \quad (71)$$

In Eq. (70) and Eq. (71), it is seen that the equivalent slenderness ratio λ_{ox} can be calculated once the shear rigidity γ is determined.

a) Battened built-up columns

Fig. 86(a) shows the plan view of isolated elements of battened built-up columns, where the four chords are the same as two chords due to symmetry. The battens serve as the web of the built-up member and transfer both shear force and bending moment in the member. Therefore, the contra-flexure points located in the middle of

chords and battens, isolated elements in Fig. 86(a) can be termed as calculating unit. When a unit shear force acts on the calculating unit, the distribution of the shear force and bending moments can be seen in Fig. 87(b)-(c).



a) Shear deformations of CFST batted members
 b) Bending moment diagram under unit shear force
 c) Bending moment diagram under unit deformation
 Fig. 86 Shear deformations of batted built-up members

Among that, the lateral deflection δ_1 originated from the shear deformation of the chord can be calculated as Eq. (72)

$$\delta_1 = \frac{l_1^3}{24E_{scm}I_{scm}} \quad (72)$$

Where E_{scm} and I_{scm} are the composite elastic modulus and moment of inertia of a single CFST chord, respectively, l_1 is the brace spacing.

The deflection δ_2 originated from the bending deformation of the brace can be calculated as Eq. (73)

$$\delta_2 = \frac{l_1^2 b}{12E_s I_1} \quad (73)$$

Where I_1 is the moment of inertia of the brace, and b is the chord spacing. Hence, the shear rigidity of batted built-up member can be obtained as Eq. (74)

$$\gamma = \frac{\delta_1 + \delta_2}{l_1} = \frac{l_1^2}{24E_{scm}I_{scm}} + \frac{l_1 b}{12E_s I_1} \quad (74)$$

Substituting Eq. (74) to Eq. (71) leads to

$$\mu = \sqrt{1 + \frac{\pi^2 (EI)_{sc}}{L^2} \left[\frac{l_1^2}{24E_{scm}I_{scm}} + \frac{l_1 b}{12E_s l_1} \right]} \quad (75)$$

The equivalent slenderness ratio can be derived as follows

$$\lambda_{ox} = \mu \lambda_x = \sqrt{\lambda_x^2 + \pi^2 (EA)_{sc} \left[\frac{\lambda_1^2}{24E_{scm}A_{scm}} + \frac{l_1 \lambda_0^2}{12E_s A_1 b} \right]} \quad (76)$$

Where λ_x is overall nominal slenderness ratio, $\lambda_x = L/r$, L is the distance between the ends of the member, r is the radius of gyration for the composite section of the built-up member, $r = \sqrt{I_{sc}/A_{sc}}$, I_{sc} and A_{sc} are the moment of inertia and total cross-sectional area of all the CFST members, respectively. Here, $A_{sc} = 4 \times \pi D^2 / 4$, $I_{sc} = 4 \times \pi D^2 / 64 + 4 \times (\pi D^2 / 4) \times (h/2)^2$; λ_1 is the slenderness ratio of a single CFST chord in one calculating unit, $\lambda_1 = l_1 / r_1$, in which r_1 is the radius of gyration for the single CFST chord and l_1 is the length in one calculating unit; λ_0 is the slenderness ratio of the batten; b is the chord center spacing; A_1 is the section areas of the brace; $E_{scm} A_{scm} = E_s A_s + E_c A_c$, $(EA)_{sc} = E_{scm} \sum A_{scm}$, where A_s and A_c are the cross-sectional areas of the steel tube and concrete for a single CFST chord, respectively; E_s and E_c are the modulus of the steel tube and concrete, respectively.

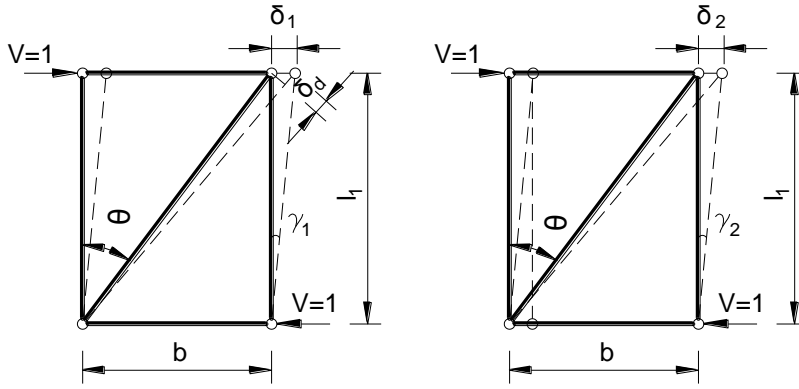
To simplify Eq. (76), define α_E is the ratio of steel elastic modulus to concrete elastic modulus, $\alpha_E = E_s / E_c$; α is the steel ratio of an individual CFST chord, $\alpha = A_s / A_c$; α_1 is the ratio of the steel area of an individual CFST chord to the steel area of the brace, $\alpha_1 = A_s / A_1$. Then the final formula to calculate the equivalent slenderness ratio of battened built-up columns can be expressed as Eq. (77)

$$\lambda_{ox} = \sqrt{\lambda_x^2 + \frac{\pi^2}{12} \lambda_1^2 + \frac{\pi^2 \alpha_1 \lambda_0^2 l_1}{6b} \left(1 + \frac{1}{\alpha \alpha_E} \right)} \quad (77)$$

b) Laced built-up columns

For the laced built-up columns, the connection of the brace and chord can be seen as hinge during calculation. Fig. 87 shows the plan view of isolated elements of

laced built-up columns, where the four chords are the same as two chords due to symmetry.



a) Deformation of diagonal brace b) Deformation of batten
Fig. 87 Shear deformations of laced built-up members

When shear force $V=1$, the tensile deformation of the diagonal brace is expressed as Eq. (78)

$$\delta_d = \frac{N_d l_d}{E_s A_d} = \frac{N_d l_1}{E_s A_d \cos \theta} = \frac{l_1}{E_s A_d \cos \theta \sin \theta} \quad (78)$$

Where N_d , l_d , and A_d are the axial force, sectional area and length of the diagonal brace, respectively. Then the lateral deformation δ_1 caused by the tension of the diagonal brace is expressed by Eq. (79)

$$\delta_1 = \frac{\delta_d}{\sin \theta} = \frac{l_1}{E_s A_d \cos \theta \sin^2 \theta} \quad (79)$$

Meanwhile, the tensile deformation of the batten is expressed by Eq. (80)

$$\delta_2 = \frac{\delta_d}{\sin \theta} = \frac{b}{E_s A_b} \quad (80)$$

Therefore, the shear rigidity of the laced built-up member can be obtained as Eq. (81)

$$\gamma = \frac{\bar{\delta}_1 + \bar{\delta}_2}{l_1} = \frac{1}{E_s A_d \cos \theta \sin^2 \theta} + \frac{b}{E_s A_b l_1} \quad (81)$$

Similarly, substituting Eq. (81) to Eq. (71) leads to

$$\lambda_{ox} = \mu \lambda_x = \sqrt{\lambda_x^2 + \frac{\pi^2 (EA)_{sc}}{E_s} \left[\frac{1}{A_d \cos \theta \sin^2 \theta} + \frac{b}{A_b l_1} \right]} \quad (82)$$

In practice, θ usually ranges from 45° to 60° and correspondingly $\pi^2 / (\cos \theta \sin^2 \theta)$ ranges from 26.3 to 27.9. To simplify Eq. (82), one may take $\pi^2 / (\cos \theta \sin^2 \theta)$ as 27 (Han et al., 2012). Then the equivalent slenderness ratio of laced member is expressed in Eq. (83).

$$\lambda_{ox} = \mu \lambda_x = \sqrt{\lambda_x^2 + 54 \alpha_d \left(1 + \frac{1}{\alpha \alpha_E}\right) + \frac{2 \pi^2 \alpha_b b}{l_1} \left(1 + \frac{1}{\alpha \alpha_E}\right)} \quad (83)$$

In which, define α_d is the ratio of the steel area of a single CFST chord to that of the diagonal brace, $\alpha_d = A_s / A_d$; α_b is the ratio of the steel area of the single CFST chord to that of the batten, $\alpha_b = A_s / A_b$, others are the same definitions as Eq. (76).

Adopted Eq. (77), all the equivalent slenderness ratios with various chord spacing, bracing spacing, diameter to thickness ratio and brace arrangements are summarized in Table 12 and plotted in Fig. 88. In Fig. 88, eliminating S12 which the chord spacing is shorter than the brace spacing, with poor ductility and relative smaller equivalent slenderness ratio, it is found that the ductility decreases as the equivalent slenderness ratio increases. Therefore, it seems more reasonable to use the equivalent slenderness ratio to evaluate the ductility that can simultaneously account for the effect of chord spacing, brace spacing, diameter to thickness ratio.

No.	λ_{ox}	$\Delta u / \Delta y$	No.	λ_{ox}	$\Delta u / \Delta y$	No.	λ_{ox}	$\Delta u / \Delta y$
S1	72.55	4.38	S21	81.09	4.4	S31	65.4	4.64
S12	51.84	3.95	S22	66.23	4.47	S32	77.58	4.39
S13	54.75	4.59	S23	69.08	4.35	S33	88.25	4.17
S14	58.26	4.82	S24	81.99	4.1	S34	97.73	4.05
S15	65.56	4.72	S25	93.3	3.89	S35	64.31	4.74
S16	79.07	4.16	S26	103.34	3.78	S36	76.27	4.49
S17	85.17	3.94	S27	66.91	4.49	S37	86.75	4.27

S18	115.17	3.65	S28	79.39	4.28	S38	96.06	4.14
S19	102.78	3.73	S29	90.32	4.03			
S20	93.75	3.78	S30	100.03	3.93			

Table 23

Summary of equivalent slenderness ratio and corresponding displacement ductility ratio

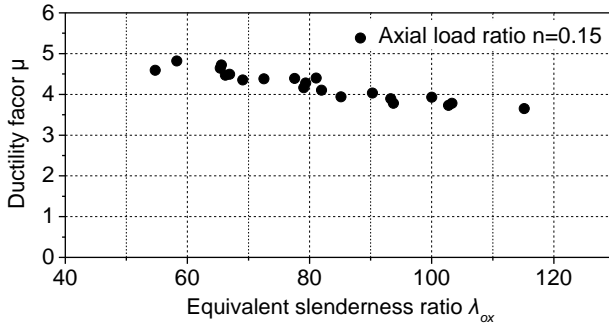


Fig. 88 Relationship between equivalent slenderness ratio and ductility

4.5.2 Regression Analysis

Regression analysis is the analysis of the relationship between one variable and another set of variables (SAS, 1999). The relationship can be expressed as an equation, predicts a response variable from a function of regressor variables and parameters. How to find the simplest model that adequately fits the observed data is a very difficult task. The selected equation should be simple (interpretable) and reliable, and the best equation is a compromise between these two. We can simulate and construct an equation similarly referred to previous literatures.

By comparison with ductility estimations obtained from cyclic tests and numerical analyses, Zhen et al. (Zhen et al., 2001) proposed method to evaluate the ductility of single CFST cantilever-type columns with unstiffened and stiffened box sections, pipe sections, and a one-story rigid frame with a stiffened box section. Among that, the formula for the cantilever columns with pipe sections can be expressed by Eq. (84)

$$\mu = \frac{0.24}{(1 + P/P_y)^{2/3} \lambda^{-1/3} R_t} \tag{84}$$

Where P/P_y is axial load ratio, $\bar{\lambda}$ is column slenderness ratio parameter and R_t is the radius-thickness ratio parameter as presented in Eq. (39), take yield strength of steel tube into account.

Also, based on 30 specimens with CFST square hollow section or rectangular hollow section, Han et al. (Han et al., 2003) developed the calculation method of the ductility coefficient (μ) of the composite beam-columns under constant axial load and cyclically increasing flexural loading, illustrated in Eq. (85)

$$\mu = 1.7 + n + 0.5\xi + \frac{E_s \xi}{65.3n^{1.2} \lambda^{0.75} f_y} \quad (85)$$

Where n is axial load ratio, ξ constraining factor obtained from $A_s f_{sy} / (A_c f_{ck})$, λ is column slenderness ratio, f_y and E_s is the yield strength and elastic modulus of steel tube.

Consult on Eq. (84)-(85), and parameter analysis in last part, the proposed equation to calculate ductility of CFST built-up columns should consider the influence of axial load ratio n , equivalent slenderness ratio λ and steel yield strength (including steel yield strength of chord, termed as F_{sy} and steel yield strength of brace, termed as f_{sy}). As observed from Fig. 88, power function can be simulated relationship between μ , n and λ . Thus, in the relationship between the ductility factor μ and these four parameters could be expressed as

$$\mu = \frac{A\varphi(F_{sy}, f_{sy})}{(1+n)^B \lambda^C} \quad (86)$$

Based on the analysis in Ch.4.4.5, relationship between ductility with F_{sy} and f_{sy} is plotted in Fig. 89.

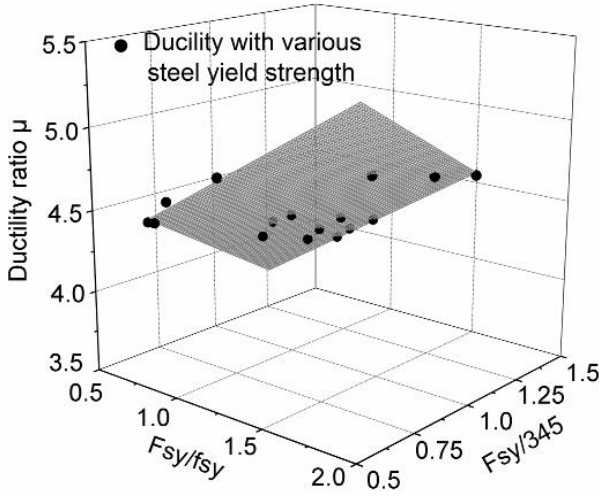


Fig. 89 Surface fitting of ductility based on steel yield strength

As observed, a plane function could be used the relationship between ductility and both variables of ratio of F_{sy} / f_{sy} and $F_{sy} / 345$. Thus, coefficient $\varphi(F_{sy}, f_{sy})$ could be expressed as

$$\varphi(F_{sy}, f_{sy}) = \frac{\mu}{\mu_{s1}} = D + E \frac{F_{sy}}{f_{sy}} + F \frac{F_{sy}}{345} \quad (87)$$

Where, μ is the result in Fig. 89 and μ_{s1} is the ductility in specimen S1 when both F_{sy} and f_{sy} are equal to 345MPa.

Determination of the regression equation is usually done using computer software, particularly when multiple variables are involved. In this study, the Surface Fitting Tool provided by OriginPro 9.0 (OriginLab Corporation, 2012) is adopted. Coefficient of D, E, F are 1.07, 0.18 and -0.25, respectively. Therefore, $\varphi(F_{sy}, f_{sy})$ is equal to

$$\varphi(F_{sy}, f_{sy}) = 1.07 + 0.18 \frac{F_{sy}}{f_{sy}} - 0.25 \frac{F_{sy}}{345} \quad (88)$$

Then in Eq. (88), we can set both F_{sy} and f_{sy} are equal to 345Mpa to keep $\varphi(F_{sy}, f_{sy})$ is equal to 1, the regression analysis can be aimed to find relationship between ductility μ with axial load n and equivalent slenderness ratio λ .

In Ch.4 4 1, when n exceed 0.3, ductility of CFST built-up columns is poor, hence n is determined ranges from 0.1 to 0.3, and slenderness ratio λ ranges from 54.75 to 115.17. A total of 98 FEMs are enlarged as sample to keep a better regression analysis. Results are shown in Fig. 90.

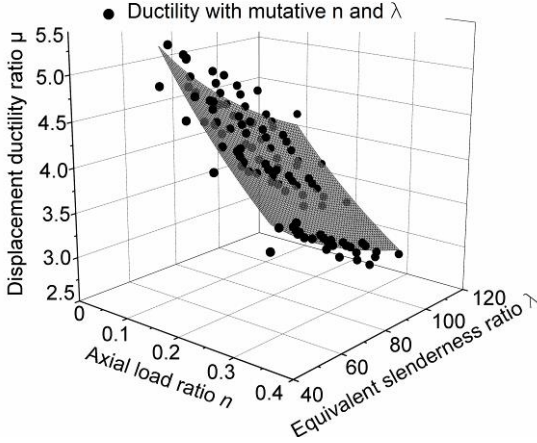


Fig. 90 Surface fitting of ductility based on axial load ratio and equivalent slenderness ratio

Coefficient of A , B , C are 27.92, 2.12 and 0.36, respectively. Substitute coefficient A , B , C and $\varphi(F_{sy}, f_{sy})$, final formula for calculating ductility of CFST laced columns is Eq. (89)

$$\mu = \frac{29.87 + 5.03 \frac{F_{sy}}{f_{sy}} - 0.02 F_{sy}}{(1+n)^{2.12} \lambda^{0.36}} \quad (89)$$

Similarly, a total of 64 FEMs are enlarged to keep a better regression analysis for CFST laced columns, through changeable diameter to thickness ratio and axial load ratio of CFST laced columns, where the equivalent slenderness ratio λ ranges from 19.84 to 30.46, and axial load ratio ranges from 0.1 to 0.3. Results are shown in Fig. 91.

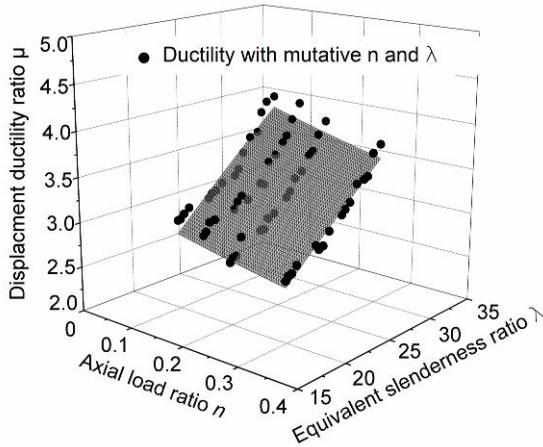


Fig. 91 Surface fitting of ductility based on axial load ratio and equivalent slenderness ratio

Coefficient of A , B , C are 0.303, 0.54 and -0.77, respectively. Substitute coefficient A , B , C and $\phi(F_{sy}, f_{sy})$, final formula for calculating ductility of CFST laced columns is Eq. (90)

$$\mu = \frac{0.32 + 0.05 \frac{F_{sy}}{f_{sy}} - 0.0002 F_{sy}}{(1+n)^{0.54} \lambda^{-0.77}} \quad (90)$$

4.5.3 Error Estimation for Proposed Formula

The most common method used to estimate the parameter values is the least-squares method, which minimizes the sum of the squares of the deviations of the theoretical data points from the experimental ones. This sum is the residual sum of squares (RSS) and is computed as Eq. (91)

$$RSS = \sum_{i=1}^n (y - y_i)^2 \quad (91)$$

The best-fit curve minimizes RSS . Fig. 92 illustrates the concept of least-squares fitting to a simple linear model.

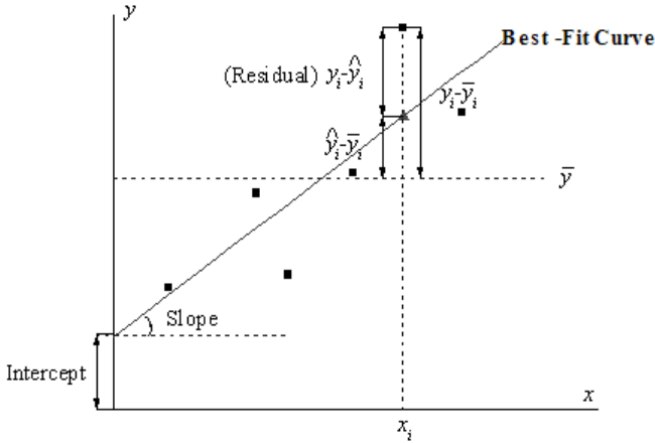


Fig. 92 The relationship between actual data and best-fit values by residuals schematic

The Best-Fit Curve represents the assumed theoretical model. For a particular point (x_i, y_i) in the original dataset, the corresponding theoretical value at x_i is denoted by \hat{y}_i . If there are two independent variables in the regression model, the least square estimation will minimize the deviation of experimental data points to the best fitted surface. When there are more than 3 independent variables, the fitted model will be a hyper-surface.

However, RSS varies from dataset to dataset, making it necessary to rescale this value to a uniform range. On the other hand, one may want to use the mean of y value to describe the data feature. If this is the case, the fitted curve is a horizontal line $y = \bar{y}$, and the predictor x , cannot linearly predict the y value. To verify this, we first calculate the variation between data points and the mean, the total sum of squares (TSS) about the mean, by

$$TSS = \sum_{i=1}^n (y_i - \bar{y})^2 \quad (92)$$

In least-squares fitting, the TSS can be divided into two parts: the variation explained by regression and that not explained by regression. Among that, the regression sum of squares, SS_{reg} , is that portion of the variation that is explained by the regression model, expressed by

$$SS_{reg} = \sum_{i=1}^n (\hat{y}_i - \bar{y})^2 \quad (93)$$

The residual sum of squares, RSS , is that portion that is not explained by the regression model, expressed by Eq. (91).

Clearly, the closer the data points are to the fitted curve, the smaller the RSS and the greater the proportion of the total variation that is represented by the $SSreg$. Thus, the ratio of $SSreg$ to TSS can be used as one measure of the quality of the regression model. This quantity is termed the coefficient of determination and computed as

$$R^2 = \frac{SSreg}{TSS} = 1 - \frac{RSS}{TSS} \tag{94}$$

From the above equation, we can see that when using a good fitting model, R^2 should vary between 0 and 1. A value close to 1 indicates that the fit is a good one.

Mathematically speaking, the degrees of freedom will affect R^2 . That is, when adding variables in the model, R^2 will rise, but this does not imply a better fit. To avoid this effect, we can look at the adjusted R^2 , termed as \bar{R}^2 and used to adjust the R^2 value for the degree of freedom,

$$\bar{R}^2 = 1 - \frac{RSS / df_{Error}}{TSS / df_{Error}} \tag{95}$$

For a perfect fit, $R^2 = 1$. Values less than that indicate that the function fits the data in a less than ideal manner. Excellent fits generally have R^2 values of 0.95. To visualize the situation of fits, the R^2 and adjusted R^2 are summarized in Table 24. It can be seen that relatively good fits can be obtained.

Formula	Coefficient of determination R^2	Adjusted coefficient of determination \bar{R}^2
Eq. (88)	0.9873	0.9853
Eq. (89)	0.9492	0.9482
Eq. (90)	0.9183	0.9156

Table 24

Summary of R^2 and adjusted R^2

Eventually, Table 25 shows the comparisons of displacement ductility factor between test results and proposed method. The errors are within 10%, indicating

that the proposed method can be used to calculate the displacement ductility factor of CFST built-up columns.

No.	Test results	Proposed method	Error %
S1	4.77	4.45	-6.71
S4	3.02	3.20	5.96
S5	4.08	3.67	-10.05
S6	3.60	3.67	1.94

Table 25

Comparisons of displacement ductility factor between test results and proposed method

5. SEISMIC PERFORMANCE OF A CFST TRUSS BRIDGE

In order to study the seismic performance of CFST built-up columns used in practice, in this chapter, an existing structure is presented as a case study, which is an innovative lightweight bridge with CFST composite truss girder and CFST built-up columns. The base dynamic characteristics and seismic performance of this bridge are discussed through response spectrum analysis,

5.1. Case Study-Ganhaizi Bridge

When a continuous girder bridge is located in the high mountains and deep valleys, reinforced concrete thin-wall hollow pier is generally adopted for the substructure. Especially the bridge with large-span and high-pier, reasonable light-duty pier shape is considered to reduce for promoting the seismic performance of the whole bridge.

The case study is Ganhaizi Bridge, completed in 2012 and located in Sichuan Province, China, with 480 km south from Wenchuan where a deadly earthquake occurred in 2008, measured at 8.0 Ms. and 7.9 Mw. Ganhaizi Bridge is one of the most unusual viaducts built in China. In fact, it is an experimental truss bridge that uses steel tubes for nearly the entire structure, see Fig. 93. The bridge is touted as the world's longest concrete filled steel tubular truss bridge with the world's highest bridge piers of concrete filled steel tubular lattice.



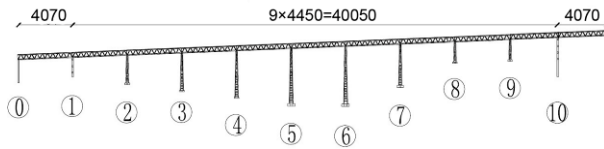
Fig. 93 Panorama of Ganhaizi Bridge

SEISMIC BEHAVIOR OF CONCRETE FILLED STEEL TUBULAR BUILT-UP COLUMNS

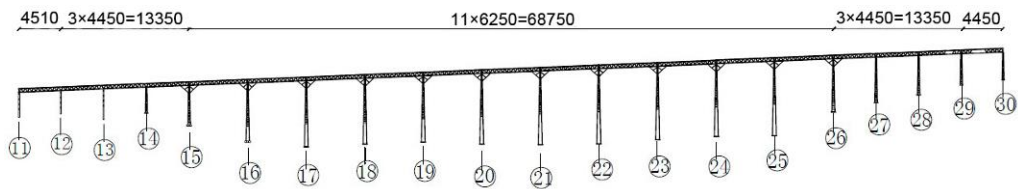
The bridge has a total length of 1811 m, with longitudinal slope 4%, composed of three continuous units, where separated by the 400mm width joints. The span arrangement is as follows,

- 1) The first units with 11 spans: $40.7\text{m}+9\times 44.5\text{m}+40.7\text{m}$;
- 2) The second units with 19 spans: $45.1\text{m}+3\times 44.5\text{m}+11\times 62.5\text{m}+3\times 44.5\text{m}+45.1\text{m}$;
- 3) The third units with 6 spans: $45.1\text{m}+4\times 44.5\text{m}+45.1\text{m}$.

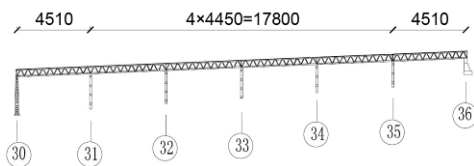
The evaluation layout of Ganhaizi Bridge is shown in Fig. 94.



a) The first units



b) The second units



c) The third units

Fig. 94 Evaluation layout of Ganhaizi Bridge (Unit: cm)

Superstructure comprises of concrete bridge deck, steel truss webs and CFST chords. General cross-section of truss girder is shown in Fig. 95. Bottom CFST chords are CFST with a diameter of 813 mm and thickness ranged from 18 mm to 32 mm, filled with C60 class concrete. Upper CFST chords are embed into concrete deck, which play a role of framework under construction. Web steel tubes have a diameter of 406 mm. For enhancing transverse stiffness, each triangle cross-sectional beam is connected by cross beam trusses, which is adopted by hollow steel tubes and set at the position of 1/3 point, 2/3 point along the beam and top of

each pier. Composite structure allows to take most of steel and concrete material properties, saves materials, and facilitates construction.

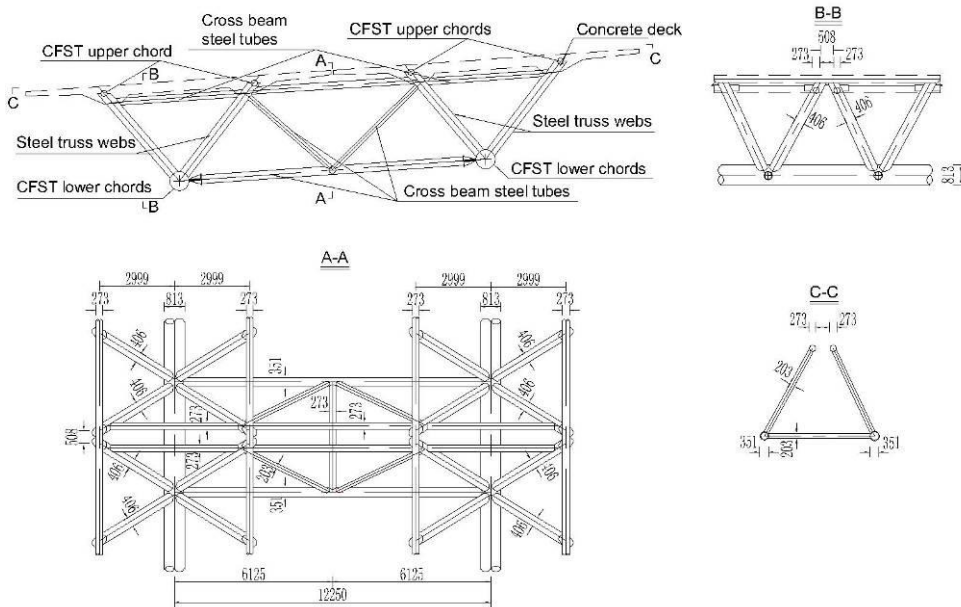


Fig. 95 CFST trusses girder (Unit: mm)

For the substructure, three types of piers were adopted: (a) reinforced concrete (RC) pier for the height less than 25m. (b) CFST pier for the height more than 25m (the tallest one is 107m). It is generally composed of four CFST columns connected together by circular hollow steel tubes, with 1:50 gradient from top to the bottom in longitudinal direction and vertical in transverse direction. The CFST columns have a diameter of 720mm with the wall thicknesses ranged from 12mm to 16mm at different height, filled with C50 class concrete. At the bottom region of 3m pier height, each column is covered by C30 class reinforced concrete protective layer with 15cm width. This type pier is termed as lattice columns, see Fig. 96. For the pier taller than 90m, the diameter of CFST columns are increased to 813mm, and the gradient is changed to 1:40. At the bottom region of 30m pier height, longitudinal connecting steel tubes are replaced with 40mm thickness of RC webs, to enhance pier stiffness. When the span of the girder is 62.5m, slant supports, with hollow steel tubes, are added on the top of CFST columns and fixed with girder together, this type pier is termed as composite columns, see Fig. 97. Due to the larger spacing in transverse direction (12.25m), the CFST columns are connected by hollow steel tubes trusses at each 12m height, which improves both the stiffness and stability in transverse direction.

SEISMIC BEHAVIOR OF CONCRETE FILLED STEEL TUBULAR BUILT-UP COLUMNS

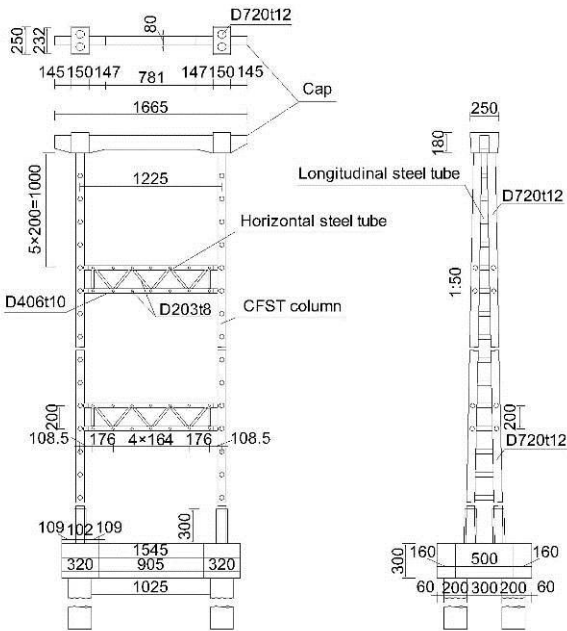


Fig. 96 CFST lattice columns (Unit: mm)

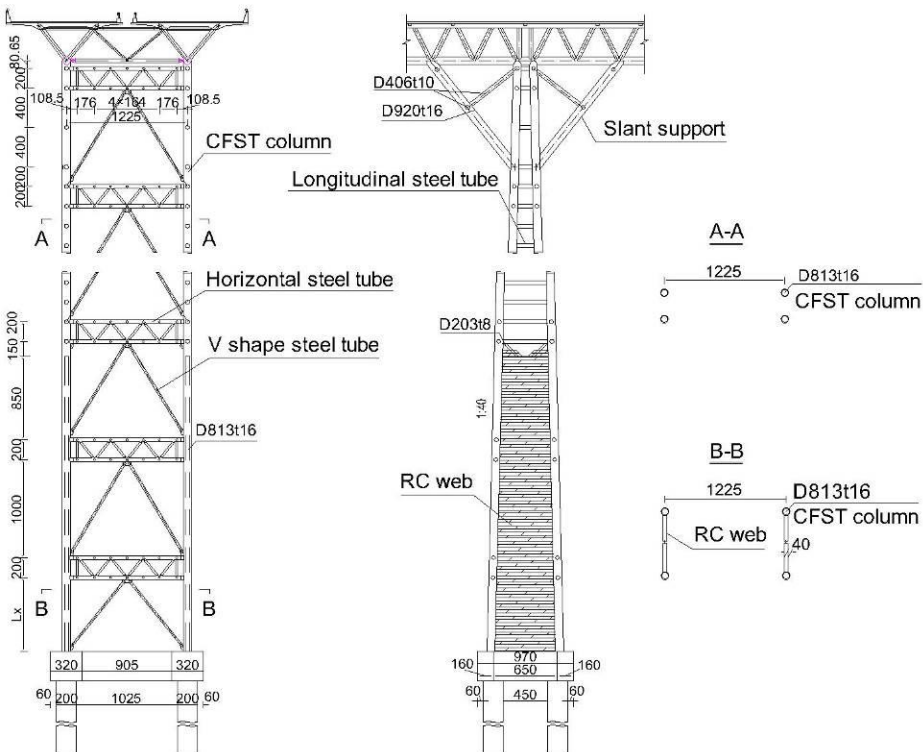


Fig. 97 CFST composite columns (Unit: mm)

With regards to connection between girder and piers, one is directly fixed between girder and piers and add slant support on the top of piers, the other type is adopting bearing supports, see Fig. 98. The pier details are summarized in Table 26. Among that, rubber bearings with high damping are designed in some piers, see Fig. 99. When the longitudinal displacement of bearing exceeds 50mm, the high damping will work though shear deformation. It can prevent excessive movement of the girder in longitudinal direction under loadings, such as temperature, automobile braking force, shrinkage and creep. In the case of the displacement exceeds 210mm under seismic loading, the bearing limit device will lock the bearing in longitudinal direction, hence the lower piers will be fixed with the girder, share and reduce the seismic forces to the higher piers. Some construction phases of Ganhaizi Bridge are shown in Fig. 100.

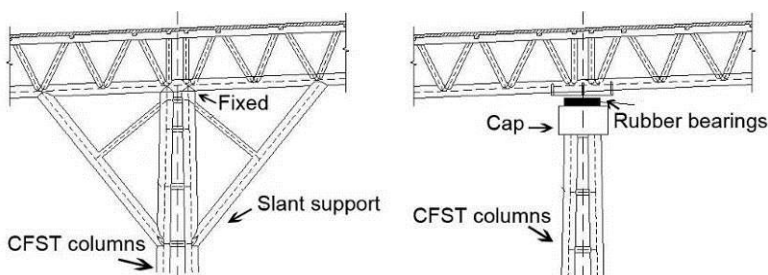
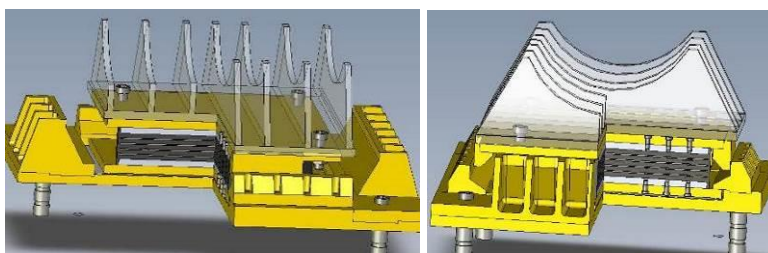


Fig. 98 Connection types



a) Longitudinal direction

b) Transverse direction

Fig. 99 Rubber bearing with high damping

No.	Pier Height (m)	Pier Types	Connection between pier and girder
1	15.664	RC pier	Rubber bearing
2	24.284	Lattice columns	Rubber bearing with high damping
3	32.227	Lattice columns	Rubber bearing with high damping
4	40.207	Lattice columns	Fixed
5	49.542	Lattice columns	Fixed
6	49.695	Lattice columns	Fixed
7	40.067	Lattice columns	Fixed

SEISMIC BEHAVIOR OF CONCRETE FILLED STEEL TUBULAR BUILT-UP COLUMNS

8	26.642	Lattice columns	Rubber bearing with high damping
9	24.153	Lattice columns	Rubber bearing with high damping
10	15.599	RC pier	Rubber bearing
11	15.316	RC pier	Rubber bearing

a) The first units

No.	Pier Height (m)	Pier Types	Connection between pier and girder
11	15.316	RC pier	Rubber bearing with high damping
12	16.432	RC pier	Rubber bearing with high damping
13	22.328	RC pier	Rubber bearing with high damping
14	34.295	Lattice columns	Rubber bearing with high damping
15	60.058	Lattice columns	Fixed
16	95.800	Composite columns	Fixed
17	104.897	Composite columns	Fixed
18	105.451	Composite columns	Fixed
19	103.961	Composite columns	Fixed
20	107.249	Composite columns	Fixed
21	107.036	Composite columns	Fixed
22	105.324	Composite columns	Fixed
23	102.111	Composite columns	Fixed
24	96.998	Composite columns	Fixed
25	95.086	Composite columns	Fixed
26	67.290	Lattice columns	Fixed
27	54.771	Lattice columns	Rubber bearing with high damping
28	42.825	Lattice columns	Rubber bearing with high damping
29	32.567	Lattice columns	Rubber bearing with high damping
30	26.701	Lattice columns	Rubber bearing with high damping

b) The second units

No.	Pier Height (m)	Pier Types	Connection between pier and girder
30	26.701	Lattice columns	Rubber bearing with high damping
31	23.889	RC pier	Rubber bearing
32	17.434	RC pier	Rubber bearing
33	13.324	RC pier	Rubber bearing
34	13.765	RC pier	Rubber bearing
35	12.656	RC pier	Rubber bearing

c) The third units

Table 26

Main features of the piers



a) Top view of the truss girder



b) Bottom view of the truss girder



c) Transverse view of the pier



d) Longitudinal view of the pier



e) Fixed welding



f) Slant support

Fig. 100 Phases on Ganhaizi Bridge during construction

5.2. Finite Element Model

5.2.1 Modelling of structure

Due to the complex CFST trusses typology and multi-span composite structure, the three-dimensional elastic beam element model is adopted as the first step to understand the seismic behaviour of Ganhaizi Bridge. The finite element model (FEM) is established by the general commercial software MIDAS/Civil 2010 (MIDAS Information Technology Co. Ltd, 2010). The second units, which including three types of pier, are chosen for analysis, see Fig. 101.

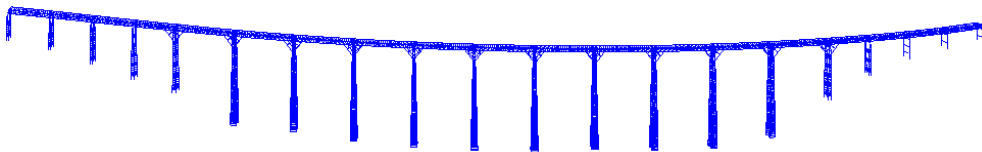


Fig. 101 FEM of Ganhaizi Bridge

There are a total of 14443 nodes and 24441 elements in FEM. Most components, including the concrete deck and all hollow steel tube trusses, are simulated by beam elements, which can reflect the global behaviour, at the same time, shorten the computing time for large bridge FEM.

The CFST chords are simulated by the separated elements with common nodes, which can analysis the internal forces and displacement of in-filled concrete and steel tube, respectively. The reinforced concrete (RC) webs in the pier No.16-25 are simulated by plate element, connecting the four nodes of CFST columns. The pile and foundation are neglected, thus all the nodes at the bottom of CFST columns are fixed. For the girder, rigid connection is adopted to link steel trussed web and concrete deck. Upper CFST chords are neglected, which are with small size and embed in the deck. When the rigid connection are used, it is not necessary to enhance the deck stiffness. The weight of deck pavement was considered by increasing density of deck. Top of No.15-26 pier are fixed with girder, rigid link are used for simulation here. The FEM details are illustrated in Fig. 102. Elastic spring elements are applied to simulate the bearings and stiffness vales are summarized in Table 27. Both the transverse and vertical stiffness are assumed positive infinity, for transferring the dead loads of the girder in vertical direction and prevent it move in transverse direction. In longitudinal direction, the values of stiffness is determined by the design document of Ganhaizi Bridge.

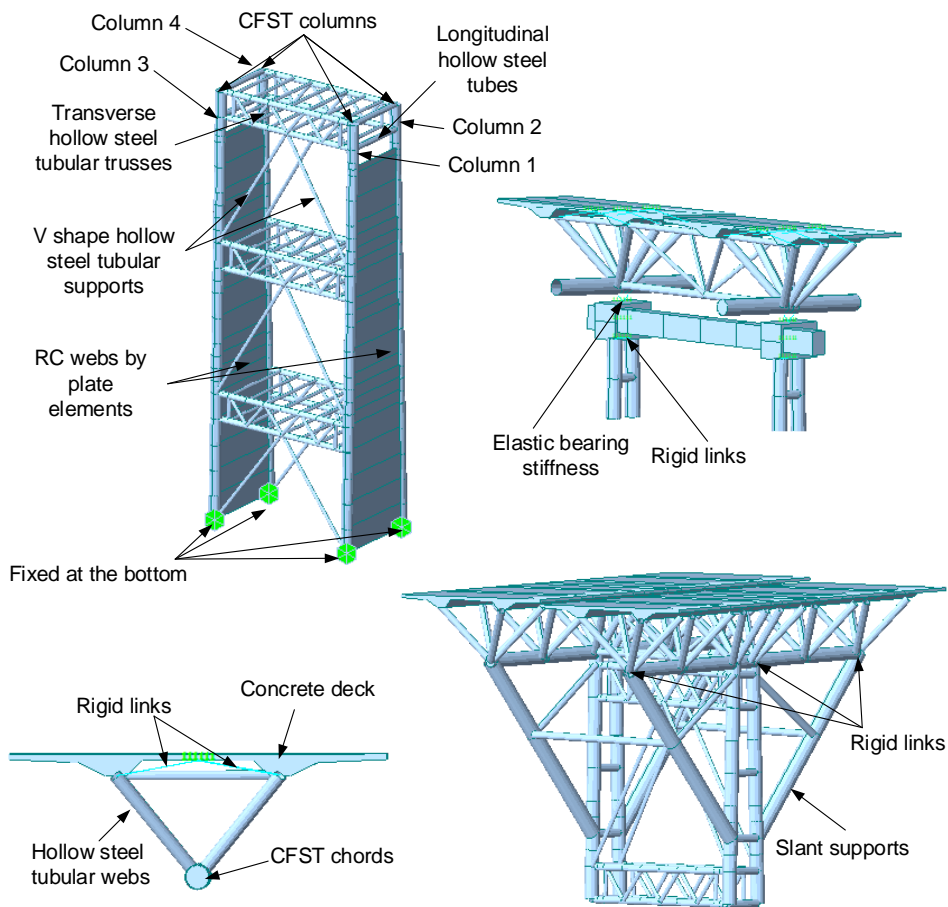


Fig. 102 FEM details

No.	Stiffness (kN/m)		
	Longitudinal direction	Transverse direction	Vertical direction
11	1000	∞	∞
12	2400	∞	∞
13	2400	∞	∞
14	2400	∞	∞
27	2400	∞	∞
28	2400	∞	∞
29	2400	∞	∞
30	1000	∞	∞

Table 27

Stiffness values of the bearing

5.2.2 Materials

The detailed material properties are listed in Table 28-29, which are defined by the Technical specification for concrete-filled steel tubular structures GB50923-2013 (Housing and urban-rural development of the People's Republic of China, 2013).

Component	Grade	f_{ck} (Mpa)	f_{cd} (Mpa)	f_{tk} (Mpa)	f_{td} (Mpa)	E_c (Mpa)	ν
RC webs and RC piers	C30	20.1	14.3	2.01	1.43	30,000	0.2
Bent cap	C40	26.8	19.1	2.39	1.71	32,500	0.2
Deck and CFST columns	C50	32.4	23.1	2.64	1.89	34,500	0.2
CFST chords	C60	38.5	27.5	2.85	2.04	36,000	0.2

Table 28

Concrete mechanical properties

Component	Grade	Thickness	f_y (Mpa)	f_{yd} (Mpa)	E_s (Mpa)	ν
Hollow steel trusses tubes	Q345	≤16	345	310	206,000	0.3
The rest of steel tubes	Q345	>16-35	325	295	206,000	0.3

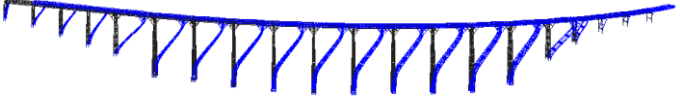

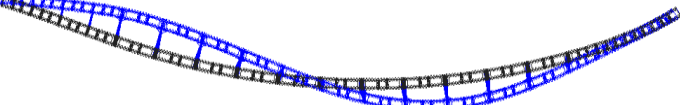
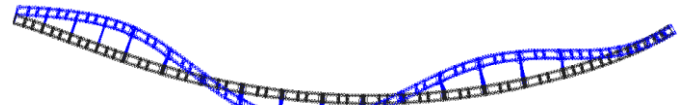




Table 29

Steel mechanical properties

5.3. Modal Analysis

The natural vibration characteristics, which includes natural frequency, modal shape, and reflects the bridge inherent dynamic performance, can be calculated through modal analysis. In this work, subspace iteration method is adopted for calculating the natural vibration characteristics. It uses generalized Jacobi iterative algorithm and the law allows the subspace to project complete stiffness and mass matrices, suitable for a large FEM with lower memory requirements for computers. Table 30 summarizes the typical modal statistics. It can be seen that the first-order frequency is 0.191Hz with modal shape of longitudinal floating. In other words, the natural periods is 5.236s, indicating that the bridge is expected to promote the seismic performance through its flexibility. From the second to ninth modes, various transverse bending modal shapes are appeared, and the accumulative modal participation mass can exceed 80%. The local mode appears until the tenth-order modal, with local bending in pier No. 27. Vertical modal appears in the twelfth-mode

with oscillation in the high piers, and twisting modal appears in the twenty third-order modal, indicating that the structure has a favorable vertical and torsional stiffness.

No.	Frequency (Hz)	Mode shape
1	0.191	 <p data-bbox="689 519 931 557">Longitudinal floating</p>
2	0.273	 <p data-bbox="608 691 1012 729">Transverse bending / Symmetrical</p>
3	0.294	
4	0.335	
5	0.406	
6	0.490	
7	0.594	
8	0.738	

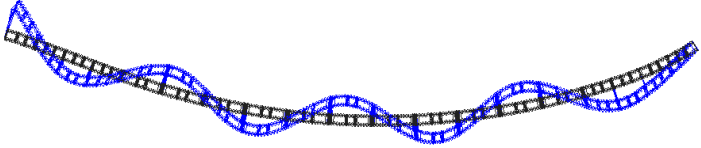
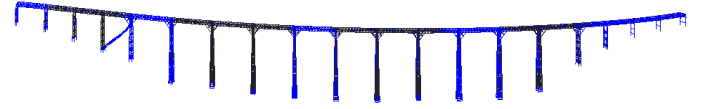
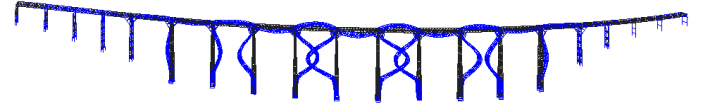
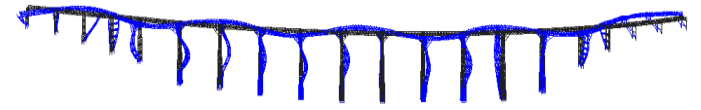
9	0.911	 <p>From mode 3 to 9: Transverse bending / Anti-symmetrical</p>
10	1.064	 <p>Local bending in pier No. 27</p>
12	1.146	 <p>Vertical bending</p>
23	1.278	 <p>Twisting and transverse bending</p>

Table 30
Modal shapes and frequencies

It is generally expected that FEM modal analysis can reliably simulate the basic dynamic characteristics. However, as a consequence of modelling uncertainties, the natural frequencies and modal shapes with the required level of accuracy is need to be checked. A possible practice to fill the lack between the FEM and real bridge performance is to carry out some form of dynamic testing in the real bridge before or during service. Usually, the Modal Assurance Criterion (MAC) approach is adopted to check the validity of FEM, which is probably the most useful tool to correlate two sets of mode shape vectors obtained experimentally or theoretically (Allemang, 2003). However, the load test report of Ganhaizi Bridge (Structural Engineering Test Center of Southwest Jiaotong University, 2012), only presents the first-order modal in the transverse and vertical direction, respectively. Hence, the results compassion is applied between test and FEM analysis through the absolute frequency discrepancy D_F .

$$D_F = \frac{|f_{Test} - f_{FEM}|}{f_{Test}} \tag{96}$$

Table 31 compares the result and shows a well agreement between the load test and FEM, where the value of D_F is within 5%, indicating that the FEM is accuracy in the modal analysis.

First-order modal	Frequency (Hz)		D_F
	Load test	FEM	
Transverse direction	0.28	0.273	2.5%
Vertical direction	1.10	1.146	4.2%

Table 31
Modal comparison between load test and FEM

5.4. Response Spectrum Analysis

5.4.1 Design conditions

In order to have a basic cognition to the seismic performance of Ganhaizi Bridge, the response spectrum analysis is firstly carried out by using the horizontal response spectrum. It is well known that the response spectrum is a linear analysis case, but can get the maximum internal forces and displacements. In the current seismic design specifications, the structural period of design acceleration response spectrum is usually within 4s, such as Eurocode 8 (Eurocode CEN, 2005b), Italian code NTC 2008 (Ministero delle Infrastrutture, 2008), which can cover most regular bridges. Due to specific structure of Ganhaizi Bridge and its location, the design spectrum response is adopted by the Guidelines for Seismic Design of Highway Bridges JTG/T B02-01-2008 (Ministry of Transport of the People's Republic of China, 2008), which make specification of bridge structural period within 10s. The following two basic requirements are defined: (a) Earthquake action E1 (The shorter return period of the earthquake action in the engineering site, which corresponds to the first level of fortification levels); (b) Earthquake action E2 (The longer return period of the earthquake action in the engineering site, which corresponds to the second level of fortification levels).

For the horizontal components of the seismic action, the elastic response spectrum S is defined by the following expressions, see Fig. 103.

$$S = \begin{cases} S_{\max}(5.5T + 0.45) & T < 0.1s \\ S_{\max} & 0.1s \leq T \leq T_g \\ S_{\max}(T_g / T) & T > T_g \end{cases} \quad (97)$$

Where, T_g is the characteristic period (s); T is structural natural periods, applied for vibration periods not exceeding 10s; S_{max} is the maximum value of horizontal design acceleration response spectrum.

$$S_{max} = 2.25C_i C_s C_d A \tag{98}$$

Where, C_i is the bridge importance factor; defined by Table 32; C_s is site coefficient, defined by Table 33; C_d is damping adjustment coefficient, defined by Table 34; A is the peak acceleration of horizontal design ground motion, defined by Table 35.

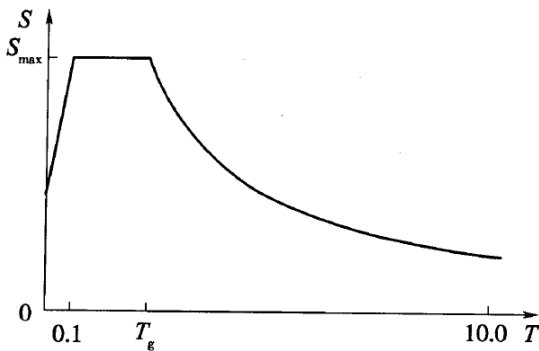


Fig. 103 Horizontal design acceleration response spectrum

Bridge classification	Earthquake action E1	Earthquake action E2
Type A	1.0	1.7
Type B	0.43 (0.5)	1.3 (1.7)
Type C	0.34	1.0
Type D	0.23	--

Table 32

Seismic importance factor C_i of various types of bridges

In which, Type A includes specially long span bridges with single-span exceeds 150m; Type B includes the bridges in the expressway and first-class highway with single-span less than 150m, and the bridge in the long span bridge in the second-class highway with single-span less than 150m. The value of bracket includes the long span bridges in the expressway and first-class highway; Type C includes medium and small bridges with single-span less than 150m, and long span bridge in the third- and forth-class highway; Type D includes the medium and small bridge in the third- and forth-class highway.

Type of site	Seismic fortification intensity					
	6	7		8		9
	0.05g	0.1g	0.15g	0.2g	0.3g	0.4g
I (Stiff)	1.2	1.0	0.9	0.9	0.9	0.9
II (Medium-stiff)	1.0	1.0	1.0	1.0	1.0	1.0
III (Medium-soft)	1.1	1.3	1.2	1.2	1.0	1.0
IV (Soft)	1.2	1.4	1.3	1.3	1.0	0.9

Table 33
Site coefficient C_s

The characteristic period T_g is determined according to the Chinese Seismic Ground Motion Parameter Zonation Map (Ministry of Transport of the People's Republic of China, 2001), see Fig. 104, then adjust the value based on Table 34.

The characteristic period (s)	Site classification			
	I (Stiff)	II (Medium-stiff)	III (Medium-soft)	IV (Soft)
0.35	0.25	0.35	0.45	0.65
0.40	0.30	0.40	0.55	0.75
0.45	0.35	0.45	0.65	0.90

Table 34
Design acceleration adjustment corresponding to characteristic period on the response spectrum

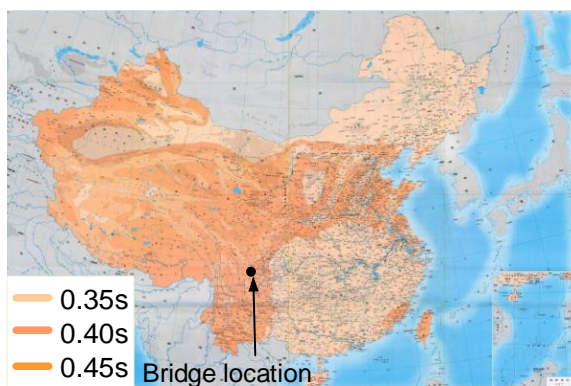


Fig. 104 Chinese Seismic Ground Motion Parameter Zonation Map

If the adoption of values for the damping ratio ξ is not 0.05, the damping adjustment coefficient C_d can be determined in the following expression

$$C_d = 1 + \frac{0.05 - \xi}{0.06 + 1.7\xi} \geq 0.55 \tag{99}$$

Seismic fortification intensity	6	7	8	9
A	0.05g	0.10(0.15)g	0.20(0.30)g	0.40g

Table 35
The peak acceleration of horizontal design ground motion

According to the site of Ganhaizi Bridge, the appropriate coefficient under Earthquake action E1 can be determined, bridge classification-Type B, $T_g=0.45s$, site classification-III, seismic fortification intensity-8, the design seismic acceleration action A is 0.362g associated with a reference probability of exceedance, $P_{NCR}=10\%$ in 50 years, damping ratio $\xi=0.05$, therefore, $C_i=0.50$, $C_s=1.00$, $C_d=1.00$, $S_{max}=0.40725g$, the design seismic response spectrum is shown in Fig. 105.

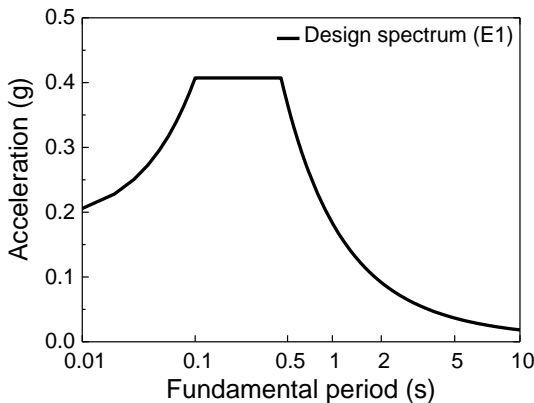


Fig. 105 Horizontal design acceleration response spectrum

For the straight bridge, the response spectrum analysis usually be conducted in both longitudinal and transverse directions. Then two combination approaches are adopted to obtain the composite action of the two directions though Envelope combination method (Eurocode CEN, 2005b). However, for the curved bridge, there is no specific direction pointed out as input direction. In order to get the most unfavorable seismic input in horizontal direction, bridge designers usually take the trial methods to calculate the bridge response under different directional ground motions. The Guidelines for Seismic Design of Highway Bridges JTG/T B02-01-2008 (Ministry of Transport of the People's Republic of China, 2008) defines that, for the curved bridge, the input direction can be parallel and perpendicular to the bearing connection on both ends, respectively. In this work, the seismic input

direction is parallel and perpendicular to the bearing connection on both ends of the bridge, respectively, illustrated in Fig. 106.

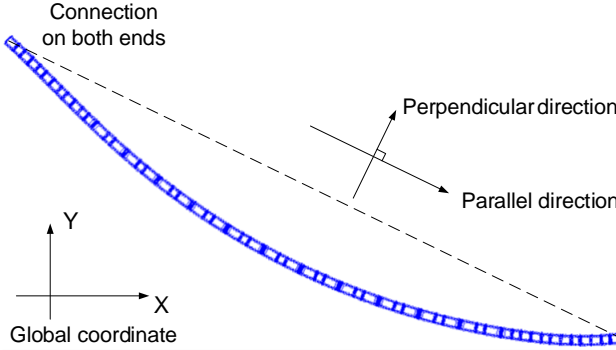


Fig. 106 Horizontal seismic input direction

Due to the adjacent orders (T_i and T_j) of natural period of Ganhaizi Bridge are closed (intensive frequencies) and natural period ratio meets the Eq. (100), if adopting the SRSS (Square Root of Sum of Squares) method, the coupling term between various modes will be neglected, lead to overestimate or underestimate the structural response. Hence, the CQC (Complete Quadratic Combination) method is adopted to calculate structural response (Wilson et al., 1981), seen in Eq. (101)-(102). In the seismic analysis, the load combination only takes into account that 1.0 dead load+1.0 seismic load.

$$\rho_T = \frac{T_j}{T_i} \geq \frac{0.1}{0.1 + \xi} \quad (100)$$

$$F = \sqrt{\sum \sum S_i r_{ij} S_j} \quad (101)$$

$$r_{ij} = \frac{8\xi^2(1 + \rho_T)\rho_T^{3/2}}{(1 + \rho_T^2)^2 + 4\xi^2\rho_T(1 + \rho_T)^2} \quad (102)$$

5.4.2 Internal forces analysis

Due to different piers with different sections and the cross-sectional dimension of each pier varies along the pier height, and in order to unify standards of comparison and show the mechanical characteristic and peak position of this type of pier. The maximum stresses, at the edge of steel and concrete cross section, are chosen as

analysis, see Fig. 107, we can see that the main bearing components is comprised of four CFST columns, here termed as column 1 to 2 on one side of pier and 3 to 4 on the others. Corresponding to local coordinates in two directions, each column with four points at the edge of steel tubes, termed as point 1 to 4, and with four points at the edge of in-filled concrete, termed as point 5 to 8. The maximum stress value are summarized from the each defined 4 points.

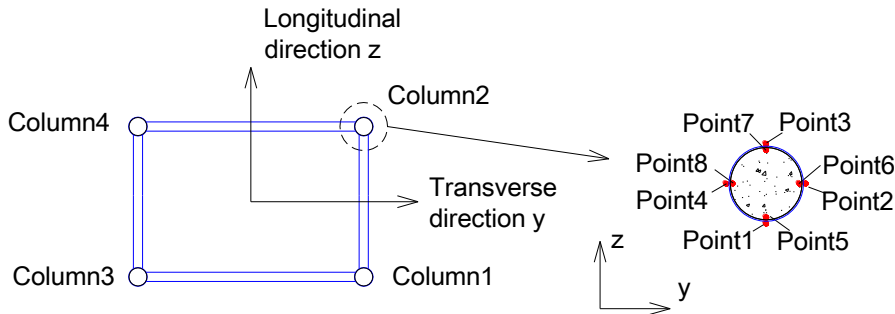
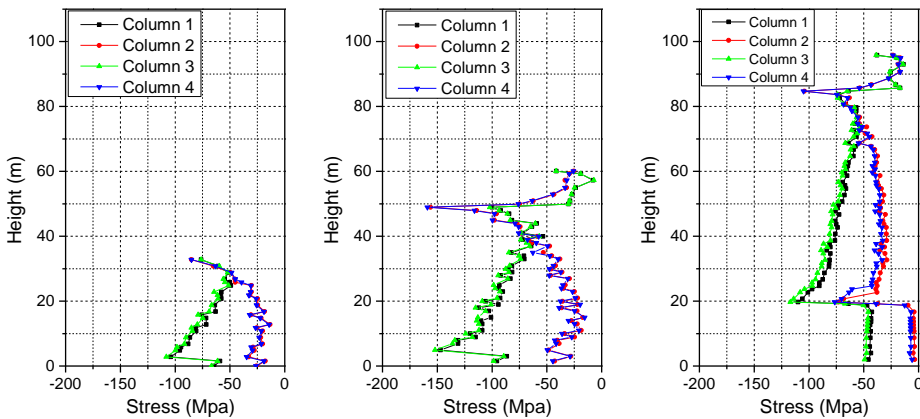


Fig. 107 Defined points at the edge of steel tubes and concrete

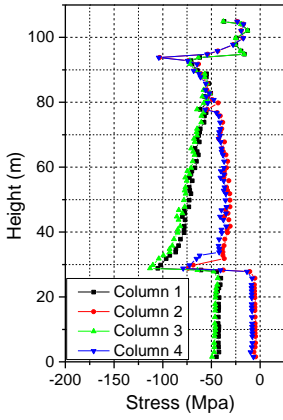
The maximum stress at the edge of steel tubular and concrete sections of each piers under parallel seismic input direction are presented in Fig. 108 and Fig. 109, respectively.



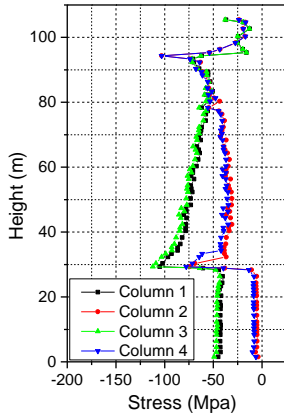
a) Pier No. 14

b) Pier No. 15

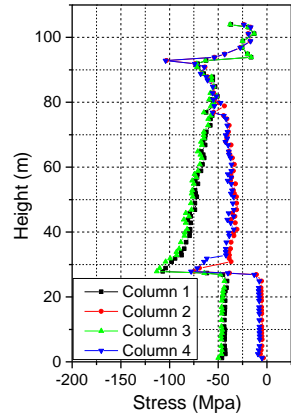
c) Pier No. 16



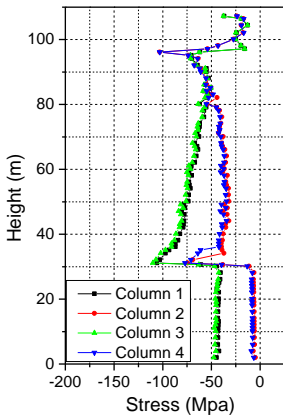
d) Pier No. 17



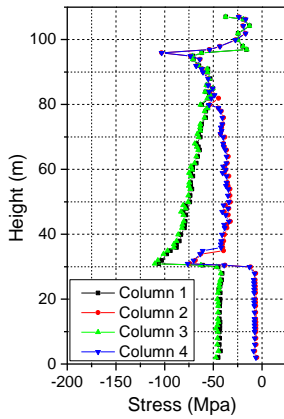
e) Pier No. 18



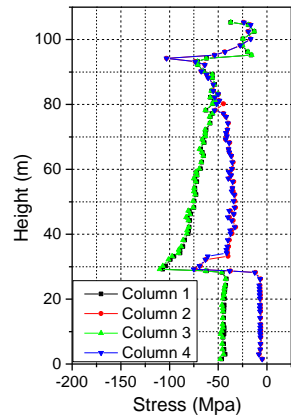
f) Pier No. 19



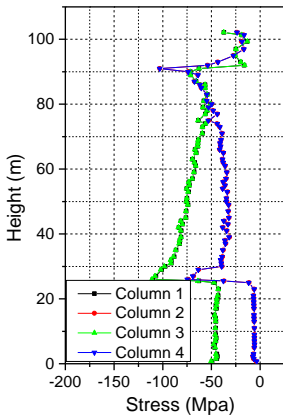
g) Pier No. 20



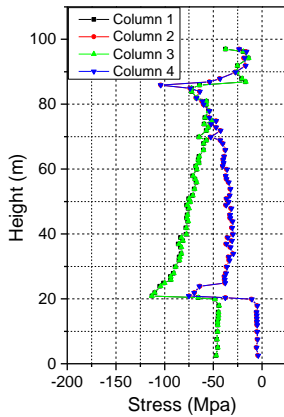
h) Pier No. 21



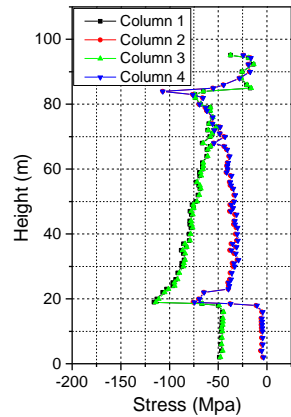
i) Pier No. 22



j) Pier No. 23

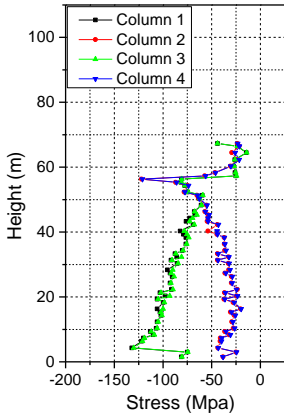


k) Pier No. 24

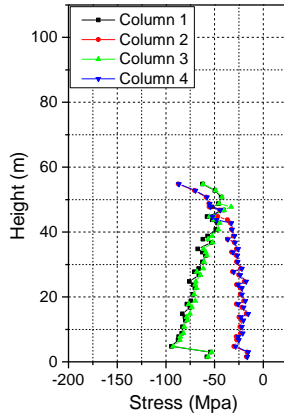


l) Pier No. 25

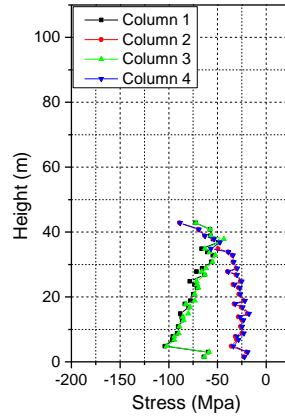
SEISMIC BEHAVIOR OF CONCRETE FILLED STEEL TUBULAR BUILT-UP COLUMNS



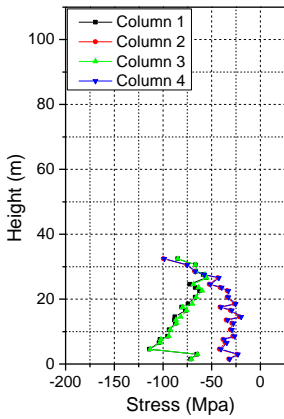
m) Pier No. 26



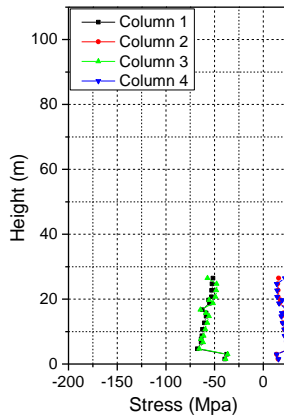
n) Pier No. 27



o) Pier No. 28

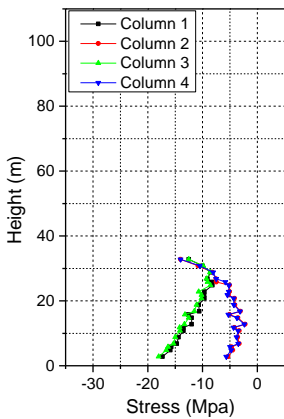


p) Pier No. 29

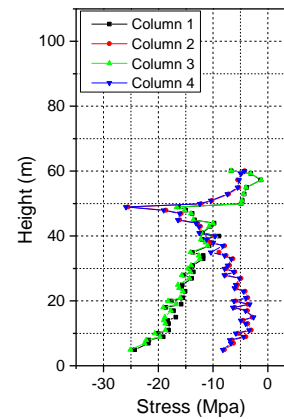


q) Pier No. 30

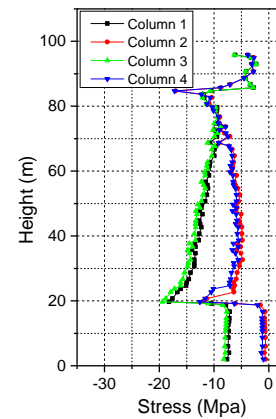
Fig. 108 Maximum stress distribution at the edge of steel tubular sections under parallel seismic input direction



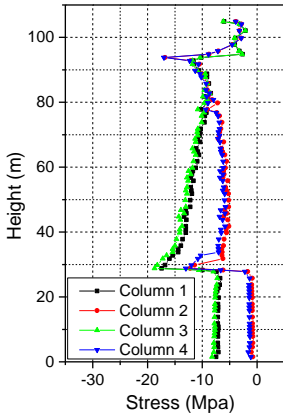
a) Pier No. 14



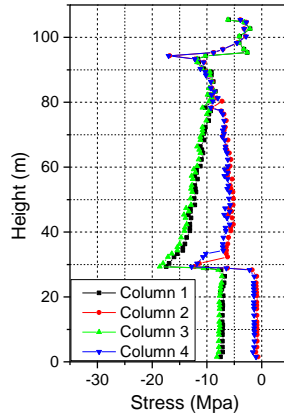
b) Pier No. 15



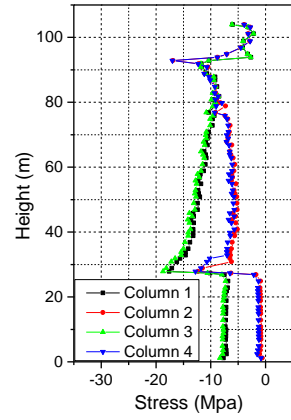
c) Pier No. 16



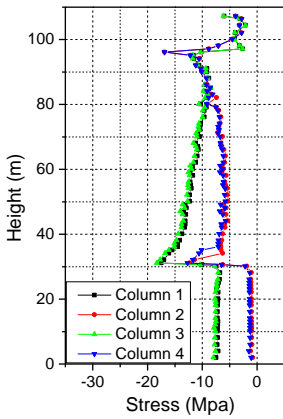
d) Pier No. 17



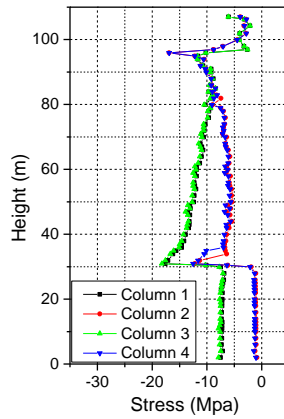
e) Pier No. 18



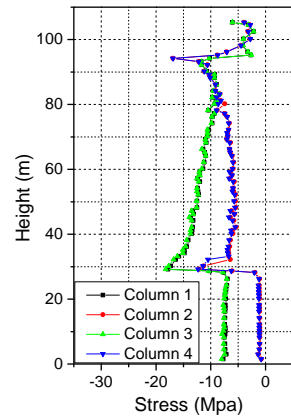
f) Pier No. 19



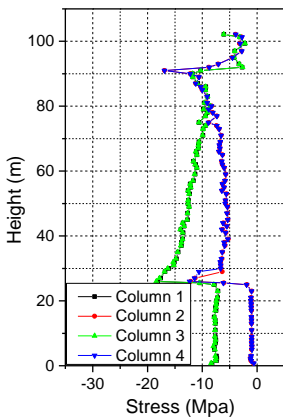
g) Pier No. 20



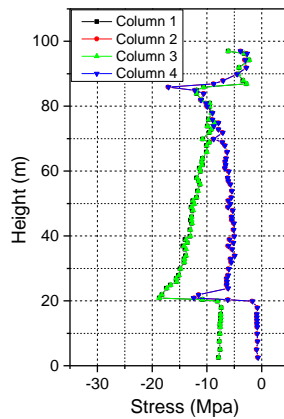
h) Pier No. 21



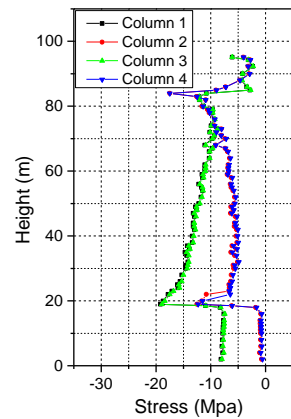
i) Pier No. 22



j) Pier No. 23

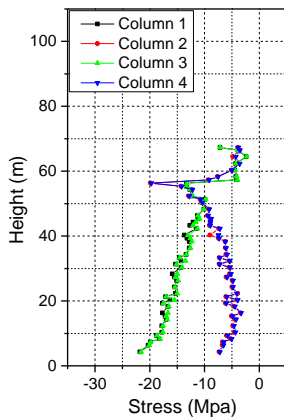


k) Pier No. 24

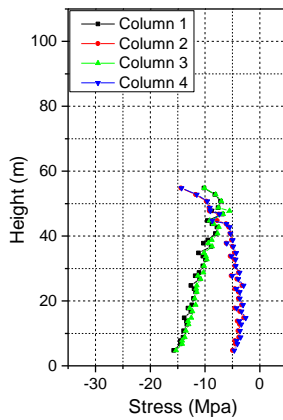


l) Pier No. 25

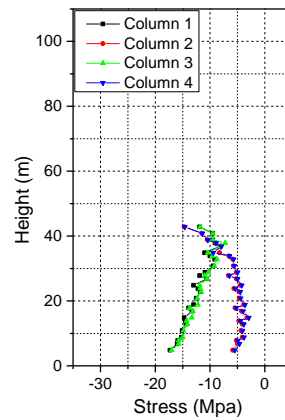
SEISMIC BEHAVIOR OF CONCRETE FILLED STEEL TUBULAR BUILT-UP COLUMNS



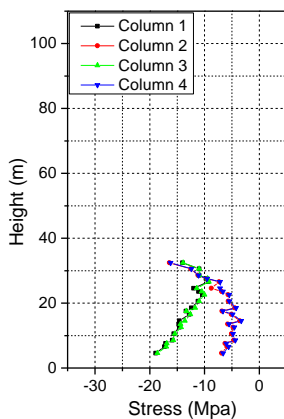
m) Pier No. 26



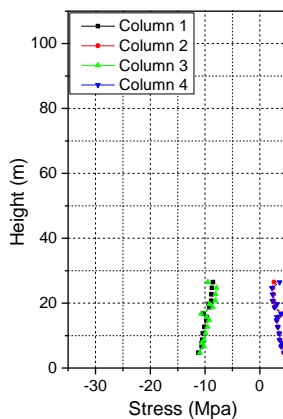
n) Pier No. 27



o) Pier No. 28



p) Pier No. 29



q) Pier No. 30

Fig. 109 Maximum stress distribution at the edge of concrete sections under parallel seismic input direction

From Fig. 108, it is found that though the pier design is symmetric, but the bridge is curved, causes the stress distributions of four columns of each pier are not consistent. Under parallel seismic input direction, which is more inclined to the longitudinal direction of each pier, the stress of column 1 and 3 are larger than column 2 and 4. In other words, in the longitudinal direction of each pier, one of the two columns are the main components.

For the lattice piers, the stress is increased from the top to the bottom. However, the maximum position is not at the pier footing, but at the top of concrete protective layer, where the concrete protective layer share the internal force. Duo to the RC webs share the internal force, the phenomenon is similarly appeared in the composite pier. At the bottom of 30m pier height, the stress of steel tubular sections

are obviously smaller than that on the above lattice zones. Moreover, the stress on the top of composite piers (from pier no. 15 to 26) is also reduced with the length above the hollow steel tubular slant supports in longitudinal direction, which will protective the higher pier under the seismic excitations. However, the stress significantly increases at the position of slant supports, which appears at the both four columns. The stress values are nearly close to the critical cross section at the position of top of RC webs, where with maximum stress.

Overall, the stress distribution is spread more evenly along the piers. Similar phenomenon in the stress at the edge of concrete sections can be found in the Fig. 109. Under parallel seismic input direction, both the stress of steel tubular and concrete sections have not exceeded the materials yielding design values.

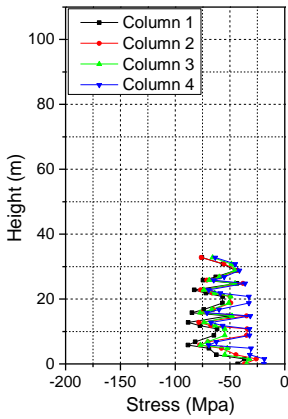
In the same way, the maximum stress at the edge of steel tubular and concrete sections of each piers under perpendicular seismic input direction are presented in Fig. 110 and Fig. 111, respectively. The perpendicular seismic input direction is more inclined to the transverse direction of each pier, therefore, in the transverse direction of each pier, the stresses of one side with two columns (column 1 and 2) are larger than the other side (columns 3 and 4).

From Fig. 110, it is seen that, along the pier height, the stress distribution is similar to that under the parallel seismic input direction, where the value is smaller both on the top and bottom. However, the stress at the slant support is not significantly increased at the position of slant support, because the columns are vertical in the transverse directional view and the seismic input direction is also along perpendicular direction. Along the pier height, the stress distribution presents a jagged shape, where at the position of transverse hollow steel tubular trusses, the value is larger than that at the adjacent positions. On the whole, for the lattice piers, the critical cross sections are at the position of bottom trusses connections. For the composite piers, the critical cross sections are still at the position of top of RC webs. The stress distribution regularities of in-filled concrete is similar to that of steel tubes, see Fig. 111.

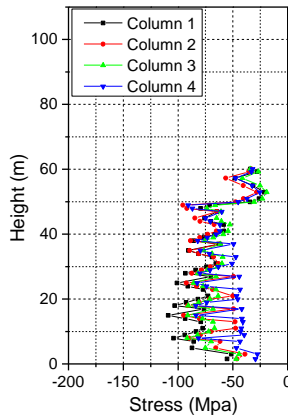
Overall, the stress distribution is spread more evenly along the piers. Under perpendicular seismic input direction, both the stress of steel tubular and concrete sections have not exceeded the materials yielding design values.

Compared with the same pier under different seismic input directions, it is found that for the curved bridge, it is difficult to define the most unfavorable seismic input

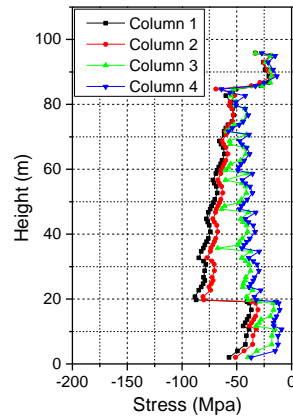
direction. To this end, if we compare the maximum stress of steel tubes of pier no. 15, see Fig. 108(b) and Fig. 110(b), the stress under parallel seismic input direction is larger than that under perpendicular seismic input direction. However, if taken comparison from pier no. 27 to no. 30, see Fig. 108(n)-(q) and Fig. 110(n)-(q). The opposite results can be found, the stress under perpendicular seismic input direction seem more unfavorable. However, with regards to the composite piers, the stress under parallel seismic input direction is slightly larger than that under perpendicular seismic input direction. Therefore, both the stress distribution should be checked under parallel and perpendicular seismic input direction, respectively.



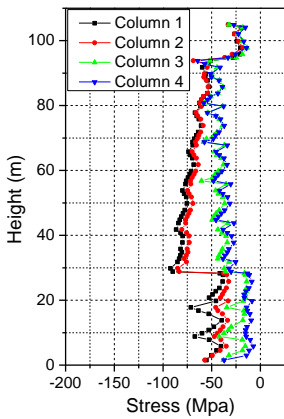
a) Pier No. 14



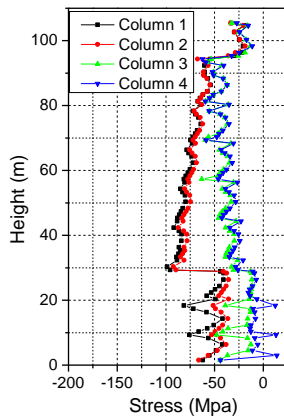
b) Pier No. 15



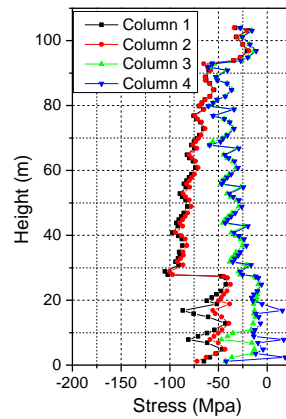
c) Pier No. 16



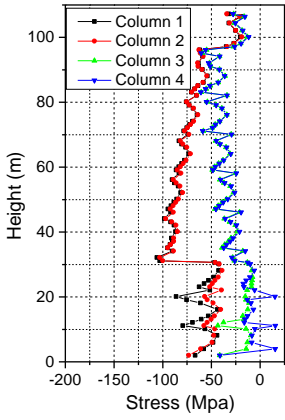
d) Pier No. 17



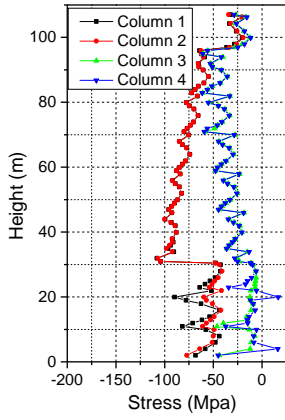
e) Pier No. 18



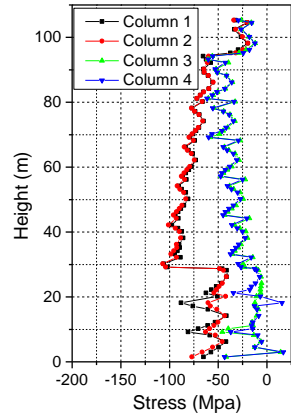
f) Pier No. 19



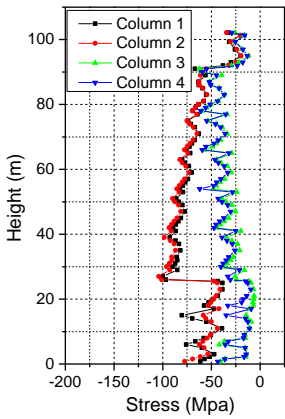
g) Pier No. 20



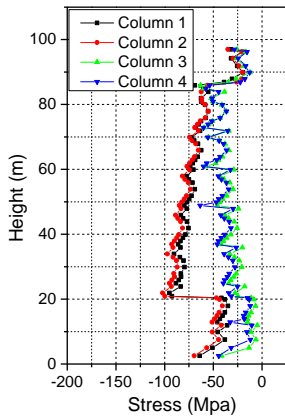
h) Pier No. 21



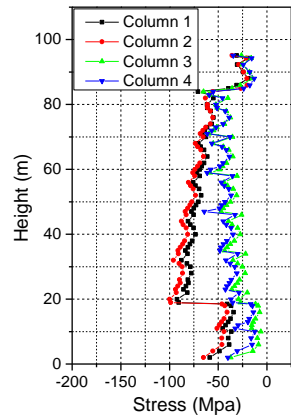
i) Pier No. 22



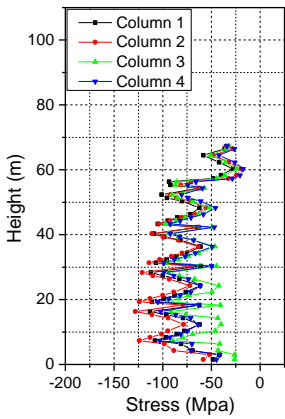
j) Pier No. 23



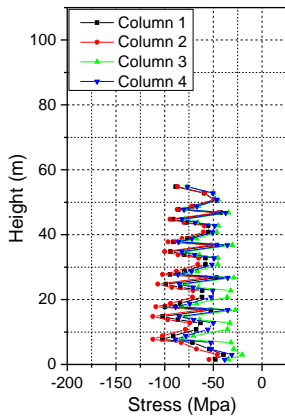
k) Pier No. 24



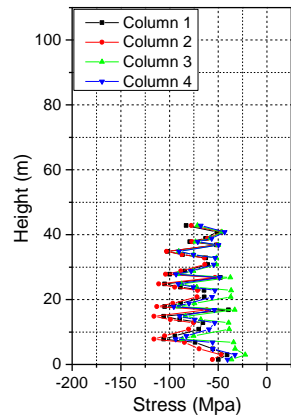
l) Pier No. 25



m) Pier No. 26

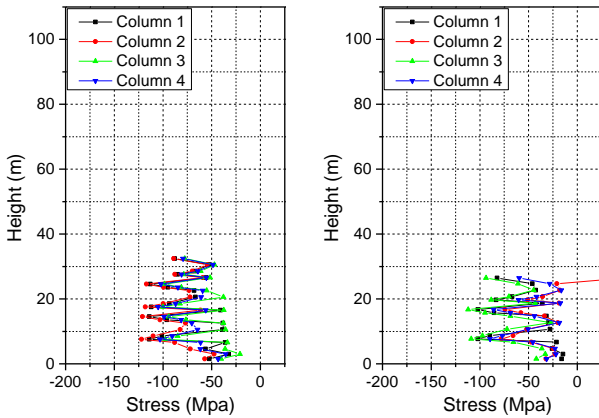


n) Pier No. 27



o) Pier No. 28

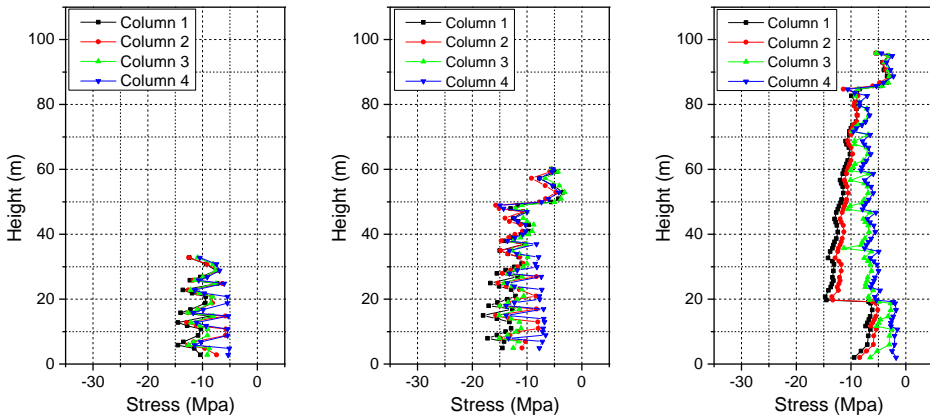
SEISMIC BEHAVIOR OF CONCRETE FILLED STEEL TUBULAR BUILT-UP COLUMNS



p) Pier No. 29

q) Pier No. 30

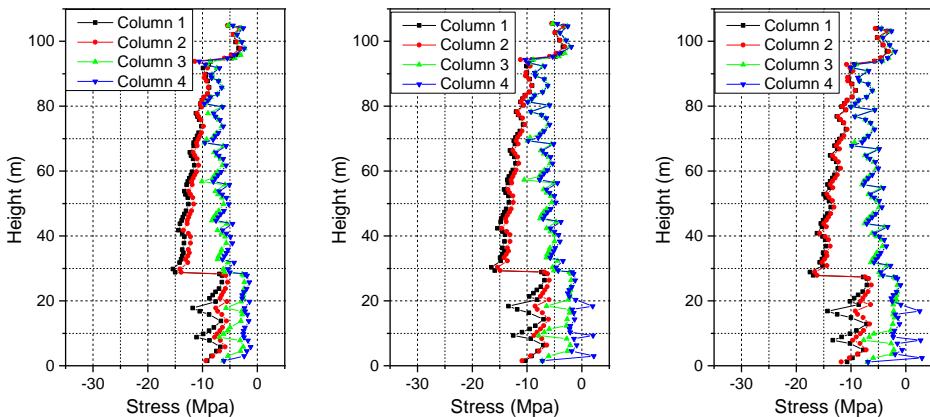
Fig. 110 Maximum stress distribution at the edge of steel tubular sections under perpendicular seismic input direction



a) Pier No. 14

b) Pier No. 15

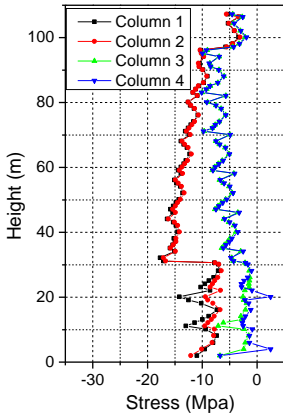
c) Pier No. 16



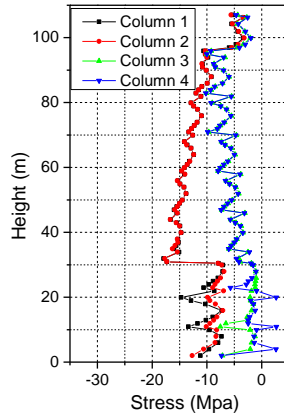
d) Pier No. 17

e) Pier No. 18

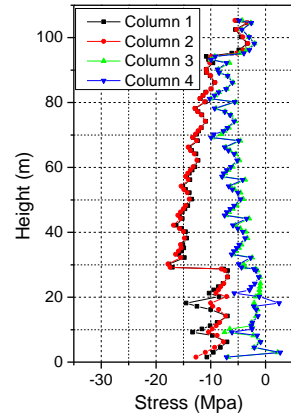
f) Pier No. 19



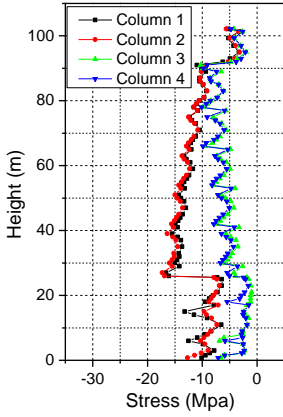
g) Pier No. 20



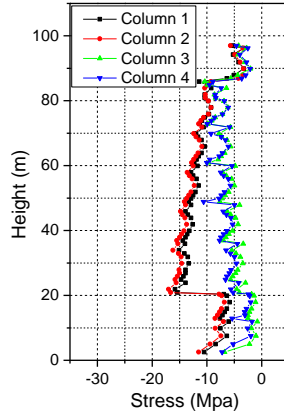
h) Pier No. 21



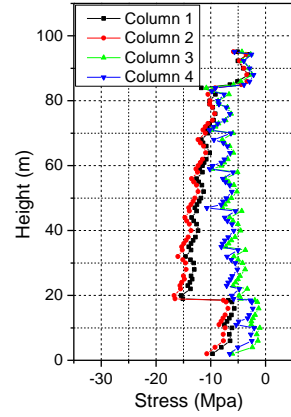
i) Pier No. 22



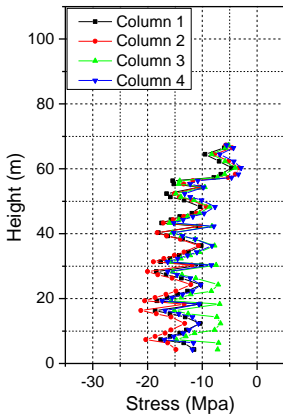
j) Pier No. 23



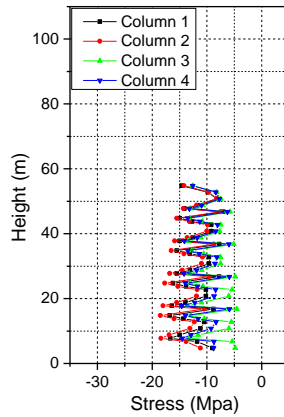
k) Pier No. 24



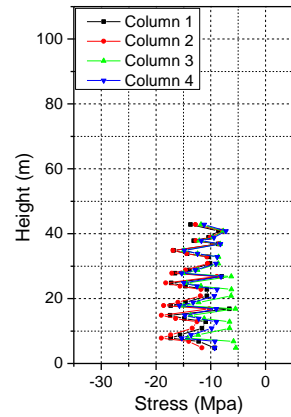
l) Pier No. 25



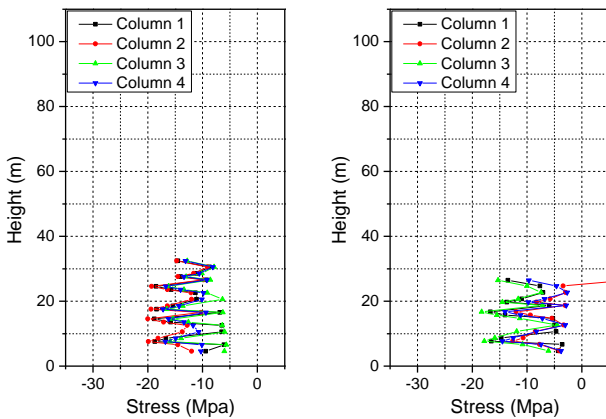
m) Pier No. 26



n) Pier No. 27



o) Pier No. 28



p) Pier No. 29

q) Pier No. 30

Fig. 111 Maximum stress distribution at the edge of concrete sections under perpendicular seismic input direction

5.4.3 Displacement analysis

For bridge with high piers, the displacement on the top of pier is another issue, as to evaluate the bridge’s seismic performance, which may be amplified due to the higher elevation of the pier. In this section, all the piers’ displacement under parallel and perpendicular seismic input direction are summarized in Table 36 and Table 37, respectively. Only one point displacement at the top one of four column are chosen, where the displacement of four column in each pier is near the same. Among that, the calculated results are the displacement in X and Y direction under global coordinate. According to the angle θ between local coordinate of each pier and the global coordinate, the converted displacement under longitudinal and transverse direction can be got through Eq. (103) and Eq. (104).

$$\text{Longitudinal direction: } X \cos \theta - Y \sin \theta \tag{103}$$

$$\text{Transverse direction: } X \sin \theta + Y \cos \theta \tag{104}$$

According to Guide to Design and Construction Technology of Road Steel Tube Concrete Bridge (Sichuan Provincial Communications Department Highway Planning Survey and Design Institute, China, 2008), horizontal displacement on the top of piers should not exceed 1/300 elevation of piers under design response spectrum. It can be seen that, except the pier no.15 under parallel seismic input

direction, all the piers meet the specification and have an adequate displacement capacities.

For a more clearly investigation, the displacement distribution are shown in Fig. 112 and Fig. 113. It is found that, under parallel seismic input direction, the displacement of high piers are in harmony, and the value is more than doubling of that in the lower piers, illustrating that the high pier have a favorable deformation capacities and ductility. Under perpendicular seismic input direction, the displacement distribution is non-uniform, higher pier with larger displacement.

No.	X direction (mm)	Y direction (mm)	Angle θ (°)	Longitudinal direction (mm)	Transverse direction (mm)	Displacement limitation (mm)
14	99	-22	7.10	101	-9	114
15	230	-54	9.62	236	-15	200
16	225	-73	12.80	236	-21	319
17	222	-87	15.96	237	-22	350
18	219	-98	19.15	239	-20	352
19	215	-107	22.32	239	-17	347
20	211	-114	25.50	240	-12	357
21	207	-122	28.65	240	-8	357
22	202	-131	31.80	241	-5	351
23	197	-141	34.99	242	-2	340
24	192	-149	38.14	243	1	323
25	186	-157	41.31	243	5	317
26	179	-161	43.93	241	9	224
27	117	-104	45.00	156	9	183
28	97	-88	45.24	131	7	143
29	73	-67	44.46	100	3	109
30	43	-45	42.16	62	-4	89

Table 36

Maximum displacement at the top of pier under parallel seismic input direction

SEISMIC BEHAVIOR OF CONCRETE FILLED STEEL TUBULAR BUILT-UP COLUMNS

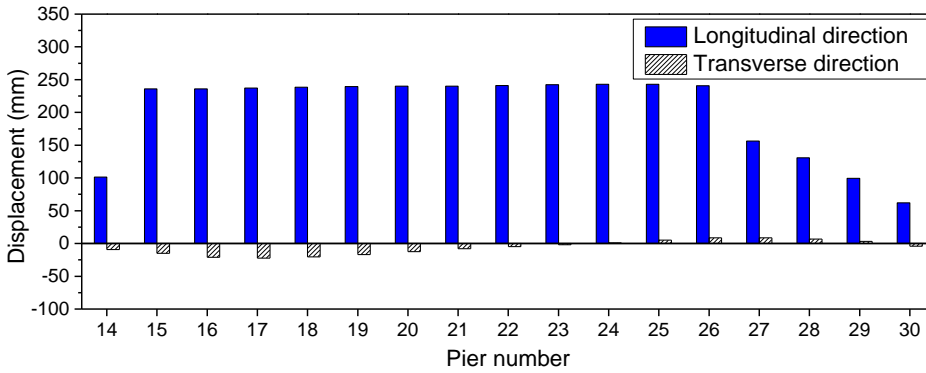


Fig. 112 Maximum displacement distribution under parallel seismic input direction

No.	X direction (mm)	Y direction (mm)	Angle (°)	Longitudinal direction (mm)	Transverse direction (mm)	Displacement limitation (mm)
14	32	43	7.10	27	47	114
15	67	68	9.62	54	79	200
16	72	101	12.80	48	114	319
17	81	129	15.96	42	147	350
18	89	153	19.15	34	173	352
19	97	172	22.32	25	196	347
20	104	187	25.50	13	214	357
21	107	196	28.65	0	223	357
22	102	190	31.80	-13	215	351
23	88	172	34.99	-26	191	340
24	76	154	38.14	-36	168	323
25	71	143	41.31	-42	154	317
26	65	133	43.93	-45	141	224
27	60	103	45.00	-30	115	183
28	50	79	45.24	-21	91	143
29	-45	59	44.46	-73	11	109
30	-31	38	42.16	-48	7	89

Table 37

Maximum displacement at the top of pier under perpendicular seismic input direction

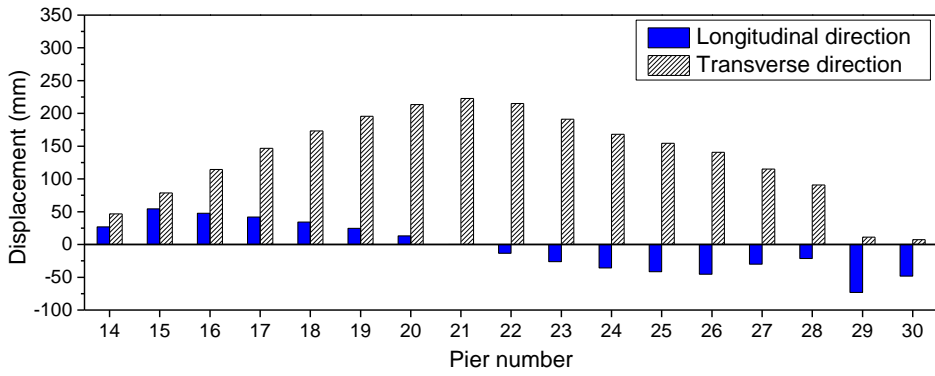


Fig. 113 Maximum displacement distribution under perpendicular seismic input direction

6. SHAKING TABLE TEST

6.1. Introduction

The innovative structure, complex mechanical characteristics and lack of similar reference experiences in literatures, reveal the necessity of experimental test of this new structure. Although the design criteria is technically and economically valid, a number of problems required information that could be obtained only from suitable experimental work, especially in structural dynamic analysis. With the development of experimental technology and equipment, more multi-shaking table systems have been constructed and adopted for investigating the seismic behavior of complex structures in the world. Compared with single shake table system, which is usually suitable for the building model test and a large number of tests have been reported in the literatures, the multi-shaking table system is more suitable for the multi-span structures, such as rail and road bridges, pipelines and electrical distribution, high rise building models, underground rail system, etc.

In order to investigate the seismic response of this new composite structures, took Ganhaizi Bridge as prototype, a 1:8 scale specimen with two spans and three lattice high piers was designed for multi-shaking tables test. The experimental campaign was designed, manufactured and finally conducted in July 2012, depending on triple bi-axial shaking tables system of Fuzhou University, China.

In this chapter, the author presented the bridge model design, manufacture, testing procedure and test results. Seismic performance of the specimen under transverse excitation, longitudinal excitation, and bi-directional excitation were investigated, respectively. In addition, the corresponding finite element simulations, using OpenSees, were carried out and the accuracy was verified. On the basis of numerical results, the plastic characteristics where the test can't achieved were predicted. Besides, influence of ground motions to this type of structure was also discussed.

6.2. Specimen Design

6.2.1 Similitude criteria theory

The dynamic test of any structures is governed by an equilibrium balance of the time-dependent forces acting on the structures. Different with the test model under static loadings, the gravity induced stress plays an important role in dynamic test and affect response of the model. Therefore, the similitude criteria depends on not only the geometric, material properties of the structures, but also the type of loading, such as intensity and durable time of the seismic excitations.

The relationships between test model and prototype can also be derived through Buckingham’s Pi Theorem (Harris & Sabnis, 1999), where the all physical behavior parameters can be expressed by three independent quantities in dynamic analysis, which are *length L*, *force F* and *time T*. The similitude criteria could also be understand thought the unit consistency of each physical parameter.

A summary of the scale factors obtained from similitude considerations under the earthquake loading is shown in Table 38 (Krawinkler et al., 1978).

It can be found that true replica models imply simultaneous duplication of inertial, gravitational and restoring forces. However, such model is impossible to manufacture because of the severe restrictions imposed on the model material properties, especially in the requirement of mass density. Therefore, artificial mass simulation is usually adopted in the test practice. Both lumped mass and distributed mass simulation can be set in the test model according to different test condition and aim.

Classify	Quantity	Dimension	Scale factors	
			True replica model	Artificial mass simulation
Loading	Force, Q	F	$S_E S_I^2$	$S_E S_I^2$
	Pressure, q	FL^{-2}	S_E	S_E
	Acceleration, a	LT^{-2}	1	1
	Gravitational acceleration, g	LT^{-2}	1	1
	Velocity, v	LT^{-1}	$S_I^{1/2}$	$S_I^{1/2}$
	Time, t	T	$S_I^{1/2}$	$S_I^{1/2}$

Geometry	Linear dimension, l	L	S_l	S_l
	Displacement, δ	L	S_l	S_l
	Frequency, ω	T^{-1}	$S_l^{-1/2}$	$S_l^{-1/2}$
Material properties	Modulus, E	FL^{-2}	S_E	S_E
	Stress, σ	FL^{-2}	S_E	S_E
	Strain, ε	-	1	1
	Poisson's ratio, ν	-	1	1
	Mass density, ρ	$FL^{-4}T^2$	S_E / S_l	$(gpl / E)_m / (gpl / E)_p$
	Energy, EN	FL	$S_E S_l^3$	$S_E S_l^3$

Table 38

Summary of scale factors for earthquake response of structures

6.2.2 Test device

The main experimental device is the three bi-axial shaking table array system for earthquake simulation at College of Civil Engineering, Fuzhou University, China, shown in Fig. 114.



Fig. 114 Panorama of the three bi-axial shaking table array system

The system consists of three biaxial vibration tables. A medium larger one is a fixed horizontal bidirectional vibration table with size of $4m \times 4m$. Two movable tables with size of $2.5m \times 2.5m$ are located on each side, see Fig. 115. All three tables are located along line direction in foundation pit with size of $11m \times 32m$, guided in the horizontal plane by hydrostatic pad bearings, and the top surfaces are at the same level with lab floor. All tables have two Y direction actuator to react unwanted

yaw moments and a single X axial actuator. The X actuator for the central table is mounted under the table to allow the moveable table to operate next to the central table. The small table to large table with 1.35m edge to edge and maximum 19.5m between the centerlines. To provide high overturning capability, the table is pre-loaded on to the pad bearings by air stroke actuators, see Fig. 116.

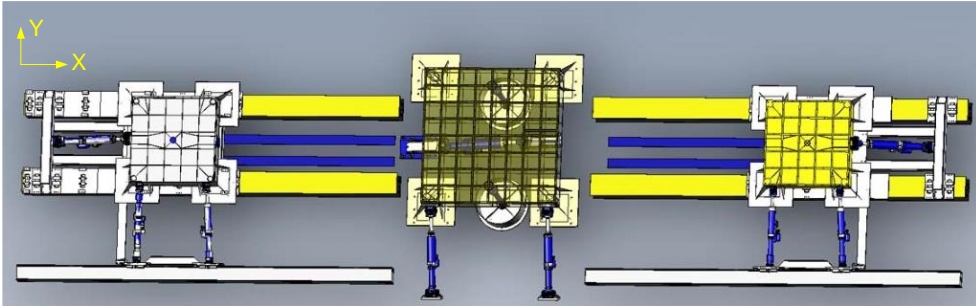


Fig. 115 Schematic drawings of the system on top view

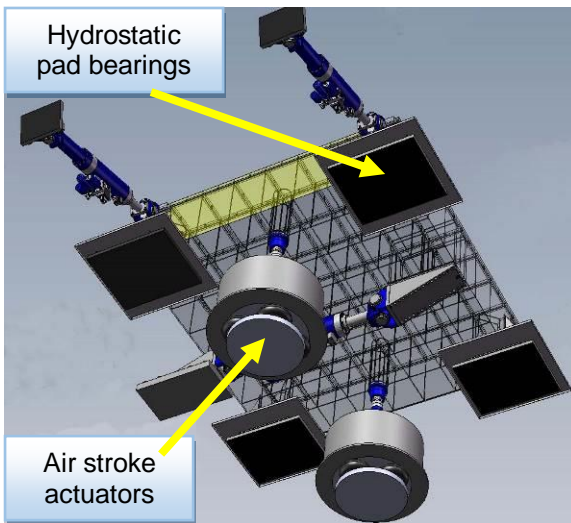


Fig. 116 Schematic drawings of the table on bottom view

A summary of the overall system capacity is condensed in Table 39.

Degree of freedom	3
Maximum payload	22t for large table, 10t for small table
Overturning moment	600kNm for large table, 110kNm for small table
Displacement X and Y	500mm
Velocity X	1500mm/sec
Velocity Y (small tables)	1500mm/sec

Velocity Y (large table)	1000mm/sec
Acceleration X	1.5g with maximum payload
Acceleration Y	1.2g with maximum payload
Identified frequency	From 0.1Hz to 50Hz

Table 39

Summary of equipment specification

6.2.3 Design parameters control

The following consideration were made in design the specimen model (Harris and Sabnis, 1999):

- According to the experimental purpose, meet similitude criteria requirement, correct reproduction of the characteristics of the structure with respect to the established goals of the model.
- Limitations imposed by the availability of suitable materials, skilled personnel, laboratory space, capacity of the testing equipment, etc.
- Limit funds available for the test.

For accurately simulating the geometrical characteristics of Ganhaizi Bridge, and have a understand about the key issues, such as whether some interconnect components is the weak link in the internal force, pier deformation caused by the $P-\Delta$ effects, distribution of internal force along the pier height, and so on. The highest no. 20 pier with 107m height is chosen as the pier prototype. Regards the girder, consider the length of the laboratory space and the hoisting conditions during specimen manufacture, the total length of girder is determined to 13.63m. Meanwhile, considering difficult to pour concrete into steel tubes for large scale proportion model in the proceeding of fabrication. Finally, the scale of the specimen is 1:8 to the prototype, with two span and three piers, specimen height is 13.9m. The specimen is maintained the same configuration as the prototype, expect some details will be adjusted due to impossible manufactured according to the 1:8 scale ratio. Consider the safety during testing and the difficulty of fixing mass on the circular steel tubes, extra mass is not attached. Some steel rings will be added on the structures used during hoisting specimen. Similarly, some components which are not the mainly structures or stress members, such as hollow trusses in the transverse connecting of the pier will be neglected. It is expected not to affect the test result, but save steel tubes and promote the speed of specimen manufacture. Elevation drawing of specimen is presented in Fig. 117. Similar materials to the real

bridge (prototype) were used for specimen. The detailed geometry of the girder and pier are illustrated in Fig. 118 and Fig. 119, respectively. In Fig. 120, the reinforcement of RC webs at the bottom of the pier is presented, where the same reinforcement ratio 2.6% with the prototype are taken into account.

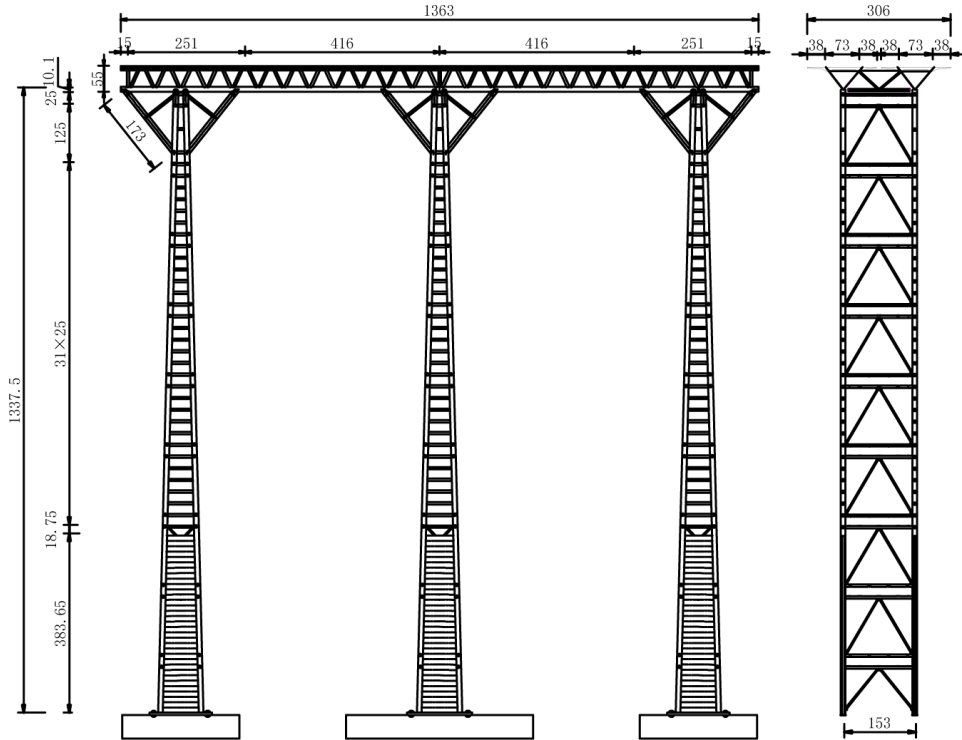
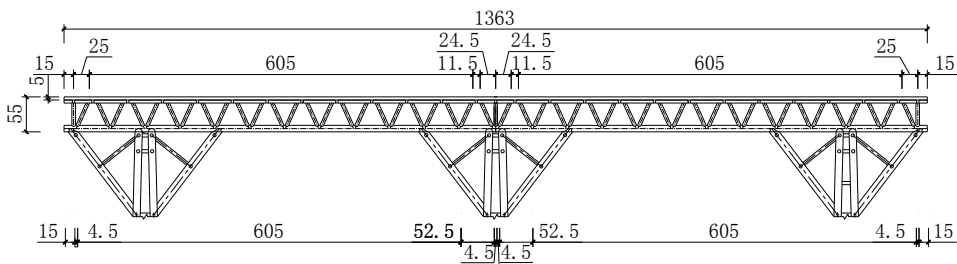
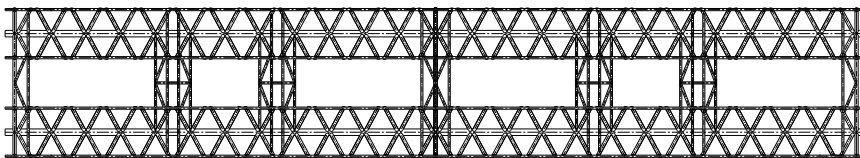


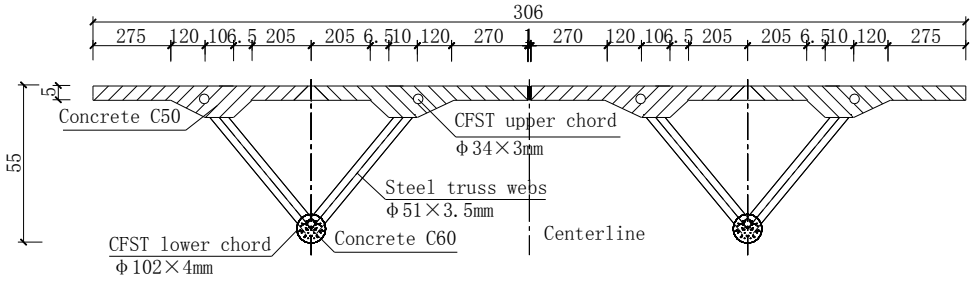
Fig. 117 Elevation layout of the specimen (unit: cm)



a) Elevation layout of girder



b) Plan layout of girder



c) Cross section of girder
 Fig. 118 The drawing of girder (unit: cm)

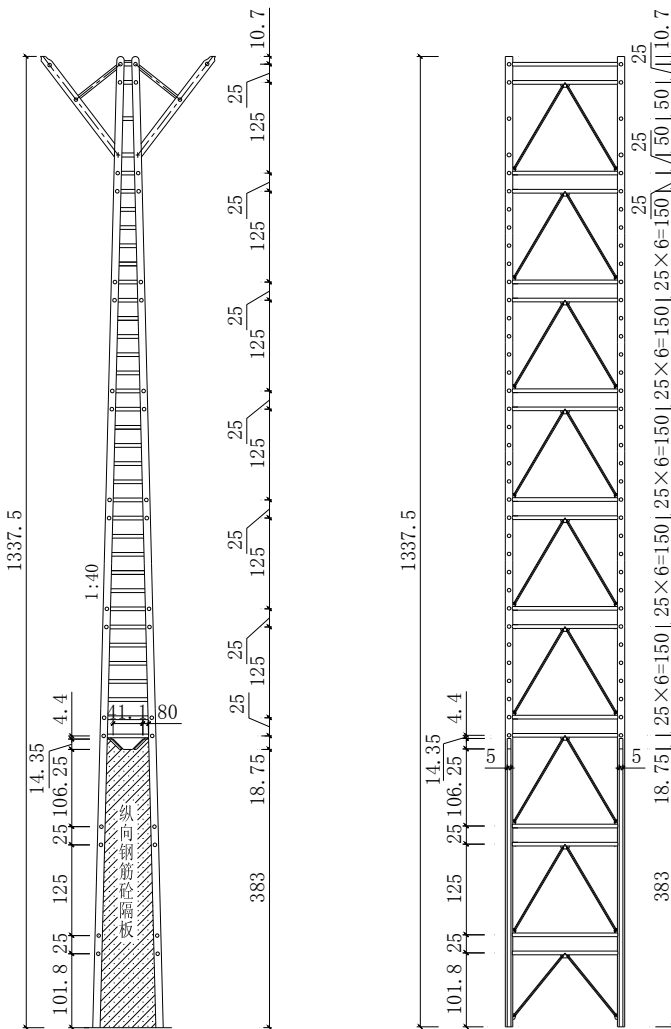


Fig. 119 Elevation layout of pier (unit: cm)

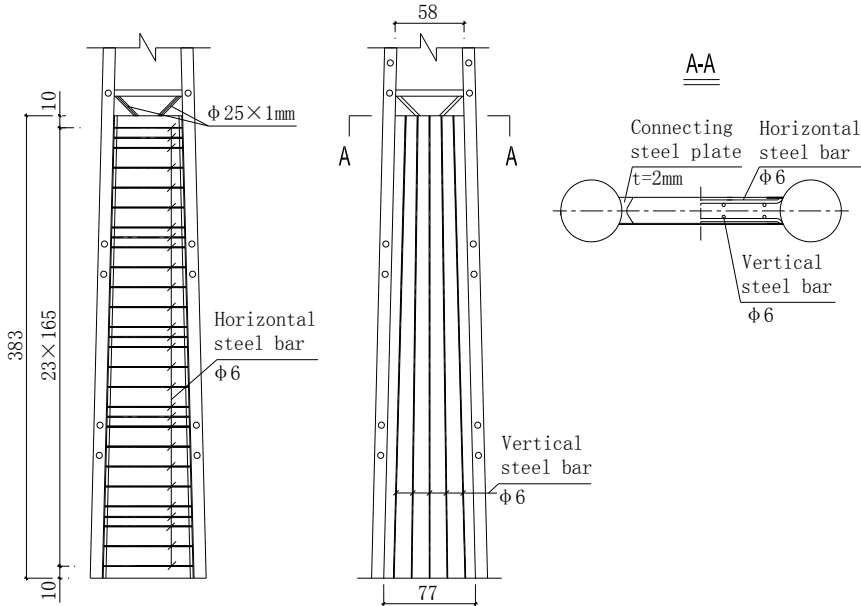


Fig. 120 Reinforcement of the RC webs (unit: cm)

6.2.4 Specimen manufacture

The specimen was divided into several parts to refabricate and splice. Each column divided into three segments, after pouring concrete into the hollow steel tubes, the joints between columns were connected through welding another steel tubes with diameter slightly larger than that of the column, then grouting the interspace of the joints. After three columns were connected respectively, it is standing-up and adjust position beside the shaking table system. The girder was lifted up and connected with the columns. Finally, the specimen was hoisted integrally to the countertops, the footing was precisely connected to the tables through high-strength bolts. The total mass is 20.9t, within the requirement of system. The procedure of manufacture are shown in a group of photo, as illustrated in Fig. 121.



a) Welding steel skeleton

b) Pouring deck concrete

c) Girder finished



d) Segment of column



e) Positioning of column



f) Strain gauges layout in RC web



g) Conservation of RC web



h) Grouting joint of column



i) Lifting column



j) Lifting girder



k) Welding girder and columns



l) Welding slant supports



m) Hoisting integrally



n) Specimen finished

Fig. 121 Specimen manufacture

6.3. Test Instruments and Setup

Piezoelectric accelerometers, which manufactured by Donghua Testing Technology co. Ltd (Donghua Testing Technology co. Ltd), were adopt in this test, see Fig. 122(a)-(b). The sensitivity of these devices is near 0.3 V/ms^{-2} and the maximum range is $\pm 20 \text{ m/s}^{-2}$, the weight is 550g, the size $63 \times 63 \times 63 \text{ mm}$ with a frequency range of 0.25–80 Hz, and the output load resistance 10000 k Ω .

The industrial Camera Prosilica GC650, with a sample rate of 66 Hz, manufactured by Allied Vision Technologies (Allied Vision Technologies), has been used to measure absolute displacements on the top of pier and girder, see Fig. 122(c)-(f). Three steps are set before recording displacement data: 1) Use the Prosilica GC650 Industrial Camera is to connect the Ethernet wire to the computer and run the software Measurement & Automation of National Instrument, check the hardware property works and adjust the zooming pointing the camera at a target which is a black circle on a white background; 2) Use software Vision Assistant, acquire and calibrate the picture previously focused. Then choose the coordinate system, define the diameter of the circular target. After drawing an outer circle on the picture around the target for defining the displacement range and its accuracy, save the script; 3) Use LabVIEW software and open the script saved, set the time interval to be recorded and the sample rate (66 Hz), ready to record displacement data.

The strain gauges used in this research work, are manufactured by ZheJiang Huangyang Testing Instrument Factory of Beijing (ZheJiang Huangyang Testing Instrument Factory), including both for steel and concrete, see Fig. 122(g).

The Acquisition Data System used in this research work is manufactured by DEWETRON Elektronische Messgerate Gesellschaft m.b.H., Austria (DEWETRON Elektronische Messgerate Gesellschaft m.b.H), see Fig. 122(h). The hardware system is composed by two mainframes DEWE-51-PCI-64, for a total of 128 channels; connected to the computer by a MAGMA Expressed Card 54/slot. The software package used is DEWEsoft 7.0.3, a powerful tool to synchronize, acquire, record, processing and analyze massive quantities of data. The sample rate used to record the data is 512 Hz, for all signal processes in both test series, accordingly with the sample rate for the input loads of the shaking table system.



a) Accelerometers on the column



b) Piezoelectric acceleration sensor



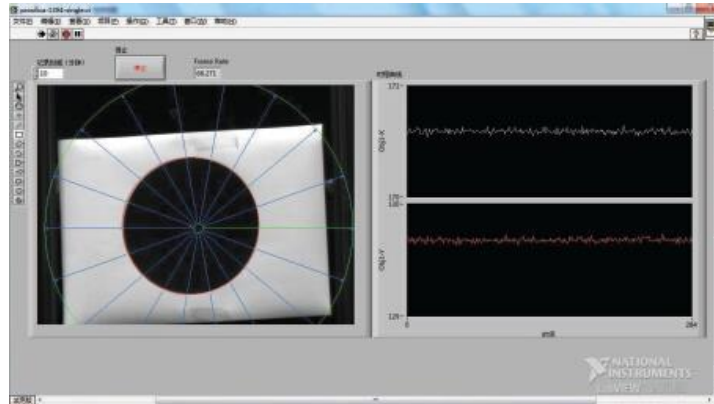
c) Displacement measured point on the deck



d) Displacement measured point on the column



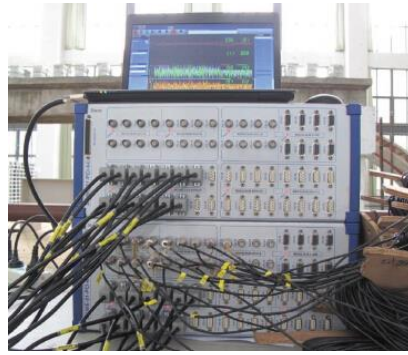
e) Industrial camera



f) Recording of the data with LabVIEW



g) Strain gauges on the top of RC web
Fig. 122 Details of instruments



h) Acquisition data system

Specimen and countertops were instrumented with 30 accelerometers, 8 displacement transducers and 60 strain gages, including longitudinal, transverse and vertical directions. Accelerometers were located at the concerned position, such as top of deck, columns center, and connecting positions with slant support and RC web. Each countertop is also located accelerometers for verifying whether export acceleration is consistent with the import value. Displacement transducers were installed at the top of deck and columns where the maximum displacement is predicted. High-speed camera was adopted to measure displacements. As stress analysis in last chapter, stress concentration were appeared at the columns where stiffness varies, strain gages were mainly located at the bottom of columns and RC web, as well as connecting slant support and RC web. The instrumentation arrangement details are presented in Fig. 123.

In order to make sure that the specimen has a similar behavior to the prototype and consider test limitation and the similitude criteria theory as mentioned above, three independent quantities *length* L , *density* ρ and *modulus* E are chosen as basic parameters in this experiment, rest quantities can be expressed through similitude criteria, list in Table 40. It consists two scale ratio relationships, one is for the test termed as no mass, the other is for the further FE analysis termed as full mass. Full mass model means keep the density of specimen is 8 times to the prototype, which will cause the strain of specimen equal to prototype but can't achieved in the test. The plastic hinge location will be predicted through the value of stress at extreme edge of steel tubes on the columns, that can be achieve through FE analysis with full mass model. It is pointed out that the acceleration relationship in the test is supposed to 8 times to the prototype, however, it will exceed the system's capacity with the maximum acceleration payload. Therefore, the input acceleration intensity in the test is kept equal to the prototype, then displacement response is 1/64 to the prototype, which equal to acceleration towards quadratic integral to the time.

Material properties in different parts of specimen were measured respectively before the test. The results are summarized in Table 41, where E_s is steel elastic modulus, f_{sy} is steel yield strength and f_{su} is steel ultimate strength; E_c is concrete elastic modulus and f_{cu} is concrete cube compressive strength.

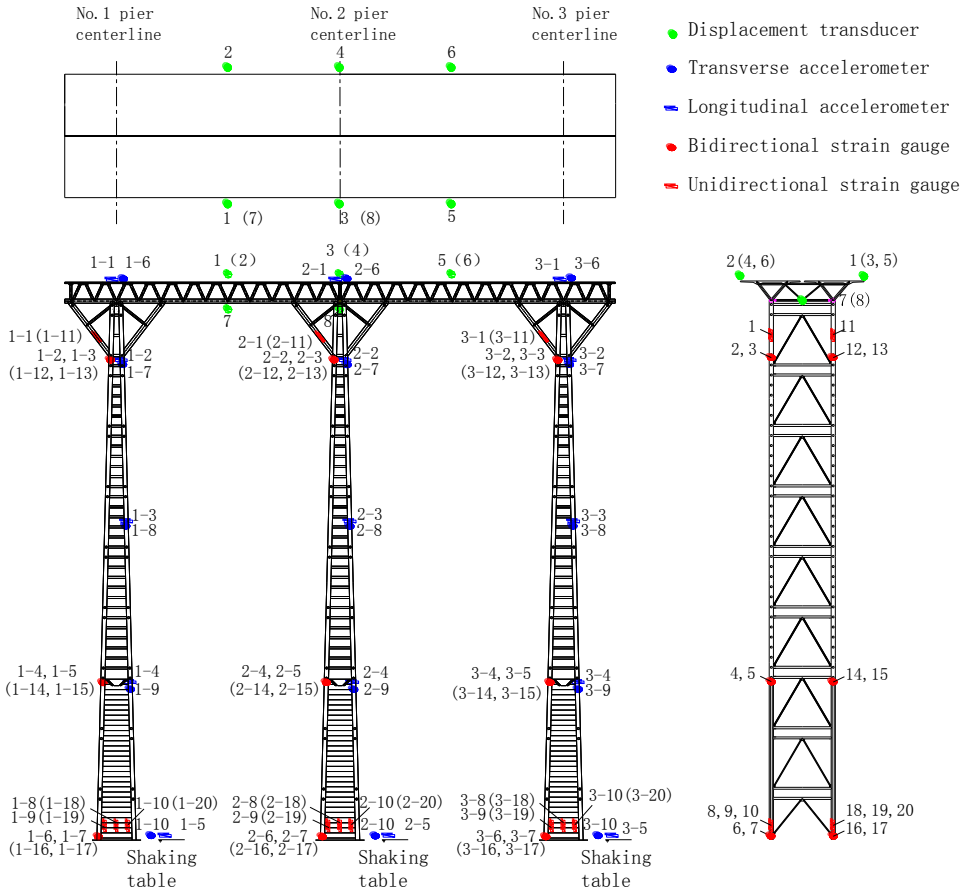


Fig. 123 View of instrument arrangement details

Quantity	Dimension	Scaling law	Scale factors	
			No mass (For specimen test)	Full mass (For FEM analysis)
Linear length	S_l	$[L]$	$S_l = 1/8$	$S_l = 1/8$
Displacement	S_δ	$[L]$	$S_l = S_a S_t^2 = 1/64$	$S_l = 1/8$
Modulus	S_E	$[E]$	$S_E = 1$	$S_E = 1$
Vertical strain	S_ϵ	-	$S_\epsilon = 1/8$	$S_\epsilon = 1$
Density	S_ρ	$[\rho]$	$S_\rho = 1$	$S_\rho = 8$
Axial force	S_N	$[EL^2]$	$S_N = 1/256$	$S_N = 1/64$
Bending moment	S_M	$[EL^3]$	$S_M = 1/2048$	$S_M = 1/256$
Acceleration	S_a	$[E\rho^{-1}L^{-1}]$	$S_a = 1$	$S_a = 1$
Frequency	S_ω	$[E^{0.5}\rho^{-0.5}L^{-1}]$	$S_\omega = 8$	$S_\omega = 2.828$
Time	S_T	$[E^{-0.5}\rho^{0.5}L]$	$S_T = 1/8$	$S_T = 1/2.828$
Damping	S_ζ	-	$S_\zeta = 1$	$S_\zeta = 1$

Table 40
Similitude relation of quantities

Steel tube	E_s (MPa)	f_{sy} (MPa)	f_{su} (MPa)	Concrete	E_c (MPa)	f_{cu} (MPa)
Steel web	2.00×10^5	314	535	Bottom chord	2.71×10^4	37.1
Bottom chord	2.00×10^5	364	501	Deck	3.96×10^4	52.7
Column	2.02×10^5	375	465	Column	3.23×10^4	42.3
Truss tubes	2.03×10^5	388	502	RC web	3.15×10^4	24.4
Slant support	2.00×10^5	380	497			

Table 41
Material properties

Due to lack of seismic waves at the bridge site, seismic excitation has been carried out by using artificial waves based on JTG/T B02-01-2008 (Ministry of Transport of the People's Republic of China, 2008) and generated according to the design response spectrum as mentioned in last chapter. The design response spectrum is

shown in Fig. 105. The relationship between power spectra and response spectrum can be expressed by Maharaj (Maharaj, 1978) as Eq. (105),

$$S_{\ddot{x}_0}(\omega) = \frac{\zeta}{\pi\omega} S_a^2(\omega) / \left\{ -\ln \left[\frac{-\pi}{\omega T} (1-r) \right] \right\} \quad (105)$$

Then, the artificially seismic wave is generated through trigonometric series model in Eq. (106) (Chen et al, 1981),

$$\ddot{x}_a(t) = I(t) \cdot \ddot{x}_0(t) = I(t) \cdot \sum_{k=1}^N A(\omega_k) \sin(\omega_k t + \varphi_k) \quad (106)$$

Where, $\ddot{x}_0(t)$ is stationary Gaussian process, $S_{\ddot{x}_0}(\omega_k)$ is the power spectra, φ_k is random phase angle, ω_k is circular frequency. The artificial seismic waves are made up of these circular frequency trigonometric series superposition; $A(\omega_k)$ is amplitude, expressed by Eq. (107),

$$A^2(\omega_k) = 4S_{\ddot{x}_0}(\omega_k) \cdot \Delta\omega \quad (107)$$

N is the partition points of the calculated response spectrum or the power spectrum in frequency domain. The precision improves as N increased. In this work, frequency domain divides into 200 points, means N is 200; $I(t)$ is a determined function of time, constituted by three segment curves, see Fig. 124, and the parameter is determined by Table 42, here the during time simulation adopts 30s.

The artificial seismic excitations fitted from design spectrum for the prototype and specimen are shown in Fig. 125 and Fig. 126, respectively. Both the peak ground acceleration (PGA) are 0.16g. In Fig. 126, the same waveform and amplitude as to Fig. 125, only input duration is compressed to 1/8 according to similitude criteria.

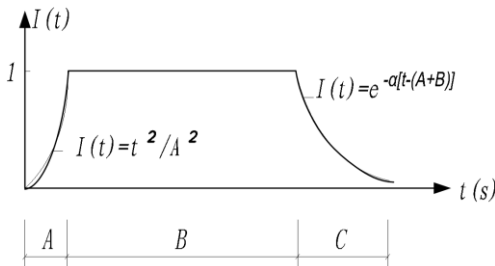


Fig. 124 Relationship between I and t

Parameters	5s	10s	20s	30s
A	0.5	1	2	3
B	3.5	6	14	22
C	1	3	4	5
α	1.5	1.15	0.8	0.64

Table 42
Parameters with different durable time

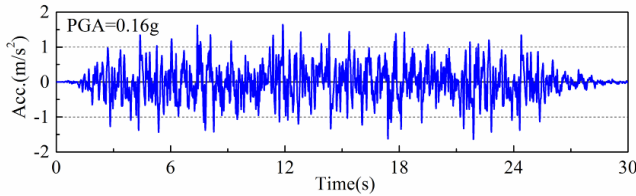


Fig. 125 Artificial seismic excitation for prototype

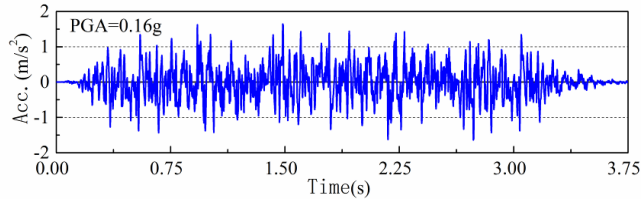


Fig. 126 Artificial seismic excitation for specimen

Fig. 127 presents normalized response spectrum of seismic excitations. Dash lines are the fundamental period of prototype and specimen by FEM calculation. It is found that, according to the similitude criteria, both of structure under fundamental period are correspond to the design spectrum and PGA are also accordance. Therefore, the results shows that the artificial seismic excitations could be fitted to the test as input seismic excitation, and in theoretical analysis, the response of specimen can reflect to the prototype.

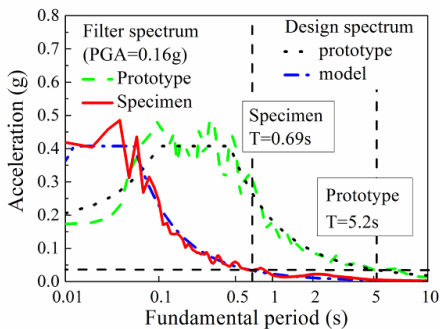


Fig. 127 Normalized response spectrum

6.4. Test Program

During testing, the natural frequencies of longitudinal (in plane) and transverse (out-of-plane) direction were firstly identified through the response under a low level random excitation (white noise excitation). Then the input excitations were adjusted from $PGA=0.05g$ to the maximum intensity countertop can afford. Since the maximum overturning moment for large table is $600kNm$, while for small one is $110kNm$, for keeping the normal operation and safety, the final test procedure was shown in Table 43. In order to investigate the effect of different input direction of seismic excitations, loading cases of longitudinal input, transverse input and combination input of both were considered. The maximum PGA in longitudinal, transverse and bi-directional excitation is $0.50g$, $0.22g$ and $0.22g$, respectively.

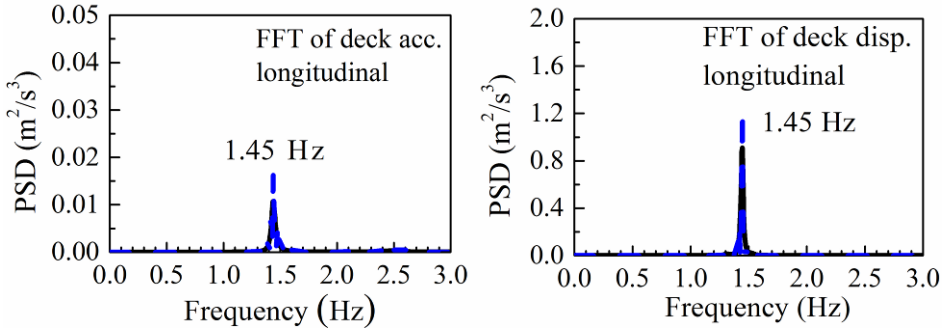
Step	PGA (g)	Input direction	Step	PGA (g)	Input direction
1	0.05	Longitudinal	14	0.20	Transverse
2	0.05	Transverse	15	0.20	Bi-directional
3	0.05	Bi-directional	16	0.22	Longitudinal
4	0.10	Longitudinal	17	0.22	Transverse
5	0.10	Transverse	18	0.22	Bi-directional
6	0.10	Bi-directional	19	0.24	Longitudinal
7	0.15	Longitudinal	20	0.26	Longitudinal
8	0.15	Transverse	21	0.28	Longitudinal
9	0.15	Bi-directional	22	0.30	Longitudinal
10	0.16	Longitudinal	23	0.35	Longitudinal
11	0.16	Transverse	24	0.40	Longitudinal
12	0.16	Bi-directional	25	0.45	Longitudinal
13	0.20	Longitudinal	26	0.50	Longitudinal

Table 43 Test procedure

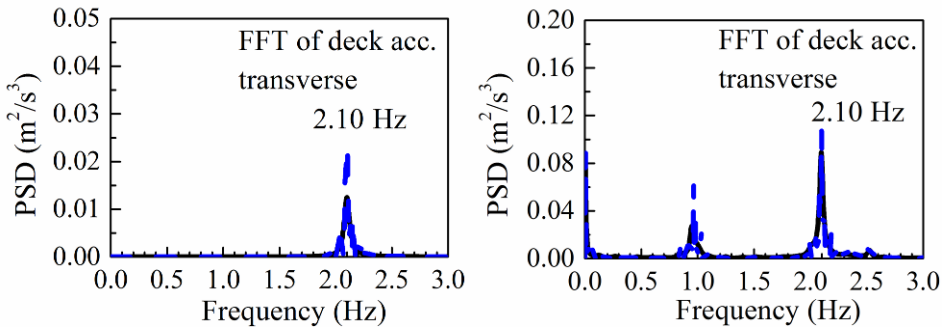
6.5. Dynamic Characteristics Analysis

After white noise excitation, the fundamental frequency of specimen is identified through power spectral analysis by fast Fourier transform (FFT). Fig. 128 presents the power spectral analysis under longitudinal, transverse and bi-directional excitations, respectively. It can be seen that regardless the acceleration power spectral or displacement power spectral, longitudinal frequency (the first order) and

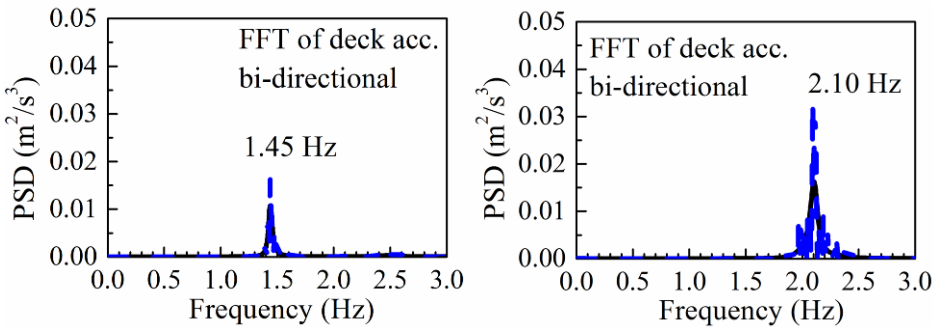
transverse frequency (the second order) are always 1.45Hz and 2.10Hz, respectively.



a) Under longitudinal excitation



b) Under transverse excitation



c) Under bi-directional excitation

Fig. 128 Power spectral analysis

Damping ratios of n^{th} mode ζ_n were calculated using power spectral analysis results, though the half-power bandwidth method (Kikunaga and Arakawa, 2012), see Fig. 129 and Eq. (108).

$$\zeta_n = \frac{f_n}{2\Delta f} \tag{108}$$

Where f_n shows natural frequency in the n^{th} mode, Δf shows the interval of frequency which corresponds to $1/\sqrt{2}$ times the amplitude of the peak.

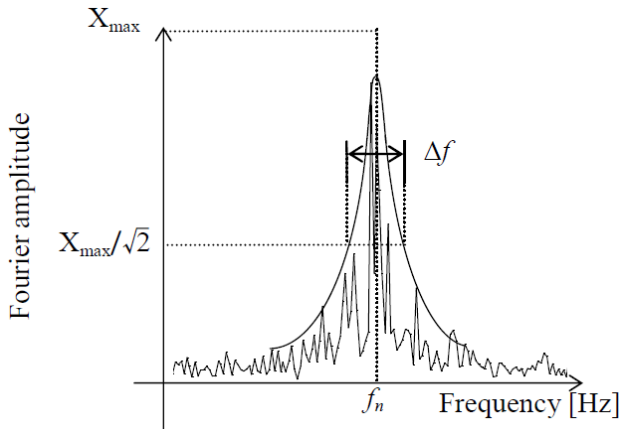


Fig. 129 Calculation method of damping ratio (Kikunaga and Arakawa, 2012)

The result of damping ratio for the first order is 0.014 and the second order is 0.019. Table 44 shows frequency comparisons between prototype, termed as (1), and specimen, termed as (2). Results indicate that frequency ratio is 1:7.47 in the first order natural frequency and 1:7.66 in the second order, which are close to the theoretical frequency ratio of 1:8. Table 45 compares the modal shapes between prototype and specimen, both of the first order are in longitudinal direction, and the second order are in transverse direction, showing a satisfactory agreement. Therefore, fundamental frequency comparison demonstrates the accuracy of theoretical similitude relationship, illustrates that the dynamic characteristics of specimen can reflect to the real bridge.

Order	(1) Prototype (Hz)	(2) Specimen (Hz)	(2): (1)	Theoretical value	Error (%)
1	0.194	1.45	1:7.47	1:8	6.63
2	0.274	2.10	1:7.66	1:8	4.25

Table 44

Fundamental frequency comparison between prototype and specimen

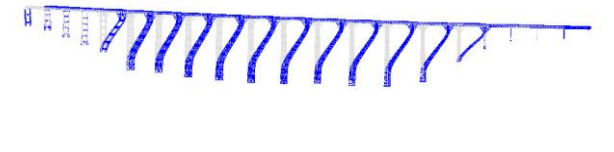
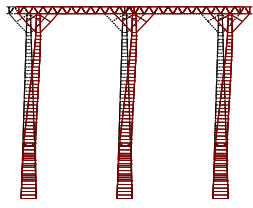
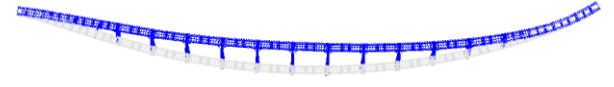
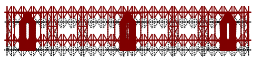
Order	Modal shape	
	Prototype	Specimen
1		
2		

Table 45

Modal shape comparison between prototype and specimen

6.6. Earthquake Response Analysis

6.6.1 Under Transverse Excitations

Displacement on the top of pier is the most concern issues for lightweight and high pier bridges. For the FE model of prototype in time-histories analysis, which is different with response analysis, the initial condition of the bridge, that is, gravity loads should be applied first, then followed by the dynamic analysis. Numerical method based on incremental Newmark- β method ($\beta = 0.25$, $\gamma=0.5$) and Newton iteration method were used to enforce equilibrium at each time step, a time step of 0.01s are integrated. A Rayleigh type viscous damping, steel damping ratio is 0.02, and concrete damping ratio is 0.05, proportional to mass and initial stiffness was adopted. Meanwhile, it is noting that prototype is a curved bridge, the input seismic along the tangent direction of the highest pier is defined as longitudinal direction, and the normal of tangential direction is defined as transverse direction.

Fig. 130 shows the displacement comparisons between measured values of specimen (top of center column, point 8) and FEM results of prototype under the same transverse excitation intensity (PGA=0.16g). In the figure, the left and bottom axis correspond to the time-history curve of prototype, and the right and top axis correspond to the time-history curve of specimen. Results indicate that displacement on the top of pier (center column of specimen and highest pier of prototype) are close to the theoretical displacement ratio of 1:8². Therefore, displacement comparison also demonstrates the accuracy of theoretical similitude relationship, test result can reflect to the displacement of prototype.

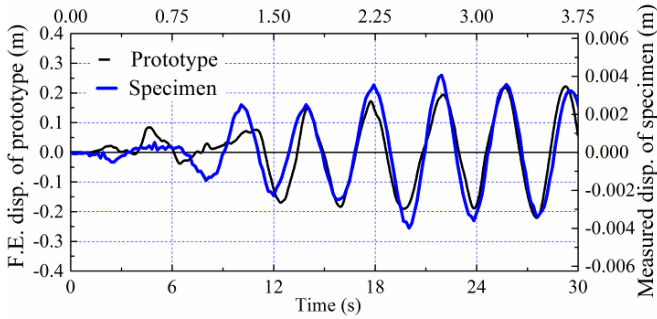


Fig. 130 Time histories of displacement under transverse excitation

The assessment of the response is based on the envelope of the maximum displacements and accelerations. Fig. 131 presents the maximum values of transverse displacement on the top of center pier under different PGA intensity. It shows that transverse displacement linearly increases as the increasing PGA intensity, while longitudinal displacement is not affected.

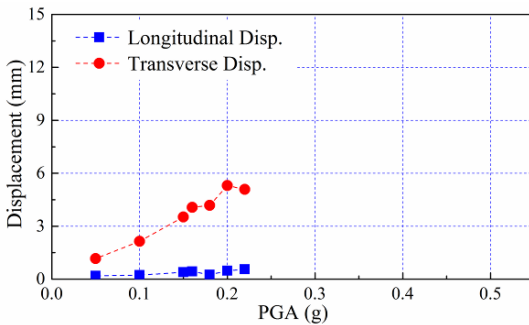
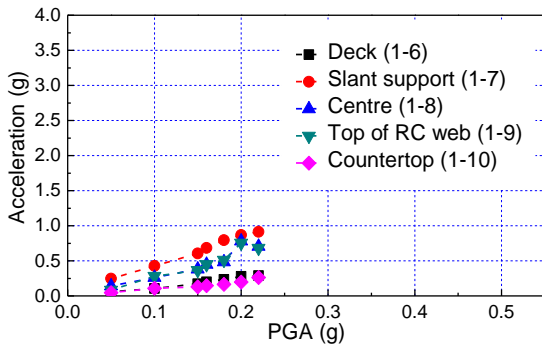


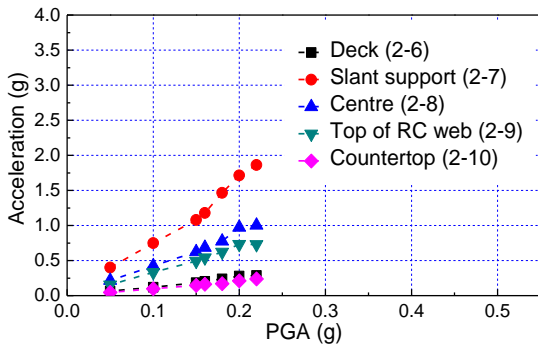
Fig. 131 Maximum transverse displacement under transverse excitation

Fig. 132 presents the maximum values of transverse acceleration on each column. It shows that acceleration value on the deck is nearly in accordance with the shaking table countertops. Acceleration amplification effect does not appear for this slender columns, illustrating that this new system has a favorable seismic performance. Because in the lattice column zone, acceleration significantly magnifies, which reduces acceleration on the deck through remarkable oscillation on the columns. Taken the center column 2 which eliminate the asymmetry of the structure as example, the maximum acceleration value is on the position of slant support, approximately 8 times to the countertop value at each seismic excitation intensities.

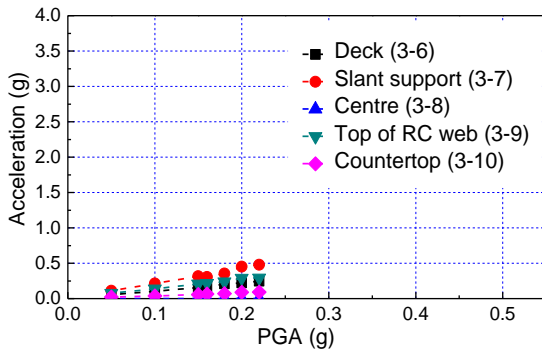
SEISMIC BEHAVIOR OF CONCRETE FILLED STEEL TUBULAR BUILT-UP COLUMNS



a) Column 1



b) Column 2



c) Column 3

Fig. 132 Maximum transverse acceleration under transverse excitation

Table 46 lists the maximum strain under $PGA=0.22g$. In transverse, the column is upright, which causes strain values increase from the top to the footing of column. While due to not adding any mass on the specimen, the value of strain is small, and specimen is in elastic stage under transverse excitations.

Position	Vertical strain ($\mu\epsilon$)
Slant support	37.83
Slant support of column	45.16
Top of RC web of column	54.32
Bottom of column	45.78
Concrete on bottom of RC web	29.91
Steel bar on bottom of RC web	48.22

Table 46 Maximum strain under transverse excitation

6.6.2 Under Longitudinal Excitations

Fig. 133 presents longitudinal displacement comparisons, the measured position is the same as Fig. 131. Longitudinal displacement are also approximately close to the theoretical displacement ratio of $1:8^2$, although prototype with curve shape in longitudinal direction and boundary conditions will lead to some errors.

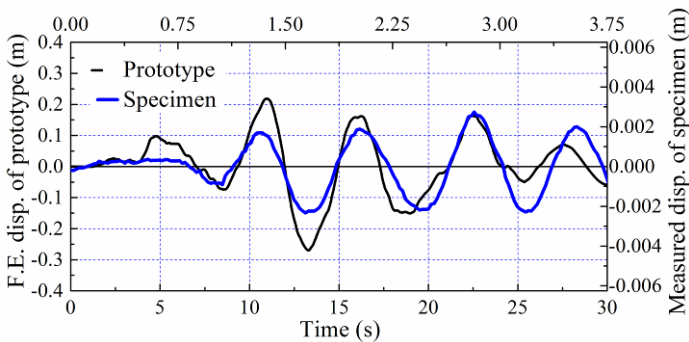


Fig. 133 Time histories of displacement under longitudinal excitation

Fig. 134 shows the maximum longitudinal displacement under longitudinal excitation. It can be found that the seismic response of specimen is similar to that under transverse excitations. Longitudinal displacement linearly increases, and transverse displacement is not significantly affected.

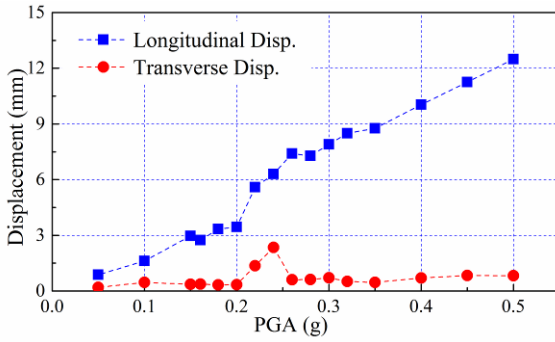
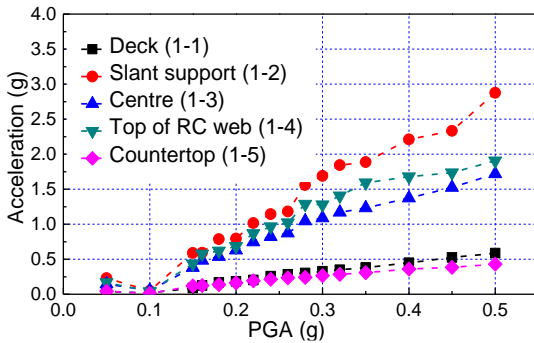
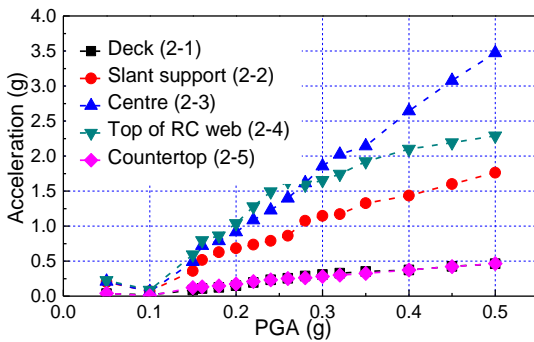


Fig. 134 Maximum longitudinal displacement under longitudinal excitation

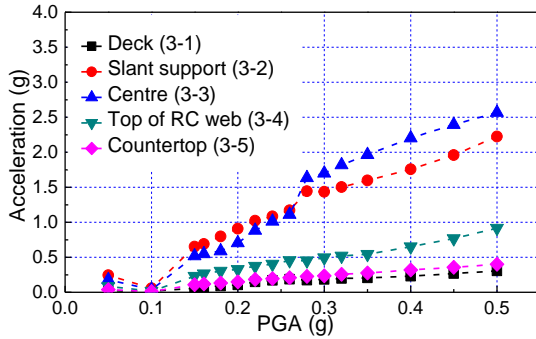
The maximum longitudinal acceleration of each column are presented in Fig. 135. It can be observed that, the same phenomenon as under transverse excitation, acceleration in lattice column zone significantly magnifies and reduces the acceleration on the deck. Similarly, taken column 2 as example, when PGA=0.5g, the maximum acceleration value of column is on the center position, approximately 7.5 times to the countertop value. CFST lattice columns also express favorable seismic performance in longitudinal direction.



a) Column 1



b) Column 2



c) Column 3

Fig. 135 Maximum longitudinal acceleration under longitudinal excitation

Table 47 lists the maximum strains under $PGA=0.50g$. The maximum strains on columns are in the position of slant support and top of RC web, where the stiffness changes. Vertical strains are significantly larger than longitudinal strains, but not yield according to strain similitude relationship. The specimen was still in elastic stage under the PGA intensity is approximate three times to the design ground motion intensity.

Position	Longitudinal strain ($\mu\epsilon$)	Vertical strain ($\mu\epsilon$)
Slant support	-	31.74
Slant support of column	32.96	117.19
Top of RC web of column	17.70	98.88
Bottom of column	13.12	84.88
Concrete on bottom of RC web	-	47.61
Steel bar on bottom of RC web	-	31.07

Table 47

Maximum strain in longitudinal excitation

6.6.3 Under Bi-directional Excitations

Wu et al. (Wu et al, 2006) discussed the seismic characteristics of CFST arch bridge by FEM, found that the analysis should consider the influence of bi-directional excitations. For this bridge, whether the structural response under bi-directional excitations will be larger than under unidirectional excitations of is also discussed. In this section, displacement and vertical strain comparisons are investigated respectively. The maximum vertical strain comparison is illustrated in Table 48 and Fig. 136. As observed, vertical strain under transverse excitations is

larger than under longitudinal direction with the same intensity level (PGA=0.22g), while under bi-directional excitations will not increase strain value than under transverse excitations. Table 49 and Fig. 137 present the maximum displacement comparisons. The same results could be found that, displacement amplification is also not obvious under bi-directional seismic excitations than that under unidirectional seismic excitation.

Position	Longitudinal excitation ($\mu\epsilon$)	Transverse excitation ($\mu\epsilon$)	Bi-directional excitation ($\mu\epsilon$)
Slant support of column	23.80	34.15	40.28
Top of RC web of column	26.25	43.95	43.33
Bottom of column	23.20	54.93	54.32

Table 48

Maximum strain comparison under different excitations

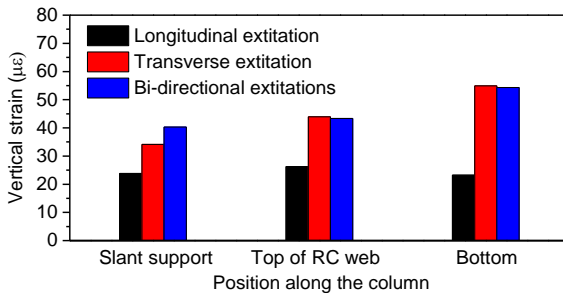


Fig. 136 Vertical strain comparison

PGA	Longitudinal excitation (mm)			Transverse excitation (mm)		
	Unidirectional (1)	Bi-directional (2)	(2)/(1)	Unidirectional (1)	Bi-directional (2)	(2)/(1)
0.05g	0.874	0.931	1.065	1.166	1.161	0.996
0.10g	1.617	1.959	1.212	2.137	2.239	1.048
0.15g	2.962	2.877	0.971	3.518	3.626	1.031
0.16g	2.742	3.317	1.210	4.062	3.760	0.926
0.18g	3.338	3.297	0.988	4.183	4.315	1.032
0.20g	3.448	5.963	1.729	5.305	5.577	1.051
0.22g	5.594	6.963	1.245	5.090	5.457	1.072

Table 49

Maximum displacement comparison under different excitations

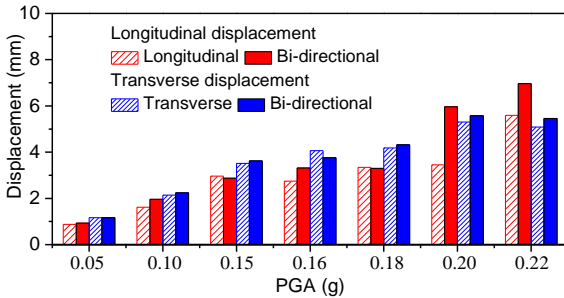


Fig. 137 Displacement comparison

Therefore, it is unnecessary to consider the influence of bi-directional excitations for this type bridge. According to horizontal displacement limitation in Table 36 and Table 37, the highest column elevation of prototype is 107m, and converted displacement limitation is 357mm. While converted transverse displacement from test results is 260mm and converted longitudinal displacement is 175mm. The horizontal displacement on the top of pier is within limitation.

6.7. Finite Element Model Analysis

6.7.1 Finite element model

Due to the favorable ductility and the limitation of test condition, there was no prospective plastic hinge on the columns. For further analysis, a three-dimensional FEM is developed in OpenSees platform (Version 2.4.4). The behavior of frame structures can be simulated commendably by using the nonlinear beam-column element from OpenSees. Tsai et al. (Tsai et al., 2004; Chen et al., 2004; Lin et al., 2004) simulated the dynamic behavior of CFST column to steel beam composite frames through OpenSees, where predicted results by OpenSees matched well with the experimental curves. Han et al. (Han et al., 2011) also used OpenSees to simulate *P-Delta* hysteretic relationships of composite frame with CFST columns under lateral cyclic loading. Compared with experimental results, it indicates that reasonable accuracy has been achieved for OpenSees in predicting the cyclic behavior of the composite frames. The CFST columns are hence modeled as nonlinear beam-columns elements which was described in Ch.2.3.

The steel fibers are simulated using elastic-perfectly plastic constitutive model, which can be implemented by the Steel02 model available in OpenSees material

library, as shown in Fig. 40. The values for concrete compressive properties were obtained from material tests. The loading and unloading rules used in the FEM were calculated based on concrete02 model. The pre-peak region of compressive stress-strain curve for the confined concrete is modeled using the equations suggested by Mander et al. (Mander J.B. et al., 1988), and confining pressure models are proposed using the equations suggested by Liang and Fragomeni (Liang & Fragomeni, 2009), which account for the effects of material properties and the column geometry, see Fig. 38. Similarly with Ch.2.5.2, relatively fine discretization schemes were selected since the initial stiffness was often of critical importance and the resulting number of fibers did not pose any computational problems. The fiber discretization is 30 in the circumferential direction, both for concrete and steel. In the radial direction, there were 16 fibers for concrete and 2 fibers for steel.

Slight response characteristics of superstructure were measured during testing and plastic hinge were expected on the CFST columns. The main mechanical components of piers, such as circular CFST columns and slant supports, were modeled using the nonlinear beam-column elements with discrete fiber section model in OpenSees. Moreover, in order to get a better convergence with less analytical time, the remaining components were simulated using elastic beam-columns elements, see Fig. 138. Meanwhile, the *P-Delta* coordinate transformation was set on the columns, considering the *P-Delta* effects existing in slender CFST columns. Local buckling of steel tubes was neglected, since no local buckling happened during testing. The columns bases were fixed in all degrees of freedom.

There were a total of 2599 nodes and 3602 elements in FEM. A Rayleigh type viscous damping, proportional to mass and initial stiffness was adopted for the first two models with coefficients determined by selecting a damping ratio of 2% for the first two modes of the model. The incremental equations of motion were integrated with Newmark's method ($\beta = 0.25$, $\gamma = 0.50$). The Newton-Raphson's iteration method was used to enforce equilibrium at each time step. Moreover, the initial inner force of the bridge was assumed to be from the dead load only before the ground motion inputted, then followed by the dynamic analysis. For full mass model, according to similitude relationship, 8 times node mass was added at each node, and duration of seismic excitation was adjusted, which could be implemented conveniently in OpenSees.

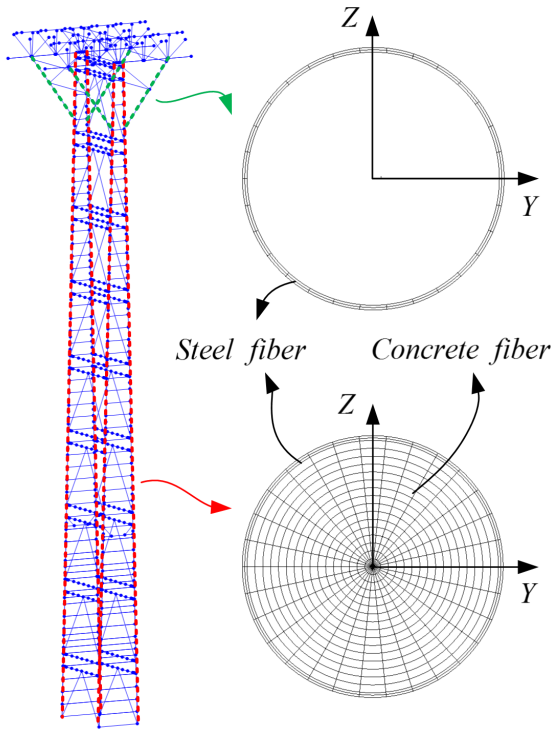


Fig. 138 FEM details

6.7.2 Validation of FEM

The accuracy of the modeling approaches is evaluated through comparisons of fundamental frequency, time histories of displacement and strain envelopes along columns. Table 50 shows the fundamental frequency comparison between specimen and no mass FEM, where specimen termed as (2) and no mass FEM termed as (3). It can be found that, numerical results of frequency are approached to test results, where the error are with 7%.

Order	(2) Specimen (Hz)	(3) No mass FEM (Hz)	Error (%)
1	1.45	1.47	1.4
2	2.10	2.24	6.3

Table 50

Fundamental frequency comparison between specimen and no mass FEM

Table 51 shows the frequency comparison between prototype and full mass FEM, where prototype termed as (1) and full mass FEM termed as (4). Results indicate

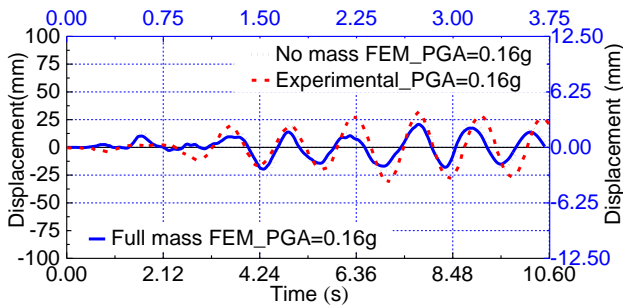
that the frequency ratio is 1:2.71 in the first order natural frequency and 1:2.93 in the second order, which are close to the theoretical frequency ratio of 1:2.828, where the error are within 5%.

Order	(1) Prototype (Hz)	(4) Full mass FEM (Hz)	(4): (1)	Theoretical value	Error (%)
1	0.194	0.526	1:2.71	1:2.828	4.10
2	0.274	0.803	1:2.93	1:2.828	3.64

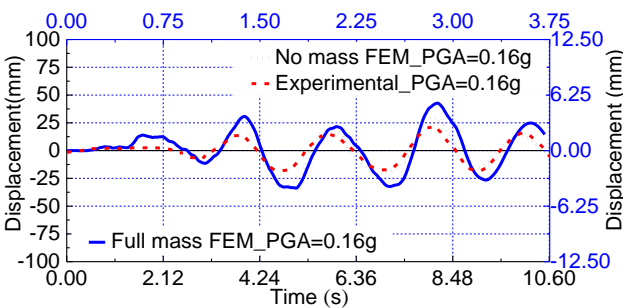
Table 51

Fundamental frequency comparison between prototype and full mass FEM

Satisfactory numerical response is further confirmed by comparison of time histories of displacement on the top of center columns under PGA=0.16g, as shown in Fig. 139. In the figure, time histories of experimental result and no mass FEM are correspond to top axis and right axis, with the same durable time. While for full mass FEM, correspond to bottom axis and left axis. It must be noted that some errors on the amplitude of time histories between measured and FEM, which is inevitably produced during the specimen manufacture and test procedure. However, the waveform and phase show a good results.



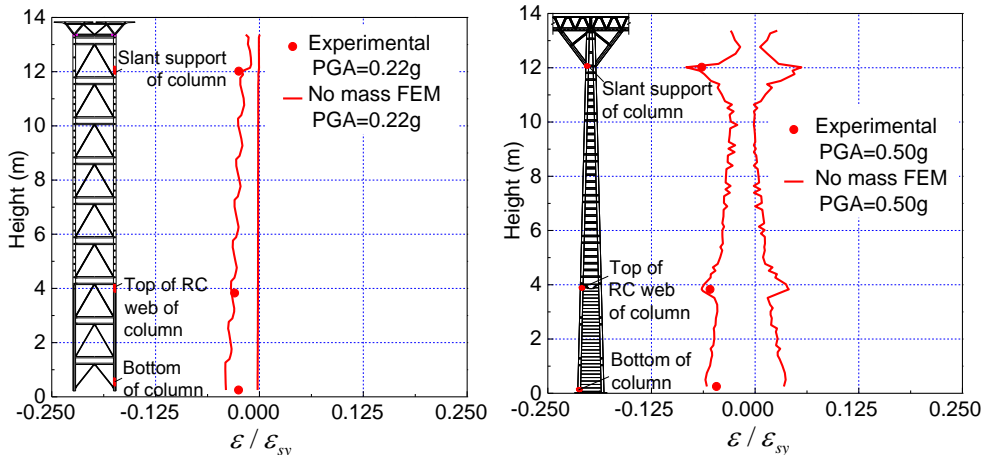
a) Transverse excitation



b) Longitudinal excitation

Fig. 139 Comparison of displacement time histories

For a more accurate assessment of the FEM, comparisons of vertical strain envelope between experimental result and no mass FEM are presented in Fig. 140. Vertical strain envelope at the edge of circular CFST columns members along the heights are chosen in no mass FEM. Longitudinal axis corresponds to the ratio of strain ε to the absolute value of yield strain ε_{sy} . The analytical values are also in good agreement with the measured strain.



a) Transverse excitation

b) Longitudinal excitation

Fig. 140 Comparison of vertical strain envelope

Therefore, good agreement between measured and FEM results are obtained through comparisons of fundamental frequency, time histories of displacement and strain envelopes. The FEM can be further evaluated the nonlinear analysis of seismic performance.

6.7.3 Predicted behavior of plastic zone

As strain analysis mentioned above, the potential plastic zone of CFST columns did not appear after the test. Full mass FEM is adopted for predicting plastic zone, which can counteract the gravity distortion effect in the vertical direction, and keep the strain ratio between FEM and prototype is 1:1.

Similarly, taking strain envelopes at the extreme edge of steel tubes on the columns as criteria, then PGA is increased until the strain turn into plastic stage, see Fig. 141. In Fig. 141(a), when subjected to PGA=0.80g under transverse excitation, the first plastic zone of the CFST column appears at the bottom of lateral connection, where the strain at the extreme edge of steel tubes exceeds the yield strain of steel tubes

($|\epsilon/\epsilon_{sy}| > 1$). The strain at each lateral connection is relatively larger than other positions. In Fig. 141(b), when subjected to $PGA=0.60g$ under longitudinal excitation, the strain of steel tube at the slant support leads to yield. On the top of RC webs, it also increases but not as far as at the position of slant support.

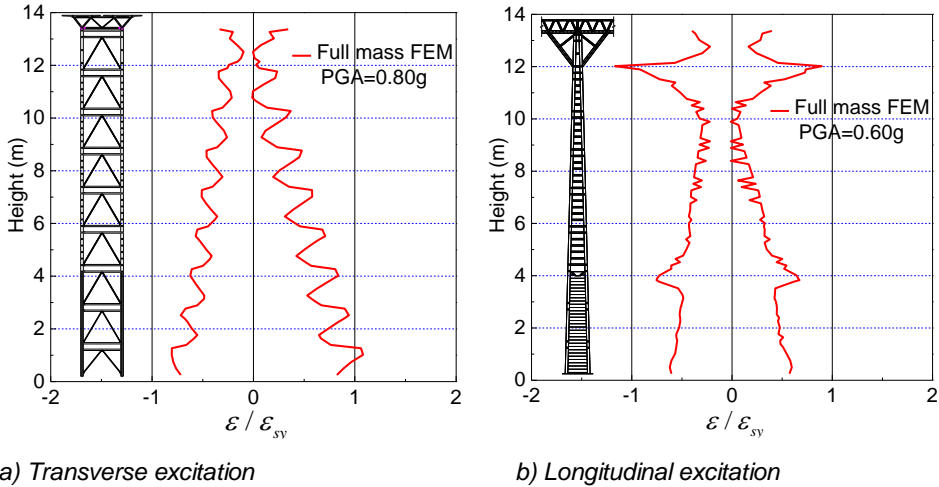


Fig. 141 Strain envelopes at the extreme edge of steel tubes

In order to investigate the deformation of high pier after the structure is into plastic stage, displacement envelopes of CFST column are firstly presented in Fig. 142. Longitudinal displacement is larger than transverse displacement. It is noting that under longitudinal direction, due to the changed stiffness both at the position of top of RC web and slant support, there are two inflection points appeared. Under transverse direction, displacement linearly increases from bottom to the top of column, shows a favorable deformation performance.

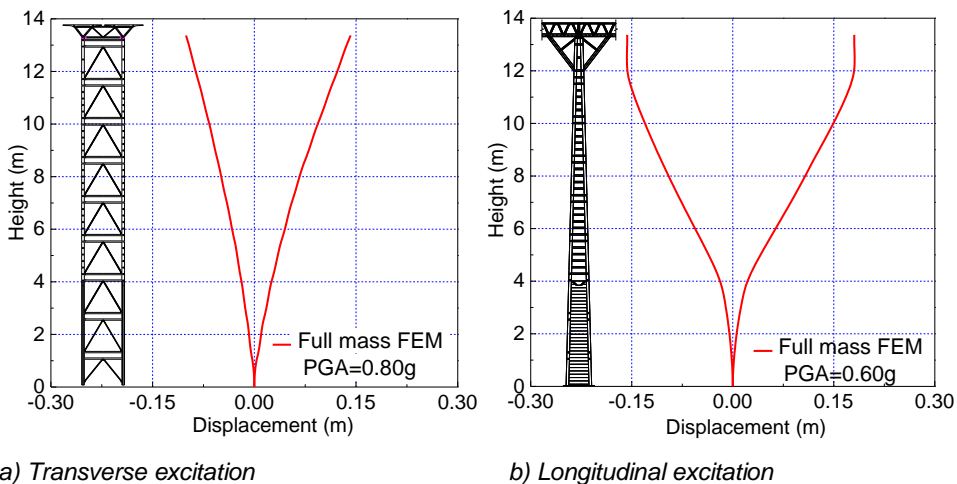
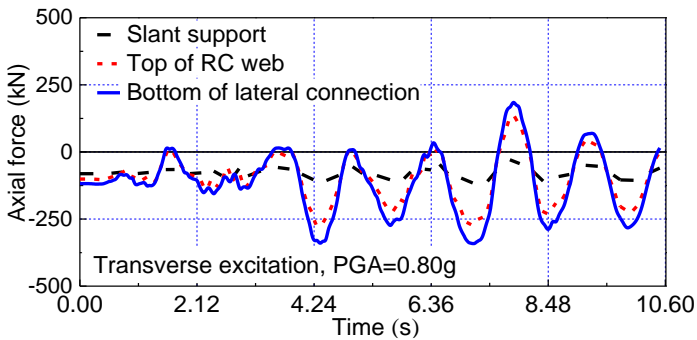
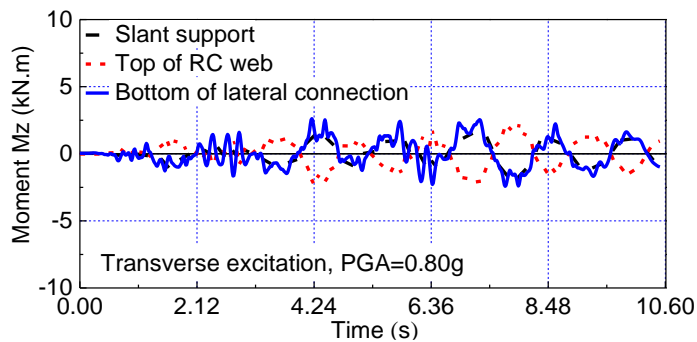
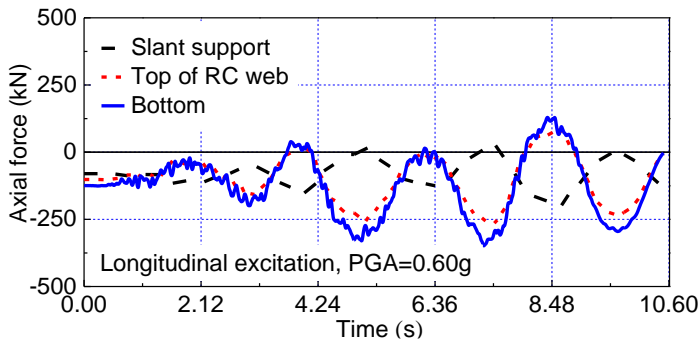


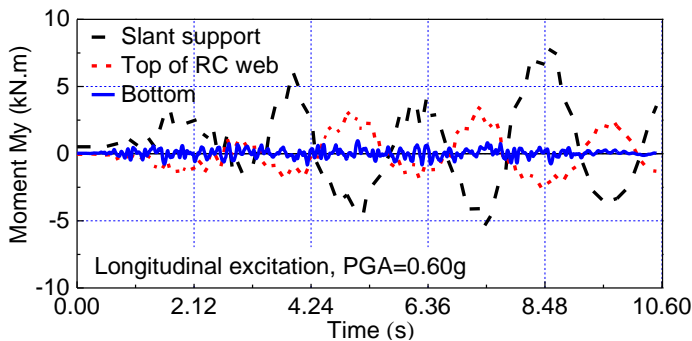
Fig. 142 Displacement envelopes of CFST column

Fig. 143 presents the time histories of internal force at the key sections of center CFST column, such as at the position of slant support, top of RC web and bottom. Under transverse excitation, axial forces N , see Fig. 143(a), increases from top to bottom and with the same in-phases angle. Regards out-of-plane bending moments M_z , see Fig. 143(b), the position on the top of RC web has different phases with others, but the value is not significantly different. Under longitudinal excitation, axial forces N , see Fig. 143(c), also increases from top to bottom. However, at the position of slant support, there is different phases with other positions. Regards in-plane bending moment M_y , Fig. 143(d), due to the RC web in longitudinal direction shares the internal forces, M_y at the bottom has relatively smaller values. It means compared with laced column without RC webs, CFST columns in composite columns will be protected through RC webs. While M_y at the position of slant support are greater than others, which causes strain of steel tubes significantly increased. Moreover, from the time histories of axial force, it can be seen that the value significantly vary, no matter when under transverse or longitudinal excitation. Therefore, it is necessary to consider the influence of axial force fluctuation during excitations. In other words, it is reasonable to adopt fiber model in nonlinear analysis, which can take into account the axial force fluctuation.

a) Axial force N b) Out-of-plane bending moment M_z



c) Axial force N



d) In-plane bending moment M_y

Fig. 143 Time histories of CFST columns

6.7.4 Influence of ground motions

In particular, structural seismic performance need be investigated under strong ground motions. In this section, according to the Japanese specification (Japan Road Association, 2002) for seismic design of highway bridge piers, two kinds of natural records with different types were adopted, among that, each type with three natural records. The first is the plate boundary type of earthquakes (Type 1), having a magnitude of about 8, and the second is the inland type of earthquake (Type 2), having a magnitude of about 7-7.2 at very short distance (Wu et al., 2006). The standard strong earthquakes of Type 1 (T111, T112, T113) and Type 2 (T211, T212, T213) in the stiff soil condition are respectively listed in the Fig. 144. Moreover, the spectral characteristics of these six ground motions are presented in Fig. 145. Since the restriction of test device, the analysis is also finished by full mass FEM. The seismic excitations move also respectively along transverse and longitudinal direction.

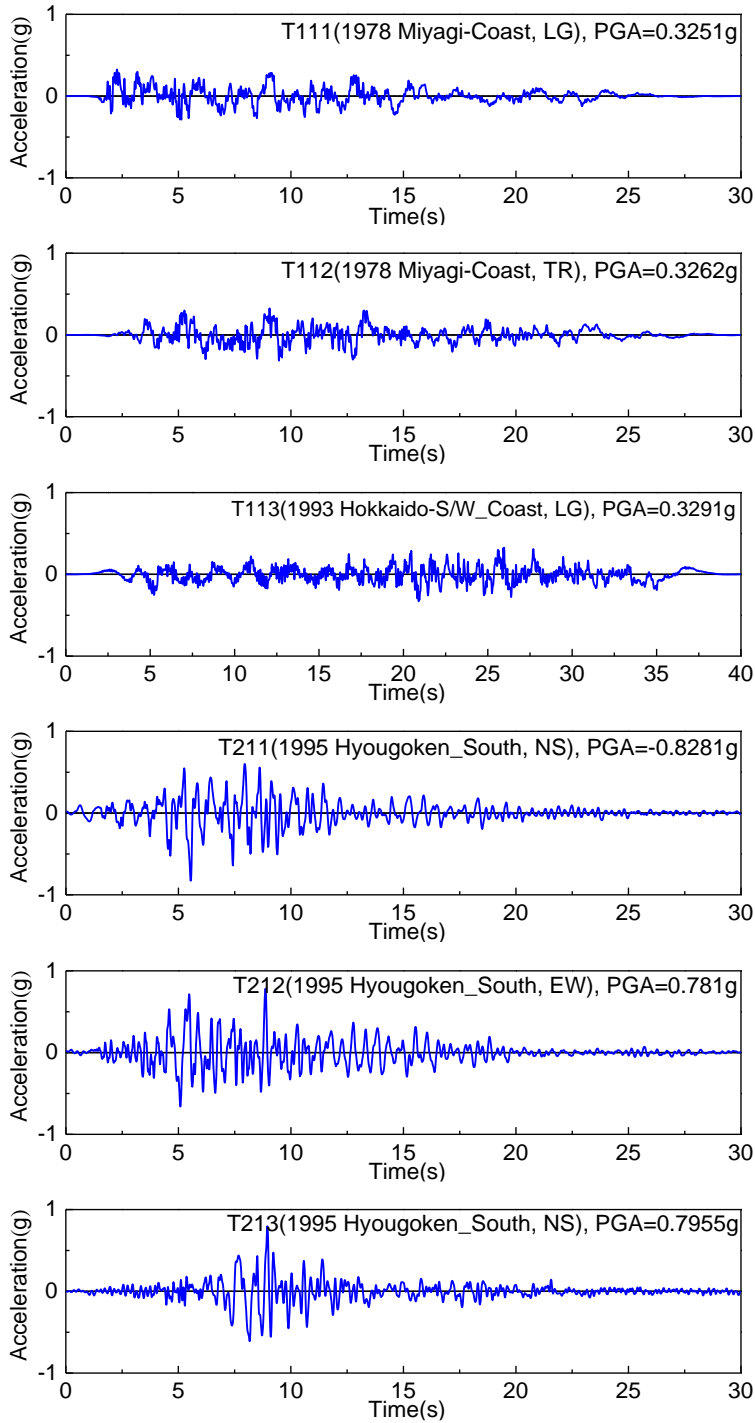


Fig. 144 Time histories of natural records

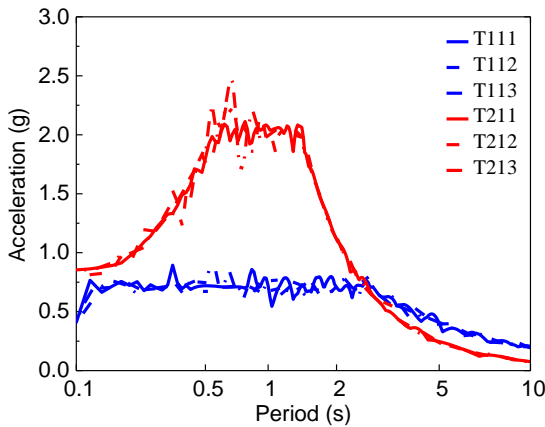
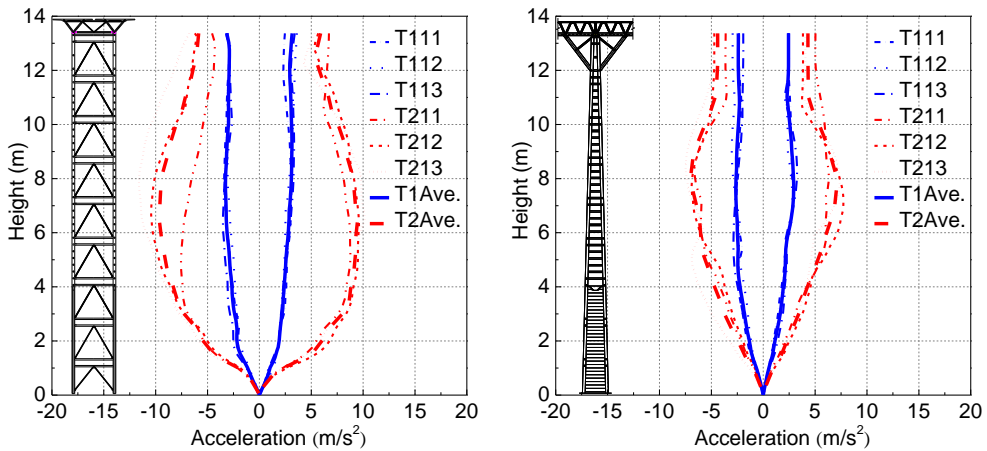


Fig. 145 Spectral characteristics

As mentioned above, each type of earthquake consists of three ground motions, hence the average values of the dynamic response are highlighted in the following results, termed as T1Ave. and T2Ave., respectively. Fig. 146 shows the acceleration envelope of one central CFST column along the pier height. It is evident that the same calculated results will be got due to four CFST columns are symmetrical both in longitudinal and transverse directions.



a) Transverse excitation

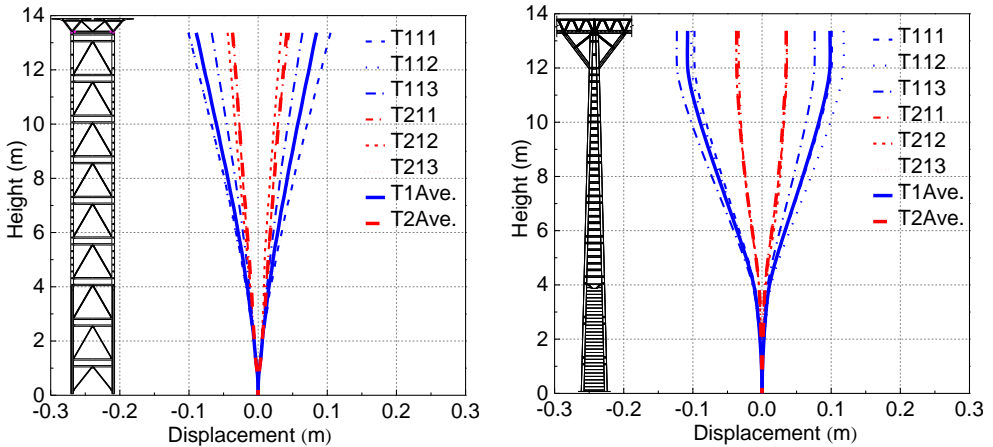
b) Longitudinal excitation

Fig. 146 Acceleration envelope of pier

Results show that no matter under the longitudinal or transverse seismic excitations, acceleration subjected to Type 2 ground motions are significantly larger than subjected to Type 1 ground motions. It means that when subjected to a strong ground motions within short distance, the column can magnifies the acceleration response through remarkable oscillation on the lattice column zones, which reduces

acceleration on the deck. Therefore, acceleration amplification effect on the top column does not appear under strong ground motions.

While displacement envelope of the column shows opposite results, see in Fig. 147. It can be found that both under longitudinal and transverse directional excitations, displacement subjected to Type 2 ground motions are smaller than subjected to Type1 ground motions.

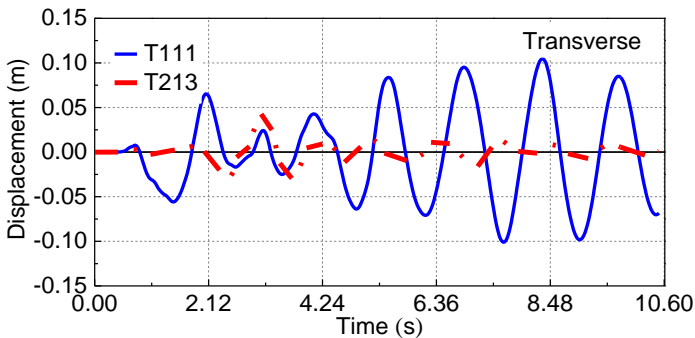


a) Transverse excitation

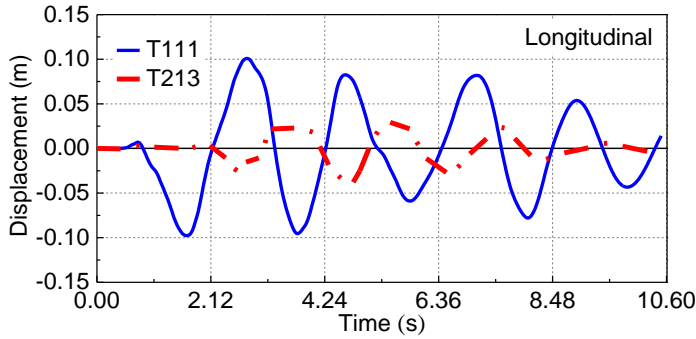
b) Longitudinal excitation

Fig. 147 Displacement envelope of pier

For lack of space and comparing clearly, Fig. 148 gives the displacement time histories comparison at the top of center column under T111 and T213 respectively. It is apparent that displacement under T111 is larger than under T213 regardless under transverse or longitudinal excitation.



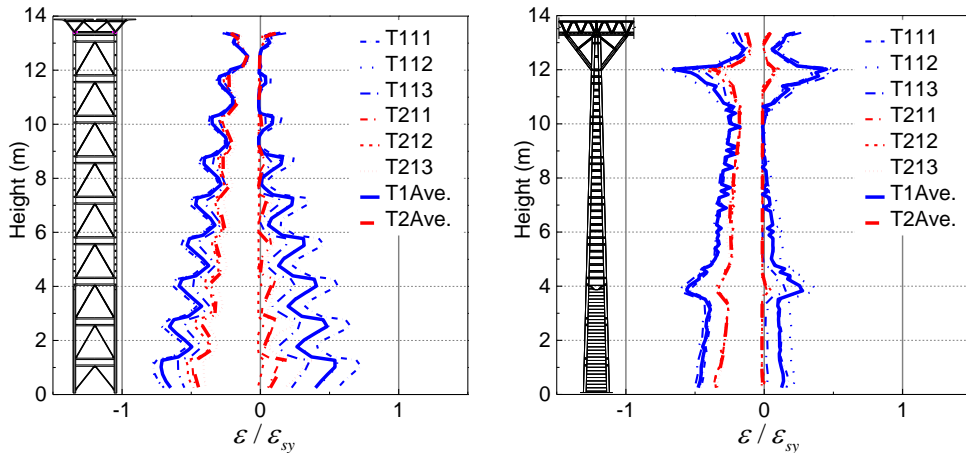
a) Transverse excitation



b) Longitudinal excitation

Fig. 148 Time histories at the top of column

The maximum extreme strain of steel tube along the height are compared in Fig. 149. Abscissa is the normalized strain, if the value exceeds 1, indicating that the CFST column turn into plastic. The values under Type1 ground motions are also larger than Type2, but all the sections are remain in elastic. Under transverse excitation, strain envelope shows spindle-shaped, each lateral connection are relatively larger than adjacent positions, and values reduce from bottom up, thus promote seismic performance. Under longitudinal excitation, the stain at the position of slant support and top of RC web will be larger than other positions. The slant support shares the internal force, protect the top connection between the CFST column and girder. Subjected to strong ground motions of Type1 and Type2, the pier remain in elastic stage, it demonstrates that this innovative lightweight bridge has a favorable seismic performance.



a) Transverse excitation

b) Longitudinal excitation

Fig. 149 Normalized strain envelope at the extreme edge of steel tube

CONCLUSIONS

The present research investigates the seismic behavior of CFST built-up columns. To provide a unitary framework, a detailed literature survey on the CFST built-up structures, including mechanical characteristics, applications, ductility in seismic design, previous experimental researches, and finite element formulation, is firstly illustrated. Then, six specimens with different grades of concrete and brace arrangements are designed and tested under cyclic loading. The hysteretic behavior, such as failure mode, deformed shape, displacement ductility, rigidity and strength degradation, and energy dissipation capacity of test specimens are analyzed. The corresponding validated FEM simulations are developed for the parametric analysis, to discuss the hysteretic behavior, affected by axial load ratio, chord spacing, brace spacing, diameter to thickness ratio, and steel yield strength. Based on extended parametric analysis and regression analysis, a simplified method is proposed to calculate the displacement ductility factor of CFST battened columns and laced columns, respectively. After that, to investigate the seismic performance of built-up columns used in practice, an innovative lightweight bridge with CFST composite truss girder and CFST lattice pier is studied as case study. For the purpose, FEM simulation and shaking table test are carried out.

Conclusions

On the basis of the findings of the literature reviews, presented approaches, experimental tests and FEM analyses, the conclusions are drawn as following:

- With the advantages of CFST built-up columns, including the higher confinement in the concrete, delay of the steel local buckling, higher compressive and flexural strength, earthquake and fire resistance, rapid construction, savings in the construction costs, CFST built-up columns are increasing adopted in structural members with larger load eccentricity ratio and slenderness ratio, such as stadium, industrial buildings, bridge pier and pillar, and electrical transmission tower, etc.
- The main researches with CFST built-up columns are focused on the static behavior, seldom studies have been reported on the dynamic

characteristics. The concept of ductility is a very significant indicators for seismic design. However, there is not specify specification on the definition of displacement ductility factor on CFST built-up columns.

- Subjected to cyclic loading, the failure mode of test specimens are the buckling waves concentrated at the bottom of chords resulting in elephant foot buckling mode, and the punching shear failure on the connection between chord and braces. The deformed shapes are overall lateral deformation. Among that, CFST battened columns and M shaped laced columns show excellent load deformation characteristics, with displacement ductility factor more than 4. The hysteretic curves of specimen are generally saturated and show spindle-shaped. Concrete grade played a slight effect to the hysteretic behavior. From the point of cumulative energy dissipation, M shaped laced columns shows the best result than others.
- For laced columns, the horizontal ultimate bearing capacities is approximately two times than battened columns. The rigidity of laced columns is approximately three times to that of battened columns. However, rigidity degradation of laced columns (decrease 80%) are even more than that of battened columns (decrease 75%). After the ultimate strength is reached, the strength decreases and generally kept in a range from 0.85 to 0.95 for battened columns, and 0.7 to 0.9 for laced column. Strength degradation is more or less 10% after each cyclic loading.
- The proposed FEM with fiber beam-columns elements, which can simultaneously take geometric and material nonlinearity into account within and implemented through OpenSees platform, can be used in simulate the hysteretic behavior of CFST built-up columns. By the comparison between test results and two previous experimental research, the predicted results of FEM show a good agreement with the test results. It reveals that the proposed FEM method can be adopted in further parametric analysis.
- Parametric analysis is carried out, to discuss the hysteretic behavior affected by different parameters, including axial load ratio, chord spacing, brace spacing, diameter to thickness ratio, and steel yield strength. Results show that the axial load ratio within 0.2 is a reasonable restrictions to exhibit columns' ductility. Poor hysteretic behavior is appeared when chord spacing is smaller than brace spacing. Properly increasing the thickness of steel tubes will promote the hysteretic behavior of CFST laced columns.

Steel yield strength shows relatively less impact than other parameters. On the perspective of cumulative energy dissipation capacity, geometrical types play a most significant impact than other parameters.

- Based on the extended parametric analysis and regression analysis, including 98 FEMs for CFST battened columns and 64 FEMs for CFST laced columns, a simplified method is proposed and suggested to calculate the displacement ductility factor. The formula is consisted of derived equivalent slenderness ratio (consider the geometrical parameters of chord spacing, brace spacing, and diameter to thickness ratio), axial load ratio and steel yield strength. The range of application is that, axial load ratio ranges from 0.1 to 0.3, steel yield strength ranges from 235Mpa to 420Mpa, and equivalent slenderness ratio ranges from 54.75 to 115.17 (for battened columns) and 19.84 to 30.46 (for laced columns). Compared with test result, the error is within 10%, indicating that the proposed method can be used for engineering reference.
- In order to study the seismic performance of CFST built-up columns used in practice, an existing structure (Ganhaizi Bridge) is presented as a case study, which is an innovative lightweight bridge with CFST composite truss girder and CFST lattice pier. The first-order frequency is 0.191Hz with modal shape of longitudinal floating. In other words, the natural periods is 5.236s, indicating that the bridge is expected to promote the seismic performance through its flexibility. From the second to ninth modes, various transverse bending modal shapes are appeared. The local mode appears until the tenth-order modal, with local bending in pier No. 27.
- By response spectrum analysis from defined parallel and perpendicular directions, respectively, the stress distribution along the pier height, presents a jagged shape, where at the position of transverse hollow steel tubular trusses, the value is larger than that at the adjacent positions. On the whole. For the battened piers, the critical cross sections are at the position of bottom trusses connections. For the composite piers, the critical cross sections are still at the position of top of RC webs. The stress distribution regularities of in-filled concrete is similar to that of steel tubes.
- The bridge under parallel seismic input direction, the displacement of high piers are in harmony, and the value is more than doubling of that in the lower piers, illustrating that the high pier have a favorable deformation

capacities and ductility. Under perpendicular seismic input direction, the displacement distribution is non-uniform, higher pier with larger displacement.

- A 1:8 scale specimen with two spans and three lattice high piers was designed for multi-shaking tables test. Seismic performance of the specimen under transverse excitation, longitudinal excitation, and bi-directional excitation were investigated, respectively. Through white noise excitation, the identified fundamental frequency of the structure is 1.45Hz in longitudinal direction and 2.10Hz in transverse direction. The frequency ratio between prototype and model is 1:7.47 in the first order and 1:7.69 in the second order, which are closed to the theoretical frequency ratio of 1:8. The accuracy of similitude relationship is verified. Displacement of specimen agrees well with prototype according to the similitude relationship.
- Under transverse excitation, acceleration significantly magnified in the lattice column zone, reduces response on the deck. The maximum strain on the column is on the top of RC web. Under longitudinal excitation, experimental response is similar to under transverse excitation. The maximum strains on columns are at the position of slant support and top of RC web, where the stiffness changes. Vertical strains are significantly larger than longitudinal strain, but less than yield strain. Under bidirectional excitations, displacement and strain are not larger than subjected to one directional seismic input. It is not necessary to consider the influence of bidirectional excitations.
- The specimen of FEM is developed by the OpenSees platform, and accuracy is calibrated through comparisons of fundamental frequency, time histories and strains with test results. Base on nonlinear fiber element-column elements, the plastic zone is predicted. Under transverse excitation with $PGA=0.80g$, CFST column at the bottom of lateral connection is first to yield. Under longitudinal excitation with $PGA=0.60g$, CFST column at the slant support is first to yield.
- Influence of ground motions are investigated with two types of seismic records, results show that Type1 earthquakes generate larger responses than Type2 earthquakes in displacement and strain of column, while the acceleration subjected to Type2 earthquakes are significantly larger than subjected to Type1 earthquakes. Subjected to strong ground motions of

Type1 and Type2, the structure remains in elastic stage, indicating that CFST built-up columns used in practice has a favorable seismic performance.

Recommendations for Future Investigations

Although the present study investigates seismic behavior of CFST built-up columns under cyclic loading, proposes method to calculate displacement ductility factor for battened columns and laced columns, respectively. Moreover, discuss the seismic performance of one lightweight bridge where CFST built-up columns are adopted in practice. However, there are still many factors and uncertainties need to be addressed.

A more experimental investigations on CFST built-up columns should be carried out, consider the influence of different height of columns, slope of columns, and other types of braces arrangement, in order to enlarge the samples, and develop theory in the seismic design, which consists of more parameters.

The connection system, the hybrid system using high performance and sustainable materials as well as the life-cycle performance evaluation should be connected with CFST built-up column, to improve the seismic performance in practice. It would be also desirable to conduct with structural optimization on CFST built-up columns in the future.

BIBLIOGRAPHY

Abed F., AlHamaydeh M. and Abdalla S., (2013), *Experimental and numerical investigations of the compressive behavior of concrete filled steel tubes (CFSTs)*, Journal of Constructional Steel Research, 80, 429-439.

American Institute of Steel Construction (AISC), (2010), *Specification for Structural Steel Buildings*, An American National Standard, Illinois, Chicago, USA. ANSI/AISC 360-10: 2005.

Alemdar B.N. and White, D.W., (2005), *Displacement, flexibility, and mixed beam-column finite element formulations for distributed plasticity analysis*, Journal of Structural Engineering, ASCE, 131, 12, 1811-1819.

Allemang R.J., (2003), *The modal assurance criterion—twenty years of use and abuse*, Sound and Vibration, 37, 8, 14-23.

Allied Vision Technologies, Homepage website: www.alliedvisiontec.com.

American Association of State Highway and Transportation Officials, (2012), *AASHTO LRFD Bridge Design Specifications (SI Units 6th Edition)*, American Association of State Highway and Transportation Officials, 444 North Capitol Street, NW, Suite 249. Washington, D.C. 20001.

Aval S.B.B., Saadeghvaziri, M.A. and Golafshani, A.A., (2002), *Comprehensive composite inelastic fiber element for cyclic analysis of concrete-filled steel tube columns*, Journal of Engineering Mechanics, 128, 428

Caltrans, (2013), *Seismic Design Criteria*, 1120 N Street, California Department of Transportation, Sacramento, California, USA.

Chang G.A. and Mander J.B., (1994), *Seismic Energy Based Fatigue Damage Analysis of Bridge Columns: Part I - Evaluation of Seismic Capacity*, National Center for Earthquake Engineering Research, State University of New York at Buffalo, Department of Civil Engineering.

Chen B.C. and Wang T.L., (2009), *Overview of concrete filled steel tube arch bridges in China*, Journal of Bridge Engineering, ASCE, 2009, 14, 2, 70-80.

Chen C.H., Hsiao P.C., Lai J.W., Lin M.L., Weng Y.T. and Tsai K.C., (2004), *Pseudo dynamic tests of a full-scale CFT/BRB frame: Part 2-Construction and testing*, 13th World Conference on Earthquake Engineering, August 1-6, Vancouver, B.C., Canada, No. 2175.

Chen Y.Q., Liu X.H. and Gong S.L., (1981), *The artificial earthquake ground motions compatible with standard response spectra*, Journal of Building Structures, 4, 34-43. In Chinese.

China National Standard, (1997), *Specification for Test Methods of Earthquake Resistant Buildings*, Architecture Industrial Press of China, JGJ101-96, Beijing, China. In Chinese.

China National Standard, (2002), *Standard for Test Method of Mechanical Properties on Ordinary Concrete*, GB/T50081-2002, Ministry of Construction, China. In Chinese.

China National Standard, (2003), *Code for Design of Steel Structure*, GB 50017-2003, China Architecture & Building Press, Beijing, China. In Chinese.

China National Standard, (2010a), *Metallic Materials-Tensile Testing-Method of Test at Room Temperature*, GB/T228.1-2010, Ministry of Construction, China. In Chinese.

China National Standard, (2010b), *Code for Design of Concrete Structure*, GB 50010-2010, China Architecture & Building Press, Beijing, China. In Chinese.

Chung K., (2010), *Prediction of pre- and post-peak behavior of concrete-filled circular steel tube columns under cyclic loads using fiber element method*, Thin-Walled Structures, 48, 2, 169-178.

De Souza R.M., (2000), *Force-Based Finite Element for Large Displacement Inelastic Analysis of Frames*, Thesis: Ph.D., University of California, Berkeley, California, USA.

Denavit M.D. and Hajjar J.F., (2010), *Nonlinear Seismic Analysis of Circular Concrete-filled Steel Tube Members and Frames*, NSEL Report Series, Report No. NSEL-023, Department of Civil and Environmental Engineering University of Illinois at Urbana-Champaign, USA.

Denavit M.D. and Hajjar J.F., (2012), *Nonlinear seismic analysis of circular concrete-filled steel tube members and frames*, Journal of Structural Engineering, ASCE, 138, 9, 1089-1098.

DEWETRON Elektronische Messgeräte Gesellschaft m.b.H. Homepage website: www.dewetron.com

Donghua Test Ltd. Homepage website: www.dhtest.com

Elremaily A. and Azizinamini A., (2002), *Behavior and strength of circular concrete-filled tube columns*, Journal of Constructional Steel Research, 58, 12, 1567-1591.

- El-Tawil, S. and Deierlein G.G., (2001), *Nonlinear Analysis of Mixed Steel-Concrete Frames. I: Element Formulation*, Journal of Structural Engineering, ASCE, 127, 6, 647-655.
- European Committee for Standardization (CEN), (2004a), *Eurocode 4: Design of Composite Steel and Concrete Structures, Part 1-1: General Rules and Rules for Buildings*, CEN 1994-1-1: 2004.
- European Committee for Standardization (CEN), (2004b), *Eurocode 8: Design of Structures for Earthquake Resistance, Part 1: General rules, Seismic Actions and Rules for Buildings*, EN 1998-1: 2004.
- European Committee for Standardization (CEN), (2005b), *Eurocode 4: Design of Composite Steel and Concrete Structures, Part 2: General Rules and Rules for Bridges*, EN 1994-2: 2005.
- European Committee for Standardization (CEN), (2005c), *Eurocode 8: Design of Structures for Earthquake Resistance, Part 2: Bridges*, EN 1998-2: 2005.
- European Committee for Standardization (CEN), (2006), *Eurocode 3: Design of Steel Structures-Part 1-1: General Rules and Rules for Buildings*, EN 1993-1-1: 2006.
- Ferrario F., (2004), *Analysis and Modelling of the Seismic Behaviour of High Ductility Steel-Concrete Composite Structures*, Thesis: Ph.D., University of Trento, Trento, Italy.
- Federal Emergency Management Agency (FEMA), (2009), *Quantification of Building Seismic Performance Factors*, FEMA P695, Washington, D.C., USA.
- Filippou F.C. and Fenves G.L., (2004), *Earthquake Engineering: from Engineering Seismology to Performance-based Engineering*, CRC Press, Boca Raton, Florida, USA.
- Filippou, F.C., Popov, E.P. and Bertero, V.V., (1983), *Effects of Bond Deterioration on Hysteretic Behavior of Reinforced Concrete Joints*, Report EERC 83-19, Earthquake Engineering Research Center, University of California, Berkeley, USA.
- Furlong R.W., (1967), *Strength of steel-encased concrete beam columns*, Journal of the Structural Division, ASCE, 93, ST5, 113-124.
- Ge H.B. and Usami T., (1996), *Cyclic test of concrete filled steel box columns*, Journal of Structural Engineering, ASCE, 122, 10, 1169-1177.
- Gourley B.C., Tort C., Denavit M.D., Schiller P.H. and Hajjar J.F., (2008), *A Synopsis of Studies of the Monotonic and Cyclic Behavior of Concrete-Filled Steel Tube Members, Connections, and Frames*, NSEL Report Series, Report No. NSEL-008, Department of Civil and Environmental Engineering University of Illinois at Urbana-Champaign, USA.

Goode C.D., (2007), *ASCCS Database of Concrete-Filled Steel Tube Columns*, From:
http://www.northeastern.edu/compositesystems/wiki/ASCCS_Database_of_Concrete-Filled_Steel_Tube_Column_Tests

Goode C.D. and Lam D., (2008), *Concrete-Filled Steel Tube Columns-Tests Compared with Eurocode 4, Composite Construction in Steel and Concrete VI*, Proceedings of the Sixth International Conference on Composite Construction in Steel and Concrete, July 20-24, Colorado, USA, 317-325.

Gourley B.C. and Hajjar J. F., (1993), *A Synopsis of Studies of the Monotonic and Cyclic Behavior of Concrete-Filled Steel Tube Members, Connections, and Frames*, Department of Civil and Environmental Engineering, Institute of Technology, University of Minnesota, Minneapolis, USA.

Gjelsvik A., (1990), *Buckling of built-up columns with or without stay plates*, Journal of Engineering Mechanics, 116, 5, 1142-1159.

Gupta A. and Krawinkler H., (2000), *Dynamic P-delta effects for flexible inelastic steel structures*, Journal of Structural Engineering, ASCE, 126, 1, 145-154.

Hajjar J.F. and Tort C., (2010), *Mixed finite-element modeling of rectangular concrete-filled steel tube members and frames under static and dynamic loads*, Journal of Structural Engineering, ASCE, 136, 6, 654-664.

Hajjar J.F. and Gourley, B.C., (1997), *A cyclic nonlinear model for concrete-filled tubes. I: formulation*, Journal of Structural Engineering, ASCE, 123(6), 736-744.

Hajjar J.F., Molodan, A. and Schiller P.H., (1998), *A distributed plasticity model for cyclic analysis of concrete-filled steel tube beam-columns and composite frames*, Engineering Structures, 20, 4-6, 398-412.

Han L.H., Huang H. and Zhao X.L., (2009), *Analytical behaviour of concrete-filled double skin steel tubular (CFDST) beam-columns under cyclic loading*, Thin-Walled Structures 47, 6-7, 668-680.

Han L.H., He S.H., Zheng L.Q. and Tao Z., (2012), *Curved concrete filled steel tubular (CCFST) built-up members under axial compression: experiments*, Journal of Constructional Steel Research, 74, 63-75.

Han L.H. and Li W., (2010), *Seismic performance of CFST column to steel beam joint with RC slab: experiments*, Journal of Constructional Steel Research, 66, 11, 1374-1386.

Han L.H., Li W. and Bjorhovde R., (2014), *Developments and advanced applications of concrete-filled steel tubular (CFST) structures: Members*, Journal of Constructional Steel Research, 100, 211-228.

Han L.H., Wang W.D. and Tao Z., (2011), *Performance of circular CFST column to steel beam frames under lateral cyclic loading*, Journal of Constructional Steel Research, 67, 5, 876-890.

Han L.H., Yang Y.F. and Tao Z., (2003), *Concrete-filled thin-walled steel SHS and RHS beam-columns subjected to cyclic loading*, Thin-Walled Structures, 41, 9, 801-833.

Harris H.G. and Sabnis G.M., (1999), *Structural Modeling and Experimental Techniques*, 2nd edition, CRC Press, New York, USA.

Hatzigeorgiou G.D., (2008), *Numerical model for the behavior and capacity of circular CFT columns, Part I: Theory*, Engineering Structures, 30, 6, 1573-1578.

Housing and urban-rural development of the People's Republic of China, (2013), *Technical Code of Concrete Filled Steel Tube Arch Bridges*, GB50923-2013, Beijing, China. In Chinese.

Hu H.T., Huang C.S, Wu M.H. and Wu Y.M., (2003), *Nonlinear analysis of axially loaded concrete-filled tube columns with confinement effect*, Journal of Structural Engineering, ASCE, 129, 10, 1322-1329.

Hu H.T., Huang C.S. and Chen Z.L., (2005), *Finite element analysis of CFT columns subjected to an axial compressive force and bending moment in combination*, Journal of Constructional Steel Research, 61,12, 1692-1712.

Inai E., Mukai A., Kai M., Tokinoya H., Fukumoto T. and Mori K., (2004), *Behavior of concrete-filled steel tube beam columns*, Journal of Structural Engineering, ASCE, 130, 2, 189-202.

Japan Road Association, (2002), *Design Specification for Highway Bridges-Part V Seismic Design*, Tokyo, Japan.

Jin M., Zhao J.C., Liu M.L. and Chang J., (2011), *Parametric analysis of mechanical behavior of steel planar tubular truss under fire*, Journal of Constructional Steel Research, 67, 1, 75-83.

Kawano A. and Matsui C., (1988), *An experimental study on hysteretic behavior of concrete filled tubular members under repeated axial loading*, Proceeding of Ninth World Conference on Earthquake Engineering, August 2-9, Tokyo-Kyoto, Japan, IV 133-138.

Kawano A. and Sakino K., (2003), *Seismic resistance of CFT trusses*, Engineering Structures, 25, 5, 607-619.

Kawano A., Matsui C. and Sakino Y., (1996), *An experimental study of the elasto-plastic behavior and deformability of concrete-filled tubular truss beam-columns under cyclic loading*, Journal of Structural and Construction Engineering, AIJ, 482, 141-150. In Japanese.

Kawano A. and Sakino K., (2000a), *Cyclic local buckling and fracture of concrete filled tubular members*, Proceedings of an Engineering Foundation Conference on Composite Construction in Steel and Concrete IV, ASCE, May 28-June 2, Banff, Alberta, Canada, 632-643.

Kawano A. and Sakino K., (2000b), *The deformation capacity of trusses with concrete filled tubular chords*, Proceedings of an Engineering Foundation Conference on Composite Construction in Steel and Concrete IV, ASCE, May 28-June 2, Banff, Alberta, Canada, 734-745.

Kawashima K., (2000), *Seismic design and retrofit of bridges*, 12th World Conference on Earthquake Engineering (WCEE), January 30-February 4, Auckland, New Zealand, No. 2828.

Kent D.C. and Park R., (1971), *Flexural members with confined concrete*, Journal of the Structural Division, 97, 7, 1969-1990.

Kikunaga Y. and Arakawa T., (2012), *The evaluation of dynamic characteristics for a middle rise building made of steel based on measurement data*, 15th World Conference on Earthquake Engineering, September 24-28, Lisbon, Portugal, No. 1032.

Kostic S.M. and Filippou F.C., (2012), *Section discretization of fiber beam-column elements for cyclic inelastic response*, Journal of Structural Engineering, ASCE, 138, 5, 592-601.

Krawinkler H., Mills R.S. and Moncarz P.D., (1978), *Scale Modeling and Testing of Structures for Reproducing Response to Earthquake Excitation*, the John A. Blume Earthquake Engineering Center, Department of Civil Engineering, Stanford University, Stanford, USA.

Kurobane Y., Packer J. A., Wardenier J. and Yeomans N., (2004), *Design Guide For Structural Hollow Section Column Connections*, Comité International pour le Développement et l'Etude de la Construction Tubulaire (CIDECT), Bouwen met Staal, Rotterdam, Netherlands.

Liao F.Y., Han L.H. and Tao Z., (2014), *Behaviour of composite joints with concrete encased CFST columns under cyclic loading: Experiments*, Engineering Structures, 59, 745-764.

Liang Q.Q. and Fragomeni S., (2009), *Nonlinear analysis of circular concrete-filled steel tubular short columns under axial loading*, Journal of Constructional Steel Research, 65, 12, 2186-2196.

Liang Q.Q. and Fragomeni S., (2010), *Nonlinear analysis of circular concrete-filled steel tubular short columns under eccentric loading*, Journal of Constructional Steel Research, 66, 2, 159-169.

Lin S.L., Weng Y.T., Tsai K.C., Hsiao P.C., Chen C.H. and Lai J.W., (2004), *Pseudo dynamic tests of a full-scale CFT/BRB frame: Part 3-Analysis and performance evaluation*, 13th World Conference on Earthquake Engineering, August 1-6, Vancouver, B.C., Canada.

Liu Z. and Goel S.C., (1988), *Cyclic load behavior of concrete-filled tubular braces*, Journal of Structural Engineering, ASCE, 114, 7, 1488-1506.

Luo Y., (2013), *Studies on the Seismic Performance of Four-tube Concrete Filled Steel Tubular Laced Columns*, Thesis: Master, College of Civil Engineering, Central South University, Changsha, China. In Chinese

Maharaj K.K., (1978), *Stochastic characterization of earthquake through their response spectrum*, Earthquake Engineering of Structural Dynamic, 6, 5, 497-509.

Mahin S. and Bertero V., (1975), *An Evaluation of Some Methods for Predicting Seismic Behavior of Reinforced Concrete Buildings*, Vol. 75, Earthquake Engineering Research Center, College of Engineering, University of California, USA.

Makino Y., Kurobane Y., Fukushima A. and Katayama M., (2001), *Experimental study on concrete filled tubular joints under axial loads*, Proceeding of the 9th International Symposium on Tubular Structures, April 3-5, Düsseldorf, Germany, 535-541.

Mander J.B., Priestley, M.J.N. and Park R., (1988), *Theoretical stress-strain model for confined concrete*, Journal of Structural Engineering, ASCE, 114, 8, 1804-1826.

Matsui C. and Kawano A., (1988), *Strength and behavior of concrete-filled tubular trusses*, Proceedings of the International Specialty Conference on Concrete Filled Steel Tubular Structures, August, Harbin, China, 113-119.

Mazzoni S., McKenna F., Michael H., Scott M.H. and Fenves G.L., (2006), *Open System for Earthquake Engineering Simulation User Command-Language Manual*, Pacific Earthquake Engineering Research Center University of California, Berkeley, California, USA.

Menegotto M. and Pinto P.E., (1973), *Method of analysis for cyclically loaded reinforced concrete plane frames including changes in geometry and non-elastic behaviour of elements under combined normal force and bending*, Symposium on the Resistance and Ultimate Deformability of Structures Acted on by Well Defined Repeated Loads, International Association for Bridge and Structural Engineering, Zurich, Switzerland, 15-22.

MIDAS Information Technology Co. Ltd (2010), *Civil 2010 Online Manual*.

Ministero delle Infrastrutture, (2008), *Nuove Norme Tecniche per le Costruzioni DM Infrastrutture 14/01/2008 (NTC 2008)*, Rome, Italy. In Italiano.

Ministry of Transport of the People's Republic of China, (2008), *Guidelines for Seismic Design of Highway Bridges*, JTG/T B02-01-2008, Beijing, China. In Chinese.

Ministry of Transport of the People's Republic of China, (2001), *Chinese Seismic Ground Motion Parameter Zonation*, JB18306-2001, Beijing, China. In Chinese.

Nukala P.K.V.V. and White D.W., (2004), *A mixed finite element for three-dimensional nonlinear analysis of steel frames*, Computer Methods in Applied Mechanics and Engineering, 193, 23-26, 2507-2545.

NZ Transport Agency, (2014), *The NZTA bridge Manual (3rd edition)*, Wellington, New Zealand.

OpenSees, (2013), *The Open System for Earthquake Engineering Simulation [2.4.4]*, Pacific Earthquake Engineering Research Center, University of California, Berkeley, California, USA. <http://opensees.berkeley.edu>.

OriginLab Corporation, (2012), *OriginLab User Guide*, Northampton, Massachusetts, USA. <http://www.originlab.com/doc/User-Guide>.

Ou Z.J., Chen B.C., Hsieh K.H., Halling M.W. and Barr P.J., (2011), *Experimental and analytical investigation of concrete filled steel tubular columns*, Journal of Structural Engineering, 137, 6, 635-645.

Pater V.I., Liang Q.Q., Hadi, M.N.S., (2014), *Numerical analysis of high-strength concrete-filled steel tubular slender beam-columns under cyclic loading*, Journal of Constructional Steel Research, 92, 183-194.

Perea T., (2010), *Analytical and Experimental Study on Slender Concrete-Filled Steel Tube Columns and Beam-Columns*, Thesis: Ph.D., Georgia Institute of Technology, Atlanta, USA.

Popovics S., (1973), *A numerical approach to the complete stress-strain curve of concrete*, Cement and Concrete Research, 3, 5, 583-599.

Rahami H., Kaveh A. and Gholipour Y., (2008), *Sizing, geometry and topology optimization of trusses via force method and genetic algorithm*, Engineering Structures, 30, 9, 2360-2369.

Richart F.E. (1928), *Tests of the effect of brackets in reinforced concrete rigid frames*, Bureau of Standards Journal of Research, 1, 1, 189-253.

Sahoo D.R. and Rai D.C., (2007), *Built-up battened columns under lateral cyclic loading*, Thin-Walled Structures, 45, 5, 552-562.

Sakino K. Nakahara H., Morino S. and Nishiyama I., (2004), *Behavior of centrally loaded concrete-filled steel-tube short columns*, Journal of Structural Engineering, 130, 2, 180-188.

SAS, (1999), *SAS/STAT User's Guide: Introduction to Regression Procedures, Version 8*, SAS Institute Inc., Cary, NC, USA.

Schneider S.P., (1998), *Axially loaded concrete filled steel tubes*, Journal of Structural Engineering, 124, 1125-1138.

Scott M.H., Fennes G.L., McKenna F. and Filippou F.C., (2008), *Software patterns for nonlinear beam-column models*, Journal of Structural Engineering, ASCE, 134, 4, 562-571.

Shanmugam N.E. and Lakshmi B., (2001), *State of the art report on steel-concrete composite columns*, Journal of Constructional Steel Research, 57, 10, 1041-1080.

Sichuan Provincial Communications Department Highway Planning Survey and Design Institute, (2008), *Guide to Design and Construction Technology of Road Steel Tube Concrete Bridge*, Communications Press, Beijing, China. In Chinese.

Structural Engineering Test Center of Southwest Jiaotong University, (2012), *Load Test Report of Ganhaizi Bridge in Highway from Ya'An to Lugu*, Southwest Jiaotong University, China. In Chinese.

Susantha K.A.S., Aoki T. and Hattori M., (2008), *Seismic performance improvement of circular steel columns using precompressed concrete-filled steel tube*, Journal of constructional steel research, 64, 30-36.

Susantha K.A.S., Ge H. and Usami T., (2001), *Uniaxial stress-strain relationship of concrete confined by various shaped steel tubes*, Engineering Structures, 23, 10, 1131-1347.

Tang J, Hino S, Kuroda I and Ohta T., (1996), *Modeling of stress-strain relationships for steel and concrete in concrete filled circular steel tubular columns*, Steel Construction Engineering, JSSC, 3, 11, 35-46.

Tao Z., Uy B., Han L.H. and He S.H., (2008), *Design of concrete-filled steel tubular members according to the Australian Standard AS 5100 model and calibration*, Australian Journal of Structural Engineering, 8, 3, 197-214.

Tao Z., Wang Z.B. and Yu Q., (2013), *Finite element modelling of concrete-filled steel stub columns under axial compression*, Journal of constructional steel research, 89, 121-131.

Taucer F., Spacone E. and Filippou F., (1991), *A Fiber Beam-Column Element for Seismic Response Analysis of Reinforced Concrete Structures*, Vol. 91. 17, Earthquake Engineering Research Center, College of Engineering, University of California, USA.

Tort C. and Hajjar J. F., (2007), *Reliability-Based Performance-Based Design of Rectangular Concrete-Filled Steel Tube (RCFT) Members and Frames*, Structural

Engineering, Report No. ST-07-1, Department of Civil Engineering, University of Minnesota, Minneapolis, Minnesota, USA.

Tsai K.C., Weng Y.T., Lin S.L. and Goel S., (2004), *Pseudo dynamic tests of a full-scale CFT/BRB frame: part 1-performance based specimen design*, 13th World Conference on Earthquake Engineering, August 1-6, Vancouver, B.C., Canada, No. 750.

Tsai W. T., (1988), *Uniaxial compressional stress-strain relation of concrete*, Journal of Structural Engineering, ASCE, 114, 9, 2133-2136.

Tu Y.Q., Shen Y.F., Zeng Y.G. and Ma L.Y., (2014), *Hysteretic behavior of multi-cell T-shaped concrete-filled steel tubular columns*, Thin-walled Structures, 85, 106-116.

Usami T. and Ge H.B., (1998), *Cyclic behavior of thin-walled steel structures-numerical analysis*, Thin-Walled Structures, 32, 1-3, 41-80.

Valipour H.R. and Foster S.J., (2010), *Nonlinear static and cyclic analysis of concrete-filled steel columns*, Journal of Constructional Steel Research, 66, 6, 793-802.

Varma H.A., Ricles J.M., Sause R. and Lu L., (2002), *Seismic behavior and modeling of high-strength composite concrete filled steel tube CFT beam columns*, Journal of Constructional Steel Research, 58, 725-758.

Viest I. M., Colaco J.P., Furlong R.W., Griffis L.G., Leon R.T. and Wyllie L.A., (1996), *Composite Construction Design for Buildings*, McGraw-Hill Professional, New York, USA.

Wardenie J., Kurobane Y., Packer J.A., Van der Vegte G.J. and Zhao X.L., (2008), *Design Guide for Curcular Hollow Section (CHS) Joints under Predominantly Static Loading*, Comité International pour le Développement et l'Étude de la Construction Tubulaire, CIDECT, Bouwen met Staal, Zoetermeer, Netherlands.

Wardenier J., Packer J.A., Zhao X.L. and Van der Vegte G.J., (2010), *Hollow Sections in Structural Applications*, CIDECT, Geneva, Switzerland.

Webb J., (1993), *High-strength concrete: economics, design, and ductility*, Concrete International, 15, 1, 27-32.

Wei J.G., Wu Q.X., Chen B.C. and Wang T.L., (2009), *Equivalent beam-column method to estimate in-plane critical loads of parabolic fixed steel arches*, Journal of Bridge Engineering, ASCE, 2009, 14, 5, 346-354.

Wikipedia, (2014, assessed 30 May 2014), *List of longest arch bridge spans*, from: http://en.wikipedia.org/wiki/List_of_longest_arch_bridge_spans

Wilson E.I., Der Kiureghian A. and Bayo E. P., (1981), *A replacement for the SRSS method in seismic analysis*, Earthquake Engineering and Structural Dynamic, 9, 187-194.

Wu Q.X., Yoshimura M., Takahashi K., Nakamura S. and Nakamura T., (2006), *Nonlinear seismic properties of the Second Saikai Bridge: a concrete filled tubular (CFT) arch bridge*, Engineering Structures, 28, 2, 163-182.

Xiao Y., Zhang Z.X., Kunnath S.K. and Guo P.X., (2011), *Seismic behavior of CFT column and steel pile footings*, Journal of Bridge Engineering, ASCE, 16, 5, 575-586.

Xu W., Han L.H. and Tao Z., (2014), *Flexural behaviour of curved concrete filled steel tubular trusses*, Journal of Constructional Steel Research, 93, 119-134.

Zhejiang Huangyan Testing Apparatus Factory, Homepage website: www.hycsyq.com.

Zheng Y., Usami t. and Ge H., (2000), *Ductility evaluation procedure for thin-walled steel structures*, Journal of Structural Engineering, ASCE, 126, 11, 1312-1319.

APPENDIX

The following papers were written during my Ph.D. research period (chronological order):

a) Journal papers:

1. **Huang Y.F.**, Fan B.K., MU T.M. and Chen B.C., (2011), *Seismic response analysis of Ganhaizi Bridge*, Journal of Harbin Institute of Technology, 43 sup2, 349-352. In Chinese.
2. **Huang Y.F.**, Briseghella B., Zordan T., Wu Q.X. and Chen B.C., (2014), *Shaking table tests for the evaluation of the seismic performance of an innovative lightweight bridge with CFST composite truss girder and lattice pier*, Engineering Structures, 75, 73-86. DOI: 10.1016/j.engstruct.2014.05.039
3. Wu Q.X., **Huang Y.F.** and Chen B.C., (2014), *Shaking tables testing study of lightweight bridge with CFST composite truss girder and lattice pier*, Engineering Mechanics, 31, 9, 89-96. In Chinese. DOI: 10.6052/j.issn.1000-4750.2013.03.0289
4. Wu Q.X., **Huang Y.F.** and Chen B.C., (2014), *Nonlinear seismic performance of lightweight bridge with CFST composite truss girder and lattice pier*, Engineering Mechanics. In Chinese. (In printed). DOI: 10.6052/j.issn.1000-4750.2014.04.0334
5. **Huang Y.F.**, Briseghella B., Zordan T., Wu Q.X. and Chen B.C., (2015), *Experimental and numerical investigation of concrete filled steel tubular (CFST) banded columns under cyclic loading*, Engineering Structures. (Under review)

b) Conference papers:

1. **Huang Y.F.**, Wu Q.X., Chen B.C. and Briseghella B., (2012), *Seismic Analysis of a Rigid Frame Continuous CFST Truss Girder Bridge with Composite Piers*, 5th International Conference on New Dimensions in Bridges, Flyovers, Overpasses & Elevated Structures, July 28-29, Wuyishan, Fujian, China.
2. **Huang Y.F.**, Briseghella B., Liu C.S., Wu Q.X. and Chen B.C., (2013), *Experimental Study on Seismic Performance of a Continuous Bridge with CFST Composite Truss Girder and Lattice High Pier*, 7th National Seismic Conference on Bridges & Highways. May 20-22, Okalnd, USA.

3. Briseghella B., Zordan T., Chen B.C., Xue J.Q. and **Huang Y.F.**, (2013), *Steel Arch Bridges in China*, 24th Italian National Steel Conference, Sep.30-October 1, Torino, Italy.
4. Zordan T., Xue J.Q., **Huang Y.F.** and Briseghella B., (2014), *Italian Road Administration Strategy to Retrofit Existing Bridges Using IABs Technology*, 1st International Conference of Jointless bridge, March 11-12, Fuzhou, Fujian, China.
5. **Huang Y.F.**, Briseghella B., Zordan T., Wu Q.X. and Chen B.C., (2014), *Seismic Performance of an Innovative Concrete Filled Steel Tubular Truss Bridge*, Istanbul Bridge Conference, August 11-13, Istanbul, Turkey.
6. **Huang Y.F.**, Briseghella B., Zordan T., Wu Q.X. and Chen B.C., (2014), *Seismic Analysis of a Concrete Filled Steel Tubular Truss Bridge*, 37th IABSE International Symposium, September 3-5, Madrid, Spain.